OPEN ACCESS

University of BRISTOL

This electronic thesis or dissertation has been downloaded from Explore Bristol Research, http://research-information.bristol.ac.uk

Author:
Fowler, Hamish

Title:
The influence of warm prestressing and proof loading on the cleavage fracture toughness of ferritic steels.

General rights
Access to the thesis is subject to the Creative Commons Attribution - NonCommercial-No Derivatives 4.0 International Public License. A copy of this may be found at https://creativecommons.org/licenses/by-nc-nd/4.0/legalcode This license sets out your rights and the restrictions that apply to your access to the thesis so it is important you read this before proceeding.

Take down policy
Some pages of this thesis may have been removed for copyright restrictions prior to having it been deposited in Explore Bristol Research. However, if you have discovered material within the thesis that you consider to be unlawful e.g. breaches of copyright (either yours or that of a third party) or any other law, including but not limited to those relating to patent, trademark, confidentiality, data protection, obscenity, defamation, libel, then please contact collections-metadata@bristol.ac.uk and include the following information in your message:

• Your contact details
• Bibliographic details for the item, including a URL
• An outline nature of the complaint

Your claim will be investigated and, where appropriate, the item in question will be removed from public view as soon as possible.

THE INFLUENCE OF WARM PRESTRESSING AND PROOF LOADING ON THE CLEAVAGE FRACTURE TOUGHNESS OF FERRITIC STEELS

by

Hamish Fowler

January 1998

A thesis submitted to the University of Bristol
in accordance with the requirements of
the degree of Doctor of Philosophy
in the Department of Mechanical Engineering
in the Faculty of Engineering

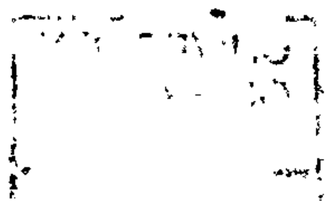

ABSTRACT

This thesis presents a combination of numerical and experimental studies performed to assess the influence of the warm prestress effect on the cleavage fracture toughness of two ferritic pressure vessel steels. The aims of the research are to gain a detailed knowledge of the materials low temperature response under uniaxial and fracture conditions; to examine, using the finite element method, crack tip stress fields during warm prestress LUCF load cycles; and provide a clear and consistent method of classifying the warm prestress effect.

An experimental programme investigated the room temperature and low temperature response of two candidate steels, A533B and BS1501. These steels were tested uniaxially under monotonic and cyclic conditions, and in the cracked condition in the as-received and warm prestressed conditions. Application of a three parameter statistical model to the experimental data showed that the distribution of data in the as received and warm prestressed conditions can be described accurately. The shift in the cleavage toughness distribution following warm prestressing was predicted by combining the statistical model with a validated analytical model of the warm prestress effect. Repeated proof loading was shown to increase cleavage toughness in A533B steel, providing the loading was load controlled. There were negligible effects of repeated proof loading on BS1501 steel. Some further enhancement of cleavage fracture toughness was observed when sub critical crack extension was introduced following warm prestressing, although the results were highly scattered.

The finite element method was employed to simulate experimental fracture events. It was found from these simulations that fracture occurs following warm prestressing, when the reloaded crack tip stress distribution matches the as-received fracture crack tip stress distribution. The stress matching was observed to occur well into the elastic stress field ahead of the crack tip. This fracture criterion was employed to provide predictions of cleavage toughness following varying applied preload levels. The results were compared to experimental data sets and various analytical models. The Chell model of the warm prestress effect was observed to provide the best agreement with the finite element predictions. Crack tip blunting during the preload steps was found to have no influence on the predictions of cleavage fracture toughness. Differences in hardening response of the material was also shown to have little influence of the predictions of cleavage toughness. Simulations incorporating sub critical crack extension prior to reloading to fracture demonstrated that cleavage toughness can be enhanced further by limited crack extension. Large increments of crack growth were shown to reduce the warm prestress effect. The finite element predictions were validated against the appropriate analytical solution proposed by Chell and experimental results.

AUTHORS DECLARATION

This thesis, submitted for the degree of Doctor of Philosophy at the University of Bristol, is entirely the work of the author. No work is the result of collaboration, nor is any work of other researchers used, except where clearly referenced.

The views and opinions expressed in this thesis are solely those of the author and not the University of Bristol.

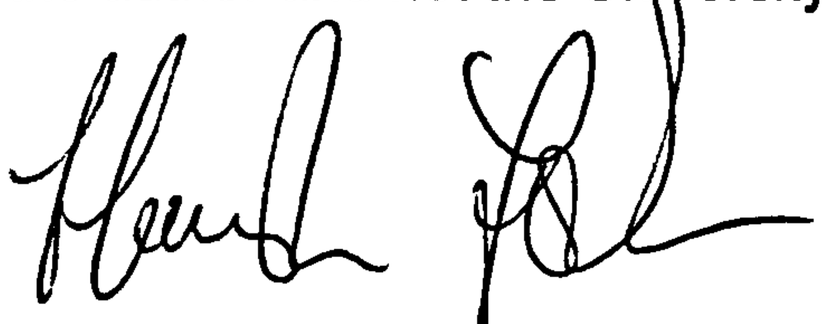

Hamish Fowler

January 1998

ACKNOWLEDGEMENTS

I would like to thank Professor David J. Smith for his guidance and support over the last four years. His Advanced Materials Research Group has provided a lively, cosmopolitan and motivating atmosphere within which it has been a pleasure to work. I would also like to thank the technical staff under Mr. Fred Silk in the Mechanical Engineering Workshop for their support, in particular the late David Ogden, Mr Troy Swankie and Mr. Ian Milnes for their assistance.

The support of The Welding Institute and EPSRC in supplying material and funding the project is also appreciated.

This PhD could not have been completed without the support and encouragement of my wife Lisa and my parents. Their support throughout the time that this thesis was prepared was invaluable. I dedicate this Work to them.

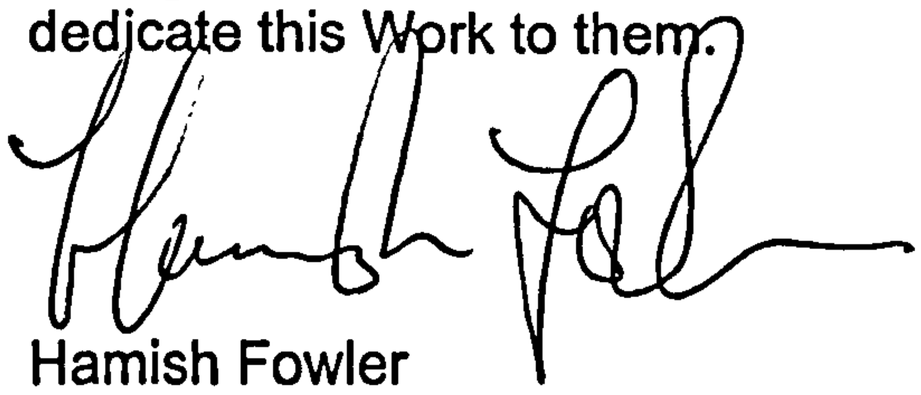

Hamish Fowler

May 1998.

LIST OF FIGURES

Figures in Chapter 2

Figures in Chapter 3

Figures in Chapter 4

Figures in Chapter 5

Figures in Chapter 6

LIST OF TABLES

Tables in Chapter 3

Tables in Chapter 4

Tables in Chapter 5

CHAPTER 1

INTRODUCTION

During the early industrial period, all machinery was driven by pressurised steam plant. Fabrication quality of these early steam pressure vessels was generally low, there being little knowledge of material strength and experience of the required methods of fabrication. This resulted in regular boiler failures, many catastrophic in nature, with loss of human life a common occurrence. The number and nature of the failures quickly became an important issue as they were expensive in terms of cost and human lives. Regional Steam Users Associations formulated vessel proving procedures which became mandatory for insurance purposes. This was reinforced by an act of Parliament, requiring that all pressure vessels have their fitness for purpose demonstrated by way of an overpressure test. The implementation of the proof test resulted in a great reduction in vessel failures over a period where technology was advancing and the vessels were being subjected to increasingly more arduous operating conditions. The proof test became the accepted route for verifying a vessels fitness for purpose in the industrialised nations and involved loading the vessel to approximately 1.5 times the operating load. This inferred that the vessel had a considerable margin of safety at its operating condition, providing the proof test load was similar in nature to the operating loading conditions.

The advent of the *fracture mechanics* technique of classifying defects and flaws allowed the proof test to be used to estimate a maximum critical defect size that could have just survived the over pressure test. Then the window of

crack sizes between the maximum defect size at the operating load and the proof test defect can be determined. The fatigue life of the vessel can then be estimated based on operating pressures and pressure cycling data. This methodology is implemented in assessment procedures such as the Nuclear Electric R6 procedure (Milne et al, 1984) and the British Standards Institution PD 6493:1991 procedure. These procedures are usually used in conjunction with Non Destructive Testing (NDT) results to classify defects in critical regions. Generally, these assessment procedures do not take the cumulative effects of regular proof testing into account.

A large amount of research was performed into characterising proof loading effects with the aid of fracture mechanics in the late 1960's. This research was exclusively experimental, the use of computational methods being prohibitively expensive at this time. Different load histories and materials examined led to a large amount of widely scattered data being accumulated, with no concise method for collating all the results. The different studies led to the various authors formulating differing conclusions as to the controlling factors in the effects of proof loading on the fracture response of the materials. The experimental studies showed that, in general, if the proof test was applied in the same direction as the operating stresses, then the resistance of the component to fracture could be increased. Several studies also demonstrated that the resistance to fracture was reduced by proof loading the component in a direction opposite in sense to the operating stresses.

More recent research in the late 1970's and early 1980's saw the development of analytical models using fracture mechanics approaches to model the effects of proof loading on the fracture behaviour of vessels. These models required a large amount of knowledge of the material properties and defect sizes to characterise the effects of the proof test. Subsequently, the comparisons of the predictive models with the available predictive models was limited to modelling general trends in behaviour. Since these models were presented, few advances have been made in characterising proof loading effects, although several large experimental programs have been performed. The importance of the statistical nature of the problem was not fully investigated and therefore the results of those studies were less conclusive than they may have been.

The aims of the work detailed in this thesis were threefold, formulated to address the issues of scatter, controlling features, such as crack tip blunting or residual stresses, and the method of characterising the effects. Specifically, these aims were:

1. To use experimental methods to determine the low temperature deformation and fracture response of cracked specimens for single and repeated proof loading.
2. To examine, using the finite element method, the influence of proof loading and subsequent low temperature loading on the near crack tip stress and strain fields.

3. To develop a fracture mechanics based model to simulate the influence and evaluate the importance of proof loading and subsequent low temperature fracture on the integrity of a component.

This thesis uses these three main aims as its framework. Following the literature review presented in the next Chapter, Chapters 3 and 4 detail the experimental methods and results. Two different materials were examined under similar loading conditions, using a standard approach, to generate sufficient data to examine the effects of proof loading using a statistical approach. Chapter 5 investigates the proof loading technique using the finite element method and presents results of simulations of experimental fracture events following proof loading. The results of predictions based on the findings of the experimental simulations are also presented.

Chapter 6 analyses the results of the various studies, examining the experimental results of this and previous studies using statistical methods. The results of the finite element simulations are used to examine the existing analytical models of proof loading effects. The analytical approaches are combined with the statistical methods to provide a method for incorporating proof loading effects on fracture toughness into current defect assessment procedures. Chapter 7 forms the main discussion of the thesis, examining all the available data in conjunction with results presented in earlier chapters. Chapter 8 presents the conclusions and an outline for future work that will enhance the work presented within this thesis.

CHAPTER 2.

LITERATURE REVIEW OF WARM PRESTRESSING AND PROOF LOADING STUDIES.

Abstract

The concepts of proof loading and warm prestressing are reviewed, from the initial motivation for proof loading to the recognition of beneficial effects arising from proof loading. The use of the techniques in industry are described and idealised as three discrete load histories. Experimental evidence for the benefits of proof loading and warm prestressing are presented and the effects of possible in service damage mechanisms on the beneficial effects of these cycles assessed. Currently available, fracture mechanics based, predictive models are described in detail and then compared to the experimental evidence.

2.1 INTRODUCTION

Proof loading is a technique used to verify the structural integrity of a component or structure. This technique has been applied to many structures ranging from bridges to pressure vessels and pipelines. The aspects of proof loading investigated within this thesis are related to pressure vessel technology and therefore the review will be limited to this area.

Proof loading has been employed as a strength test since pressure vessels were first used in industry circa 1850 (Harrop, 1983). The only motivation for performing this procedure (which involves loading the vessel to levels exceeding the service load) during this initial period was to prove that the vessel could withstand sustained loading at the operating condition. Early operators were reluctant to perform the strength test, as pressure vessels were generally of low quality. It would prove extremely expensive should a boiler fail before it had entered service. The procedure was also fraught with technical problems and therefore many vessels were left untested. As pressure vessel technology developed, and operating conditions became more demanding, operators found that obtaining insurance was difficult without demonstrating that the vessel in question was strong enough for its' appropriate use. Insurance companies developed their own proof testing procedures and these varied from organisation to organisation. Harrop (1983) in reviewing the early failure rates of pressure vessels, found that only about twenty percent of the vessels in service in the late nineteenth century were insured and therefore regularly inspected. During 1879 one insurance company recorded forty six explosions resulting in forty one deaths. None of these vessels were insured by that particular company. The following year an estimate of the uninsured vessel failure rate was one in three thousand vessels. The failure rate of insured vessels was one in twenty thousand. The government of the day considered the high vessel failure and human mortality rates too high and passed the Boiler Explosion Act in 1882 which markedly increased the number of vessels required to be inspected. The passing of this act halved the vessel failure rate from 5.10^{-4} per boiler year in 1881 to

2.10^{-4} in 1882. The success of the proof testing technique was evident from the figures, and it is interesting to note that the failure rate dropped even during this period of rapid increases in operating pressures and temperatures. During this period, operators were forming associations, to rationalise design and manufacturing techniques. Effective safety assessments were virtually impossible at this time as engineers had little knowledge of stress analysis and the strength of components. Design was based on experience and the early assessment techniques were largely empirical.

Proof testing became accepted as a final part of the manufacturing process and therefore engineering organisations set about standardising the proof testing technique further. Such industry bodies, such as the American Society for Mechanical Engineers (ASME) formed the Boiler and Pressure Vessel Committee in 1911, who's procedures are now the American National Standard. Similar organisations formed in Europe, with the Manchester Steam Users association in the 1850's and the Technischer Überwachungs-Verien (TÜV) in West Germany in 1872, when boiler inspection became a generally accepted procedure.

In Britain, the current proof testing procedure is set down in BS5500. According to this standard, a hydrostatic pressure test must be used to demonstrate, as far as possible, the structural integrity of the pressure vessel. The test pressure must exceed the design operating pressure by at least twenty five percent and by as much as fifty percent. This is achieved via hydraulic pressurisation at water temperatures in the range of 7 to 20°C.

Care must be taken to ensure that the water does not freeze in the narrower sections of the vessel. Specific cases may be tested to lower pressures if it is considered that significant yielding of any component could occur at the higher pressures.

Towards the end of the nineteenth century the importance of sharp cracks and discontinuities (stress concentrations) was realised, and failures due to crack growth mechanisms such as fatigue and stress corrosion cracking were observed as early as 1917 (British Engine Insurance, 1978).

These types of failure were increasingly evident in other industrial components and during the winter of 1942-43 a large number of mass manufactured merchant ships experienced severe failures at welds (Anderson, 1992). Such failures were classified as brittle failures and extensive investigations found that other welded structures such as pressure vessels, penstocks and pipelines failed via the same mechanism. This prompted research into the effect of sharp defects on the strength of structures containing such flaws and lead to the development of *fracture mechanics* techniques. These methods were advanced rapidly in the 1950's and now form the central feature of the safety assessment procedures used for pressure vessels (BSI PD6493,1991).

Burdekin (1982) reviewed the role of proof loading and the use of fracture mechanics techniques in the safety assessment of pressure vessels. The design codes available at the time provided little advice to assess the

likelihood of brittle fracture occurring in a component. A designer was merely cautioned to select a material of 'adequate' toughness for the range of operating conditions expected during service.

The use of the hydrostatic test in identifying poorly manufactured and unsafe pressure vessels were highlighted by Burdekin (1982), who described several failures of pressure vessels during proof testing. The vessels were considered to have received sub-standard post weld heat treatments which caused cracking in the weld and the surrounding areas.

The resistance of a material to failure induced by crack like defects is known as fracture toughness. Consequently, the effects of proof loading on a components structural integrity is measured in terms of the fracture toughness of the material, which is accepted as a material property. Burdekin (1982) suggested that fracture mechanics techniques provide a means of quantifying the combination of crack length, applied loading and material properties which cause fracture. The parameters used to describe the magnitude of the stress field near to the crack tip are, K, applied stress intensity factor, the J - integral and also crack tip opening displacement, δ. When these parameters reach critical values, K_{Ic}, J_{Ic} and δ_{Ic}, failure occurs and the values are treated as material properties and termed toughness. These parameters will be developed in the following sections. (More in depth descriptions can be found in dedicated texts to which the reader is referred (Anderson, 1992)).

A similar approach to proof loading is that of warm prestressing, which aims to introduce favourable compressive residual stresses in the region of an

assumed crack tip. These residual stresses need to be overcome before fracture can occur, and therefore via the increased load bearing capacity of the component, the effective cleavage fracture toughness of the component can be raised. Other influencing factors such as a reduction in the acuity of a crack (blunting of the crack tip) and the work hardening of the material in the region of the crack tip were considered by Nichols (1968) to increase the load bearing capacity of a cracked component. One could speculate that if a prior warm prestress cycle been applied to the structures described by Burdekin (1982) prior to proof testing, the failures during proof testing may have been avoided.

The proof test therefore was developed to assess a components strength at or above it's operating condition. No consideration was initially given to the effects of the overload cycle on the subsequent behaviour. Later studies (Harrison and Fearnehough, 1972, Nichols, 1982) showed that an increase in the components resistance to brittle fracture occurred following the high temperature overload if the material became embrittled over a period of time, or if operated at a temperature on or below the ductile / brittle transition of a ferritic steel. This effect is known as the warm prestress effect.

2.2 OVERLOADING EFFECTS ON UNNOTCHED COMPONENTS.

One of the effects of overloading a component is recognised to be the mechanical relief of residual stresses, generated in the structure during fabrication (Nichols, 1968). Manufacturing process such as welding and hot forming cause residual stresses to develop as the material contracts during cooling. The use of mechanical stress relief was reviewed by Smith and Garwood (1990a) in an overview of warm prestressing studies. Figure 2.1 shows that by applying an overload of magnitude σ_a to a material of yield strength σ_y, the final residual stress σ_r, is given by

$$\sigma_r = \sigma_y - \sigma_a \qquad (2.1)$$

Leggatt and Davey (1987) and Smith and Garwood (1990a) collated experimental data and found that a simple linear - elastic / perfectly - plastic material model led this relationship to overestimate reduction in residual stress. Leggatt and Davey suggested that the applied overload would be only partially effective as distortions caused by the cooling process reduced the effectiveness. The effects of the local geometry on the relief of the residual stresses can expressed by introducing an elastic stress concentration factor (SCF)

$$\sigma_r = \sigma_y - SCF\sigma_{PT} \qquad (2.2)$$

where σ_{PT} is the applied stress transverse to the weld during proof testing. In this situation, the elastic stress concentration factor may not be known. However, Leggat and Davey (1987) measured values of 0.7 to 1.78. As the stress concentration approaches unity, then equation (2.2) tends towards equation (2.1). Nichols (1968) in reviewing the effects of overloading on the residual stress state of welded components, states that the higher the proof stress, the more complete the mechanical relief of the residual stresses will be as more extensive yielding will take place on proof testing. A conservative estimate of the total stress, σ_{tot} , under a service stress also transverse to the weld, σ_{ST}, was given by Leggatt and Davey (1987):

$$\sigma_{tot} = \sigma_y - SCF(\sigma_{PT} - \sigma_{ST}) \qquad (2.3)$$

The expression within the brackets in equation (2.3) will always be positive since a prime requirement of the proof test is that it's magnitude exceeds that of the service stresses. Therefore the total stress must be less than the yield stress, regardless of the value of the stress concentration factor. The study by Leggatt and Davey (1987) also highlighted the importance of measuring residual stresses locally as well as across the global structure. Smith and Garwood (1990a) observed that residual stress measurements taken globally provided lower peak stresses than those measured locally to the defect or weld. Based on experimental results equation (2.2) can be seen in Figure 2.2 to provide more conservative assessments of the peak residual stresses than equation (2.1).

The mechanical stress relief brought about by proof loading is regarded by Nichols (1968) to be of primary importance in the motivation for proof loading a component, especially where thermal stress relief methods may not be easily performed. A drawback of proof loading to stress relieve a component is that while it may increase the load bearing capacity, the ductility will not be altered as in thermal stress relief.

2.3 PROOF TESTING AND WARM PRESTRESSING OF CRACKED COMPONENTS.

Yukawa (1969) described the effects of proof testing by detailing a pressure vessels' resistance to different sized flaws at different pressures and temperatures, Figure 2.3. The vessel is constructed from a ferritic steel, where the fracture resistance exhibits a strong temperature dependence as shown in Figure 2.3. The vessels design operating conditions are temperature T_2 and pressure P_1. If the vessel is overloaded to pressure P_2, which is approximately 1.25 to 1.5 P_1, at temperature T_1 and does not fracture or show significant deformation, then it can be inferred that the structure does not contain any 'large' defects. At the operating conditions, there is now known to be a considerable margin of safety, and that excursions to pressures up to the proof test can be withstood. A maximum possible flaw size at critical sections can be evaluated from this pressure test, and subsequent safety analyses would be based on this postulated largest flaw. Proof testing at the operating temperature would also illustrate it's safety, but the maximum estimated flaw size could be larger than actually exists. However, the risks associated with overloading a structure at temperatures where the risk of brittle fracture is high do not justify the associated reduction

of uncertainty in flaw size. Therefore, proof testing is not usually performed at temperatures lower than the operating conditions.

Warm prestressing is similar in application to proof testing, but the motivation to perform the cycle is much different. Warm prestressing is used to enhance a component's resistance to fracture by modifying the stress field ahead of a postulated crack tip. An inherent assumption of the process is that a significant flaw exists. Consider the critical pressure distribution for a large flaw in Figure 2.3. By applying an overload to pressure P_2 at temperature T_3, where the risk of brittle fracture is low, the basic premise of warm prestressing is that fracture cannot occur at T_1 or T_2 until pressure P_2 has been exceeded.

An important feature in the application of both proof loading and warm prestress load cycles is that they should act in the same sense as the operating stress (Nichols, 1968). If the applied stress during preload were opposite in sense to the service stress, the residual stresses will act in the same sense as the operating stress and the total service stress would be higher than the actual applied service stress. This would thereby increase the risk of fracture at the operating condition. If the proof stress is performed at higher temperatures than the operating temperature, then this will also constitute a warm prestress cycle.

In order for a warm prestress benefit to be conferred on the pressure vessel, the yield properties of the material are required to increase following unloading from the prestress. The increase in yield strength associated with

embrittlement through temperature (or other mechanisms described in later sections) prevents further yielding taking place until additional loads higher than the prestress have been applied (Harrison and Fearnehough, 1972).

Warm prestressing effects may be imparted to a structure due to accidental thermal cycles. One such scenario is a Loss Of Coolant Accident (LOCA) in Pressurised Water Reactors (PWR) described by Harrop (1979) . The reactor vessel operating temperature increases beyond it's design level. While maintained at load, yielding will occur as the material has now a lower yield stress. When coolant is restored the vessel will return to operating conditions, sometimes with severe thermal shock. The vessel, if not damaged by the overload at high temperature, will have had it's integrity improved and any defects that have evolved since the last proof test will have been subjected to a warm prestress, providing the prestress acts in the same sense as the operating stress. As mentioned previously, a proof load at temperatures where the material flow properties are low with subsequent operation at lower temperatures constitutes a warm prestress. The mechanism by which the material may become embrittled is not necessarily a temperature change. Neutron embrittlement, strain ageing and hydrogen embrittlement are all acknowledged mechanisms that increase the yield strength and decrease the ductility of ferritic steels (Yukawa, 1969).

2.4 EFFECT OF WARM PRESTRESSING ON CRACK TIP CONDITIONS.

2.4.1 Load History Idealisation.

To describe the effects of complex loading histories, some idealisation of the actual cycles is required. There are three different load cycles that have been considered in the past to define the limiting bounds of warm prestressing (Andrews, 1970). These are shown in Figure 2.4 and discussed below.

(i) Load - Cool - Fracture (LCF). The specimen is loaded to the proof test level, cooled to the test condition and then fractured.

(ii) Load - Cool - Unload - Fracture (LCUF). The specimen is loaded to the proof stress level, cooled to the test temperature and unloaded. The specimen is then reloaded to fracture.

(iii) Load - Unload - Cool - Fracture (LUCF). The specimen is loaded and unloaded at high temperature then cooled to the test temperature. The specimen is then reloaded to fracture.

In service, the choice of prestress history would be dependent on the operating conditions of the vessel, difficulties associated with the application of the proof load, and cost. The LUCF cycle is the most common laboratory cycle applied (Smith and Garwood, 1990a) as it represents an idealisation of the proof test load cycle and the warm prestress cycle of a vessel that has been proof tested and then subjected to lower temperature or had become embrittled.

2.4.2 Experimental Evidence for the Warm Prestress Phenomenon.

Over the last three decades there has been a considerable number of experimental studies performed with the intent of identifying the causes and effects of warm prestressing, such as those by Brothers and Yukawa (1963) on Ni-Mo-V steel, Andrews (1970) on A508 steel, Loss, Gray and Hawthorne (1978) on A533B, Smith and Garwood (1990b) on A533B and Reed and Knott (1992) on A533B weld metal. Periodic reviews of warm prestressing such as those of Nichols (1968), Pickles and Cowan (1983) and Smith and Garwood (1990a) have collated and discussed many data sets. Several of those sets previously reviewed, plus work published since the last critical review in 1990 by Smith and Garwood, will be discussed here.

2.4.3 Effects of Notches on the Influence of Prestrain.

Steigerwald (1961) investigated the effects of notches on the influence of prestraining. By uniformly prestraining bars and then machining notches in, and comparing the results to prestrained notched bars, the work hardening effects discussed by Nichols (1968) could be isolated. Steigerwald (1961) found that prestraining only influences the behaviour of the specimen if the notch was present during prestraining. Further corroborative results as to the importance of residual stresses were obtained from experiments where the prestrain temperature was increased: the specimens prestrained at higher temperatures were observed to have lower subsequent cleavage toughness. This was attributed to the residual stresses being limited by a low yield stress value at the higher temperature. Steigerwald (1961) states that the most effective prestrains were those applied at the lowest temperature possible and to the maximum level possible.

2.4.4 Effect of Applied Load Cycle.

Andrews (1970) studied the effects of different loading histories on the fracture behaviour of A508 steel. The specimens were heat treated to four different conditions in order to simulate the various interior locations in water quenched thick walled forgings. The three cycles described above were applied to three point bend bars and the results compared to specimens tested in the non prestressed conditions. The results, normalised by the cleavage fracture toughness in the non-prestressed condition, can be seen in Figure 2.5. The LCF cycle is shown to increase the load bearing capacity (and hence effective cleavage fracture toughness) by the largest degree, with LCUF results being bounded by the LUCF and LCF cases. The LUCF cycle was shown to provide the lowest benefit in terms of increased load bearing capacity with respect to applied preload level. Brothers and Yukawa (1963), who examined the LUCF cycle only, illustrated that there was a point beyond which the fracture strength no longer increased in proportion to the prestress level, as seen in the LCF case by Andrews (1970). This prestress level was identified as that at which tearing was induced. In their review, Smith and Garwood (1990a) showed by compiling all the available data that this limit in benefit for increased prestress levels was consistent throughout all the studies. In order to describe the effects more fully Harrison and Fearnehough (1972) considered the stress / strain response of the material in the region of the crack tip. This theory is illustrated in Figure 2.6 and described below.

A specimen that was fractured at lower shelf temperatures has a fracture stress σ_f, and yield strength σ_{y2}. The specimen is loaded to fracture at this temperature via path ABC. The material yields by a small degree and then fractures at σ_f. At the prestress temperature, T_1, the material has yield strength σ_{y1}.

If the specimen is subjected to an LCF cycle, with the prestressing occurring at T_1, then the material follows path ABD on initial loading. The specimen is then held at this load level while cooled to the fracture temperature, T_2 and then loaded to fracture. The overall loading path is therefore ABDF. As it can be seen, additional load is required to cause the required additional plasticity before the fracture stress is reached. This is due to the state of stress equilibrium developed by the elastic-plastic processes at the prestraining temperature. This equilibrium persists at the lower temperature until further load is applied and additional plasticity can occur (Cottrell, 1987). In many cases, Andrews (1970) found that only a small increase in applied load is needed to cause fracture. Therefore, the material, provided that it has been prestressed to a stress intensity factor higher than it's as-received plane strain fracture toughness at low temperature, will have had its fracture toughness increased by this load cycle.

Consider the LUCF cycle shown in Figure 2.6 (the cycle that confers the lowest increase in toughness). The initial loading path is, say, ABD. The structure is then unloaded to zero load, path DE, and the material being examined is forced into compression, unloading elastically.

On reloading to fracture, the material reloads via path EDF. Fracture cannot occur until the fracture stress is reached at F below the notch. Since the general load applied is roughly proportional to the local strain, a load in excess of the preload must be applied before the local fracture stress can be reached. However, if the preload strains are high, say path ABG, then on unloading the bulk material forces the local material into compression and subsequent reversed plastic flow takes place, path GHJ. The total load - unload path is ABGHJ and the magnitude of the residual stress is limited by the value of the compressive yield stress. On reloading to fracture the material reloads along path JK. It can be seen that although the load to cause fracture in this case is greater than the load to cause fracture when the unloading was purely elastic, the relative increase in comparison to the preload level is much less. This provides an explanation for the reduction in benefit relative to the applied preload seen by the experimental investigations of the warm prestress effect.

The phenomenon described for the LUCF case also holds for the LCUF case, except that larger returns on prestress will be expected. On unloading, the materials yield strength is increased and therefore less reversed plastic flow occurs for a given load when compared to the LUCF cycle. The above descriptions do not consider the Bauschinger effect. The Bauschinger effect (Bauschinger, 1886) is a phenomenon where a materials yield strength in compression is reduced from the virgin level if the material has been

prestrained in tension. If a material exhibits a strong Bauschinger effect, then this would encourage more reversed yielding to occur.

2.4.5 Effect of Compressive Preload Cycles.

Harris et al (1986) investigated the effects of compressive preloading on subsequent cleavage fracture toughness on A508 specimens subjected to four point bending. Compressive prestressing was found to reduce the load bearing capacity below the as-received value and the authors suggest that this reduction was due to tensile residual stresses being introduced on unloading. Therefore, a reduced applied tensile stress would be required for the total stress to reach the critical cleavage fracture stress. Nakamura and Tsuya (1977) also performed compressive preloading studies on structural steel four point bend fracture specimens. Figure 2.7 contrasts data from Harris et al (1986) with those of Nakamura and Tsuya (1977). The results are normalised by the non-prestressed fracture loads. Compressive prestraining is shown by both investigations to be detrimental. However, Harris et al (1986) observed a more pronounced drop in load bearing capacity than Nakamura and Tsuya (1977) for the compressive prestrains. Reed and Knott (1996) also found that compressive prestress cycles decreased the subsequent fracture load in blunt notched specimens. By normalising the fracture load by the calculated collapse load of the specimen, Reed and Knott (1996a) categorised their results in terms of the percentage of general yielding or collapse load fraction at which fracture occurred. Reed and Knott (1996a) demonstrated that the decrease observed in subsequent percent change of collapse load fraction at fracture after a compressive LUCF cycle

was greater than the increase observed in collapse load fraction at fracture following a tensile LUCF cycle.

The usefulness of the LCF and LCUF cycles in practical applications are limited and in general the LUCF cycle is applied when proof testing components. The LCF cycle does however illustrate the influence of prior plasticity on the toughness. Harrison and Fearnehough (1970) compared the fracture stress distribution of a virgin specimen at low temperature with the stress distribution developed on preloading at high temperature to a higher stress intensity factor than the K_{1c} value. On testing at low temperature, the specimen requires additional loading before the critical fracture stress is reached.

Harrison and Fearnehough (1970) suggested from LCF results that the benefit was not associated with the introduction of residual compressive stresses. They explained that the benefit from the LCF was likely to be caused by the formation of large plastic zones at the crack tip which modified the stress distribution at fracture as compared with a virgin specimen. The decreased return in the increase in cleavage toughness for increasing preload following an LUCF cycle was attributed to reversed plastic flow, generated on unloading. Harrison and Fearnehough (1970) concluded from this that reversed plastic deformation reduces the degree of enhancement in cleavage toughness with increased preload. Reed and Knott (1996a) found that by overloading uncracked tensile specimens, the effects of warm prestressing on a materials' yield stress and fracture stress could be

evaluated. The materials' yield strength was observed to increase with increasing preload, however no difference was observed between the LUCF and LCF results. They found that the nominal fracture stress at -196°C of an A533B weld metal was significantly reduced by high levels of prestrain following LUCF and LCF cycles. Reed and Knott (1996a) concluded that this may counteract the increase in fracture toughness brought about by the residual stresses generated by the warm prestress cycle. The plastic strain imposed during a preloading event was therefore considered to be deleterious to the warm prestress effect.

2.4.6 Influence of Thermal Stress Relief and Strain Ageing on the Warm Prestress Effect.

The degree by which the near crack tip residual stress influences the warm prestress effect has been investigated by thermally stress relieving specimens that have been warm prestressed. Stress relief makes use of the fact that the yield stress of a material decreases as the temperature is raised. If a welded joint is heated to, say, 600°C, the residual tensile stress, which was equivalent to the yield stress at room temperature is in excess of the yield stress of the metal at 600°C. Localised plastic deformation occurs and the tensile residual stresses are reduced. At the same time, the compressive residual stresses which were in equilibrium with the tensile stresses are also reduced, to restore the equilibrium. In stress relieving practice, the temperature is raised until the yield stress has fallen to a low value at which residual stresses can no longer be supported. This clearly depends on the metal being treated since the relationship between yield stress and

temperature is critically influenced by alloy content. BS5500 (1985) recommends stress relief temperatures for a range of pressure vessel steels.

Succop et al (1970), Beremin (1977), Nakamura et al (1981) and Reed and Knott (1992) all indicate that a reduction in cleavage fracture toughness following thermal stress relief compared to warm prestressed, non-stress relieved specimens. Succop et al (1970) examined A516 and A533B steels, Beremin examined A508 steel and Nakamura et al examined A533B steel. Reed and Knott studied A533B weld metal. Following stress relief, Reed and Knott (1992) show a total loss of benefit and the toughness equal to the as-received cleavage fracture toughness following six hours exposure, whereas Beremin (1977), Succop et al (1970) and Nakamura et al (1981) show a partial reduction in benefit. The stress relief temperatures were between 593°C and 650°C for these studies and the exposure times ranged from 1.5 hours to 8 hours. Sugino, Pense and Stout (1979) studied a range of steels (A533B, A508, A516 and A515 steels) and found that the effect of stress relief was dependant on the specific steel. It was noted that A533B and A508 steels showed a slight increase in toughness following stress relief treatment performed after straining precracked compact tension specimens (Sugino et al, 1979). Therefore, it appears that near crack tip residual stresses provide a major contribution to the warm prestress effect following an LUCF cycle.

Concern for the effect of prolonged exposure of pressure vessels to temperatures which may cause ageing prompted investigations into the effect of strain ageing on the stability of the warm prestress effect. Strain ageing is

a type of behaviour in which the strength of a metal is increased and the ductility is decreased on heating at a relatively low temperature (200°C) after prestraining. Pense et al (1960), Yukawa (1969), Harrison and Fearnehough (1970) and Satoh, Toyoda and Mutoh (1983) performed investigations in to the effect of strain ageing on the warm prestress effect. The results of these studies depended on the ageing temperature, duration of exposure, and different material. Yukawa (1969) found that for A302B and A533B steels mild strain ageing may be experienced for temperatures between 200 and 370°C. Pense et al (1960) observed only a small shift in the transition temperature of A302B steel these higher temperatures. Strain ageing studies by Yukawa (1969) found that prestressing at temperatures where strain ageing has been observed was more deleterious on the warm prestress effect than strain ageing after a preload at room temperature. Satoh et al (1983) found that specimens prestrained at higher temperatures and those strain aged were subject to the initiation of cleavage cracking at temperatures higher than those in the as-received condition. A significant reduction in cleavage toughness was also observed for those specimens prestressed compared to the as-received specimens. Ductile crack initiation was found to occur at lower deformation levels than the as-received material. Sugino et al (1979) found that stress relief following strain ageing had no effect on the toughness of A533B steel. Succop et al (1970) found that the combination of uniform prestrain and ageing reduced the as-received fracture toughness of A516 steel. When strain ageing followed warm prestress cycles of low level, the toughness was reduced further. Following higher level warm prestress cycles, the effect of ageing and stress relief was not so large as to reduce the

toughness to as-received levels. Overall, warm prestress effects are diminished following strain ageing as shown in Figure 2.8

2.4.7 Influence of Crack Tip Blunting on the Warm Prestress Effect.

The complete removal of the warm prestress effect by thermal stress relief found by Reed and Knott (1992) suggests that crack tip blunting is not as significant a factor as suggested by Nichols (1968) and Sugino et al (1979) where the reduction of the severity of the crack tip was credited with 45% of the warm prestress benefit. Studies by Harris et al (1980) on blunt notched specimens also suggest little effect from crack tip blunting. By examining blunt notched specimens, where the percentage change in notch radius during prestressing will be small, the relative influence of blunting was evaluated. Harris et al (1980) conclude that as the same warm prestress effect was conferred in blunt notched specimens as in sharp notched specimens and therefore blunting played a minor role. Reed and Knott (1992) presented evidence that a microcrack blunting mechanism may have an influence on the warm prestress effect. They observed that the cleavage failure event was initiated by 'small' inclusions rather than 'large' inclusions in the same locality. These 'large' inclusions were observed to be de-cohered (micro-cracks had formed) from the surrounding ferrite matrix. The micro-cracks had not propagated into the matrix, i.e., the cracks had blunted out.

Pokrovsky et al (1992), studying a number of structural steels and weld metals, presented results that pointed to crack tip blunting contributing significantly to the warm prestress effect. At preload levels of K_1 / K_{Ic} less

than 0.6, the crack tip opening displacement after warm prestressing (δ_{res}) increased as preload was increased. The final CTOD (δ_c) at fracture after warm prestressing also increased. At preload levels of K_1 / K_{Ic} greater than 0.6, δ_{res} and δ_c both remained constant. Pokrovsky et al (1992) reached an overall conclusion that residual stresses appeared to have no effect on the warm prestress benefit observed for those steels examined. These results are therefore not in agreement with the majority of studies presented above. The results are, however, presented for fracture in the transition regimes, which suggests that there is a warm prestress phenomenon in these regimes for the steels examined. The mechanism that provides the benefit appears to be related to the crack tip opening displacement.

2.4.8 Effect of Constraint on the Warm Prestress Effect.

The effect of constraint on the as-received cleavage fracture toughness of ferritic steels is well known (Anderson, 1992) and has been examined experimentally by Ingham et al (1989), who showed that for a particular temperature the mean or lower-bound fracture toughness at cleavage decreased with increasing specimen size. The probability of obtaining cleavage fracture in specimens, or components, is influenced by two phenomena: firstly the materials inherent resistance to cleavage (it's toughness) and secondly the way in which applied stresses are distributed throughout the body. If the material has low toughness or if high levels of stress intensification occur, then the probability of failure is high. Both of these phenomena also contribute to the frequently observed effect that, at a

given temperature within the brittle - ductile transition regime, increasing specimen size decreases the average fracture toughness at failure. Material properties are important in the sense that heterogeneous materials have a distribution of toughness properties ranging from 'tough' to 'weak'. Consequently, larger specimens have an increased statistical probability of sampling localised regions of 'weak' material, which could trigger global fracture of the specimen under applied load. Similarly, levels of constraint are generally higher in large specimens leading to suppression of yielding and higher stress intensification. Ingham et al (1989) demonstrated the size effect on toughness in the transition regime.

The influence of constraint on the warm prestress effect has been examined by Sankey (discussion at end of Brothers and Yukawa, 1963). The discussion was based on the influence of constraint on the warm prestress effect, i.e., that thinner components, closer to a state of plane stress would, for a given level of preload, experience more plasticity than thicker specimens that could be regarded as being in plane strain. A comparison of the warm prestress effect in thin specimens and thick specimens is given in Figure 2.9. The introduction of large scale plasticity in thin specimens would invalidate the use of linear elastic fracture mechanics parameters being employed to evaluate the effects of warm prestressing (Smith and Garwood,1990a).

2.4.9 Effects of Repeated Proof Loading on Cleavage Fracture Toughness.

It is common practice for pressure vessels and pipelines to be subject to repeated proof testing as part of a maintenance schedule or as an insurance

requalification, following any major repair or modifications to a component. This procedure can be expensive both in terms of time and cost and may present the operator with awkward technical problems. It is therefore cost effective to eliminate unwarranted repeated proof testing and identify where repeated proof testing is desirable. The influence of repeated proof testing on the warm prestress effect has been investigated by Pokrovsky et al (1992) who found, for the structural steels examined there was a reduction in the fracture toughness following up to 200 warm prestress cycles. This reduction was attributed to embrittlement at the crack tip due to damage effects under cyclic loading. Arndt et al (1997) performed finite element simulations of repeated preloading events. Their simulations included two factors never previously implemented in FE studies of the warm prestress effect, namely a combined large deformation cyclic plasticity material model and a damage model for ductile crack extension. The material model was designed to simulate a kinematically hardening material. The analyses showed that repeated preloading events develop a residual stress distribution similar to that obtained by Smith et al (1992) for a single preloading event. Arndt et al (1997), did not perform simulations of fracture following warm prestressing, and as such, the effects of damage accumulation and cyclic plasticity models on the warm prestress effect remain undefined.

2.5 PREDICTION OF CLEAVAGE FRACTURE TOUGHNESS FOLLOWING WARM PRESTRESSING AND PROOF LOADING.

2.5.1 Analysis of Monotonically Loaded Cracked Components.

The basis of the currently available predictive models of the warm prestress effect is the principle of plastic superposition proposed by Rice (1968) when describing analytical models of fatigue crack growth. By invoking this principle, Rice was able to use continuum mechanics to describe crack tip stress, strain and displacement fields in different loading states, combine them and provide a final solution for the crack tip fields at that load state,, The method is simplified by assuming that the material responds in an elastic / perfectly plastic manner and that no Bauschinger effect is exhibited by the material. Rice (1967) described the stress, strain and displacement fields for a cracked body subjected to a monotonic load by the following equations.

$$\frac{\sigma_{ij}}{\sigma_y} = \Sigma_{ij}\left[\frac{r}{a}, \theta, \frac{\sigma_{app}}{\sigma_y}\right] \qquad (2.4a)$$

$$\frac{\varepsilon_{ij}}{\varepsilon_y} = E_{ij}\left[\frac{r}{a}, \theta, \frac{\sigma_{app}}{\sigma_y}\right] \qquad (2.4b)$$

$$\frac{u_i}{\varepsilon_y a} = U_i\left[\frac{r}{a}, \theta, \frac{\sigma_{app}}{\sigma_y}\right] \qquad (2.4c)$$

where r and θ are polar co-ordinates centred on the crack tip, a is the half crack length, σ_{app} is the remotely applied stress and σ_y and ε_y are the yield strength and strain of the material respectively. Σ_{ij}, E_{ij} and U_i are dimensionless functions of their arguments. The square brackets represent function statements. Providing that the components of the stress and strain tensors remain in constant proportion to each other during the loading cycle, the plastic superposition principle can be applied to describe the response of

a structure under cyclic loading conditions (Rice, 1967; Chell and Curry, 1981).

2.5.2 Analysis of Cyclically Loaded Cracked Components.

The use of the theories developed in section 2.5.1 can be extended to cyclically loaded structures by invoking the principal of plastic superposition (Rice, 1967). This principle can be demonstrated in the following manner, Figure 2.10. Assume that the material has a yield strength σ_y in tension and $-\sigma_y$ in compression. The stress state after being overloaded and then unloaded to some load (say the service load) can be considered as the sum of the states of the crack at the two different loading states. State 1 is described as the state of the body when under an applied load of level P_1, Figure 2.10a. A plastic zone of size R_1 forms. State 2, Figure 2.10b, is described as the state of the body when the original cracked body is subjected to an applied load of $-\Delta P$. The material has an effective yield strength of $-2\sigma_y$. A plastic zone of size R_2 forms at this load level, and is smaller than R_1 because of the higher effective yield stress for this load step. The net result is shown in Figure 2.10c by superimposing states 1 and 2 and describes the residual stress state imposed by loading to P_1 and unloading by level ΔP.

This method allows the stress states following warm prestress and proof loading cycles to be estimated and predictions have been developed on this principle by Chell et al (1981), Curry (1981) and Smith and Garwood (1990b).

Chell et al (1981) superimposed displacements within the plastic deformation zones formed during the loading cycle. The model proposed by Curry (1981) is based on the superposition of the stress states, in a manner similar to that described by Figure 2.10. The Smith and Garwood model is an adaptation of the Curry model and considers the stress state at some point in the singular stress field where the stress is dependent on strain hardening.

The LUCF cycle has three possible outcomes with regard to the relative plastic zone sizes formed by loading and unloading at high temperature and reloading at a lower temperature, illustrated in Figure 2.11. These three outcomes are categorised as Case 1, Case 2 and Case 3 as follows.

Case 1 occurs when the plastic zone formed on initial loading at temperature T_1, (size S_1) is bigger than the plastic zone formed on unloading (size S_2). The plastic zone formed on reloading to fracture at low temperature (size S_3) is contained within plastic zone S_2.

Case 2 occurs when S_1 contains plastic zone S_3 which is greater than S_2, i.e. on reloading at low temperature the plastic zone wipes out the residual plastic deformation zone S_2 formed on unloading at the prestress temperature.

Case 3 occurs when, on reloading, the plastic deformation, S_3, wipes out both the unloaded plastic deformation, S_2, and the plastic deformation formed on initial loading, S_1. The stress, strain and displacement states for all these three cases can be defined via equations (2.4a-c).

For case 1, therefore, the stress state, at the applied stress, σ_{app}, (state 1) is simply given by

$$\frac{\sigma_{ij}}{\sigma_{y1}} = \Sigma_{ij}\left[r/a, \theta, \frac{\sigma_{app}}{\sigma_{y1}}\right] \qquad (2.5a)$$

The stress state of the component following complete unloading from σ_{app} (state 2), is given by

$$\frac{\sigma_{ij}}{2\sigma_{y1}} = \Sigma_{ij}\left[r/a, \theta, \frac{\sigma_{app}}{2\sigma_{y1}}\right] \qquad (2.5b)$$

The stress state of the component, when subjected to the failure stress, σ_f, (state 3) is given by

$$\frac{\sigma_{ij}}{\sigma_{y1}+\sigma_{y2}} = \Sigma_{ij}\left[r/a, \theta, \frac{\sigma_f}{\sigma_{y1}+\sigma_{y2}}\right] \qquad (2.5c)$$

The resultant stress state, state 4, is found by adding equations (2.5a, 2.5b and 2.5c) as follows

state 4 = state 1 - state 2 + state 3 (2.5d)

The above methodology can be applied to any combination of loading or temperature cycle. Chell et al (1981) and Curry (1981) develop the solutions for displacements and stresses respectively for cases 1, 2 and 3 of the LUCF cycle and the analogous cases within the LCF and LCUF cycles.

2.5.3 Prediction of cleavage fracture with no prior load history.

The stress state described by the above method can now be combined with a suitable cleavage fracture criterion to predict the load at which fracture can occur. One such criterion that is well established and validated as a cleavage fracture criterion is the Ritchie, Knott and Rice (RKR) model. Ritchie et al (1973) assume that the cleavage fracture event is stress controlled, and that fracture will occur when the normal stress ahead of the crack tip achieves a critical fracture stress, σ_f^* across a micro-structurally critical distance X_o. These two parameters are experimentally determined and are assumed to be material properties. Ritchie, Server and Wullaert (1979) determined the critical fracture stress and micro-structural distance for two pressure vessel steels. The fracture stress intensity factor for a cracked component was then determined by Ritchie et al (1979) analytically using the Hutchinson (1968), Rice and Rosengren (1968) expressions (or HRR) expressions for the stress, strain and displacement fields ahead of a crack tip in a hardening material in conjunction with the Ritchie, Knott and Rice (1973) model of cleavage fracture. The so-called HRR fields scale with the applied J - integral, which, in the small scale yielding regime is proportional to the applied stress intensity factor. By assuming that the applied stress intensity factor, K, equals the

critical stress intensity factor, K_{Ic}, when the normal stress σ_{yy} achieves the critical fracture stress σ_f^* over the critical micro-structural distance X_0, the fracture load can be determined for a given component. Ritchie et al (1979) concluded that this critical distance was approximately equal to two grain diameters. Curry and Knott (1976) showed that the cleavage fracture stress increases with the grain size of the material. Continuum descriptions of the crack tip states can therefore be linked to the micro-structural behaviour of the material.

Anderson and Dodds (1991) proposed another cleavage fracture criterion for steel. Under small scale yielding conditions, when the crack tip stresses and strains are uniquely characterised by the *J* - integral, the onset of fracture is uniquely defined by a critical value of *J*, irrespective of the mechanism of failure. When *J* dominance is lost (the crack tip stress and strain fields no longer increase in proportion to each other) the critical *J* values are size dependent. The magnitude of the size dependence is reliant upon the mechanism by which failure occurs, for example, if failure occurs via a critical strain mechanism, the size dependence will be different from that exhibited by a steel fracturing via a critical stress mechanism.

Again, the crack tip stress and strain fields must be related to a local fracture criterion before fracture can be predicted. The RKR model described earlier has been superseded by a number of micromechanical models based on weakest link statistics (Wallin et al, 1984, Lin et al , 1986, Anderson and Stienstra, 1989). Weakest link statistical models assume that cleavage is

initiated by the largest or most favourably orientated fracture triggering particle, such as a grain boundary carbide. The actual trigger event involves a local Griffith instability of a microcrack formed by the carbide(s) or inclusion(s); the Griffith energy balance is satisfied when a critical stress is reached in the vicinity of the microcrack. The size and location of the critical micro-structural feature dictate the fracture toughness; thus the cleavage toughness is subject to considerable scatter. The statistical sampling nature of cleavage fracture initiation (i.e., the probability of finding a critical micro-structural feature near the crack tip) suggests that the volume of the process zone is also important. Anderson and Dodds (1991) therefore express the probability, F, of cleavage fracture in a cracked specimen in the following general form:

$$F = F[\sigma_1, V(\sigma_1)] \tag{2.6}$$

where σ_1 is the maximum principal stress at a point and $V(\sigma_1)$ is the cumulative volume sampled where the principal stress is greater than or equal to σ_1. For a specimen in plane strain, the volume, $V = BA$, where A is the cumulative area on the x-y plane. Anderson and Dodds (1991) used dimensional analysis to show that the principal stress ahead of the crack tip can be written as

$$\frac{\sigma_1}{\sigma_y} = f\left[\frac{J}{\sigma_y r}, \theta\right] \tag{2.7}$$

where r is the radial distance from the crack tip and θ is the angle from the crack plane. Equation (2.7) can be re-written in terms of the radius corresponding to a given stress and angle:

$$r\left[\sigma_1/\sigma_y, \theta\right] = \frac{J}{\sigma_y} g\left[\sigma_1/\sigma_y, \theta\right] \tag{2.8}$$

Solving for the area inside a specific principal stress contour gives

$$A\left[\sigma_1/\sigma_y\right] = \frac{J^2}{\sigma_y^2} h\left[\sigma_1/\sigma_y\right] \tag{2.9}$$

Thus, for a given stress, the area scales with J^2 when small scale yielding prevails. Anderson and Dodds (1991) then develop the large scale yielding result, where the area inside a given principal stress contour is less than that predicted from small scale yielding for a given J value, due to the loss of constraint. By the introduction of a constraint factor, ϕ (less than or equal to 1), an *effective* J in large scale yielding is defined that relates the area inside the principal stress contour to the small scale yielding case.

$$A\left[\sigma_1/\sigma_y\right] = \phi \frac{J^2}{\sigma_y^2} h\left[\sigma_1/\sigma_y\right] \tag{2.10}$$

If J_{ssy} is the effective small scale yielding J ; that is the J that would result in the area $A[\sigma_1 / \sigma_y]$ if the structure were large compared to the plastic zone size, then the ratio of the applied J to the effective J is given by

$$\frac{J}{J_{ssy}} = \sqrt{\frac{1}{\phi}} \qquad (2.11)$$

The ratio of J/J_{ssy} quantifies the size dependence of cleavage fracture toughness.

2.5.4 Superposition of Displacements to Assess Warm Prestress Effects.

The model proposed by Chell (1979) superimposes the displacements within the plastic zones formed at each loading state and relates the displacements to the J - integral via the relationship

$$J = \sigma_y \delta \qquad (2.12)$$

The displacement δ is defined as the crack tip opening displacement, evaluated using the strip yield model. The strip yield model was developed by Dugdale (1960) for a cracked component in plane stress. The evaluated J -integral is then related to the plane strain fracture toughness and failure is assumed to occur when

$$J = K_{Ic}^2 (1-\nu^2) / E \qquad (2.13)$$

The definition of the J - integral within this model is markedly different to that commonly used in fracture mechanics analyses, where total strains and displacements are included in the calculation. Consider an LUCF case 1 load history. The final plastic zone at fracture is contained within the plastic zone formed on unloading at high temperature and the initial plastic zone formed on initial loading. The plastic deformation imposed on initial loading and unloading are no longer true plastic zones at low temperature, due to the associated rise in yield stress with the temperature decrease. These zones therefore become zones of residual plastic deformation, where plastic flow is unable to occur until the stress within these zones is raised above the low temperature yield stress. Chell et al (1981) demonstrated this by considering the deformations zones as regions where dislocations are mobile and immobile at the fracture temperature, Figure 2.12. Within the final plastic zone, dislocations are mobile and free to move elastically. Outside this zone, within the residual deformation zones formed on loading and unloading, the dislocations are unable to move. On this basis, Chell et al (1981) evaluate the J - integral around a contour shrunk onto the boundary between the regions where the dislocations are mobile and the region where dislocations are immobile. This modified J - integral is termed the J_e - integral. This J_e- integral represents the force acting on the region where plasticity is possible, i.e. the plastic zone at fracture and when $J_e = J_{Ic}$, failure is assumed to occur. Since J_{Ic} is proportional K_{Ic}, the fracture criterion becomes

$$J_e = K_{Ic}^2 (1-\nu^2) / E \tag{2.14}$$

The modified J_e - integral is given by

$$J_e = \int_{\Gamma} \left(W dx - \sigma_{ij} \beta_{ij}^e dS_i \right) \tag{2.15}$$

where β_{ij}^e is the elastic distortion tensor, dS an arc length and W is the strain energy density, given by

$$W = \int \sigma_{ij} d\beta_{ij}^e \tag{2.16}$$

The contour Γ is illustrated in Figure 2.13 and encloses only those regions where plastic flow can occur. This contour integral is path dependant if the contour cuts through part of the plastic zone because the component of force associated with the excluded plasticity does not contribute to the integral.

As mentioned earlier, the displacements used to evaluate this J - integral are determined using the strip yield model proposed by Dugdale (1960). The yielding ahead of the crack tip is considered to lengthen the crack by the extent of the yielded region, S, for a cracked component in plane stress. Stresses of yield magnitude, σ_y are assumed to restrain the extended crack surface. Figure 2.13 shows a schematic representation of the plastic deformation ahead of the crack tip for case 1 using the strip yield model. The displacement discontinuity, $\varphi(x)$, across the plastic and residual zones at the point x is given by the addition of three displacements, $\varphi_{ij}(x)$, arising from the three independently derived states, Figure 2.14 (Chell, 1980). The ij subscript

refers to the loading path that has been followed during a particular step. For example, the displacement at the end of step 1 will be denoted $\varphi_1(x)$, whereas the displacement and the end of step 2, unloaded from state 1 will be $\varphi_{21}(x)$

Thus for case 1:

$$\varphi(x) = \varphi_1\left(x,\sigma_1,\sigma_{y1}\right) - \varphi_{21}\left(x,\sigma_1-\sigma_2,2\sigma_{y1}\right) + \varphi_{32}\left(x,\sigma_3-\sigma_2,\sigma_{y1}+\sigma_{y2}\right) \quad (2.17)$$

similarly for case 2:

$$\varphi(x) = \varphi_1\left(x,\sigma_1,\sigma_{y1}\right) + \varphi_{31}\left(x,\sigma_3-\sigma_1,\sigma_{y2}-\sigma_{y1}\right) \quad (2.18)$$

and for case 3 the solution is simply made up of the final load step:

$$\varphi(x) = \varphi\left(x,\sigma_3,\sigma_{y2}\right) \quad (2.19)$$

where

$\varphi_1(x) = 0, x > a_1$; $\varphi_{21}(x) = 0, x > a_2$; $\varphi_{32}(x) = \varphi_{31}(x) = \varphi_3(x) = 0, x > a_3$

and $a_i = c + S_i$, where c is the crack length and S the plastic zone size. The plastic zone for the final step in case 1 is defined as $c < x < a_3$ and hence J_e

must be evaluated along a path Γ_3 enclosing this region, Figure 2.13. The strip yield model defines the modified J_e - integral as

$$J_e = \sigma_{y2} \{ \varphi[c] - \varphi[a_3] \} \tag{2.20}$$

where $\varphi[c]$ is the displacement at the crack tip and $\varphi[x]$ is given by equations (2.11) - (2.13), Chell (1980). Setting equation (2.14) equal to J_{Ic}, the critical value at T_3 provides the failure criterion under warm prestress conditions. Chell (1980) then shows the displacements φ of the extended crack surface at a distance x within the plastic zone S to be

$$\varphi(x, K, \sigma_y) = \frac{(1-\nu^2)K^2 F\left[\frac{x}{S}\right]}{E\sigma_y} \tag{2.21}$$

where

$$F(z) = (1-z)^{1/2} - \frac{z}{2}\ln\left|\frac{1+(1-z)^{1/2}}{1-(1-z)^{1/2}}\right|, \quad 0 \le x \le S \tag{2.22}$$

Chell (1980) offers equation (2.15) as applicable to extended cracks in arbitrary structures subject arbitrary loading conditions and also to extended cracks in axi-symmetric geometries and penny shaped cracks subjected to arbitrary radially symmetric loading conditions. Equation (2.15) provides a

powerful tool for the assessment of warm prestressing effects. If, in equation (2.15), $x = S_3$, the size of the plastic zone at failure in a component in plane strain, then for case 1

$$S_3 = \frac{\pi}{8}\frac{K_3^{\ 2}}{\left(\sigma_{y1} + \sigma_{y2}\right)^2} \tag{2.23}$$

For case 2:

$$S_3 = \frac{\pi}{8}\frac{\left(K_3 - K_1\right)^2}{\left(\sigma_{y2} - \sigma_{y1}\right)^2} \tag{2.24}$$

and for case 3 simply

$$S_3 = \frac{\pi}{8}\frac{K_3^2}{\sigma_{y3}^2} \tag{2.25}$$

The analytical models obtained by Chell for cases 1, 2 and 3 when equations (2.23) - (2.25) are substituted into equations (2.17) - (2.19) and equation (2.20), provide expressions for J_e (i.e., K_3) that includes K_3 in the function F. Therefore, a solution can only be obtained by resorting to numerical methods. However, Chell (1980) proposed an approximation for the function $F(z)$.

$$F(z) = (1 - z)^2 \tag{2.26}$$

By setting $K_f = K_3$, this approximation yields the following expressions for K_f for cases 1, 2 and 3.

Case 1:

$$(K_f - K_2)^2 = (\sigma_{y1} + \sigma_{y2})^2 K_1^2 \times \left(\frac{(\sigma_{y2} - \sigma_{y1})(K_1 - K_2)^2}{2\left(K_1^2(\sigma_{y1} + \sigma_{y2})^3 - (K_1 - K_2)^2 \sigma_{y1}^3\right)} \times \left[\left\{ \sqrt{1 + \frac{4K_{Ic}^2 (K_1^2(\sigma_{y1} + \sigma_{y2})^3 - (K_1 - K_2)^2 \sigma_{y1}^3)}{\sigma_{y2}(\sigma_{y2} - \sigma_{y1})^2 K_1^2 (K_1 - K_2)^2_{tt}}} \right\} - 1 \right] \right) \quad (2.27)$$

Case 2:

$$(K_f - K_1)^2 = \frac{(\sigma_{y2} - \sigma_{y1})^2 K_1^2}{\sigma_{y1}^2} \left(\frac{(\sigma_{y1} + \sigma_{y2})}{2\sigma_{y1}} \times \left[1 - \sqrt{1 - \frac{4\sigma_{y1}^3 K_{Ic}^2}{\sigma_3 (\sigma_{y1} + \sigma_{y2})^2 K_1^2}} \right] \right) \quad (2.28)$$

and for case 3,

$$K_f = K_1 \quad (2.29)$$

Figure 2.14 compares the experimental data of Loss and Hawthorne (1977), Reed and Knott (1992) and equation (2.27).

It should be noted that for an in-service assessment, exact material properties, local applied stress intensity factors and crack size, shape and distribution can only be estimated. Therefore, the assessor would have to provide predictions for all three cases and infer the change in toughness due to warm prestressing from the lowest result. These approximate solutions have been shown by Chell to be accurate to within 1%. Smith and Garwood (1990b) assessed the degree by which the numerical solutions and the

approximated solutions were in agreement and it was found that at low temperatures, the differences were not large. As the fracture temperature increased, the approximate solution deviated significantly from the numerical result. The original derivation of the above models uses flow stress (the average of the yield and ultimate strengths) rather than the yield stress. For the majority of pressure vessel steels, which are high strength and low strain hardening materials, the flow stress is replaced with the yield strength. If the material exhibits a high degree of strain hardening then the flow stress should be used.

Changes in flow stress provide the principle reason for the occurrence of a warm prestress benefit since areas of residual plastic strain are formed as discussed earlier. These contribute only indirectly to the failure parameter J_e and Chell's (1980) proposed theory of warm prestressing is therefore applicable to any situation where a change in yield stress occurs while a structure is under load.

The proposed models were developed with respect to stationary cracks that do not extend following the warm prestress load cycle. Any such sub-critical crack growth is assumed to directly redistribute the residual stresses and strains. A final assumption is that the failure event must be cleavage type failure. The small scale yielding assumption in relating J_e to K_I may also be violated during the preloading event and the use of the plane stress strip yield model in the formulation of the predictive model may also lead to

inaccuracies. The models also neglect the Bauschinger effect and the possibility of non-proportional unloading.

Chell and Haigh (1986) investigated the sensitivity of the models to the input variables and concluded that the criterion is relatively insensitive to the absolute value of the applied preload stress intensity factor and principally dependent only on the relative changes in the applied stress intensity factors, i.e., only on the degree of unloading relative to the applied preload stress intensity factor. The dependence of the predictions on the cleavage fracture toughness of the material in the embrittled condition (i.e. after any radiation or ageing effects have been accounted for) showed a similar degree of influence as the load / unload stress intensity factor ratio. The influence of the value of yield stresses used within the models was found to be limited, inferring that the need for exact values of yield stress (or flow stress) is not great when assessing any warm prestress effect on a structure in service. It is necessary that the yield stress increases as temperature decreases. Nevertheless Chell and Haigh (1986) provide a 'lower bound' equation, which is based on experimental results and the above conclusions that eliminates yield stress entirely from the model, and is only dependant on K_1 and K_{1c}.

$$\frac{K_f}{K_{Ic}} = 0.2\frac{K_1}{K_{Ic}} + 0.87 \qquad (2.30)$$

To summarise, Chell and co-workers have developed a model, based on the superposition of elastic displacements within the regions of residual plastic deformation. The model is applicable when small scale yielding conditions

prevail and no sub - critical crack extension takes place between unloading and reloading to fracture. The final failure mechanism must be cleavage fracture. Simplified empirical relationships are proposed, to eliminate the requirement of detailed knowledge of the material properties at the critical region.

2.5.5 Superposition of Stresses to Predict Fracture Toughness following Warm Prestressing.

Curry (1981) proposed a model based on the plastic superposition of stresses following the conclusions of Harrison and Fearnehough (1970) that the warm prestress benefit occurred via the requirement that the residual crack tip stress system needed to be modified before fracture could occur at low temperature. The central fracture criterion is the RKR model (Ritchie et al, 1973) described earlier. The RKR criterion can be summarised via the following relationship:

$$\sigma_{yy}[X] \geq \sigma_f^*, X \leq X_0 \qquad (2.31)$$

Curry then applied this criterion to the finite element stress distribution for a loaded crack tip in plane strain, in an elastic plastic material with a hardening exponent, *n*, of 0.1. Tracey (1976) presented this stress field in terms of normalised distance ahead of the crack tip, $X(\sigma_y/K)^2$ versus the local stress intensification σ_{yy}/σ_{ys}. Since K_{Ic} and σ_f , are known, the micro-structural distance X_0 can be calculated. Using the same method of plastic

UNIVERSITY OF BRISTOL LIBRARY

superposition as Chell et al (1979), the stress distribution at a crack tip in a non-work hardening material subjected to several load reversals (such as warm prestressing) may be obtained by the superposition of appropriate monotonic loading distributions, as described earlier following the method proposed by Rice (1967).

The different load cases are again discretised into LCF, LCUF and LUCF cycles and the different solutions presented by Curry (1981). For the LUCF cases 1,2 and 3 analysed in section 2.7 the equivalent solutions are as follows:

For case 1 the final plastic zone is smaller than both the initial plastic zone formed on preloading and the plastic zone formed by reversed yielding on unloading. The final plastic zone forms with an effective yield stress of $(\sigma_{y1}+\sigma_{y2})$. Therefore, the final plastic zone will be smaller than the unloading plastic zone if the following inequality is true:

$$\frac{K_f}{(\sigma_{y2}+\sigma_{y1})} < \frac{K_1}{2\sigma_{y1}} \qquad (2.32)$$

The stress distribution at fracture is therefore given by the superposition of the appropriate loading, unloading and reloading stress distributions as follows:

$$\sigma_{yy}[K_f] = \sigma_{yy}[K_1,\sigma_{y1}] - \sigma_{yy}[K_1,2\sigma_{y1}] + \sigma_{yy}[K_f,(\sigma_{y1}+\sigma_{y2})] \qquad (2.33)$$

In case 2, the plastic zone at fracture is larger than the unloading plastic zone but smaller than the initial loading plastic zone. During the final load step the effects of unloading are completely wiped out and the final plasticity develops under a loading equivalent to (K_f - K_1) and with an effective yield stress of (σ_{y2} -σ_{y1}). Hence the final stress distribution at fracture involves contributions from the initial load step and the reloading step at low temperature.

$$\sigma_{yy}[K_f] = \sigma_{yy}[K_1, \sigma_{y1}] + \sigma_{yy}[(K_f - K_1), (\sigma_{y2} - \sigma_{y1})] \qquad (2.34)$$

Finally, when the final plastic zone becomes larger than the initial plastic zone formed on prestressing, the effects of prior plasticity are removed and the warm prestressing does not influence the final stress distribution. These solutions for the final stress state following warm prestressing are then combined with the RKR criterion and the normalised stress distributions of Tracey (1976) for a work hardening material and Ostergren (1969) for an elastic perfectly plastic material to provide predictions for K_f.

Smith and Garwood (1990c) incorporated the analytical solution for the stress distribution ahead of a loaded crack tip in a strain hardening material (Hutchinson, (1968), Rice and Rosengren, (1968)) into equations (2.33) and (2.34) to provide an analytical solution for a warm prestressed component.

For case1,

$$\frac{K_f}{K_{Ic}} = \left(\frac{\sigma_{y1}}{\sigma_{y2}}\right)^{m/q} \left\{1 - \left(\frac{\sigma_{y1}}{\sigma_{y2}}\right)^{m} \left(\frac{K_1}{K_{Ic}}\right)^{q} (1 - 2^m)\right\}^{1/q} \qquad (2.35)$$

where $m = (n-1)/(n+1)$ and $q = 2/(n+1)$. It is assumed that the micro-structural critical distance, X_o, is unchanged throughout the warm prestressing cycle and subsequent low temperature service. This method therefore incorporates hardening into the model to predict the final fracture toughness. Smith and Garwood (1990c) showed that the predictions were relatively insensitiye to changes in n. The model is also insensitive to the final fracture temperature. Figure 2.14 compares experimental data to the predictions of equation (2.35).

2.5.6 A Reference Stress Model to Predict Fracture Toughness following Warm Prestressing.

Smith and Garwood (1990c) proposed a model to predict the warm prestress effect, based not on the local crack tip stress and strain distributions, but on a reference stress in the net section of the component. Smith observed that there is a point in a singular crack tip field where the stress is approximately independent of the hardening exponent, n, of the material. This point is called the reference stress point, X_R, and the stress at X_R is called the reference stress, σ_R. The reference stress analysis method was originally used within creep studies, whereby a uniaxial test can be performed and the reference strain can be measured at a reference stress. This provides an overall measure of the deformation of the component. Within the current framework, the reference stress approach is used to provide an approximate description of the global behaviour that leads to differences between prestressed and non-prestressed components. The reference stress is generally limited by the value of the materials yield stress and is usually some fraction of the yield

stress. This fraction is conventionally determined by the ratio of the applied load P_{app} to the collapse load P_{col}, of the component. The reference stress approach to modelling the effects of warm prestressing simply modifies the analytical solution obtained by Smith and Garwood (1990c) for the model proposed by Curry (1981). The ratio K_f/K_{Ic} is replaced by the ratio σ_{Rf}/σ_{Rc} in equation (2.35) to yield the following result:

$$\frac{\sigma_{Rf}}{\sigma_{Rc}} = \left(\frac{\sigma_{y1}}{\sigma_{y2}}\right)^{m/q} \left\{1 - \left(\frac{\sigma_{y1}}{\sigma_{y2}}\right)^{m} \left(\frac{\sigma_{R1}}{\sigma_{Rc}}\right)^{q} \left(1 - 2^{m}\right)\right\}^{1/q} \qquad (2.36)$$

where σ_{Rc} is the critical reference stress without warm prestressing at the fracture temperature, σ_{Rf} is the failure reference stress following warm prestressing and σ_{R1} is the proof load reference stress. By definition, the reference stress at fracture cannot exceed the yield stress at the fracture temperature nor can the proof load reference stress exceed the yield stress at the proof load temperature. Therefore, strict limits on the benefits and proof load levels are set using this approach enabling a structure to be proof loaded with no possibility of gross yielding occurring in the structure. Figure 2.14 compares the reference stress model (equation 2.36) to experimental data.

2.5.7 Comparison of Predictive Models.

Both the Chell and Curry models proposed earlier do not have any limiting bounds as regards the proof load or fracture load levels. Between the limits imposed by the yield stresses at the appropriate temperatures, the Curry

model and the Smith and Garwood model are identical. Both K and σ_R are load based parameters and therefore the two models yield identical results. The range of application of equation (2.36) is much more limited than either the Chell or Curry models however. As the fracture temperature increases, the ratio of the proof load reference stress to the critical reference stress tends to unity and equation (2.36) will tend towards

$$\frac{\sigma_{Rf}}{\sigma_{Rc}} = \left(\frac{1}{2}\right)^{m/q} \left\{1-\left(1-2^m\right)\right\}^{1/q} \qquad (2.37)$$

Equation (2.36) is therefore limited to either high preload levels or to lower preload levels where fracture occurs on the lower shelf. Figure 2.14 illustrates the relative predictions of the three models described above. The following material properties were used in evaluation of each of the models. The yield strengths at room temperature and –170°C were 500 MPa and 810 MPa respectively. The cleavage toughness at –170°C was assumed to be 47.4 MPa$\sqrt{m}$. A hardening exponent of n =10 and critical reference stress, σ_{Rc}, of 155 MPa were used in to evaluate the reference stress model proposed by Smith and Garwood (1990c) (equation 2.36). The Curry Model used a critical micro-structural distance of X_0=57 μm.

2.5.8 Prediction of Warm Prestress Effects Following Sub-Critical Crack Extension.

The models of warm prestressing discussed above are subject to some restrictions. Firstly, the mechanism of failure should be by cleavage and

secondly that there should be an increase in flow stress of the steel between the warm prestress load cycle and final fracture. There is no restriction on the mechanism by which the yield stress increases. It could occur by cooling or as a result of embrittling mechanisms such as strain ageing and irradiation damage. There is a further implicit assumption in the three approaches discussed above, namely that there should be no sub critical crack growth between the time of warm prestress cycle and final fracture. The latter is not a problem in the application of warm prestress cycles to the thermal shock of pressure vessels, but could be of considerable importance in the assessment of a proof tested pressure vessel.

Chell (1986) extends his theory of warm prestressing described above to include the effects of sub – critical crack growth occurring at the temperature the vessel or component is at following unloading from the prestress. Chell (1986) presents solutions for a range of warm prestress load cycle, crack extension histories and temperature differentials between prestress and fracture events.

The predictions for each of these different analytical models all followed the same trends. Specifically, the cleavage fracture toughness following warm prestressing and sub critical crack extension was shown to be elevated above its value in the absence of crack extension, providing that the crack extension was not greater than the compressive yield zone that forms at the crack tip following warm prestressing.

Chell (1986) also predicted that failure could occur during crack growth under constant load following warm prestress, because the new tensile yielding produced by crack extension under a stress intensity factor K_2, is sufficiently high that the failure criterion expressed in equation (2.12) is satisfied. This situation was found to occur when

$$\frac{K_{3\cdot}}{K_{Ic}} = \left(\frac{K_2}{K_1}\right)\left(\frac{K_1}{K_{Ic}}\right) \qquad (2.38)$$

2.6 SUMMARY OF LITERATURE REVIEW.

The preceding review of warm prestressing and proof loading studies has shown that there is a large amount of experimental and analytical data available to the engineer to assess the influence of proof loading and warm prestressing on cleavage fracture toughness of ferritic steels. „The experimental data available has been obtained using a variety of specimen geometries, from fracture toughness specimens such as the CT and SENB specimens to uniaxial round bar tensile specimens, for investigation of the effect of warm prestressing on the tensile properties of ferritic steels. Where the prestress direction was in the same sense as the operating load (tensile), then depending on the load history applied, the cleavage fracture toughness is enhanced to a greater or lesser degree. If the prestress was compressive in nature then the cleavage toughness was shown to be reduced. Analytical models based on continuum mechanics and micro structural investigations have been developed by various investigators and these have been used successfully to predict the trends in the influence of warm prestressing and proof loading on cleavage fracture toughness of ferritic steels. However, the application of these models to predict the behaviour of the steels accurately has been shown to be difficult, due to the inability of the models to cope with inherent scatter in material properties. The use of finite element analysis to date in simulating the effects of warm prestressing and proof loading is limited, the conclusions again being limited to observing general trends.

The aims of this study are therefore to investigate the warm prestress and proof loading effects using a combination of finite element simulations and experimental studies to identify the controlling factors in the warm prestress phenomenon. It is intended to develop a fracture mechanics based approach that will enable the comprehensive modelling of warm prestress effects in the cleavage fracture regime where scatter in material properties is high.

CHAPTER 3.

EXPERIMENTAL METHODS AND MATERIALS.

Abstract

.The effects of warm prestressing load histories on two ferritic pressure vessel steels, BS1501 steel 490Gr B LT50 and A533B steel-1 are investigated. Both these materials have been extensively examined and characterised, with much data available in the literature. The apparatus and methods used in this testing programme are described together with details of analysis techniques.

3.1 MATERIALS

3.1.1 BS1501 490Gr B LT50 Steel.

BS1501 Steel is a structural Carbon Manganese (C-Mn) steel used in the fabrication of pressure vessels. This material was chosen after consultation with the sponsoring parties of the project through The Welding Institute (TWI), Cambridge. An extensive material characterisation program was performed on this material prior to the launch of this project (Smith, 1986). TWI provided the material from end pieces of large scale specimens previously tested. The chemical composition of the particular plates obtained by TWI is given in table 3.1 and is compared to the British Standard specification for the material. Due to the extensive information already available on this materials' as-

received properties, a limited study on as-received properties was performed to ensure that results were consistent with the previous work. The material is generally of medium strength with high ductility at room temperature. Fully brittle fracture behaviour is observed below -110°C.

3.1.2. A533B - 1 Steel.

A533B steel is also a ferritic steel, and is more commonly used in the fabrication of reactor pressure vessels in Pressurised Water Reactor (PWR) nuclear power installations. This material was also supplied by TWI, again extensively studied in the as-received and warm prestressed conditions as part of a previous project (Smith and Garwood, 1990b). Only a limited test program in the as-received condition was required to confirm the results obtained in the previous studies before embarking on the proof loading test program. The chemical composition of the material is given in table 3.2. This steel is of higher strength than BS1501 steel with a high ductility at room temperature. Fully brittle behaviour is exhibited below approximately -150°C.

3.2 TEST PROCEDURES.

All testing performed was carried out on an Instron 1342 test frame of 250 kN capacity, with an environment chamber capable of cryogenic temperatures. Load and displacement data was recorded on an XY chart recorder and also a personal computer. The data logging rate was about three data pairs per second.

3.2.1 Uniaxial Tensile Testing.

Tensile testing was performed using standard uniaxial round bar specimens shown in figure 3.1. The tests were performed under strain control, with the extensometer attached to the gauge section of the specimen as shown in figure 3.2. In order to determine the tensile response of the materials at temperatures below ambient, a climatically controlled environment chamber was placed around the specimen and liquid nitrogen was introduced to the chamber by way of valves controlled by thermocouples. The temperature of the specimen was monitored using spot welded thermocouples. This arrangement provided temperature control to within ±2°C. It should be noted that the thermocouple attached to the specimens had no direct control over the chamber temperature. During cooling to the required temperature, the specimen was maintained at constant load to ensure that no thermal stresses were introduced.

Three loading cycles were investigated so that the tensile response of the steels to complex load / temperature histories could be evaluated. These were:

(i) monotonic loading at 20°C, -70°C, -120°C and -170°C;

(ii) strain controlled cyclic testing at these temperatures;

(iii) Load - Unload - Cool - Reload cycles akin to those used in warm prestressing load cases.

3.2.2 Fracture Toughness Testing.

To determine the cleavage fracture toughness of a material it was necessary to test precracked specimens. All the tests performed within this study were carried out following the guidelines laid down in BS5447 (1991). As such, the specimen geometry was chosen as Compact Tension (CT), illustrated in figure 3.3. The specimen thickness of 25 mm was limited by the size of the clevis grips used on the test frame. The extensometer used to monitor the displacement of the specimen was a standard clip gauge attached to knife edges fixed to the specimen, figure 3.4. Some A533B steel specimens were of a thinner section of 6mm. These tests were performed to examine the effects of constraint on the warm prestress effect. All fracture toughness test specimens, to provide valid toughness results should be of specified minimum thickness, defined in BS5447 (1991) as

$$B, a_0 \geq 2.5\left(\frac{K_Q}{\sigma_y}\right)^2 \qquad (3.1)$$

where K_Q is the stress intensity factor based on the load at which the load versus displacement trace as a gradient of 95 % of the gradient of the initial linear portion of the curve, or the **maximum load** achieved in the case of purely elastic fracture. For A533B steel fractured at -170°C, the minimum thickness that provides valid K_{Ic} results is 5.2 mm, based on the minimum toughness value presented by Smith and Garwood (1990b). At -120°C the minimum thickness for BS1501 steel specimens is 31 mm. Therefore, the 25 mm thick BS1501 steel specimens tested at this temperature violate the minimum thickness requirements for valid K_{Ic} results. All specimens failed by

cleavage fracture however, with no evidence of shear lips or ductile fracture and therefore the results are regarded as acceptable.

Prior to testing, all the BS1501 Steel specimens were fatigue precracked from the machined notch at room temperature according to BS7448 (1991) to an initial nominal crack depth of 25mm giving a crack length to width (a/W),ratio of 0.5. The fatigue precracking stress intensity factor was between 24 MPa√m and 28.5 MPa√m. Some later specimens had a 'crack' introduced by the wire electric discharge machining (edm) technique. This provided a notch of width 0.1mm and was found to provide comparable results to the fatigue precracked specimens. The wire edm method was much faster than the fatigue precracking technique (10 minutes compared to 4 hours), and provided a straight crack front. The only drawback is that material was physically removed and the 'crack' faces could not be in contact and therefore could not transmit compressive stresses. It was assumed that the edm process did not introduce residual stresses in the region of the crack tip.

To determine the fracture toughness of the material in the as-received condition, the specimen was placed in the rig with the clip gauge and thermocouple attached. The chamber was then closed and any gaps filled with ceramic wool. The chamber was cooled to the required temperature using the liquid nitrogen apparatus described above. Fracture toughness testing of BS1501 steel was performed at -70°C and -120°C, with the A533B steel being tested at -170°C. These temperatures were selected to be consistent with the previous studies carried out at TWI.

Following fracture, the specimen was measured on a MONDO '3D' measurescope, which magnifies the specimen to enable accurate non contacting measurement of the crack length and specimen dimensions can be made. Some specimens were sectioned, mounted in acrylic and polished for metallographic studies. Once polished, the surfaces were etched using a 2% Nital solution to reveal the grain structure of the material. Fracture surfaces were examined using a Hitachi S-2300 scanning electron microscope.

3.2.3 Analysis Methods.

Fracture toughness was evaluated in terms of plane strain fracture toughness, K_{Ic}, according to

$$K_{Ic} = \frac{P_{max}}{B\sqrt{W}} f\left(\frac{a}{W}\right) \qquad (3.1)$$

where P_{max} was the maximum load attained and $f(a/W)$ is defined as follows for a CT specimen:

$$f\left(\frac{a}{W}\right) = \frac{2+\frac{a}{W}}{\left(1-\frac{a}{W}\right)^{3/2}}\left[0.886+4.64\left(\frac{a}{W}\right)-13.32\left(\frac{a}{W}\right)^{2}+14.72\left(\frac{a}{W}\right)^{3}-5.60\left(\frac{a}{W}\right)^{4}\right] \qquad (3.2)$$

The elastic - plastic fracture mechanics parameter J_{Ic} was also evaluated from the results, according to ASTM E813-92 (ASTM, 1992).

For estimation purposes the J integral is divided into elastic and plastic components:

$$J = J_{el} + J_{pl} \tag{3.3}$$

The elastic component is evaluated from the elastic stress intensity factor via the relationship

$$J_{el} = \frac{K^2\left(1-\nu^2\right)}{E} \tag{3.4}$$

where K is calculated using equation (3.1). The plastic component is then computed by evaluating the plastic area, A_{pl}, under the load displacement trace, figure 3.5.

$$J_{pl} = \frac{\eta A_{pl}}{Bb_0} \tag{3.5}$$

where b_0 is the initial ligament length, η is a dimensionless constant dependant on the geometry of the specimen. For a compact tension specimen this is given by

$$\eta = 2 + 0.522b_o / W \tag{3.6}$$

The plastic area under the load / displacement trace was obtained using the trapezoidal rule. The critical J_{Ic} values were converted to equivalent K_{Jc} values using the equation

$$K_{Jc} = \sqrt{\frac{J_{Ic}E}{(1-\nu^2)}} \qquad (3.7)$$

This approach enables equivalent stress intensity factors to be evaluated when there has been significant plastic deformation prior to fracture and LEFM assumptions have been violated.

3.3 SPECIMEN PROOF LOADING

All preloading events were performed at ambient temperature, where the materials are ductile and therefore can withstand loads well beyond yield strength. The procedures were largely determined by previous studies at TWI, where preloading events are performed to BS7448 (1991), the room temperature CTOD test standard. Preloading levels were calculated as percentages of the plastic collapse (or limit) load based on the yield strength of the material. The limit load of a compact tension specimen is given by

$$P_L = 1.455\zeta B b \sigma_y \qquad (3.8)$$

where ζ is given by

$$\zeta = \left\{\left(\frac{2a}{b}\right)^2 + \frac{4a}{b} + 2\right\}^{1/2} - \left(\frac{2a}{b} + 1\right) \qquad (3.9)$$

In order to maintain a constant applied displacement rate, it was necessary, when loading beyond the general yield of the specimen, to use displacement control. If loading was performed under load control, at the onset of yielding the displacement rate would increase rapidly and therefore cause fracture to occur. The applied displacement rate during preloading was 0.5 - 0.6 mm per minute.

Loading events were all of Load - Unload - Cool - Fracture (LUCF) type with the preloading performed at room temperature. Subsequent fracture testing was performed at the temperatures given above. The proof loading stress intensity factor was calculated based on the fatigue crack length plus any tearing that took place during preloading. This was measured after fracture at low temperature as insignificant amounts of tearing were assumed to occur prior to cleavage fracture.

Multiple preloadings were performed on selected specimens to assess the effects of repeated proof loading. Two control methods, load and displacement control were used. In load control, the specimen was loaded to the prescribed percentage of collapse, unloaded and then reloaded at the same temperature to the same load. The reloading was repeated up to six times. The specimen was then cooled and fractured as before. Under displacement control, the initial loading was to the same displacement as applied to the load control specimen during the initial preload. Following

unloading, the subsequent reloading applied the same displacement as applied in the initial preload. This was repeated between four and six times.

CHAPTER 4.

EXPERIMENTAL RESULTS

Abstract

This chapter summarises the experimental results performed to characterise the mechanical and fracture response of the two steels, BS1501 and A533B. Uniaxial studies were undertaken to obtained data for finite element modelling. Fracture toughness testing was performed to determine the response of the steels to different preloading histories. Improvements in cleavage fracture toughness were obtained following preloading. However, some load histories were shown to be more beneficial than others.

PART A: BS1501 Steel 490 Gr. B LT50 STEEL

4.1 UNIAXIAL RESPONSE.

4.1.1 Monotonic Loading.

The monotonic stress - strain response of BS1501 Steel at room temperature, -70°C and -120°C is illustrated in figure 4.1. There are several distinct characteristics that are present in all three curves. Firstly, the Young's moduli at these temperatures were 203 GPa, 223.5 GPa and 207.3

GPa respectively. These Young's moduli are subject to a degree of scatter. The variation may also be an artefact of the extensometer setup on the specimens. Upper and lower yield points were a distinct feature in the response of the steel throughout the study. The upper and lower yield stresses at the three temperatures are detailed in table 4.1. The yield stress increased as the temperature was reduced, as expected. Following yielding, the steel responded in an perfectly plastic manner in all three cases.

4.1.2 Uniaxial Response to Cyclic Loading.

The response of BS1501 Steel to cyclic loading at 20°C, -70°C and -120°C is shown in figures 4.2a to 4.2c. The behaviour of the material in the initial cycles is seen to be, as expected, the same as the monotonic response. However, following unloading to zero strain and then reloading under strain control, it was observed that the strong upper and lower yielding behaviour exhibited earlier was not repeated. The ultimate stress did not appear to be altered by the prior straining. The perfectly plastic material response was retained at -70°C. However at room temperature, some hardening was observed following three loading and unloading cycles. The ultimate stress was not increased beyond the initial upper yield stress prior to the specimen buckling. The variation in yield and ultimate stresses are consistent with the reduction in temperature.

Under cyclic loading the yielding response in tension and compression was observed to vary. It is observed in figures 4.2a-c, for example, that following the initial tensile load, the sharp upper and lower yield points are not

reproduced when loaded in compression. The relationship between yield strength in compression following a tensile preload is known as the Bauschinger effect (Bauschinger, 1886). The Bauschinger Effect Factor (BEF), defined here as the ratio of the compressive yield strength and tensile yield strength is evaluated by determining the yield strengths in tension and compression for each individual cycle, figure 4.3. The magnitude of the Bauschinger effect factor observed was therefore dependent on the definition of yield strength adopted. For the purposes of this study, the 0.2% compressive yield strength was adopted for evaluating the BEF.

Bauschinger Effect Factors were evaluated for this steel at 20°C and –70°C. Figure 4.4 illustrates the response of BS1501 Steel to prior plastic deformation. It is observed that at both 20°C and -70°C approximately isotropic behaviour is observed, based on the compressive yield strength. The Bauschinger effect factor, σ_{yc} / σ_{ys} , becomes more pronounced as temperature decreases, dropping from 0.78 to 0.57 at -70°C and 0.3 at -120°C.

4.1.3. Uniaxial Response at -120°C following Prestraining at 20°C.

Figure 4.5 illustrates the stress - strain response at -120°C of the steel following a prior prestrain at room temperature. On initial straining at 20°C the familiar upper and lower yielding behaviour was observed. The specimen was then unloaded to zero strain at room temperature, thus forcing the material into compression. The specimen was then held at constant load during cooling prior to reloading to failure at -120°C. The low temperature

response was observed to be similar to the monotonic response at this temperature, except that the characteristic upper and lower yielding behaviour was not observed. The ultimate stress of the material was unchanged by the prior load history.

4.2 FRACTURE PROPERTIES.

4.2.1 As-Received Fracture at -120°C and -70°C.

Three as-received specimens were tested at -120°C. The results are given in table 4.2. The range of toughness' obtained at -120°C were between 58 MPa√m and 75 MPa√m. The load - displacement traces for these specimens were linear and therefore failure stress intensity factors were calculated using the maximum load at fracture. This method of evaluating K_f was maintained throughout the study. These results were compared with results obtained from Bell (1992) where 50 mm thick SENB specimens were tested. It can be seen from figure 4.6 that the results for the 25mm thick CT specimens compare very well with those the previous study. A mean value of K_{Ic} from both studies was 66 MPa√m. The observed agreement between the two studies provided confidence that no further as-received toughness testing was required and that the test rig was calibrated and functioning correctly. On this basis, the experimental study was extended to examine the effect of Load - Unload - Cool - Fracture (LUCF) cycles on the cleavage toughness of this steel.

At -70°C the as-received toughness varied between 87 and 97 MPa√m, providing a mean toughness of 92 MPa√m. The load versus displacement traces at fracture showed no or little non-linear behaviour. These results were compared against those of Smith and Garwood (1992) where an average cleavage toughness of 85.9 MPa√m using 50mm thick SENB specimens was obtained. This result , while slightly lower than the 25 mm CT specimen results was sufficiently close to allow progression to proof testing experiments. It was observed that the maximum toughness obtained was greater than the maximum toughness observed by Smith and Garwood (1992) as shown in figure 4.6.

4.2.2. Fracture Following A Single LUCF Cycle.

Ten specimens were loaded to varying proof load levels and then fractured at –120°C. The proof loading level was described as a percentage of the collapse load of the specimen. The collapse load (P_L) of the specimen was calculated using a standard solution for the geometry and is based on the yield stress of the steel at the temperature of interest. Figure 4.7 shows a typical proof load versus displacement trace, with different proportions of collapse indicated. It can be seen that only a small increase in the proportion of collapse load ($1.2*P_L$ to $1.35*P_L$) can lead to a large increase in the applied crack mouth opening displacement. Three specimens were proof loaded to approximately the collapse load and the remaining seven specimens to greater than $1.3*P_L$. The specimens preloaded to collapse load level and fractured at –120°C exhibited a mean toughness of 97 MPa√m, an increase of 47% compared with the as-received toughness. The remaining seven

specimens, subjected to higher level preloads and fractured at –120°C gave a mean toughness of 109 MPa√m, an increase of 66 % on the mean as-received toughness. Complete details of each fracture test are given in table 4.3. It is observed that the failure stress intensity increases with increased preload stress intensity, based on this limited study. Figure 4.8 compares the proof loaded fracture toughness data with the as-received fracture toughness data.

It should be noted that the percentage increases quoted above and in forthcoming sections are based on limited data sets and the effects of scatter have not been addressed within this chapter. Scatter will be addressed explicitly in Chapter 6.

Three specimens were preloaded to approximately collapse load level at room temperature prior to fracture at -70°C. The toughness was observed to increase to a mean value of 97 MPa√m, an increase of 5 MPa√m from the mean as-received toughness value of 92 MPa√m. Four further specimens were preloaded to approximately 1.2 $*P_L$. Following fracture at -70°C, the toughness was observed to increase to a mean value of 129 MPa√m, an average of 40 % greater than the as-received toughness. Figure 4.9 illustrates the results compared to the as-received data.

4.2.3 Fracture Following Repeated Proof Loading in Displacement Control.

Six specimens were preloaded following the load versus displacement history of specimen 13e, illustrated in figure 4.10, that is, repeated loading with the

same increment of displacement in each cycle. The specimen was loaded to a prescribed crack mouth opening displacement, then unloaded to zero load. The process was repeated a number of times prior to unloading to zero load for cooling to -120°C. The specimen was then loaded monotonically to fracture. Table 4.4 details the preload and fracture parameters of each specimen. It can be seen that the mean toughness increased to, 112 MPa√m, which represents a marginal increase in benefit beyond the single preload specimens of 3 MPa√m, or 4% (based on the mean as-received toughness). The mean proof loads applied to the single preload specimens and the repeated preload specimens were approximately the same at 102 and 106 MPa√m, respectively. This suggests that repeatedly proof loading this material did not significantly alter the influence of the single cycle warm prestress effect on the materials' toughness. It should be noted that the preload stress intensity factor was based on maximum load and not the applied *J* integral value.

4.2.4 Fracture Following Repeated Proof Loading in Load Control.

Eight specimens were preloaded repeatedly to a certain proportion of collapse load, following the load displacement history of specimen 20a illustrated in figure 4.11. The specimens were loaded initially in displacement control to the calculated load. This was necessary because under load control, at the onset of non-linear material behaviour, the loading rate would increase and cause dynamic fracture. Following unloading from the first load cycle, the reloading would be elastic and therefore could be performed in load control. The results are detailed in table 4.5. It is observed that mean

toughness following repeated preloading in load control is increased to 110 MPa√m, an increase of 66% on the mean as-received toughness and very similar to both the previous load history results.

4.2.5. Summary of BS1501 Steel Fracture Toughness Results.

Figure 4.12 illustrates the cleavage toughness of BS1501 Steel as a function of the number of preload cycles applied. It has been observed that the critical failure stress intensity factor of this steel increases with a single preload. The magnitude of the increase is observed to depend on the applied preload level, a larger increase being observed for larger applied preloads. When subjected to repeated proof loads in either load or displacement control, the increase in observed K_f remains consistent with the increase in K_f for single preloads of the same intensity. These results are consistent with the tensile response of this steel. Cyclic loading of the steel at 20°C did not affect the maximum load attained by the steel and therefore cyclic loading of a cracked specimen at room temperature could be expected to have the same final residual stress distribution as a specimen subjected to a single preload of the same intensity. At -70°C, broadly similar results were obtained to those at -120°C, although the relative increase in toughness with respect to the as-received toughness at that temperature was not as great.

PART B: A533B Class 1 Steel.

4.3 UNIAXIAL RESPONSE.

This steel has been extensively characterised in previous studies (Smith and Garwood, 1990c, Smith et al, 1992). Two monotonic uniaxial tests were performed to confirm the steel properties, provided from the same plates analysed by the above authors. Figure 4.13 illustrates the response of this steel at the two temperatures, 20°C and -170°C. This steel exhibited broadly similar yielding behaviour to that of BS1501 steel, with sharp upper and lower yielding behaviour observed at both temperatures. At room temperature an upper yield stress of 561 MPa, a lower yield stress of 500 MPa and a Young's modulus of 202 GPa were recorded. At -170°C the steel was found to behave in a similar manner with upper and lower yield stresses of 953 and 873 MPa respectively. The Young's modulus was slightly higher at 209 GPa than that observed at 20°C. It is noticeable at both temperatures that this material hardens following yielding. The ultimate strength of the steel was 668 MPa at room temperature and 960 MPa at -170°C.

These values compare well with the values observed by Smith et al (1992). Smith et al (1992) also investigated the influence of prior plastic deformation on subsequent yielding in compression for this steel. An initial Bauschinger effect factor of 0.3 was observed at room temperature. The steel responded in a kinematic manner in subsequent load cycles, a quite different response to that observed in BS1501 Steel steel. No further data was available for low temperatures.

4.4 FRACTURE TESTING, B=25mm.

4.4.1 As-Received Fracture at -170°C.

A total of six specimens were fractured at -170°C in the as-received condition. Three of these specimens were fatigue pre-cracked and three were pre-cracked using the wire electro-discharge machining (edm) technique described in Chapter 3. The results obtained for the two types of specimens showed that fatigue precracked specimens had a lower mean toughness 65.7 MPa√m which lower than results from edm specimens, which had a mean cleavage toughness of 80.8 MPa√m. The difference between the two sets of data could be attributable to inherent scatter in the cleavage toughness of the steel, but the edm technique may also have affected the toughness. The scatter in the cleavage toughness of A533B Steel at -170°C has been investigated by Smith and Garwood (1990b). A series of fourteen 50mm thick SENB specimens were fractured. The maximum toughness obtained by Smith and Garwood (1990b) was 74.5 MPa√m. This comparison suggests that the edm technique, through metallurgical effects or the slightly blunted crack tip, had increased the toughness of the material beyond that of fatigue pre-cracked specimens.

The fatigue precracked specimens however, were contained within the distribution of the Smith and Garwood (1990b) data and it was therefore decided to progress with the proof loading studies. The results are detailed in table 4.7 for all the as-received cases examined. Figure 4.14 illustrates the

relative distributions of the edm and fatigue precracked specimens in relation to the data set obtained by Smith and Garwood (1990b).

Figure 4.15 shows the fracture surface of an A533B steel 25mm thick CT specimen in the as-received condition. The edm notch 'crack' tip is clearly visible with a blunted profile. The cleavage fracture surface is shown in greater detail in figure 4.16 where large numbers of cleavage initiation sites are in evidence. There is some evidence in this figure of local plasticity prior to fracture. Figure 4.17 provides an overview of the crack tip area in the same specimen, which shows the absence of large scale plasticity prior to fracture. Figure 4.18 shows a detail of the microcrack visible towards the centre of figure 4.16, where limited plasticity has occurred.

4.4.2 Fracture Following a Single LUCF Cycle.

Seven specimens were subjected to single LUCF cycles in the manner described in Chapter 3. The mean applied preload stress intensity factor was 116 MPa$\sqrt{m}$, which represents approximately 98% of the collapse load. The mean critical stress intensity factor obtained following these proof loads was 74.3 MPa$\sqrt{m}$. This represented a 13% increase in mean critical stress intensity factor (based on the mean fatigue precracked cleavage fracture toughness) at -170°C. Table 4.8 details the preload and fracture test results. The results are illustrated in figure 4.19, where the data is presented in terms of the number of preload cycles and final critical stress intensity factor. In this figure the as-received toughness data set was obtained by combining the two CT data sets presented in figure 4.14.

Local damage accumulation during the warm prestress event has been investigated previously by Reed and Knott (1992), who observed that large inclusions in the crack tip area were instigating the formation of large voids in the metal matrix. This is attributed to these inclusions experiencing large local stresses due to dislocation pile up mechanisms, which cause the inclusions to decohere from the surrounding material. Further plastic flow will cause neighbouring voids to coalesce into micro-cracks, which subsequently blunt on further loading. It was further suggested by Reed and Knott that these large inclusions could take no part in initiating fracture on reloading at low temperature and that fracture must initiate from smaller inclusions, which will require a larger applied stress to cause fracture.

Figure 4.20 shows the fracture surface of a specimen subjected to a low proof load from a fatigue crack tip. The same fracture surface at higher magnification is illustrated in figure 4.21. This fracture surface is barely distinguishable from the as–received fracture surface detailed in figures 4.15 to 4.18, however, under closer scrutiny in figure 4.22, small nucleated voids, formed during the preload step, are visible. This figure is directly comparable with figure 4.17. In overview, in figure 4.23, there is only limited numbers of these voids, however, and therefore low damage accumulates during a low proof load cycle

4.4.3 Fracture Following Repeated Proof Loading in Load Control.

A further two specimens were proof loaded repeatedly in load control. Figure 4.24 illustrates the load versus displacement trace for specimen a9rpl. The

initial preload cycle was to approximately the same fraction of collapse as the initial cycle of the displacement controlled specimen, described earlier. The specimens were then cycled repeatedly between this load and zero load. The average preload stress intensity was 128.6 MPa√m, or 105% of the collapse load of the specimens. The critical stress intensity factors obtained from specimens a9rpl and a10rpl were 122 MPa√m and 123 MPa√m respectively, an increase of 86% in the as-received cleavage fracture toughness. This also represents a large increase in toughness compared to the repeated displacement control specimens, which had been preloaded to far greater proportions of collapse than these specimens. Figure 4.19 compares the two sets of repeated proof load data to the single LUCF and as-received data.

Repeated proof loading can be expected to cause greater damage to the microstructure of the material, as figure 4.25 illustrates. This is the crack tip region of the specimen, which has been fatigue precracked prior to proof loading. This specimen was cyclically proof loaded in load control. Crack tip blunting is evident when compared to figure 4.20. A significantly higher number of voids formed during the preload step are visible, however, these remain small, of approximately 10μm in diameter, figure 4.26.

4.4.4 Fracture Following Repeated Preloading in Displacement Control.

Due to a shortage of material, it was only possible to perform two tests using this load history. The preloading procedure described in section 4.2.3 was used for these tests. Figure 4.27 illustrates the load versus displacement trace for specimen a8rpd. Two specimens, a7rpd and a8rpd, were preloaded

to a stress intensity of 153 MPa√m and 146 MPa√m respectively (approximately 131% of the collapse load of the specimens), based on maximum applied load. When fractured at -170°C critical stress intensity factors of 93 MPa√m and 87 MPa√m were obtained. This represented a 37% increase on the as-received cleavage toughness of the steel. It should be noted that the total applied preload in this case was much greater than the total applied preload applied to the single preload specimens. The preload and fracture test details are given in table 4.9, with the results illustrated in figure 4.19.

Repeated displacement controlled proof loading has a considerably increased influence on the local microstructure of the material, figure 4.28. At this magnification, the as-received and low proof loaded specimens, were seen to have very little damage. This figure shows the formation of micro-cracks into small macro-cracks, large amounts crack tip blunting and tearing clearly visible. Figure 4.28 shows a void nucleated around a small inclusion of diameter approaching 0.2mm within the cleavage fracture zone. Figures 4.29 and 4.30 show that the cleavage event is initiated by small inclusions, rather than the large void visible at the bottom of the figure. Figure 4.31 provides an overview of the crack tip region following repeated proof loading in displacement control. The tearing zone, progressively extended during each preload cycle, contains voids that have coalesced into micro cracks at room temperature, when the yield stress was low enough to allow significant plastic flow to occur. The stretch zone was formed during the final preload step, with large numbers of voids of varying sizes being formed, but not joining together

to form micro cracks as seen in the tearing zone. The cleavage fracture event initiates beyond this damage zone in the relatively undamaged material at the front on the stretch zone.

4.4.5 Fracture Following A Single Proof Load and Subsequent Crack Growth.

Nine specimens were pre-cracked using the wire edm technique to a nominal a/W of 0.5. These specimens were then proof loaded to a preload stress intensity factor of between 120 MPa√m and 123 MPa√m. The wire edm technique provided greater control of the crack length of the specimens as the process was computer controlled. The applied preload stress intensity factor was therefore controlled to a much greater degree. Following the preload, applied in the normal manner, the specimens then had further crack extension introduced, again using the wire edm technique. The sub-critical crack extension was postulated to occur following unloading from the preload as this was considered to be the most likely in service cracking process, whether from fatigue crack growth or other crack extension mechanisms such as stress corrosion cracking.

The added control allowed accurate and repeatable increments of crack extension that remained along the original crack plane. It was observed throughout the study that fatigue precracking lead to crack fronts being out of plane through the thickness. The edm process also eliminated interaction between cyclic fatigue loading and residual stresses arising from proof loading. Three different crack growth increments were used following proof loading: 0.5mm, 1mm and 2.5mm. Three specimens of each crack increment

were used. The specimens were then fractured at -170°C following the earlier procedures.

The results are presented in figure 4.32 as a function of the crack growth increment and failure stress intensity factor, and also in table 4.10. It is observed that the maximum toughness at -170°C, for a given crack extension, appears initially to increase and then decrease to a toughness close to the mean toughness for a single proof load. The minimum toughness values tend to decrease with increasing crack extension to reach a value close to that of the as-received cleavage toughness.

4.5. A533B FRACTURE TESTING, B=6mm.

In order to examine the effects of warm prestressing on thin specimens, a series of tests were performed on 6mm thick compact tension specimens. All other dimensions were maintained as before, with W=50mm and an a / W ratio of 0.5. This process was to achieve two main objectives.

Firstly, by proof testing at room temperature, where ductility was high, these thin specimens were in a stress state where plasticity could occur through the section thickness. This stress state is known as *plane stress*. At the fracture temperature of –170°C, where the yield stress is high, the specimens were in a stress state where only limited plasticity could occur. This was due to material in the middle section of the specimen constraining the surrounding material, thereby limiting the spread of plastic deformation to the surface of the specimens. This stress state is known as *plane strain*. In Chapter 3, it was found that a thickness of 6mm was the minimum required thickness for

valid K_{Ic} results at -170°C. Therefore, a transition from plane stress during proof load to plane strain at fracture was occurring. The 25mm thick compact tension specimens were effectively in plane strain throughout their loading history, as even at room temperature, the material was well constrained across the section.

Secondly, this would provide results for finite element simulation under plane stress conditions. Repeated proof loading cycles were also applied to the specimens as before. All specimens examined at this thickness were edm notched.

4.5.1 As-Received Fracture Testing At -170°C.

Five specimens were fractured in the as-received condition at -170°C, following the same procedures described earlier. The results are given in table 4.11, and shown on figure 4.33. The average cleavage fracture toughness was 128 MPa√m. This value is considerably higher than the mean toughness of the as-received 25mm thick specimens. There was a degree of scatter associated with the results. However, no previous data is available for 6mm thick A533B steel specimens and so comparisons may not be drawn.

4.5.2 Fracture Following Single LUCF Cycles.

Six specimens were subjected to single LUCF cycles as before. The mean preload stress intensity factor was 103 MPa√m, and was equivalent to 96.3% of the collapse load of the specimens. Following fracture at -170°C, the mean critical stress intensity factor obtained was 174 MPa√m. This was an

increase of 36 % on the mean as-received cleavage fracture toughness. The results are detailed in table 4.12. There was a notable difference observed between the load versus displacement traces at the fracture condition for the 25mm and the 6mm thick specimens, figure 4.34. It was observed that there was more non-linearity occurring prior to fracture in the 6mm thick specimens. Therefore, the critical stress intensity factor was evaluated based on the maximum. load achieved at fracture and also using the J integral values obtained from the experiments. Figure 4.35 illustrates the cleavage toughness following warm prestressing, K_{Jcrit}, based on the critical J value, J_{crit}. Figure 4.33 illustrates the cleavage toughness following warm prestressing based on the maximum load attained, K_{max}. When comparing the as-received values in terms of maximum load toughness, K_{max}, there was an increase of 36% on the mean as-received cleavage fracture toughness. If the comparison was based on equivalent stress intensity factors, as shown in figure 4.35, the apparent increase in mean equivalent cleavage toughness was 45%. The equivalent preload stress intensity factor evaluated using J increased by approximately 20% in comparison to the value calculated from maximum applied load.

4.5.3 Fracture Following Repeated Proof Loading in Displacement Control.

Three specimens were proof loaded repeatedly using the displacement control procedure as described earlier in section 4.4.3. The mean preload stress intensity factor applied was 116 MPa√m, equivalent to 108% of the collapse load. Following fracture at -170°C, a mean critical stress intensity factor of 121 MPa√m was obtained. This represents a slight drop in critical

stress intensity factor of 5% compared to the mean as-received cleavage toughness, despite the high level of proof load applied. This is the first time that a reduction in critical stress intensity factor had been observed following proof loading under any conditions within this study. Figure 4.36 compares the results with the as-received and single LUCF results. Table 4.12 details the preload and fracture information. The preload and critical stress intensity factors were also evaluated using the experimental *J* integral values, figure 4.35. The values of preload stress intensity factor increased by approximately 75% for the repeated displacement controlled tests. The equivalent critical stress intensity factor increased by 12% compared to the value calculated based on maximum load.

4.5.4 Fracture Following Repeated Proof Loading in Load Control.

Three specimens were proof loaded repeatedly under load control following the procedures described in section 4.4.4. The mean proof load stress intensity factor (based on maximum load) for these specimens was 105 MPa√m. This was approximately the same as the single proof load and roughly 100% of the collapse load of the specimens. Following fracture at -170°C a mean critical stress intensity factor of 153 MPa√m was obtained, an increase of 20%. While this is a lower critical stress intensity factor than that obtained via the single proof load cycle, it is considerably higher than the value obtained following repeated proof loading in displacement control. The results in figure 4.36 and table 4.13 reflect these results. When the results were calculated using the experimental *J* integral results, the equivalent fracture stress intensity factors was increased. The preload stress intensity

factor was only increased by less then 5 percent, whereas the critical stress intensity factor was increased by 21%. These results are illustrated in figure 4.35.

4.6. SUMMARY OF EXPERIMENTAL RESULTS

Monotonic loading of BS1501 steel has shown that the material exhibits clear upper and lower yield points at all the temperatures examined. The material behaved in an elastic - perfectly plastic manner, except during one cyclic test at room temperature, where a small amount of hardening was observed following several loading and unloading cycles. The material was found to respond isotropically at 20°C and -70°C, with a strong Bauschinger effect at all temperatures. A533B steel was observed to have similar upper and lower yielding characteristics. This steel was seen to harden following yield, in contrast to the BS1501 steel. Previous studies had shown that A533B steel exhibits kinematic hardening under cyclic loading. This steel had a higher yield stress than the BS1501 steel at 20°C. The response of both steels under fracture conditions, showed that the critical stress intensity factor can be improved by preloading the materials at room temperature prior to embrittlement. Greater improvements in the fracture resistance of the steels were observed with increased preload levels. Repeated preloading in load control was observed to have little additional effect on the low temperature fracture toughness of the steels. Repeated proof loading in displacement control had no additional effect on the low temperature fracture toughness of BS1501 steel. However, it was shown that A533B steel had it's resistance to fracture reduced to levels approaching the as-received cleavage fracture

toughness following repeated proof loading in displacement control. The effects of specimen size on cleavage toughness in the absence of warm prestressing is clearly demonstrated when the as-received toughness of A533B Steel 25mm and 6mm thick compact tension specimens is compared. This thickness effect appears to be consistent throughout the experimental study. In thinner specimens, a reduction in mean fracture toughness was observed following repeated preloading in displacement control. Limited sub - critical crack growth following a single preloading event at room temperature was observed to increase fracture toughness. If crack extension was sufficiently long no improvement in toughness following proof loading was found.

CHAPTER 5

FINITE ELEMENT STUDIES

Abstract

This chapter describes the numerical investigations carried out to investigate the effects of warm prestress load histories on A533B steel. Elastic - plastic finite element studies were performed to provide an insight into the crack tip stress fields during the cycle and at fracture. Simulations of experimental fracture events preceded the use of the finite element method in predicting fracture following warm prestressing. A stress matching technique was used to predict fracture. It was found that the stress state outside the near tip stress field was the controlling factor in the fracture event.

5.1. INTRODUCTION.

The aims of these finite element studies were to investigate the response of cracked components to the proof loading cycles described earlier and to gain an insight into crack tip stress fields at fracture following proof loading. In the first instance, experimental load cycles and geometry's were examined and the crack tip stress fields investigated. Stress intensity factors were evaluated using the *J* integral estimation method available within ABAQUS (versions 5.3 and 5.4), the finite element code employed throughout the study (Hibbitt,

Karlsson and Sorenson, 1994, 1995). Estimates of cleavage fracture toughness were also evaluated from the failure loads of the specimens.

The earlier review of existing experimental work and analytical models has found that little finite element work has been performed to investigate the effects of proof loading. Comparisons between the analytical models and the experimental results have shown that there can be some difficulty in accurately predicting the effects of proof loading on the cleavage fracture toughness of the candidate steels unless a statistical approach is adopted. These finite element studies aim to investigate the stress state of a preloaded component at fracture, by examining the effects of as-received cleavage fracture toughness on the critical stress intensity factor following proof loading.

A533B steel was the chosen material for the finite element studies, due to the large amount of tensile deformation and fracture test data available at the start of the finite element program. There were less data available for the BS1501 steel at that time. The proposed finite element studies would need to incorporate several factors to accurately simulate the proof loading and fracture events. At room temperature, the candidate material, A533B steel, has been shown to have high ductility and ultimate strength and therefore the effects of plastic deformation around the crack tip were considered. It was also necessary to model the elastic plastic response of the material in order to generate the compressive deformation in the crack tip region that occurs on unloading from the proof load. The *J* integral is defined only for a non-linear elastic material, and so when the specimens are unloaded, the validity of the

values estimated by ABAQUS is questionable where non – proportional unloading has occurred. It was therefore anticipated that some degree of interpretation of the *J* integral estimates provided by ABAQUS would be required. It was shown in the experimental section that the larger preload levels gave rise to high applied crack mouth opening displacements and it was therefore considered appropriate to investigate the influence of large strain as well as small strain theory on the finite element simulations.

5.2 MATERIAL MODELLING IN ABAQUS.

Figure 5.1 illustrates the experimental data compared to the idealised material properties at room temperature. The experimental data was extracted from Smith et al (1992), as the experimental data described in Chapter 4 did not become available until later in the program. Low temperature material data was scaled from the room temperature data using the Irwin relationship (1968)

$$\sigma_y = \sigma_{y(RT)} + \frac{10^5}{491+1.8T} - 189\, N/mm^2 \qquad (5.1)$$

where T is the temperature in °C. Therefore, for tests at –170°C,

$$\sigma_y = \sigma_{y(RT)} + 351\, N/mm^2 \qquad (5.2)$$

The post yield stress values were assumed to increase by this same margin, thereby ensuring no change in hardening characteristics with temperature. Later experimental results observed that this was not strictly the case.

Smith et al (1992), found that A533B steel under cyclic loading exhibited kinematic hardening, as described in Chapter 4. Within ABAQUS it is possible to model both isotropic and kinematic hardening materials.

5.2.1 Isotropic Hardening within ABAQUS.

The isotropic hardening model implemented within ABAQUS is illustrated in figure 5.2. The figure describes the expansion of the Mises yield surface following tensile yielding, for an isotropic material undergoing cyclic loading. The material is assumed to harden in a non-linear manner beyond the yield strength, σ_y, to a maximum stress, σ_{max}^t. At strains beyond $\varepsilon(\sigma_{max}^t)$, the strain at which the maximum stress is achieved, the material is assumed to respond in a perfectly plastic manner, as shown. On unloading from maximum load, the material is able to unload elastically by an amount $2 \times \sigma_{max}^t$ prior to the onset of yielding in compression, as the yield surface, of initial radius σ_y, has been expanded to have a larger radius σ_{max}^t. The maximum stress that can be achieved in compression, σ_{max}^c, is therefore $(\sigma_y - 2 \times \sigma_{max}^t)$.

5.2.2 Kinematic Hardening Model As Implemented within ABAQUS.

The kinematic hardening model is illustrated in figure 5.3. This figure details the Mises yield surface and the associated stress – strain curve for a material exhibiting kinematic hardening. Within ABAQUS, it is necessary to model the stress – strain response as a bi – linear relationship, with linear post yield hardening. This is achieved by specifying just two stress – plastic strain pairs in the input file, one identifying the yield point (zero plastic strain) and one

identifying the stress at the maximum plastic strain anticipated to be introduced to the model.

On tensile loading, the material is assumed to yield in a smooth fashion, with no upper or lower yield points. The material then hardens at a constant rate, the hardening coefficient being defined as the gradient of the post yield portion of the curve. In contrast to the isotropic model described above, the kinematic model continues to harden at the same rate at strains beyond the maximum specified plastic strain.

On unloading, as the yield surface is assumed of be of constant radius, the material unloads elastically by twice the tensile yield strength prior to the onset of yielding in compression. Figure 5.3 illustrates that the yield strength in compression following a tensile overload has been reduced to σ_{yc2}, from the original yield strength in compression, σ_{yc1}, in the absence of a tensile preload. On reloading in tension, the yield strength is now the previous maximum stress achieved, σ_{max}^{t}.

There are therefore significant differences between the isotropic and kinematic hardening models as implemented within ABAQUS.

5.3 DESCRIPTION OF GEOMETRIES ANALYSED

Three different specimen geometries were analysed as part of this finite element study. Initially, a single edge notch bend bar (SENB) specimen, with span (S) of 220mm, thickness (B) of 12.5mm and width (W) of 50mm. This was used to reproduce previous finite element studies performed by Smith et

al (1992) who used the Welding Institute Finite Element System (WIFES) to investigate residual stress distributions in crack bars following an overloading event. They then compared their finite element predictions to experimental measurements of residual stress.

The second part of this finite element study examined the same SENB geometry, but with larger dimension of S=400mm, B=50mm and W=100mm. This geometry was studied experimentally by Smith and Garwood (1990b). Finally, compact tension (CT) specimens, detailed in Chapter 4 were analysed. All of the above specimens were analysed in two dimensions using plane strain elements. The simulations of the small (B=12.5mm) SENB specimens also included plane stress simulations. All of these geometries are symmetrical about the crack plane, which allowed half models to be used in the analysis. Symmetry was exploited about the crack plane by constraining the crack plane in the normal direction. All the meshes were focussed on the crack tip. Crack length was consistently half of the specimen width.

The meshes were suitably refined along the crack plane to enable accurate predictions of stress distributions to be obtained. The crack tip was modelled using degenerate quadrilateral elements in which the three nodes on one side of the element were collapsed onto a single point. The coincident nodes at the tip were free to move independently of each other. Equi-spaced mid-side nodes on the element sides radiating form the node cluster were chosen to produce the appropriate plastic stress singularity at the crack tip. Figures 5.4 to 5.8 illustrates the mesh configurations for all the geometries analysed. Loads and reactions were assumed to act through single nodes as indicated

in figure 5.4 to 5.8. Figures 5.6 and 5.8 illustrate the crack tip configurations used when simulating a blunted crack tip in SENB and CT specimens. In both cases 20 elements were used around the quadrant of the crack tip modelled. The radius of curvature used was 0.1mm in the case of the SENB specimen model (Figure 5.6) and 0.05mm in the CT specimen model (Figure 5.8).

5.4 INVESTIGATION OF RESIDUAL STRESSES IN CRACKED BEND BARS.

5.4.1 Description of Analyses.

Two dimensional plane stress and plane strain finite element studies of experimental load cases described by Smith et al (1992) were investigated, following the procedures detailed above. The mesh configuration illustrated in figures 5.4 and 5.5 was used in this study, assuming an element thickness of 12.5mm. The aim of this study was to compare the results of the two studies such that the ABAQUS finite element code was then verified for the purposes of this work. The solutions obtained from the initial load step would provide *J* integral estimates, which would then be used to compare finite element crack tip stress fields using the analytical predictions of Hutchinson (1968) and Rice and Rosengren (1968), otherwise known as the HRR field. Hutchinson and Rice and Rosengren derived the analytical solution for the crack tip stress and strain field in the crack tip region. Their analytical solutions were based on a non-linear elastic material that can be represented using the Ramberg – Osgood power law relationship described in the following equation.

$$\frac{\varepsilon}{\varepsilon_y} = \frac{\sigma}{\sigma_y} + \alpha\left(\frac{\sigma}{\sigma_y}\right)^n \qquad (5.3)$$

Hutchinson, Rice and Rosengren showed that the crack tip stress field can be described using a single scaling parameter *J*, equivalent to Rice's (1968) non – linear energy release rate. The following expression for the crack tip stress field was derived:

$$\sigma_{ij} = \sigma_y \left\{\frac{J}{\alpha\varepsilon_y I_n \sigma_y r}\right\}^{1/n+1} \tilde{\sigma}_{ij} \qquad (5.4)$$

where $\tilde{\sigma}_{ij}$ is a dimensionless function of θ and *n*, I_n is an integration constant, a function of *n* and *r* is the distance ahead of the crack tip. Shih (1983) approximated I_n as

$$I_n = 10.3\sqrt{0.13 + \frac{1}{n}} - \frac{4.6}{n} \qquad \text{for plane strain} \qquad (5.5)$$

$$I_n = 7.2\sqrt{0.12 + \frac{1}{n}} - \frac{2.9}{n} \qquad \text{for plane stress} \qquad (5.6)$$

This methodology allows the crack tip stress field to be characterised using a single parameter, *J*, the amplitude of the stress singularity being proportional to $1/r^{(n+1)}$ for limited distances ahead of the crack tip, within the plastic zone. For a linear elastic material, where *n* = 1, the stresses become proportional to $1/\sqrt{r}$, which is consistent with linear elastic fracture mechanics theory.

Under monotonic loading, the critical J integral, J_{Ic}, can be substituted into equation (3.4) to provide a prediction of the critical near tip stress distribution at fracture, σ_{ij}^{crit}.

$$\sigma_{ij}^{crit} = \sigma_y \left\{ \frac{J_{Ic}}{\alpha \varepsilon_y I_n \sigma_y r} \right\}^{1/n+1} \tilde{\sigma}_{ij} \qquad (5.7)$$

Preload and residual stress distributions obtained from ABAQUS were compared to those obtained experimentally and numerically by Smith et al (1992). The mesh configuration shown in figure 5.4 was used for this study.

5.4.2 Isotropic Plane Strain Analysis.

The specimen was loaded incrementally to a load of 51 kN, then fully unloaded. This coincided with the load applied in the experimental study by Smith et al (1992) The stress distribution normal to the plane of the crack, (σ_{22}), at maximum load is illustrated in figure 5.9, compared to the predictions of Smith et al (1992) and the analytical HRR field, estimated using the average value of J extracted from the ABAQUS analysis. It is observed that the analytical HRR solution and the ABAQUS predictions of normal stress field are in excellent agreement in the crack tip region. The predictions of Smith et al (1992), referred to as WIFES in the legend, representing the finite element code used for those analyses. The WIFES predictions are observed to be in general agreement and any digression from the analytical or ABAQUS predictions are attributed to the lower mesh refinement and minor differences in the material behaviour input to the model.

Following unloading, the WIFES residual stress predictions are shown to be of similar magnitude in the far field as the ABAQUS predictions reaching a peak tensile stress of approximately 250 MPa, figure 5.10. Results obtained from neutron diffraction measurements by Smith et al (1992) and are also shown agree well with the different numerical predictions at distances well away from the crack tip. Close to the crack tip the predictions of all three solutions diverge. . The WIFES predictions of crack tip stress are shown to be approximately half the maximum stress predicted using ABAQUS very close to the crack tip. The neutron diffraction measurements, however, were observed to be significantly lower in magnitude than the WIFES, with the peak residual stress being measured at –200MPa approximately 1mm ahead of the crack tip. The difference between the ABAQUS and WIFES crack tip residual stress magnitude is considered to be a factor of mesh density in the crack tip region. It can be seen from figure 5.10 that in the ABAQUS analyses, a significantly more refined mesh in the crack tip region was used. It is seen that the ABAQUS analyses averaged gauss point stresses over eight nodes, whereas the WIFES analyses averaged over only two nodes within 1.2 mm of the crack tip.

Smith et al (1992) postulated that the kinematic hardening behaviour of the material was responsible for the difference between the numerical predictions and the experimental measurements, as the ratio of the maximum experimental compressive residual stress to the maximum predicted compressive stress obtained from WIFES was approximately 0.3. This was approximately the same as the Bauschinger effect observed under uniaxial loading conditions.

It was therefore considered appropriate for a kinematic hardening law, available within ABAQUS to be implemented in an analysis of the same problem. This allowed direct comparison between finite element studies and the experimental results, although the experimentally measured residual stresses were shown to be approximately 10% of the crack tip stress predicted by ABAQUS using isotropic hardening.

5.4.3 Kinematic Plane Strain Analysis

An identical analysis to that above was performed implementing the kinematic hardening law available within ABAQUS, described in section 5.2.2.

The stress – strain pairs were carefully selected to ensure that the hardening response is as similar as possible to the isotropic hardening model. Figure 5.1 illustrates the stress-strain curve used for kinematic studies.

Figure 5.11 compares the crack tip stress distributions normal to the plane of the crack to the isotropic analyses at maximum load. It is observed that there is little difference between the two predictions of the crack tip stress field. The HRR field is therefore also in agreement with the kinematic model. Following unloading, the residual stress fields are noticeably different up to 0.4 mm from the crack tip, Figure 5.12. The ratio of the maximum kinematic residual stress to the maximum isotropic principal stress of 0.53 is greater than the experimentally observed Bauschinger Effect of 0.3 observed by Smith et al (1992). The residual stresses predicted by the kinematic analysis were of the magnitude predicted by the isotopic finite element study of Smith et al (1992).

5.4.4 Plane Stress Analysis.

The results of the plane strain analyses showed that there was no agreement with neutron diffraction measurements of residual stresses close to the crack tip. A plane stress study of the same problem was then performed. The model was incrementally loaded to the maximum experimental crack mouth opening displacement (CMOD) used in the experimental study of Smith et al (1992) and then incrementally unloaded.

Figure 5.13 illustrates the results of the isotropic and kinematic plane stress studies at maximum CMOD, compared to the numerical predictions of Smith et al and the analytical HRR predictions. It is observed that all three finite element predictions agree well, predicting the extent of plasticity up to 10mm from the crack tip. The kinematic study predicted higher stresses at the crack tip due to the very high strains imposed in this region.

Following unloading to zero displacement, the crack tip stress distributions of the ABAQUS, WIFES and Neutron Diffraction studies differ significantly, figure 5.14. Comparing the residual stress distribution obtained from the isotropic ABAQUS plane stress analysis with that obtained from the isotropic WIFES study, the maximum compressive stresses at the crack tip are shown to be of similar magnitude. However, it is seen that the WIFES analysis was not able to model the detail of the residual stress field due to lack of mesh refinement. Agreement between the two isotropic predictions is not observed within 1mm of the crack tip. It is noticeable that the WIFES and the ABAQUS results are in very close agreement for distances greater than about 1mm from the crack tip. It is evident that the neutron diffraction measurements were

approximately 20% of the maximum predicted compressive stress in comparison to the isotropic results. Further away from the crack tip, the experimental measurements were about the same as the numerical predictions, but do not agree to the same degree as the plane strain analyses.

Comparing the kinematic plane stress study to the neutron diffraction results, it is seen that the predicted residual stresses were approximately one third of the measured stresses in the crack tip region. The lack of agreement between the experimental and finite element predictions indicates an apparent difficulty in measuring stresses accurately across small volumes of material. The low residual stress magnitudes measured by neutron diffraction are likely to be a factor of averaging effects across the high strain region. It is also shown in figure 5.14 that the extent of compressive deformation ahead of the crack tip was measured to within 1 mm of the finite element predictions.

5.4.5 Summary of Residual Stress Investigations in Previously Loaded Cracked Bend Bars.

The above analyses have shown that the residual stress state ahead of a crack tip in a specimen that had previously been overloaded in tension can be predicted using the finite element code ABAQUS. Validation of the results has been performed by directly comparing results obtained in a separate study using a different finite element code and also experimental measurements. It was found that the crack tip stress field at maximum preload can be predicted using the analytical approach of Hutchinson (1968) and Rice and Rosengren (1968), based on *J* integral estimates provided by

ABAQUS. Differences between the results of the original study and the results determined using ABAQUS illustrate the importance of mesh refinement in the crack tip region in accurately describing the stress field in this area.

5.5. SIMULATION OF FRACTURE FOLLOWING WARM PRESTRESSING.

5.5.1 Description of Analyses.

The following analyses were all performed using load cases extracted from the literature, Smith and Garwood (1990b). The material studied was A533B steel, as modelled previously. The SENB geometry studied is described in section 5.3, using the configuration shown in figures 5.4 and 5.5. Finite element simulations of fracture were performed for the following experimental load histories:

1. No previous loading, described as the *As-Received* condition;

2. Fracture at low temperature following prior loading at a higher temperature, described as the *Warm Prestressed* condition.

Experimental results for fracture at –120°C were selected and the loading conditions used in the studies. As the experimental specimens were large enough to satisfy thickness requirements for cleavage fracture toughness measurements, plane strain analyses were performed. The analysis simulating the LUCF cycle were performed in three discrete steps:

1. Loading of the specimen to the maximum experimental applied load at room temperature;

2. Incremental unloading of the specimen at room temperature to zero load and

3. Reloading the specimen at –120°C to the experimental fracture load." The material properties were modified prior to starting the load step to simulate the change in temperature.

The yield and ultimate tensile strengths used for this study were 495 MPa and 735 MPa respectively at room temperature and 675 MPa and 910 MPa respectively at –120°C, following equation (5.2). The stress –strain curves illustrated in figure 5.1 were used for these studies, which were performed using both the isotropic and kinematic hardening laws described in section 5.2.

5.5.2 Simulation Of As – Received Fracture At –120°C.

This simulation involved the monotonic loading of a cracked bend bar to the experimental fracture load of 173.9 kN. Figure 5.15 illustrates the stress distribution in the remaining ligament directly ahead of the crack tip, normal to the plane of the crack. This stress distribution is compared to the HRR field, obtained using the value of J = 60 MPamm extracted using ABAQUS. This numerical prediction of J is lower than the experimental value of 66.9 MPamm. The cleavage fracture toughness of this specimen was 117 MPa$\sqrt{m}$. This difference was attributed to the analysis implementing plane strain

elements, thereby limiting the plasticity that can occur. In practice the specimen experiences more plasticity than is predicted in this analysis. The value of *J* obtained from ABAQUS is the average value of fifty contour estimates, where the contours extend to the surface of the specimen. It was considered appropriate to average the 50 contour estimates of *J* obtained, as path independence was observed in the evaluation of the contours, figure 5.16. The stress field as predicted by the analytical HRR expression of near tip stress field, equation (3.4), using the average *J* value as described above, is shown to agree with the finite element prediction up to 0.4 mm from the crack tip in figure 5.15.

It was also evident that there was little difference between the predictions obtained using isotropic and kinematic hardening laws. This was also observed in section 5.4. As described in section 5.4, Smith et al (1992) concluded that A533B steel responds in a kinematic manner following a tensile overload, and as such, the analyses described from this point onwards will all implement the kinematic hardening law except when stated otherwise.

Having determined the as-received fracture response of the specimen at –120°C and compared the normal stress field successfully to the analytical predictions of Hutchinson (1968) and Rice and Rosengren (1968), simulations of fracture following warm prestress cycles of different magnitudes were performed and these are detailed in the next section.

5.5.3 Simulation of Fracture Events Following A Warm Prestress Cycle.

Experimental load cases were selected from Smith and Garwood (1990b) who performed an extensive study into the warm prestress effect in 50mm thick A533B SENB specimens over a range of temperatures. Two load cases were selected for analysis, where fracture at –120°C was preceded by a warm prestress load cycle at room temperature. Both load cases selected were performed on specimens cracked in the L-T orientation with an a/W ratio of 0.5. The two load cases differed in the magnitude of the preload applied. In the first case, load case *A*, the specimen was preloaded to a maximum stress intensity factor of 90 MPa$\sqrt{m}$, which corresponds to a maximum load of 132.4 kN. The second load case, load case *B*, was preloaded to a maximum stress intensity factor of 153 MPa$\sqrt{m}$, a maximum load of 227 kN.

The normal stress distributions at maximum preload are illustrated in figure 5.17, compared to the appropriate HRR fields, obtained using the *J* integral estimates obtained from ABAQUS. Figures 5.18 and 5.19 illustrate the extent of the plastic zone after each load step in case A and case B respectively. Figure 5.20 illustrates the residual stress distributions following unloading from maximum load. It is observed that for case *A*, the peak compressive residual stress was –1294 MPa, with the compressive deformation region extended 1.13mm from the crack tip. The maximum tensile residual stress was 138 MPa, occurring 2.26 mm in front of the crack tip. In case *B*, the peak compressive residual stress was 1280 MPa, fractionally lower than case *A*, however, the compressive region extended 3.1 mm ahead of the crack tip. The peak tensile residual stress was 241 MPa, 7.65 mm from the crack tip.

After unloading, reloading was carried out using material properties appropriate to the new, lower temperature. Figure 5.21 illustrates normal stress distributions at the respective fracture loads. From this figure the fracture stress distributions were observed to be in agreement up to 1.1mm from the crack tip, which suggested that the as-received toughness and its appropriate stress distribution controlled the fracture process in some manner.

Figure 5.21 also compares the fracture stress distributions to the HRR fields calculated using the *J* integrals obtained for this load step. Figure 5.22 compares the *J* integrals for each fracture case as a function of contour distance from the crack tip. It is evident that there is a region of strong path dependence in the crack tip region for case *B*, beyond which the estimates become path independent. These regions of path dependence occur due to the non-proportional unloading that occurs in the crack tip region during unloading from the preload. Path independence is *only* observed in regions where elastic unloading has occurred and therefore the *J* integral validity requirements on unloading have not been violated. It is the average *J* integral value across the region of path independence that has been used to scale the HRR stress field in figure 5.21. It is shown here that the warm prestressed fracture stress fields are of the same magnitude as the as-received case at distances of up to 1.1mm which is larger than the 0.4mm over which the HRR fields agree. Therefore the *J* integral alone cannot be used to predict the critical stress field. The lowest value of *J* would predict a stress field which matched in the near tip regions but not in the far field regions beyond the region of applicability of the HRR field.

Figure 5.23 illustrates this further, where the *J* integral chosen to evaluate the HRR field is the mean path independent *J* as shown in figure 5.22. There is good agreement between the as-received and reloaded stress fields close to the crack tip, but further from the crack tip, the stress field is still strongly influenced by the residual stress state. Fracture will not occur following warm prestressing until the residual stress field is overcome on reloading and the stress field is of the magnitude of the as-received stress field at distances greater than the plastic zone normally associated with controlling a cleavage fracture event, the extent of which is illustrated in figures 5.18 and 5.19. Prediction of fracture has been based on the matching of stress fields visually, without recourse to using the *J* integral as the fracture criterion. The use of the *J* integral has been limited to estimating a final stress intensity factor, rather than being used to predict a critical stress field on its own merits, as described by equation (5.7).

5.5.4 Prediction of Fracture Toughness Following Warm Prestressing.

The results of section 5.5.3 show that it is possible for the cleavage fracture toughness of a component be predicted by matching the stress field formed on reloading to the stress field corresponding to the material's critical stress intensity factor. Several finite element analyses were performed to examine this further by simulating pre-loading events of different magnitudes, unloading to zero load and reloading incrementally at low temperature. At each increment, the crack tip stress field was compared to the stress field corresponding to the as-received cleavage fracture toughness. Predictions of critical stress intensity factor were made based on the load achieved at the

increment where the stresses were considered to be in best agreement with the stress field for the as-received toughness. The final load step was performed at -170°C. The material properties were altered accordingly using equation (3.2)

Five different preload stress intensities were applied to the same SENB geometry studied in section 5.5.3. These were 63.2, 79.1, 94.9, 126.5 and 158 MPa$\sqrt{m}$ at 20°C. The residual stress fields formed on unloading from each of these preload levels is illustrated in figure 5.24. It can be seen that the peak compressive residual stress is about the same in all five cases, while the region of compressive residual stress increases with increasing preload level. The materials' room temperature yield stress limits the peak compressive stress. The extent of residual compressive plastic deformation increased with preload stress intensity factor as the degree of plasticity imposed on preloading increased with stress intensity factor. These residual stress distributions can be normalised to provide a dimensionless residual stress distribution, figure 5.25. This shows that the residual stress distribution magnitude and extent is proportional to the stress intensity factor applied during the preload step. The as-received cleavage fracture toughness for A533B was chosen as 47.4 MPa$\sqrt{m}$ from a data set presented by Smith and Garwood (1990b) where fracture occurred at -170°C. An example of the method used to match the crack tip stress field is illustrated in figure 5.26 for a proof load of 63.2 MPa$\sqrt{m}$. It can be seen that an excellent match is obtained with the as-received fracture stress field and the HRR field estimated by extracting the *J* integral from the path independent values output by ABAQUS.

This *J* value of 18.6 MPamm corresponds to an equivalent stress intensity factor of 62 MPa√m, which is in good agreement with the stress intensity factor of 66 MPa√m, based on load. This process of incremental loading until the best possible stress match was obtained was repeated for each of the different load cases and the results plotted on figure 5.27 as a function of K_1, K_f and K_{fJ}. Values of K_{fJ} were obtained by selecting the average value the *J* integral estimates in the region where only elastic loading had taken place, as described in section 5.5.3. These *J* integral values were then converted to equivalent stress intensity factors using equation (3.7). It can be seen that the two estimates are within 8% of each other, with the numerical *J* predictions leading to more conservative predictions.

The study was extended to examine the same proof load levels but different toughnesses at the same temperature in an attempt to investigate the effects of inherent scatter in the cleavage toughness exhibited in Chapter 4. A further three cleavage toughness values were selected from Smith and Garwood (1990b). These were 63.2, 69.6 and 82.2 MPa√m. The same methodology was followed to predict failure stress intensities. All stress intensity factors presented are based on load unless otherwise stated. Figure 5.28 illustrates the stress intensity factors at the predicted failure loads. It is observed that the failure stress intensity factor, for a given level of preload increases with increased as-received cleavage fracture toughness.

5.5.5 Comparison Between Predictions Using Isotropic and Kinematic Hardening Laws.

The results of the FE analyses reported in the earlier sections were obtained using a kinematic hardening law. It was observed earlier in sections 5.4.2 and 5.4.3 that the magnitude of the residual stress field for a given level of preload depends on the hardening model employed during the analysis. A study was performed to investigate the influence of hardening law on the warm prestress effect. This involved performing a complete set of analyses in the same manner for an as-received cleavage toughness of 47.4 MPa√m. Figure 5.29 illustrates the predictions based on isotropic and kinematic hardening laws. This figure clearly shows that there is no difference in the failure predictions.

This strongly indicates that the peak compressive residual stress field does not influence the degree of benefit conferred by a given level of preload, as the peak stress is limited by the material model employed. This is consistent with the procedure used to predict the fracture event following warm prestressing, as the very near crack tip stress field is considered unimportant in the fracture event following warm prestressing. This is because the elastic stresses further ahead of the crack tip must also agree with the critical stress distribution, as defined by the cleavage toughness of the material in the as-received condition.

5.6 INFLUENCE OF BLUNTING ON WARM PRESTRESS EFFECT.

Load cases taken from section 5.5.4 were used to examine the influence of an initially blunted crack tip on the crack tip stress field at fracture. The load case examined was that for an SENB specimen of the same global geometry as in the previous section, assuming an as-received cleavage toughness of 47.4 MPa√m. The same material properties as described in section 5.2.2 were used in these analyses, although large scale yielding was introduced to the model by way of the *NLGEOM flag in ABAQUS. This parameter allows the rotations of the nodes to be taken into account when evaluating nodal displacements from increment to increment.

The crack tip was modelled as shown in figure 5.6, with a finite radius of 0.1mm. Eighteen elements were modelled around the crack tip, with the minimum element length of approximately 0.05mm directly ahead of the crack tip.

5.6.1 Normal stress field for as-received fracture in specimens with blunted crack tips.

The stress field normal to the plane of the crack for as-received fracture is shown in figure 5.30, for both the blunt and sharp notched analyses. It can be seen that the near tip stress singularity does not persist in the blunt notched specimen, where it was observed to be dominant in the sharp crack analysis. Furthermore, the peak tensile stress for the blunt notch case is shown to occur at distances beyond those of the sharp notch case. As r increases, the two stress fields converge, at r = 1mm, both stress fields have an identical

distribution. It is observed that the peak tensile stress in the blunt notch case intersects the analytical prediction based on the HRR expression for a sharp crack and the ABAQUS *J* integral estimates.

For both cases, ABAQUS provided path independent *J* integrals of approximately 9.6 MPamm, the slightly lower prediction of *J* for the sharp crack tip model, illustrated in figure 5.31. Figure 5.32 shows the stress distributions of both sharp and blunt crack tip models in dimensionless quantities. Both axes are normalised in such a way that results can be compared from different cases, providing small scale yielding can be assumed. The analytical HRR prediction, based on *J* Integral estimates obtained from the finite element analyses, is also illustrated in figure 5.32 to show the loss of *J* dominance in describing the crack tip stress field in the presence of a blunted crack tip.

For the case where a sharp crack tip was modelled, the *J* integral has been shown in figure 5.32 to be descriptive of the as-received fracture stress field in the crack tip region, for distances up to $0.5\times(r\ \sigma_y/J)$. In the case of the blunted crack tip, the analytical HRR field is shown to deviate from the numerical prediction, for distances less than approximately $1.5\times(r\ \sigma_y/J)$. This concurs with the findings of McMeeking and Parks (1979) who showed that the HRR fields are only valid at distances greater than approximately twice the CTOD, or approximately $1.0\times (r\ \sigma_y/J)$ where blunted notches are analysed.

5.6.2 Validation of stress matching technique for prediction of fracture in blunt notched specimens following warm prestressing.

Having obtained numerical predictions for the crack tip stress field at fracture for a blunt notched specimen in the as-received condition, the influence of warm prestress load cycles on the cleavage toughness of blunt notched specimen was then investigated. The mesh configuration described in section 5.6.1 was implemented in this study.

The specimen was preloaded at room temperature to 63.2 MPa$\sqrt{m}$ and unloaded to zero load. The specimen was then reloaded until the stress field was matched, using the same incremental loading technique implemented in section 5.5.4. The stress distribution normal to the plane of the crack at maximum preload and at zero load following unloading from the preload are illustrated in figure 5.33, and is compared to the stress distributions from the sharp crack case. At maximum preload, the stress distribution is compared to the HRR prediction defined using the estimate of J extracted from ABAQUS. It is observed that the stress distribution close to the crack tip is not defined by the J based HRR expressions, as observed in the preceding section where as-received fracture was discussed. The magnitude of the stress field at distances, say $r > 0.3$mm, where the HRR expression deviates from the sharp crack tip stress field can be described by modifying the HRR expression. The modification involved changing the value of the work hardening coefficient, n, in equation (5.7) from 12.5 to 1, such that the HRR expression then represents elastic material behaviour. Modification of n also modifies the value of the integration constant I_n in equation 5.7, as this parameter is a

function of *n*, equation (5.5). Figure 5.33 shows that the stress field, at distances of great than 0.3mm from the crack tip, varies as $1/\sqrt{r}$, in accordance with LEFM theory.

The residual stress field distributions for the blunted and sharp crack tip configurations are also shown in figure 5.33, following unloading from the preload at room temperature. This residual stress distribution is seen to differ in form in comparison to the sharp crack case close to the crack tip. For the blunted crack configuration, the crack tip stress is shown to be approximately -500 MPa, and the peak compressive stress –1000MPa at approximately 0.2mm from the crack tip. The compressive region extends to 0.55mm from the crack tip, which is observed to be identical to the sharp crack tip case. In the sharp crack tip case, the peak crack tip residual stress is observed to be –1000 MPa, double that of the blunted crack tip, with the peak compressive residual stress of –1170 MPa 0.02mm from the crack tip. Therefore, crack tip blunting and large deformation theory only have an influence on the very near crack tip stress distribution during and following a preload event.

In order to validate the applicability of the stress matching technique for predicting fracture following a warm prestress event, it is necessary to compare the fracture stress distributions for the sharp and blunt notched models with the respective as-received fracture stress distribution. These distributions are illustrated in figure 5.34.

It is shown in figure 5.34 that the blunt notch as-received and warm prestressed fracture stress fields match for distances up to 0.3mm from the

crack tip. The matching distance, r_{match}, for the blunted case was observed to be greater than for the sharp notch case. It was observed from figure 5.34 that the distance over which stresses were matched exceeds the distance over which the HRR field matches the stress distribution. This confirms the findings of section 5.5.4 where it was shown, for sharply notched specimens, that the stress field would need to be matched beyond the region of applicability of the HRR expressions.

5.6.3 Simulation of fracture in Compact Tension Specimens with blunt notches.

Further simulations of fracture following a warm prestress were performed to investigate the fracture conditions in 25mm thick compact tension (CT) specimens with blunted crack tips. Experimental results obtained from experiments on 25mm thick CT specimens, presented earlier in Chapter 4 were used to provide an input to the simulations. The material properties as described in section 5.2.2 were used in these analyses. The mesh used for these analyses is illustrated in figures 5.7 and 5.8, where the crack tip was assumed to have a radius of 0.05mm, which represented half the diameter of wire used in machining the edm notch in the experimental specimens. Plane strain elements were used throughout the simulations.

The simulations involved loading the model to the experimental preload and fracture load levels of ab1n and ab5wps. Specimens ab1n was fractured in the as-received condition at –170°C and specimen ab5wps as preloaded at

room temperature, unloaded to zero load, cooled and reloaded to fracture at –170°C. Table 5.1 details the loading conditions for this series of simulations.

Figure 5.35 illustrates the fracture stress distribution of specimen ab1n compared to the *HRR* prediction based on the *J* integral estimate obtained from the simulation. It can be seen that the same features were exhibited in the compact tensions specimen as were observed in the blunt notched SENB specimens. The stress field close to the crack tip is reduced due to the blunt notch and deviates from the HRR solution in the near tip region. The peak stress is achieved at a distance consistent with the theory of McMeeking and Parks and the previous findings of section 5.6.1, figure 5.36. Figure 5.36 illustrates the as received fracture stresses normalised by yield stress, and the distance ahead of the crack tip ,r, normalised by *J* and yield stress. Figure 5.37 illustrates the fracture stress fields in the as-received and warm prestressed conditions. It is observed that these stresses match for distances of up to 0.5 mm ahead of the crack tip, greater than the distance over which the HRR field agrees with the numerical distribution.

5.7 SIMULATION OF FRACTURE FOLLOWING WARM PRESTRESSING AND SUB-CRITICAL CRACK GROWTH.

Experimental work in Chapter 4 studied the effects of sub-critical crack growth on the warm prestress effect. A program of simulations was embarked upon to investigate the use of the stress matching criterion to simulate fracture following a warm prestress event and sub-critical crack growth in compact

tension specimens. The simulations were performed in three discrete steps as before, however the boundary conditions of the model were varied throughout the analysis. The simulation of sub critical crack extension was achieved by releasing nodal constraint in the plane of nodes ahead of the crack tip, up to the required distance in front of the crack, figure 5.38. The crack extension was performed at zero load and therefore in the presence of compressive residual stresses. It was necessary to constrain the new free surfaces from crossing the plane of symmetry, while still being free to displace away from the symmetry plane. This was achieved by the introduction of contact surfaces on the crack plane. It was assumed that the contact elements on the crack plane would simulate a rigid surface. This surface was termed the master surface. The nodes of the elements in the crack plane of the original mesh were used to define the slave surface, which was considered to be deformable. The master – slave surface contact formulation implemented within ABAQUS does not allow penetration of the master surface by the slave surface. As additional non linearity has been introduced to the problem, severe discontinuity iterations are performed within the finite element code to calculate the distance between the integration points of the deformable and rigid surface elements. If this distance is positive, then there is no contact occurring. If the distance is zero, then contact is occurring and the normal pressure between the deformable and rigid surface is transmitted. Several of these iterations are performed to ensure that the stresses and displacements of the entire model are in equilibrium. Friction between the contact surfaces was neglected.

Throughout this programme, small strain theory was implemented although the original crack tip was modelled using a finite radius mesh. This radius was 0.05 mm, as shown in figure 5.9.

Initially, simulations of experimental fracture events following warm prestressing were performed to investigate the influence of sub critical crack growth on the fracture stress field. These experimental fracture stress fields were compared to fracture stress fields obtained for the extended crack length in the as received condition.

5.7.1. Simulation of Experimental Fracture Events Involving Sub-Critical Crack Growth Following Warm Prestressing.

Simulations of experimental Load - Unload - Crack Growth Cool - Fracture events were performed for specimens 4596, 6596 and 12596. Details of the experimental conditions for each of these specimens is given in Table 4.10. All the specimens were preloaded to approximately 120 MPa$\sqrt{m}$ and then unloaded. Sub critical crack extension was achieved by releasing nodes on the crack plane ahead of the crack tip for distances equal to the crack growth increment imposed experimentally. The residual stress field following unloading, prior to crack extension is illustrated in figure 5.39. The positions of the respective crack tip positions for each of these specimens is indicated on figure 5.39. It can be seen that the extended crack tips of specimens 4596 and 6596 extended approximately half way across the residual compressive region. The extended crack tip of specimen 12596 is seen to extend through the compressive stress field and into the region of tensile stress. It can be

seen from figure 5.39 that the crack tip was close to the position of maximum tensile residual stress.

Figures 5.40 and 5.41 illustrate the stress distributions of specimens 4596 and 6596 at fracture at –170°C. These stress fields have been matched to fracture stress distributions for specimens in the as-received condition, with crack lengths equal to those of each specimen. This stress matching was attempted for a range of toughnesses between 40 MPa√m and 85 MPa√m. This range of as-received toughnesses represented the distribution of experimental as received toughness for fatigue precracked and edm notched specimens. It was noted that the range of toughness obtained for the edm notched specimens was based on limited data (three specimens). It was therefore possible that the distribution of cleavage toughness for edm notched specimens could extend higher than the maximum obtained toughness of 85 MPa√m.

It can be observed from figures 5.40 and 5.41 that the two fracture stress fields can be matched to stress fields representing as received cleavage toughnesses of 40 MPa√m and 85 MPa√m respectively.

Figure 5.42 illustrates the fracture stress distribution of specimen 12596. This specimen had a growth increment of 2.57mm which extended the crack tip into the region of tensile residual stress. The fracture stress field for an as received toughness of 85 MPa√m is compared to the stress field of specimen 12596. It is observed that the stress distributions only agree in the region of the peak stress. This limited degree of matching between the stress field

does not allow the continuation of the stress matching technique used for the specimens where crack extension was within the compressive residual stress region. The fracture stress distribution of specimen 12596 was matched to the stress distribution for a specimen of cleavage toughness of 113 MPa√m. It can be seen from figure 5.42 that the stress distribution for that toughness matches the stress distribution of specimen 12596 closely, except at distances within 1.5mm of the extended crack tip.

While there was no experimental justification for matching this higher as received toughness stress distribution to the fracture stress field of specimen 12596, there was no evidence in the literature that could justify matching the peak crack tip stress distributions of an as-received specimen with that of a specimen that had been warm prestressed. The matching of the higher as received cleavage toughness provides a more justifiable means of predicting the fracture toughness of a specimen following warm prestressing and sub critical crack growth. The only assumption that has been taken is that the cleavage toughness distribution of edm notched specimens extends to toughnesses greater than those obtained from a limited experimental testing program.

5.8. Prediction of Cleavage Fracture Following Warm Prestressing and Sub-Critical Crack Extension.

5.8.1 Description of Analysis Methods.

Following the simulations of experimental fracture events following warm prestressing and sub critical crack extension the results of the previous section were used to predict the effect sub critical crack growth on cleavage toughness following warm prestressing. This stage considered twenty one different toughness and crack extension combinations. Table 5.2 details the matrix of toughness and crack growth increments studied. Three as-received toughness levels of 40, 60 and 85 MPa√m were selected as representative of the range of toughness obtained experimentally in Chapter 4 for this geometry. A single proof load of 120 MPa√m, corresponding to the experimental proof load, was applied to the specimen, which was then unloaded. Nodes on the crack plane were released to represent different crack extensions up to a maximum of 4mm from the crack tip prior to reloading.

The techniques used in predicting the cleavage toughness of the specimens following warm prestressing and sub critical crack extension prior to reloading at zero load were based on the findings of section 5.7.1 and were as follows.

- For crack growth increments that resulted in the new crack tip being contained within the extent of the residual compressive stress distribution, the stress matching technique used in section 5.5.4 was applied. The stress ahead of the crack tip was matched with the as-received stress

distribution toughness for that crack length for as great a distance as possible.

- For crack growth increments that resulted in the extended crack tip being contained within the region of tensile residual stress, the stress fields of the warm prestress specimens were matched to the as received stress field for that crack length. The criterion applied was that at no point ahead of the crack should the stress distribution be greater than the as-received distribution.

5.8.2 Definition of as –received stress fields for as received fracture.

As described above, three as received cleavage toughnesses were selected to predict the cleavage toughness following warm prestressing and sub critical crack extension. It was necessary to calculate the stress field for each cleavage toughness and crack length such that the stress fields could be matched with confidence. Therefore, a critical stress distribution for each crack length and as received cleavage toughness was obtained. Figure 5.43 illustrates the as received critical stress distributions for crack length increments of 0.3mm, 0.7mm, 1mm, 2mm 3mm and 4mm. It is observed that the peak stress magnitude reduces with increasing crack extension increment.

Figure 5.44 presents the same data as figure 5.43, with the distance ahead of the original crack tip normalised by subtracting the crack growth increment from the distance ahead of the original crack tip. It is shown that a single

master curve is obtained for this cleavage toughness. This curve can therefore be normalised further with respect to K_{Ic} and σ_y, figure 5.45. This curve provides a means of determining the critical stress distribution for a given toughness, crack length, and crack growth increment.

5.8.3 Prediction of cleavage toughness following warm prestressing and sub critical crack growth.

This section presents predictions of cleavage toughness following warm prestressing and sub critical crack extension for the conditions described in section 5.8.1.

Figures 5.46 to 5.53 illustrate the predicted stress distributions for each crack growth increment, during reloading and for cleavage fracture at –170°C, based on an as-received cleavage toughness of 85 MPa√m. For the condition where no sub critical crack growth occurs, a failure stress intensity of 120 MPa√m is obtained. The stress fields for the as-received and warm prestressed distributions are matched for distances up to 1mm from the crack tip, figure 5.46.

For a crack growth increment of 0.3mm, figure 5.47, which positions the new crack tip at the position of maximum compressive residual stress, the as-received stress distribution and the final stress distribution for the warm prestressed specimen can be matched at a failure stress intensity of 153.7 MPa√m, with matching achieved up to 0.7mm ahead of the original crack tip.

In this case, it is observed that compressive stresses are obtained directly behind the new crack tip , indicating that the crack faces are closed. This is due to the fact that the stresses are obtained for the first plane of nodes that are fully contained within the mesh. Nodal averaging results in these compressive stresses being predicted. Figure 5.48 illustrates that at the predicted failure increment, the crack faces are not in contact.

Figure 5.49 illustrates the predicted stress distribution following 0.7mm sub critical crack growth. The new crack tip is still contained within the residual compressive region and also the residual plastic zone, which extends up to 0.8mm from the crack tip. Failure is predicted to occur at K_{app} = 127.8 MPa$\sqrt{m}$.

Figure 5.50 illustrates the predicted distributions following 1mm sub critical crack growth, which is inside the compressive residual stress zone, but outside the compressive plastic zone. Failure is predicted to occur at K_{app} = 120 MPa$\sqrt{m}$.

Figure 5.51 illustrates the distribution for a crack growth increment of 2mm. The crack tip is now in the tensile residual stress region and therefore a reduction in the failure stress intensity factor would be expected due to these tensile residual stresses. The failure stress intensity factor is predicted to be K_f = 94.2 MPa$\sqrt{m}$.

Following 3mm sub critical crack growth the new crack tip is at the position of peak tensile stress ahead of the crack tip. In order to obtain a match it was necessary to match the entire distribution with the as-received distribution. Figure 5.52 illustrates the increment immediately prior to fracture, the failure stress intensity factor predicted as being 42 MPa√m.

Sub critical crack extension of 4mm represents little change from the above condition and uses the same matching technique as for the above case, figure 5.53. There appears to be little change in the prediction for this crack growth increment, the predicted failure stress intensity factor being 42 MPa√m.

The same procedure was also applied to provide predictions for as received toughnesses of 40 MPa√m and 60 MPa√m. Figure 5.54 illustrates the predictions for K_f as a function of crack growth increment and as received cleavage toughness and compares the results to the experimental results presented in table 4.10.

The predictions are shown to follow the same trends as the experimental results. Some of the experimental results exhibit failure stress intensities in excess of those predicted by the finite element predictions. These results therefore suggest that the cleavage toughness distribution for specimens that have been edm notched was more extensive than the distribution obtained from the limited experimental study, as discussed in section 5.7.1.

Figure 5.55 illustrates the technique used to match peak crack tip stresses in order to obtain a prediction of cleavage toughness following warm prestressing an sub critical crack growth prior to loading to fracture. This technique is based purely on the results of the simulations of experimental fracture events such as those illustrated in Figures 5.41 and 5.42. This stress matching procedure was repeated for all the load cases described above where far field stresses had been matched and a new set of predictions obtained. These are illustrated in Figure 5.56. It is observed in Figure 5.56 that the finite element predictions obtained from matching the peak crack tip stress exhibit greater agreement with the experimental data than those predictions obtain by matching the far field stress. The lower bound finite element predictions are observed to agree well with the lower bound experimental results for crack extensions of up to 1mm .

CHAPTER 6

ANALYSIS OF CLEAVAGE TOUGHNESS DATA AND FINITE ELEMENT PREDICTIONS.

6.1 INTRODUCTION.

Scatter within experimental cleavage toughness data was identified in section 2.5.3. The work of authors such as Weibull (1951), Wallin(1984) and Anderson and Stienstra (1986) provide us with statistical approaches that use weakest link theory as their basis to describe the distribution of cleavage toughness data. In order to analyse the experimental data gathered during this study, and to compare this data with results from the literature, a single model of cleavage fracture has been selected and developed for use throughout this analysis of warm prestress effects in ferritic pressure vessel steel. The model of cleavage fracture selected was that proposed by Wallin (1984). In this Chapter, this model will be briefly developed before being used to describe the various distributions of cleavage toughness obtained as part of this study.

Finite element predictions of cleavage fracture obtained in Chapter 5 are compared to analytical models described in Chapter 2. The predictions are also compared to experimental data obtained from a variety of sources. The predictions for cleavage fracture toughness following warm prestressing and

sub critical crack growth are also compared to analytical models and experimental results.

6.2 GENERAL STATISTICAL MODEL FOR CLEAVAGE FRACTURE INITIATION

The basis of the statistical model is presented in figure 6.1. It is assumed that an element of material in the region of the crack tip contains a number of randomly distributed particles capable of initiating cleavage fracture or cleavage initiators. The cumulative probability distribution (CPD) for a single initiator being critical can be expressed as

$$CPD = P(a \geq a_c) \tag{6.1}$$

This cumulative distribution function forms the basis of the 'weakest link' theory proposed by Weibull (1951). In the case of cleavage fracture, this cumulative distribution function is a complex function of initiator size and distribution, stress, strain, grain size, temperature and applied loading rates. For the case of the sharp crack, Wallin (1991) assumed that the initiator distribution and origin was not important, providing that it was assumed that no global interaction between the cleavage initiators occurs. That is to say that only local interactions are permitted. Thus, a cluster of cleavage initiations may be required for macroscopic initiation. In such a case, the cluster of initiators can be considered to be the critical initiator and therefore the initiation treated as a single event. Also, this assumption did not cause any restrictions to be placed on whether initiation or propagation is the most

critical event. All the above factors can be neglected as long as no attempt is made to determine the shape of the distribution.

Wallin (1991) expressed the cumulative failure probability of a volume element with a uniform stress state as

$$P_f = 1 - \{1 - P(a \geq a_c)\}^{N_v \cdot V} \qquad (6.2)$$

where N_v is the number of initiators in a unit volume and V is the volume of the element. In the case of several independent homogeneous volume elements, with size V_i having different states of stress the total cumulative probability becomes

$$P_f = 1 - exp \sum_{i=1}^{n} V_i \cdot ln\{1 - P_i(a \geq a_{ci})\}^{N_v} \qquad (6.3)$$

where n is the number of elements.

Equation (6.3) contains the limiting assumption that the volume elements are homogeneous, i.e., the number of cleavage initiators in a volume element is defined as $N = N_v \times V$. In reality, the initiators are randomly distributed, which causes N not to be constant, but Poisson distributed (Wallin, 1991). Incorporating the Poisson distribution into equation (6.3) and performing the single summation, the probability of initiation in one volume element becomes

$$P_f = 1 - exp\left[-\overline{N} \cdot P(a \geq a_c)\right] \qquad (6.4)$$

where $\overline{N}$ is the mean number of initiators in a unit volume element. Thus the form of equation (6.3), when assuming randomly distributed initiators is

$$P_f = 1 - exp\sum_{i=1}^{n} -\overline{N}_v \cdot V_i \cdot P(a \geq a_{ci}) \qquad (6.5)$$

where $\overline{N}_V$ is the mean number of initiators per unit volume.

Wallin then develops the model by incorporating the stress and strain distributions described by Hutchinson (1968) and Rice and Rosengren (1968) (the HRR expressions) for a sharp crack in small scale yielding. One property of the HRR field is the angular dependence of the stress field. Thus the stress field can be divided into small fan-like elements with an angle increment $\Delta\theta$ as shown in figure 6.2. In this case Wallin (1991) showed the failure probability to be

$$P_f = 1 - exp\sum_{\theta=0}^{2\pi} \left\{\sum_{x=0}^{Xp} -\overline{N}_v \cdot B \cdot \Delta x \cdot x \cdot sin(\Delta\theta) \cdot P(a \geq a_c)\right\} \qquad (6.6)$$

where the volume element size in the x direction, described by Δx, must be larger than the initiator size a and B is the thickness of the sample. The double summation indicates that the summation is performed over the whole plastic zone.

Due to the properties of the HRR field, it is possible to normalise the distance ahead of the crack tip with the stress intensity factor as follows

$$U = \frac{x}{(K_I/\sigma_y)^2} \tag{6.7}$$

When equation (6.7) is inserted into equation (6.6), and the double summation performed, the cumulative failure probability becomes

$$P_f = 1 - exp\left(- const. \cdot B \cdot K_I^4\right) \tag{6.8}$$

The constant term in equation (6.8) is a result of the double summation in equation (6.6) which is always negative and independent of K_1. The scatter of fracture toughness is therefore independent of the cleavage initiator distribution and Wallin (1991) made no assumptions in developing this theory, save that the initiators behave independently on a global scale, or in other words, it is assumed that the volume elements are independent for a given K_I. This distribution function assumes that the cleavage fracture process zone is equivalent to the plastic zone. Wallin (1991) states that this expression is not sensitive to the definition of the process zone as long as it is assumed that the process zone size correlates with K_I, *CTOD or J*. Equation (6.8) is identical to the Weibull (1951) distribution function:

$$P_f = 1 - exp\left(- n\varphi(x)\right) \tag{6.9a}$$

where n is the number of cleavage initiators in this context and $\varphi(x)$ is the distribution of cleavage initiators (in this context). The function $\varphi(x)$ is defined by Weibull (1951) as

$$\varphi(x) = \frac{(x - x_u)^m}{x_o} \tag{6.9b}$$

The Weibull probability function has a variable shape function, *m*, whereas the equivalent term in the Wallin probability function is fixed at a value of 4. The result presented by Wallin(1991), equation(6.8) is not related to Weibull statistics in any way but to assume that failure occurs by a weakest link mechanism.

In developing this theory further, Wallin introduces a lower limiting value of K, K_{min}, below which cleavage fracture is considered impossible. This factor was introduced as equation (6.8) implies that an infinitesimal K_I value might lead to a finite failure probability. For very small K_I values, the demand for Δx to be clearly larger than the initiator size is violated. Also for very small K_I the stress gradient at the crack tip becomes so steep that even if cleavage fracture can initiate, it will arrest almost immediately.

Allowing for K_{min} the equation describing fracture toughness scatter was re-written by Wallin (1991) as follows:

$$P_f = 1 - exp\left[-\frac{B}{B_o} \left\{ \frac{K_{Ic} - K_{min}}{K_o - K_{min}} \right\}^4 \right] \qquad (6.11)$$

where B_0 and K_0 are normalisation constants. The normalisation thickness B_0 can be made equal to any desired reference thickness. The scale parameter K_0 corresponds to a 63.2 percent fracture probability, for thickness B_0 and is approximately given by $K_0 = 1.1 \times K_{mean}$.

6.3 ANALYSIS OF EXPERIMENTAL DATA

Smith and Garwood (1990b) present two sets of data for A533B steel fracture at –170°C: one in the as-received condition and one in the warm prestressed condition. This statistical nature of this data is analysed using the general statistical model for cleavage fracture proposed by Wallin (1991) and described in section 6.2. Data obtained by Smith and Garwood for fracture at –100°C is also examined here. This is previously unpublished data.

Equation (6.10) was fitted to the as-received cleavage toughness data for A533B steel at –100°C and –170°C as shown in figure 6.3. When fitting these two data sets to equation (6.10) K_{min} and K_0 were the free variables used in the curve fitting procedure. K_{min} and K_0 at –170°C were 8.91 and 64.2 MPa√m respectively and 82.5 and 163.7 MPa√m respectively at –100°C. The values of K_{min} determined from the curve fits were found to be within 1% and 5% of the experimental minimum values at –170°C and –100°C respectively.

The ability of the statistical model to describe the distribution of cleavage toughness at both temperatures has been shown to be good. The next step was to extend the model to describe the distribution of cleavage toughness following warm prestressing. It is clear from figure 6.4, which illustrates the cleavage toughness distribution function following a warm prestress load cycle for fracture at –170°C, that the minimum toughness following warm prestressing has increased and that the 63.2% value of toughness has also increased. Therefore, it was considered appropriate to use an analytical

model of the warm prestress effect to modify the parameters K_{min} and K_0 to describe the upward shift in toughness. The Chell model was used to predict the change in cleavage toughness at -170°C for a prestress event of average magnitude of 89 MPa√m. The Chell model can also be presented as a 'design curve' when presented in terms of K_I/K_{Ic} and K_f/K_{Ic}, as illustrated in figure 6.5 for specific values of the yield stress. The values of K_{Ic} equivalent to K_{min} and K_0 in the as-received toughness distribution were modified using the Chell model (equation (2.21)). For the average proof load, the ratios of K_1/K_{min} and K_1/K_0 for fracture at –170°C are 9.98 and 2.33 respectively. Using equation (2.21) or figure 6.5, values for K_{0f} *and* K_{minf} of 91.2 and 20.78 MPa√m are obtained respectively. Using these values in equation (6.10) the predicted distribution is close to the experimental results as shown in figure 6.4. The ratio of K_{0f} (obtained by fitting equation 6.10 to the distribution) from experimental results to the predicted K_{0f} is 1.14.

A similar analysis was applied for the LUCF cycle with fracture at –100°C. The results are shown in figure 6.6. In figure 6.6 it is observed that the predicted cleavage toughness distribution following warm prestressing is in very good agreement with the experiments at –100°C. The ratio of the experimental to predicted K_{0f} is 0.965. This prediction is marginally non-conservative (3.5%) based on the limited data set available.

The same analytical method was applied to cleavage toughness data obtained from BS1501 steel in the as-received and warm prestressed conditions. The results are illustrated in figure 6.7. The as-received

toughness distribution is comprised of data obtained from two different experimental studies. Six data points were obtained from 50mm thick SENB specimens, presented by Bell (1992). This material was of the same plate as the 25mm thick CT specimens tested and described in Chapter 4. The two data sets were combined as there were too few points in either data set to accurately describe the distribution of cleavage toughness in the as received condition. The warm prestressed data set is comprised solely of data obtained from 25mm tick compact tension specimens, all of which are detailed in Chapter 4.

The prediction of the combined Wallin and Chell theory as previously implemented is compared to the experimental distribution in figure 6.7. It is shown that the combined approach predicts a lower cleavage toughness following warm prestressing than the experimental results show to be the case. However, the result, if characterised by comparing the ratio of K_{0f} (predicted) to K_{0f} (experimental) is 0.9. The predictions are therefore within 10% of the experimental values.

Figures 6.8 to 6.10 illustrate each of the above data sets normalised by K_{min} and K_0. The relationship between the normalised critical fracture toughness and the natural log of the probability of failure is shown to be linear as follows:

$$(-ln\{1-P_f\})^{0.25} = \frac{K_f - K_{min}}{K_0 - K_{min}} \qquad (6.11)$$

The as-received cleavage toughness distributions of each data set are observed to lie directly on the 1:1 line described by the modified Wallin function, equation (6.11). If the warm prestressed data is normalised by the values of K_{0f} and K_{minf} predicted by the combined Wallin and Chell approach, the conservative nature of the prediction for A533B steel at –170°C (figure 6.8) and BS1501 steel at –120°C (figure 6.10) is demonstrated by the data lying underneath the 1:1 curve described by equation (6.11). The marginally optimistic prediction of the Wallin / Chell approach at –100°C for the A533B steel is shown in figure 6.9 by the data lying above the 1:1 line of equation (6.11). However, if all three warm prestressed data sets are normalised by their fitted values of K_{0f} and K_{minf}, that data lies on the 1:1 line. Therefore, if the cumulative distribution function is presented as equation (6.11), a linear relationship between the probability of fracture and the cleavage fracture toughness is found. The values of K_0 and K_{min} can be found using the combined Wallin / Chell approach and a probability of failure determined. This probability of failure has been shown to be conservative for the two materials for temperatures up to –120°C. The approach was shown to be marginally optimistic for A533B fractured at –100°C.

6.4. SIZE EFFECT IN CLEAVAGE TOUGHNESS IN THE AS RECEIVED AND WARM PRESTRESSED CONDITIONS.

The effects of warm prestressing and proof loading on the cleavage toughness of specimens of varying size have been investigated in the above study. It is well known that specimen size has a significant effect on the

cleavage toughness of the material (Anderson, 1992). This thickness effect is observed in the experimental work described in the above sections. The statistical model proposed by Wallin, described above, includes specimen thickness in the description of the distribution of cleavage toughness. As it has been shown, this cleavage toughness distribution function can be modified to describe the effects of warm prestressing on the cleavage toughness distribution. The influence of size on the warm prestress effect has been quantified by Wallin (1985) as follows:

$$K_{B1} = K_{B2}\left\{\frac{B_2}{B_1}\right\}^{0.25} \qquad (6.12)$$

where subscripts B1 and B2 refer to two different thicknesses respectively. Figure 6.11 illustrates the effects of the thickness corrections on A533B steel mean as-received cleavage fracture toughness at –170°C. It is observed in figure 6.11 however, that the accuracy of this method is dependent on the data set available being of sufficient size to accurately describe the distribution of cleavage toughness for the as-received condition. The thickness corrected toughness for the 6mm thick specimens is seen to be above the value at B=50mm. This is considered to be due to the small data set obtained at 6mm. At 25mm, the corrected cleavage toughness is shown to be the within the scatter band cleavage toughness for the 50mm thick specimens. Ideally, the thickness correction would result in the cleavage toughness at all thicknesses having the same value.

The aim of implementing the statistical method described in section 6.2 is to describe the distribution of cleavage toughness following warm prestressing and proof loading. This was shown to be an accurate method of describing the range of toughness obtained and showed that the Chell model can be used to predict the change in cleavage toughness when used in conjunction with a three parameter statistical model, with the value of the shape function *n* fixed at 4.. Figure 6.12 illustrates the toughness predicted by the Chell model for 6mm, 25mm and 50mm thick specimens, prior to and following correction using equation (6.12). It is observed that the correction predicts a consistent toughness for all specimens when corrected to the toughness for 50mm.

Figure 6.13 illustrates the experimental cleavage toughness for the three thicknesses following warm prestressing, compared to the Chell model predictions in the uncorrected condition. It is shown that the Chell model is conservative at 6mm and 50mm but non conservative at 25mm thickness. This is attributed to the 25mm data set being of limited size. Following thickness correction, the 6mm cleavage toughness values were corrected to within 5 MPa√m of the cleavage toughness of the 50mm thick specimens. The cleavage toughness of the 25mm thick specimens following warm prestressing, when corrected to 50mm, is shown to be below the mean toughness obtained at 50mm. However, the corrected cleavage toughness value is within the toughness distribution obtained following warm prestressing in 50mm thick specimens as shown in figure 6.13.

The thickness correction procedure was extended to correcting experimental data for as-received cleavage toughness data for all thicknesses. This enabled all the data to be collated into a single data set, figure 6.14. The fit of equation (6.10) is found to be good when comparing K_0, (for the corrected data) = 92.1 MPa√m, with K_0, (from fitting equation 6.10) = 94.2 MPa√m. The thickness correction procedure was also applied to the cleavage toughness data obtained following warm prestressing. Cleavage toughness data from 6mm thick specimens was corrected based on the results illustrated in figure 6.13, where the results are shown to be within 5 MPa√m of the 50mm thick specimens. Figure 6.15 illustrates the cleavage toughness distribution of the 50mm thick specimens following warm prestressing and the toughness distribution of the 6mm specimens following warm prestressing. As shown earlier, the 6mm specimens are of considerably higher toughness than the 50mm thick specimens, but following correction using equation (6.15), the toughness has been corrected to that at 50mm.

The use of thickness corrections has therefore been validated prior to and following warm prestressing, with the results compared to the Wallin cleavage toughness distribution function. It is shown in figure 6.15 that the lower end of the distribution is not well described by equation (6.10), however the majority of the distribution is seen to be in excellent agreement with the analytical solution.

6.5 ANALYSIS OF FINITE ELEMENT PREDICTIONS.

6.5.1 Comparison of Finite Element Predictions with Experimental Results.

The cleavage fracture toughness of A533B steel single edge notch bend specimens following an LUCF warm prestress event was predicted in Chapter 5 for a range of toughness. It was shown in Chapter 2, in figure 2.14 that the cleavage toughness of a material following warm prestressing was subject to a considerable degree of scatter. This distribution of cleavage toughness following warm prestressing has been successfully quantified, in the previous sections of this chapter.

The finite element predictions obtained in Chapter 5 show that the cleavage toughness following warm prestressing increases with increasing preload. The predictions were based on a stress matching criterion that was formulated following simulation of experimental fracture events with and without warm prestressing.

Figure 6.16 illustrates those predictions and compares them to the experimental results obtained by Smith and Garwood (1990b), Reed and Knott (1991) and Loss et al (1977). It is observed that the predictions provide a good description of the experimental results, although some data points lie outside the bounds described by the finite element results. This is not unexpected, however, as these experimental results are obtained from different data sets with different as-received cleavage toughness distributions.

In addition to this factor, the experimental conditions will not have exactly matched those simulated in the finite element simulations.

6.5.2 Comparisons with Analytical Models of the Warm Prestress Effect.

There are currently three different analytical approaches to modelling the warm prestress effect available. These were each described in Chapter 2.

Recall from Chapter 2 that the model proposed by Chell (1980) uses the superposition of elastic displacements outside the regions of plastic deformation to evaluate an equivalent J integral, J_e, using the strip yield model. When this J_e equates to the critical J integral, J_{Ic}, cleavage fracture is predicted to occur.

The model proposed by Curry (1981) again implements the principal of superposition, using the alternative approach of combining the stress state at the end of each of the load steps. This method provides a definition of the stress distribution at the fracture event in the near crack tip region. This stress distribution is used in conjunction with the RKR cleavage toughness model. This cleavage fracture criterion states that cleavage fracture will occur when a critical stress is exceeded over a critical distance which is dependant on the microstructure of the material.

Figure 6.17 compares the predictions of cleavage toughness following warm prestressing obtained from finite element analysis with the three analytical models described above. The data is presented normalised by the as-

received cleavage toughness. It is observed in figure 6.17 that the best agreement with the finite element predictions is obtained with the Chell model. The Curry model is observed to significantly under-predict the cleavage toughness. At higher ratios of K_1 / K_{Ic}, the Chell model also deviates from the finite element predictions.

The agreement observed between the Chell model and the finite element predictions is considered to be due to the stress matching method used. It was shown in Chapter 5 that the prediction of cleavage toughness can be obtained by matching the stress distribution formed by reloading the warm prestressed specimen to the stress distribution obtained at the as-received cleavage fracture toughness of the material at distances far greater than normally associated with cleavage fracture.

It was shown in figure 5.27 that the stress intensity factor obtained based on load was very similar to that estimated by selecting the path independent *J* integral as shown in figure 5.22. The path independent *J* was extracted from the region where only elastic stresses exist in the residual stress state, and therefore the *J* integral used to evaluate the critical stress intensity factor only included elastic distortions, as specified in the Chell model. If the *J* integral chosen to evaluate the critical stress intensity factor was selected from the near crack tip region were plasticity had occurred, the inclusion of plastic distortions in the *J* integral would mean that the critical *J* would be achieved at a lower load.

The path independent *J* integral can then be used to evaluate the stress field for an elastic material, figure 6.18. It is observed that this stress distribution describes the region of the predicted fracture stress field where the stress matching is performed with the as-received cleavage toughness stress distribution. The Curry model is therefore considered to describe the conditions of cleavage fracture used to predict cleavage fracture in the finite element simulations described in Chapter 5.

The Curry model of cleavage fracture, shown in figure 6.17 predicts lower values of cleavage toughness following warm prestressing than the finite element analysis. The Chell model is now considered in more detail to investigate the reasons for the lower predictions.

The application of this model was investigated using the experimental SENB as-received fracture case and case B selected from Smith and Garwood (1990b), described in Chapter 5. Recall that these experimental simulations provided the basis for the stress matching criterion implemented to predict the results that are compared to the models in figure 6.17.

Figure 6.19 illustrates the as-received fracture stress distribution, the warm prestressed fracture stress distribution, and the fracture stress distribution predicted by the Curry model.

This figure has the magnitude of the stress distributions normalised by the yield stress of the material. The distance ahead of the crack tip is normalised

by the effective yield stress of the material and the applied stress intensity factor. The effective yield stress, σ_y^{eff} depends on the prior loading history of the specimen. This assumes that the material behaves in an isotropic manner. For example , the yield stress of the material for an unload step from the maximum preload level is $2\sigma_{y1}$, whereas the effective yield strength for the fracture load step, reloading from the residual stress state is $\sigma_{y1} + \sigma_{y2}$ where σ_{y1} and σ_{y2} refer to the yield strengths at the preload and fracture temperatures in the as-received condition. The ordinate axis of figure 6.19 is given as $r^*(\sigma_y^{eff} / K_{app})^2$, which is equivalent to the ratio of the distance ahead of the crack tip and the radius of the plastic zone formed at the end of each load step.

It is observed in figure 6.19 that the stress distributions obtained from the experimental fracture loads agree with one another up to 0.04 r/r_{p3}, whereas the prediction obtained using the Curry model only matches up to r/r_{p3} of 0.008. The predicted value of K_f obtained using the Curry model was 145 MPa$\sqrt{m}$, less than the experimental fracture stress intensity factor of 171 MPa$\sqrt{m}$. It is therefore shown that the Curry model does not succeed in predicting the cleavage toughness of a material following warm prestressing because the distance over which the critical stress must be achieved is too small, and for that matter fixed by the micro structure of the material. It was observed in Chapter 5, figure 5.23, that the near tip critical stress distribution could be matched at loads far less than the load at which the fracture event occurs at.

It has therefore been demonstrated that the Curry model does not describe the critical conditions for fracture following warm prestressing due to the distances over which the critical stress must be achieved being too small and within the zone of residual compressive deformation.

6.6 ANALYSIS OF FINITE ELEMENT PREDICTIONS OF CLEAVAGE TOUGHNESS FOLLOWING SUB-CRITICAL CRACK GROWTH.

Section 5.8.3 described the two methods used to predict the cleavage toughness following warm prestressing and subsequent sub critical crack growth. These predictions were based on the stress matching method used in the previous sections of Chapter 5 to predict the cleavage toughness in the absence of any crack growth. This proved to be an acceptable approach up to the point where the sub critical crack extension extended the crack tip into the region of tensile residual stress.

The finite element simulations of experimental load case 12596 showed that the peak near tip stress matched the peak crack tip stress defined by the as - received cleavage toughness distribution for that extended crack length. Chapter 5, section 5.8.3 and figures 5.55 and 5.56 described the methods and results of obtaining predictions based on matching the peak crack tip stress. The predictions obtained using this method showed similar trends tos the experimental results, although half of the results at higher crack lengths were greater than the upper bound predicted by the finite element. The lower bound experimental results were found to lie close to the lower bound predictions obtained from the finite element study.

Predictions of cleavage fracture toughness following warm prestressing and sub critical crack growth were also obtained by matching the far field stress distributions to the as - received stress distribution for that crack length. This was considered a possible fracture criterion for several reasons.

Firstly, no classical fracture criterion currently in use states that fracture can occur when the peak stress at the crack tip reaches a critical value. All modern fracture criteria, such as that incorporated into the Wallin cleavage toughness distribution function, assumes that the critical stress must be achieved over a certain distance or volume ahead of the crack tip.

Secondly, there was no guarantee that the maximum as-received cleavage toughness obtained for the edm notched specimens during the experimental study was the maximum possible as received cleavage toughness for this configuration due to the limited number of tests performed.

Therefore, the stress distribution for the as-received cleavage toughness of 85 MPa$\sqrt{m}$ was scaled until it matched with the far field stress distribution of the warm prestressed specimen, specimen 12596, figure 5.42. This corresponded to a toughness of 113 MPa$\sqrt{m}$. Predictions were made based on this criterion and it was found that the predicted cleavage toughness for cracks that extended into the zone of tensile residual stress was significantly lower than that predicted by matching the peak stress. There was also no observed correlation between the experimental results and these predictions.

Chell (1986) describes an extension to the model of warm prestressing previously proposed to incorporate the effects of sub critical crack growth. This is achieved by the use of the strip yield model, and applying traction's to the extended crack faces such that these crack faces carry no stress. The appropriate models proposed by Chell (1986) were selected and plotted against the predictions obtained using both methods described above.

Figure 6.20 compares the predictions obtained by matching the peak crack tip stress with the Chell model. It is observed that for all cases, the finite element predictions agree reasonably with the analytical model solutions, and therefore the majority of the experimental data. Once again, the lower bound defined by the Chell model represents a lower bound to the experimental data.

Figure 6.21 compares the predictions obtained by matching the far field stress distribution with the as-received stress distribution to the Chell model predictions. When the crack growth increment is less than 1mm, the predictions follow the same trends as the Chell model due to the same fracture criterion being applied. When the crack growth increment exceeds 1mm, and the predictions are based on matching the far field stress, the finite element results deviate from the Chell model solutions which were observed to agree well with the experimental trends.

It is therefore concluded that the peak stress matching technique as implemented here provides the best agreement with the experimental results

and Chell model solutions. This criterion was based on the simulation of experimental fracture events and does not depend on any classical fracture criterion as its basis. The reasons for the agreement with the Chell model are not clear.

CHAPTER 7

DISCUSSION

7.1 INTRODUCTION

The influence and importance of the warm prestress effect has, to date, been difficult to classify due to the inherent scatter in a materials cleavage toughness in the as-received condition. To this end, the success of analytical models (Chell, (1980) and Curry, (1981)) that attempt to predict the warm prestress has been limited, as the cleavage toughness of a material following a warm prestress event is also subjected to high levels of scatter.

This discussion aims to address the issues of scatter in as-received cleavage toughness and its influence on the warm prestress effect using the results obtained from the experimental study detailed in Chapter 4 and numerical predictions obtained in Chapter 5. By combining currently available statistical models with analytical models, a consistent method of classifying the warm prestress effect is presented.

This discussion also analyses the effect of repeated warm prestress cycles and single warm prestress cycles followed by sub critical crack extension cleavage toughness. Current analytical models stipulate that no sub critical crack extension should occur prior to fracture. Chell (1986) has proposed a model to incorporate the effects of sub critical crack growth. However, there is

limited experimental evidence to support this model. The results of experimental and numerical investigations discussed in Chapters 4 and 5 will be discussed in an attempt to provide some validation to the approaches used in the analytical and numerical models.

7.2 EXPERIMENTAL AND NUMERICAL STUDIES.

The experimental investigations detailed in Chapters 3 and 4 aimed to complement previous investigations performed by Smith and Garwood (1990b) and Bell (1992) by providing additional data for various loading conditions. In order to maximise the efficiency of the experimental programme, only the LUCF cycle was investigated, although later experiments addressed the issue of multiple load – unload cycles prior to cooling and brittle fracture. Prior to the fracture studies being performed on the two candidate steels, uniaxial tensile tests were performed to provide data for implementation in finite element investigations, which were being performed in parallel to the experimental studies.

The results of these uniaxial tests highlighted the differences between the two materials, A533B and BS1501 steels. These are both commonly used in the fabrication of pressure vessels, although their properties were not at all similar. It was found that the BS1501 steel behaved in an elastic – perfectly plastic manner under monotonic loading conditions, in contrast to the strong post yield hardening behaviour of A533B steel. Both steels exhibited strong upper and lower yield points as demonstrated in Chapter 4. The influence of

prior plastic deformation on the hardening behaviour of the steels was also markedly different. In the case of BS1501 steel the material was shown to respond in an approximately isotropic fashion, with the yield strength in compression increasing linearly with the tensile yield strength on successive load cycles. It was noted that this increase in compressive yield strength was very small in comparison to the increase in tensile yield strength. In contrast however, the A533B steel was shown by Smith et al (1992) to respond in a kinematic fashion, whereby the yield strength in compression reduces linearly with the increase in tensile yield strength for successive load cycles.

The hardening response of the material subjected to a warm prestress load cycle was investigated using finite element studies in section 5.5.5. This section compared the isotropic and kinematic material hardening laws as implemented within ABAQUS. It was shown during that study that the cleavage fracture toughness following warm prestressing was independent of the material hardening law used. This was despite the demonstration that the magnitude of the residual stress formed near to the crack tip on unloading an isotropic material was approximately double that formed on unloading a kinematically hardening material.

Further tensile testing of BS1501 steel demonstrated that this materials' yield strength and hardening properties in tension at –120°C are not modified by a tensile overload and unload cycle performed at 20°C. The only difference that was observed between the virgin material at –120°C and the prestressed material at –120°C was the absence of the sharp upper and lower yield points

that characterise the monotonic response of this steel at all temperatures. The upper yield point is associated with small amounts of interstitial or substitutional impurities. During the initial yielding caused on preloading, where dislocations are forced past these impurities, on unloading and reloading these obstacles, having already been passed, offer no resistance and smooth yielding behaviour is observed.

The fracture toughness testing performed on both steels following a single warm prestress cycle provided data sets for each loading condition that were subject to a degree of scatter. The analyses presented in Chapter 6 showed that an analytical model based on the weakest link failure theory and the analytical solutions describing the crack tip stress and strain field could be used to describe the cumulative distribution function of failure in the as - received and warm prestressed conditions.

Once the influence of scatter in the results had been quantified by performing these statistical analyses, the effect of a single warm prestress cycle could be clearly represented. It was shown in Chapter 6 that the cleavage toughness of both of the candidate steels was enhanced by a single warm prestress load cycle and that this increase could be predicted by using the Chell model of the warm prestress effect. It was noted that the predictions for A533B steel and BS1501 steel at –170°C and –120°C were conservative, under predicting the increase in toughness by between 10% and 15%, based on the 63.2 percentile failure probability toughness value.

The experimental results obtained from the uniaxial and fracture test programmes provided data for performing simulations of warm prestress and subsequent fracture events using the finite element method. Following simulations of experimental load cases, the stress distribution of an as-received specimen was compared to that of the warm prestressed specimen at the experimental fracture load. These distributions were found to match one another for a significant distance ahead of the crack tip. As cleavage fracture is generally a stress controlled event, the concept of a critical stress was not new. When the stress distributions at fracture were compared to the analytical HRR predictions of the crack tip stress field, it was found that the stresses agreed with one another at distances much greater than the HRR fields matched the fracture stress. It was therefore concluded that for fracture to occur following a warm prestress event, a critical stress must be achieved ahead of the crack tip. It was also concluded that this critical stress was not a fixed value, nor was the critical distance over which that stress should be achieved a predetermined value. The fracture criterion proposed was as follows: the critical stress distribution was defined by the stress distribution ahead of the crack tip at the as-received fracture load. The distance over which this stress distribution should be achieved was a function of the preload level applied. The greater the preload intensity, and hence the greater the extent of the residual compressive deformation, the greater the distance over which the stresses can be matched.

This criterion was used to predict the cleavage fracture toughness of A533B steel specimens subjected to increasing preload intensities and different as-

received toughnesses. The results of the predictions were shown in Chapter 5 to not only agree well with the bounds of available experimental data, but also to agree well with the predictions obtained using the analytical Chell model (Chell, 1981) within the small scale yielding regime. This provided analytical validation of the fracture criterion implemented. The main justification for the agreement between the Chell model and the stress matching fracture criterion is that the distance over which matching must be performed is much greater than the extent of the plastic zone formed following full unloading. At those distances the stress field was shown to be purely elastic. This was confirmed by the predicted path independent *J* integrals in this region, where it was shown that the associated elastic HRR stress field described the actual stress field in the region where the stress matching is to be performed. Agreement with the Chell model was found as the model only includes the elastic displacements in evaluation of the critical stress intensity factor.

The finite element predictions were shown to disagree with the analytical model proposed by Curry (1981) as the stress matching is performed at a fixed micro-structural distance which is within the plastic zone at fracture. It has been shown in Chapter 6 that if the stress distribution of the reloaded specimen was matched to the critical stress distribution over the reduced distance as proposed by Curry, the prediction of cleavage toughness obtained was significantly lower than the finite element and Chell model predictions.

7.3 INFLUENCE OF SIZE ON THE WARM PRESTRESS EFFECT.

The influence of specimen size on the warm prestress effect was demonstrated in section 2.4.8. It was shown in this section that specimens that were close to conditions of plane strain, exhibited a lower degree of warm prestress benefit than specimens close to a state of plane stress. The differences between the specimen size could only be clearly observed at preload levels in excess of 1.5 times the unprestressed notch strength.

The results presented for in this study for different thickness A533B CT specimens show the same trends as the results presented in figure 2.9. The 6mm thick compact tension specimens exhibited a larger increase in toughness than the 25mm thick CT specimens. The analysis presented in Chapter 6 showed that, providing there was sufficient data available for a specimen size and preload condition, the data from the 6mm thick CT specimens could be 'thickness corrected' to lie within the distribution of cleavage toughness for the 25 mm and 50 mm thick CT and SENB specimens. This analytical technique allows an estimate of cleavage toughness following a warm prestress cycle to be performed for small and large specimens alike, providing that there is sufficient data to describe the materials fracture response in the as-received condition.

7.4 REPEATED WARM PRESTRESS LOAD CYCLES

The influence of repeated warm prestress load cycles at room temperature was also examined experimentally. As detailed in Chapter 4, the specimens

were loaded under two different loading conditions, load control and displacement control. The aim of the study was to examine the cumulative effects of these warm prestress load cycles on the cleavage toughness.

The response of the two steels to the repeated proof loading was observed to be significantly different, as may be expected by the variation in the uniaxial behaviour of each of the steels. Repeated proof loading in either load or displacement control was shown to have an insignificant effect on the cleavage fracture toughness of BS1501 steel in comparison to the toughness following a single cycle. The specimens that were repeatedly preloaded in load control were observed to have a slightly higher mean toughness than that of the repeated displacement control specimens. The investigations of Bell (1992) showed that repeated load control warm prestress cycles had little or no influence on the cleavage toughness, therefore concurring with the results of this study presented in Chapter 4.

The effects of repeated warm prestress load cycles on the A533B steel were considerably different to those observed in the BS1501 steel. It was found in Chapter 4 that repeated displacement control warm prestress cycles, on average, increased the of the material cleavage toughness by 37% beyond that observed for an as - received specimen. The effect of repeated preloading in load control increased the cleavage toughness by 86% beyond the as-received cleavage toughness. This marked increase in toughness in the case of the load controlled specimens prompted metallurgical investigations into the condition of the material surrounding the crack tip.

It was found that there was a large degree of local damage occurring during the repeated displacement control tests, with large voids forming around the crack tip and significant ductile tearing also being introduced at the high applied displacement. The influence of inclusion 'removal' from the crack tip area was discussed by Reed and Knott (1992) who considered that this void formation was changing the distribution of critical initiators in the crack tip region. However, the statistical model used to classify the cumulative probability of fracture for any given distribution of cleavage toughness was developed on the premise that the size and shape of the distribution of cleavage initiators, can be neglected providing no global interaction occurs. Applying this theory to the case of the repeated displacement control preloading cases implies that this local damage was not an important factor in the differences between the final cleavage toughness of the load and displacement controlled specimens.

Similar investigations of the damage that occurred in the crack tip region of the repeated load controlled specimens showed that a large degree of crack tip blunting had occurred. There were no large voids formed during this load cycle, and yet the toughness was vastly increased in comparison to that of the displacement controlled specimens. This finding adds more store to the conclusion drawn above that the effective removal of large inclusions from the metal matrix in the crack tip region was not influencing the cleavage toughness in any significant fashion. The effect of crack tip blunting will be discussed later.

The reasons for the difference in the response of the BS1501 specimens and the A533B specimens to repeated proof loading are considered to be due to the hardening responses of the two steels. The strain hardening behaviour of the A533B steel would, under load cycling conditions, increase the tensile yield strength of the material that is plastically deforming in the crack tip region. This would result in the compressive yield strength being reduced, and therefore the extent of plasticity ahead of the crack tip would increase on unloading from each successive load cycle.

7.5 INFLUENCE OF CRACK TIP BLUNTING ON THE WARM PRESTRESS EFFECT.

The positive influence of blunting on the warm prestress effect has been credited by several authors (Pokrovsky et al (1992), Nichols (1968), and Sugino et al (1979)). Harris et al (1980) on the other hand, demonstrated an equivalent warm prestress effect on blunt notched specimens as in sharp notched specimens. There is therefore a degree of uncertainty on the influence of crack tip blunting on the warm prestress effect.

This uncertainty prompted the detailed finite element investigations into the warm prestress effect on blunt notched SENB specimens presented in Chapter 5. These numerical investigations showed that the stress distribution ahead of the crack tip was influenced by the crack tip. The crack tip stress singularity associated with sharply notched specimens was truncated by the blunted tip. Following the warm prestress event, the as-received and warm

prestressed fracture stress fields were observed to agree at distances that exceeded the influence of the blunt tip. Subsequent finite element analysis of bluntly notched CT specimens showed the same effects, which indicated that not only was blunting not influencing the warm prestress effect, but also that the stress matching criterion of fracture was equally applicable to blunt notched specimens as it was to sharply notched specimens. This was due to the distance over which the stress matching was being performed exceeds the zone of influence of the blunted crack tip.

This conclusion concurs with the work of Reed and Knott (1992) who stress relieved specimens that had been subjected to warm prestress preload cycles. The subsequent fracture toughness of the warm prestressed and stress relieved specimens was the same as the as-received specimens. This therefore indicates that the warm prestress benefit was controlled by the residual stresses and not the reduction in acuity of the crack tip caused by the preload. Recall the case of repeated warm prestress cycles carried out in load control on 25mm thick A533B steel CT specimens, where significant crack tip blunting was observed. Based on the above analysis, the large increase in cleavage toughness is therefore due to hardening of the crack tip material rather than the crack tip blunting.

7.6 INFLUENCE OF SUB CRITICAL CRACK EXTENSION ON THE WARM PRESTRESS EFFECT.

The effect of sub critical crack extension on the warm prestress effect was investigated using both experimental and numerical techniques. The results

of both studies were compared to the appropriate analytical model proposed by Chell (1986). The experimental results were shown to obey the same trends described by the Chell model, with the lower bound experimental results following the lower bound predicted by the Chell model for $K_1 / K_{Ic} = 3$. Some of the experimental data points were of significantly higher toughness than the numerical predictions. However, due to the small number of tests performed on the specimens in the as-received conditions it is possible that specimens with higher as-received toughness may have been tested following warm prestressing and sub critical crack growth.

The finite element analyses that simulated experimental fracture events following warm prestressing and sub critical crack extension showed that at low crack growth increments, the stress matching technique used in previous sections could be applied to predict cleavage toughness. This was shown to apply for crack growth increments that extended the crack tip to the limit of the compressive residual stress distribution.

For large crack growth increments, where the crack tip was extended well into the tensile residual stress distribution, simulation of an experimental load case indicated that the peak stress at the crack tip could be matched with the as-received fracture stress distribution. Given that there exists no cleavage fracture model which uses a peak crack tip stress as its critical parameter, an alternative approach was adopted. This approach attempted to match the far field stress distribution to the as-received stress distribution. This approach

could not be justified against any experimental results, however, it provided a more intuitive fracture criterion.

The results predicted by the peak crack tip stress matching technique were compared to the experimental and analytical predictions in Chapter 6. These predictions matched the analytical models especially well. The experimental results were also in good agreement, with some results still being considerably higher than the numerical and analytical predictions. The results based on the far field matching criterion were shown to be predicting extremely low cleavage toughness, and did not agree with the analytical or experimental results.

CHAPTER 8

CONCLUSIONS AND RECOMMENDATIONS

In this thesis, experimental and finite element studies were undertaken to investigate the influence of warm prestress load cycles on the cleavage fracture toughness of two ferritic pressure vessel steels. The experimental studies provided fracture toughness data for specimens fractured following single and repeated warm prestress cycles, and following sub critical crack extension prior to fracture. The finite element simulations investigated the crack tip stress field conditions at fracture and during the preload cycles. Estimates of the cleavage toughness were obtained from the finite element analyses following single warm prestress cycles and following varying degrees of sub critical crack growth. The numerical predictions were compared to analytical models to provide validation of the techniques used.

8.1 CONCLUDING COMMENTS.

The experimental and numerical analyses presented in the preceding Chapters lead to the following conclusions, listed in order of perceived importance:

1. Cleavage fracture toughness is enhanced by a high temperature preload, providing that the preload acts in the same sense as the applied load at the low temperature.

2. Predictions of cleavage fracture toughness can be performed using the finite element method. The fracture criterion used to predict cleavage fracture is as follows. The critical stress distribution is defined as the stress distribution at the as - received fracture load. This as – received fracture stress distribution is matched to the warm prestressed stress distribution when reloaded at low temperature. Fracture is predicted to occur when the as-received stress distribution matches the warm prestressed stress distribution at distances exceeding those normally associated with cleavage fracture.

3. Cleavage toughness data in the as – received and warm prestressed conditions is highly scattered. This scatter can be accounted for by using the Wallin three parameter statistical model based on weakest link theory. The model, although based on small scale yielding assumptions, has been shown to accurately describe the cumulative distribution function of several data sets of the candidate steels.

4. Finite element predictions of cleavage fracture toughness following a warm prestress event have been obtained using the fracture criterion detailed in conclusion (2). These predictions were compared to analytical models. The model proposed by Chell (1980) was shown to describe analytically the fracture criterion used in the finite element predictions in small scale

yielding conditions. This model was shown to be less accurate in predicting cleavage fracture toughness outside the small scale yielding regime.

5. The analytical model proposed by Curry (1981) was shown to use the incorrect physical fracture criterion as its basis, as the critical distance X_0 has been shown to increase with increasing preload. This model therfore under predicts cleavage fracture toughness following a warm prestress event.

6. The cumulative distribution function of warm prestressed cleavage fracture toughness can be predicted using the Chell model of warm prestressing combined with the three parameter Wallin statistical model. The Chell model is used to modify the as-received values of K_0 and K_{min} in the Wallin model. The resulting distribution was found to be within 15 % for all cases analysed.

7. The cleavage fracture toughness of a specimen can be estimated using the stress matching fracture criterion described above and the critical stress intensity factor estimated by selecting the path independent J integral at the predicted fracture increment. Predictions of critical stress intensity factor can also be obtained based on the applied load at the predicted fracture increment.

8. A533B steel specimens subjected to repeated preload cycles under load control exhibited cleavage toughness values up to 86 % greater than the as-received toughness. Those specimens subjected to repeated preloading in displacement control exhibited cleavage toughness 37% greater than the as-received case.

9. BS1501 steel specimens subjected to repeated preload cycles in either displacement or load control did not exhibit toughness that was significantly greater than that exhibited following a single preload cycle.

10. Crack tip blunting was shown to have no influence on the warm prestress effect. Finite element studies comparing the predictions of sharply notched and blunt notched specimens illustrated that no difference between the cleavage toughness of the two crack tip configurations is expected.

11. Experimental studies showed that the cleavage fracture toughness following warm prestressing and sub-critical crack growth increased beyond the value obtained where no crack extension occurred where the crack growth increment was less than 0.5mm. Following 1mm crack extension, the cleavage toughness returned to the uncracked warm prestressed value.

Following further crack extension, the cleavage toughness continues to reduced. The toughness was not predicted to reduce to as-received cleavage toughness value for any of the crack growth increments studied.

12. Cleavage fracture toughness following warm prestressing and sub critical crack growth can be predicted by matching the stress field formed on reloading at low temperature with the as-received fracture stress distribution. Where the crack growth increment is small and the extended crack tip is contained within the compressive residual stress zone, the cleavage toughness can be estimated using the fracture criterion described in (2) above. Where the crack growth increment is large, extending the crack tip into the zone of tensile residual stress, fracture was predicted to occur when the peak stress at the crack tip matched the as-received cleavage stress distribution peak stress.

13. The above fracture criterion was validated by comparison with the analytical model proposed by Chell (1986) and with experimental results obtained as part if this study. The Chell model and finite element predictions for an as-received cleavage toughness of 40 and preload of 120 MPa$\sqrt{m}$ represented a lower bound to the experimental results.

14. Specimen size was shown to have a significant influence on the degree of warm prestress benefit that may be expected for a given preload level. A thickness correction method, based on the Wallin three parameter cleavage toughness model, was successfully used to correct the small specimen data to the cleavage toughness values expected in large specimens.

8.2 RECOMMENDATIONS FOR FUTURE WORK

1. The present work has investigated the warm prestress effect in specimens that were assumed to be in conditions of plane strain throughout the load history. A three dimensional numerical investigation of the warm prestress effect would provide a greater understanding of the effects of constraint on the warm prestress effect.

2. Further experimental studies investigating the warm prestress effect in small section specimens would provide more data to provide a clear understanding of the effects of specimen size on the warm prestress effect. Specifically, the data presented in this thesis would be complemented by further testing in the as-received and warm prestressed conditions following a single warm prestress cycle.

3. The influence of sub critical crack extension has been demonstrated within this thesis, however, the lack of

experimental data has provided grounds for uncertainty in using the finite element method to predict cleavage toughness. While the current method appears to provide a good description of the experimental trends, further experimental testing would enhance the data set.

4. Further testing of edm notched specimens in the as received condition is required to obtain a clear description of the extent of the scatter in specimens notched in this fashion.

REFERENCES

Anderson, T. L. and Dodds, R. H., Jr., 1991, *Specimen Size Requirements for Fracture Toughness Testing in the Transition Region.* Journal of Testing and Evaluation, JTEVA, Vol. 19, No. 2 pp123 –134.

Anderson, T. L., and Stienstra, D., 1989, *A model to Predict the Sources and Magnitude of Scatter in Toughness Data in the Transition Region.* Journal of Testing and Evaluation, JTEVA, Vol. 17, No. 1 pp 46-53.

Anderson, T. L., 1989, *A Combined Statistical and Constraint Model for the Ductile – Brittle Transition Region.* Non - Linear Fracture Mechanics: Volume II – Elastic Plastic Fracture, ASTM STP 995, J. D. Landes, A. Saxena and J.G. Merkle, Eds, American Society for Testing and Materials pp563 - 583

Anderson, T. L., 1992, *Fracture Mechanics: Fundamentals and Applications.* CRC Press.

Andrews, W. R., 1970. *Effect of Loading Sequence on Notch Strength of Warm Prestressed Alloy Steel.* Journal of Engineering For Industry. ASME, pp785 – 791.

ASTM E813 – 93, 1993, *Standard Test Method for J_{Ic}, a Measure of Fracture Toughness.* American Society for Testing and Materials, Philadelphia, 1993.

Bauschinger, J., 1886, *Ueber die Veränderungen der Elastizitatsgrenze und der Festigkeit des Eisens und Stahls durch Streckne, Questchen, Erwärmen Abkühlen und durch Oftmals Wiederholte Belastung,* Mitt: Mech –Tech Lab., XIII München, GERMANY

Bell, K., 1992. *The effects of Multiple preloads on subsequent low temperature fracture - progress report for PRAD.* TWI internal report 7162.01/93/767.1.

Beremin, F. M., 1981. *Numerical Modelling of Warm Prestress Effect Using a Damage Function for Cleavage Fracture.* In Proc. 5th Int. Conf. Fracture, ICF5. Pergamon Press, Oxford, 1981, Vol.2, pp 825 – 832.

British Engine Insurance Ltd., 1978. Technical Report, Vol. XIII p9, Manchester.

Brothers, A. J. and Yukawa, S., 1963. *The Effect of Warm Prestressing on Notch Fracture Strength.* Journal of Basic Engineering, Transaction of American Society of Mechanical Engineers, ASME, Ser. D, Vol. 85 pp 97 - 104

British Standards Institution, BS 5447, 1991. Methods of Test for Plane Strain Fracture Toughness (K_{Ic}) of Metallic Materials. BSI London.

British Standards Institution BS5500, 1994. *Specification of Unfired Fusion Welded Pressure Vessels.* BSI, London.

British Standards Institution PD6493:1991, *Guidance on Methods For Assessing the Acceptability of Flaws In Welded Joints.* BSI, London.

British Standards Institution BS 7448, 1991. *Fracture Mechanics Toughness Tests - Method for Determination of K_{Ic}, critical CTOD and critical J values of Metallic Materials.* British Standards Institution, London.

Burdekin, F. M., 1982. *The Role Of Fracture Mechanics In The Safety Analysis of Pressure Vessels.* Int. Journal Mech. Sci. Vol. 24 No. 4, pp 197 – 208. Pergamon Press, Oxford.

Chell, G. G., 1980. *Some Fracture Mechanics Applications Of Warm Prestressing To Pressure Vessels.* In Proc. 4th Int. Conf. Pressure Vessel Technology. Institution of Mechanical Engineers, 1980, pp 117 124.

Chell, G. G., 1986. *The Effects of Sub – Critical Crack Growth On The Fracture Behaviour Of Cracked Ferritic Steels After Warm Prestressing.* Fatigue and Fracture Of Engineering Materials and Structures, Vol. 9, No. 4, pp 259 – 274.

Chell, G. G. and Haigh, J. R., 1986. *The Effect of Warm Prestressing on Proof Tested Pressure Vessels.* Int. J. Press. Vess. & Piping. Vol. 23, pp 121 – 132.

Chell, G. G., Haigh, J. R. and Vitek, V., 1981. *A Theory of Warm Prestressing: Experimental Validation and the Implications for Elastic Plastic Failure Criteria.* International Journal Of Fracture, Vol. 17, No. 1, pp 61 – 81.

Cottrell, A., 1987. *Warm Prestressing and Fractures in Structural Steel.* Engineering Fracture Mechanics, Vol. 28, No. 5 / 6, pp 481 – 483. Pergamon Press Ltd.

Curry, D. A., 1980. *Comparison Between Two Models of Cleavage Fracture.* Metal Science, February 1980, pp 78 – 80.

Curry, D. A., 1981. *A Micromechanistic Approach to the Warm Prestressing of Ferritic Steels.* International Journal of Fracture, Vol. 17, No. 3, pp 335 – 343.

Curry, D. A., 1984. *Influence of Microstructure On Yield Stress and Cleavage Fracture Stress at -196°C of SA508 Class 2 Pressure Vessel Steel.* Metal Science, Vol.18, pp 67 – 76.

Curry, D. A. and Knott, J. F., 1976. *The Relationship Between Fracture Toughness and Microstructure In The Cleavage Fracture Of Mild Steel.* Metal Science, January 1976, pp 1 – 6. The Metals Society.

De Jong, B., 1986. *Strain Hardening Effects of the Warm Prestressing of Ferritic Steels.* Conf. Fracture, ECF 6, Fracture Control Of Engineering Structures, Vol. 1. Eds H. C. van Elst and A. Bakker. EMAS Ltd, pp 335 – 350.

Dugdale, D. S., 1960. *Yielding of Sheets Containing Slits.* Journal of Mechanics and Physics of Solids, Vol. 8, pp 100 – 104.

Fearnehough, G. D. and Jones, D. G., 1978, *An Approach to Defect Tolerance in Pipelines.* In Proc. Conf. Tolerance of Flaws In Pressurised Components, IMechE Paper C97/78. Institution of Mechanical Engineers, London.

Fowler, H. and Smith, D. J., 1997. *Finite Element Analysis of Warm Prestressing Of Pressure Vessel Steel.* Transactions of the 14th International Conference on Structural Mechanics in Reactor Technology (SMiRT 14), Vol. 4, pp 61 – 66

Fowler H., Smith D. J. and Bell, K., 1997. *Scatter in Cleavage Fracture Toughness Following Proof Loading.* In. Proc. Int. Conf. Fract., ICF 9.

Harris, C. P., Bowen, P. and Knott, J. F., 1986. *Warm Prestressing of Blunt Notches.* Conf. Fracture, ECF 6, Fracture Control Of Engineering Structures, Vol. 1. Eds H. C. van Elst and A. Bakker. EMAS Ltd, pp 335 – 350.

Harrison, T. C., and Fearnehough, G. D., 1972. *The Influence of Warm Prestressing on the Brittle Fracture of Structures Containing Sharp Defects.* Journal of Basic Engineering. Transactions of the American Society of Mechanical Engineers, ASME, Vol. 94 pp 373 –376.

Harrop, L. P., 1979. *Warm Prestressing During Severe Thermal Shock Loading of a Pressure Vessel.* Int. J. Press. Vess. & Piping, Vol. 7. pp 463 - 482

Harrop L. P.,1983. *The Integrity of Pressure Vessels.* Sci. Prog., Oxf, Vol. 68 pp 423 – 457.

Hibbit, Karlsson and Sorenson Inc. 1995. *ABAQUS Users Manuals.* HKS Inc. 1080 Main Street, Pawtucket, RI 02680-4847, U. S. A.

Hutchinson, J. W., 1968. *Singular Behaviour at the End of a Tensile Crack in a Hardening Material.* Journal of the Mechanics and Physics of Solids, Vol. 16, pp 13 – 31.

Ingham, T., Knee, N., Milne, I., and Morland, E., 1989. *Fracture Toughness in the Transition Regime for A533B Steel: Prediction of Large Specimen Results From Small Specimen Tests.* Fracture Mechanics: Perspectives and Directions (Twentieth Symposium) ASTM STP 1020, R. P. Wei and R. P. Gangloff, Eds., American Society for Testing and Materials, Philadelphia, pp 369 – 389.

Irwin, G. R., 1968. *Linear Fracture Mechanics, Fracture Transition and Fracture Control.* Engineering Fracture Mechanics, No. 1, pp 241 – 257.

Jesensky, M., and Vargova, J., 1981. *Calculation and Measurement of Stress in Thick Walled Welded Pressure Vessels.* Zvaracske Spravy / Welding News, Vol. 3, No. 36, pp 79 - 87

Kihara, H., Masubuchi, K., Kusuda, T., and Iida, K., 1959. *Initiation and Propagation of Brittle Fracture in Residual Stress Field.* IIW Doc. X-219-59.

Leggat, R. H., and Davey, T. G., 1987. *Measurements of the Reduction due to Proof Loads of Residual Stresses in Simulated Pressure Vessel Welds.* Presented at the ASTM Specialists Symposium on Mechanical Relaxation of Residual Stresses, April 1987.

Lin, T., Evans, A. G., and Ritchie, R. O., 1986. *A Statistical Model of Brittle Fracture by Transgranular Cleavage.* Journal of the Mechanics and Physics of Solids, Vol. 34, pp 477 – 497.

Loss, F. J., Gray, R. A. Jr., and Hawthorne J. R., 1978. *Significance of Warm Prestress to Crack Initiation During Thermal Shock.* Nuclear Engineering and Design, Vol. 46, pp 395 – 408.

Loss, F. J., Gray, R. A. Jr., and Hawthorne J. R., 1979. *Investigation of Warm Prestress For The Case of Small ΔT During a Reactor Loss – of – Coolant Accident .* ASME Journal of Pressure Vessel Technology, Vol. 101, No. 4, pp 298 – 309.

McClintock, F. A., 1971. *Plasticity Aspects of Fracture.* In FRACTURE, Ed H. Leibowitz, Academic Press.

McMeeking, R. M., and Parks D. M., 1979. *On the Criteria For J Dominance of Crack Tip Fields in Large Scale Yielding.* ASTM STP 668, American Society for Testing and Materials, Philadelphia, pp175 - 194

Nakamura, M., and Tsuya, K., 1977. *The Influence of Preloading on Brittle Fracture of Notched Steel Specimens.* Transactions of National Research Institute For Metals, Vol. 19, No. 5, pp 211 – 218.

Nakamura, M., Kobayashi, H., Kodaira, T., and Nakazawa, H., 1981. *On The Effects of Preloading On The Fracture Toughness of A533B-1 Steel.* In Advances in Fracture Research. Proceeding of Fifth International Conference on Fracture, ICF5, Vol. 2, pp 817 –824.

Neville, D. J., 1987. *Statistical Analysis of Fracture Toughness Data.* Engineering Fracture Mechanics, Vol. 27, No. 2, pp 143 – 155.

Nichols, R. W., 1968. *The Use of Overstressing Techniques to Reduces the Risk of Subsequent Brittle Fracture, Parts 1 and 2.* Br. Welding Journal. (January and February 1968).

Nordell, W. J., and Hall, W. J., 1965. *Two Stage Fracturing in Welded Mild Steel Plates.* Welding Journal, Vol. 44, pp 1245 - 1345

Ostergren, W. J., 1969. Masters Thesis, Brown University, U. S. A. (quoted by Curry, D. A., 1981)

Pense, A. W., Gross, J. H., and Stout, R. D., 1960. *Effect of Elevated Temperature Exposure on Heavy Section Pressure Vessel Steels.* Welding Jnl. Re. Suppl., Vol. 39, 1960, pp 231 – 235.

Pickles, B. W., and Cowan A., 1983. *A Review of Warm Prestressing Studies.* International Journal of Pressure Vessels and Piping. Vol. 14, pp 95 – 131.

Pineau, A., 1994. *Modelling Micro-mechanisms and Statistical Features of Ductile Fracture.* In Proc. ECF10 – Structural Integrity: Experiments, Models and Applications, Vol. 1, Eds K-H. Schwalbe C. Berger, pp 37 - 51

Pineau, A., 1997. *Modelling Of Scatter and Size Effects in Ductile and Brittle Fracture.* Transactions of the 14th International Conference on Structural Mechanics in Reactor Technology (SMiRT 14), Vol. 4, pp 619 – 630

Pokrovsky, V.V., Troshchenko, V.T., Kopchinsky, G.A., Kaplуneneko, V.G., Fiodorov, V.G., and Dragunov, Yu. G., *The influence of plastic prestraining on brittle fracture resistance of metallic materials with cracks*. Fat. Fract. Eng. Mat. Struct. Vol. 18 No 6, pp 731-746.

Reed, P. A. S., and Knott, J.F., 1992. *An Investigation Of The Warm Prestressing (WPS) Effect In A533B Weld Metal.* Fatigue Fract. Engng. Mater. Struct. Vol. 15, No 12, pp. 1251 - 1270

Reed, P. A. S., and Knott, J.F., 1996a. *Investigation Of The Role Of Residual Stresses In The Warm Prestressing (WPS) Effect Part I - Experimental.* Fatigue Fract. Engng. Mater. Struct. Vol. 19, No 4, pp. 485 - 500

Reed, P. A. S., and Knott, J.F., 1996b. *Investigation Of The Role Of Residual Stresses In The Warm Prestressing (WPS) Effect Part II - Analysis.* Fatigue Fract. Engng. Mater. Struct. Vol. 19, No 4, pp. 501 – 513

Rice, J. R., 1967. *Mechanics of Crack Tip Deformation and Extension by Fatigue.* Fatigue Crack Propagation, ASTM STP 415, American Society for Testing and Materials, pp 247 – 309

Rice, J. R., 1968. *A Path Independent Integral and the Approximate Analysis of Strain Concentrations by Notches and Cracks.* Journal of Applied Mechanics, Vol. 35, pp 379 – 386.

Rice, J. R., and Rosengren, G. F., 1968. *Plane Strain Deformation Near A Crack Tip in a Power Law Hardening Material.* Journal of Mechanics and Physics of Solids, Vol. 16, pp 1 – 12.

Rice, J. R., and Tracey, D. M., 1968. In Numerical and Computer Methods in Structural Mechanics, S. J. Fenves et al, eds., Academic Press, New York, pp 585 – 623.

Ritchie, R. O., Knott, J. F., and Rice, J. R., 1973. *On The Relationship Between Critical Tensile Stress and Fracture Toughness in Mild Steel.* Journal of Mechanics and Physics of Solids, Vol. 21, pp 395 – 410.

Ritchie, R. O., Server, W. L., and Wullaert, R. A., 1979. *Critical Fracture Stress and Fracture Strain Models for the Prediction of Lower and Upper Shelf Toughness in Nuclear Pressure Vessel Steels.* Metallurgical Transactions A, Vol. 10A, pp 1557 –1570.

Sankey, G. O., 1963. Discussion at end of Brothers and Yukawa: *The Effect of Warm Prestressing on Notch Fracture Strength.* Journal of Basic Engineering, Transaction of American Society of Mechanical Engineers, ASME, Ser. D, Vol. 85 pp 102 – 103.

Satoh, K., Toyoda, M., and Mutoh, Y., 1983. *Effect of Prestrain at Elevated Temperature on the Fracture Behaviour of High Strength Steels.* Journal of Engineering and Materials Technology, Transactions of the ASME, Vol. 105, pp 16 – 20.

Shih, C. F., 1981, *Relationship Between the J Integral and the Crack Opening Displacement for Stationary and Extending Cracks.* Journal of the Mechanics and Physics of Solids, Vol. 29, pp 305 – 326.

Shih C. F., and German, M. D., 1981. *Requirements for a One Parameter Characterisation of Crack Tip Fields by the HRR Singularity.* International Journal of Fracture, Vol. 17, pp 27 – 43.

Slatcher, S., 1986. *A Probabalistic Model for Lower – Shelf Fracture Toughness – Theory and Application.* Fatigue and Fracture of Engineering Materials and Structures, Vol. 9, No. 4. Pp 275 – 289.

Slatcher, S., and Evandt, Ø., 1986. *Practical Application of the Weakest Link Model to Fracture Toughness Problems.* Engineering Fracture Mechanics, Vol. 24, No. 4 pp 495 – 508.

Smith, D. J., 1986. *The Influence of Proof Testing On Component Reliability: Progress Report 1 – Parent Material Characterisation.* Welding Institute Report No. 5561/1/86.

Smith D. J., and Garwood, S. J., 1990a. *The Significance of Prior Overload on Fracture Resistance: A Critical Review.* Int. J. Press. Vess. and Piping. Vol. 41, pp 255 -296

Smith D. J., and Garwood, S. J., 1990b. *Experimental Study of Effects of Prior Overload on Fracture Toughness of A533B Steel.* Int. J. Press. Vess. and Piping. Vol. 41, pp 297 -331

Smith D. J., and Garwood, S. J., 1990c. *Application of Theoretical Methods to Predict Overload Effects on Fracture Toughness of A533B* Int. J. Press. Vess. and Piping. Vol. 41, pp 333 - 357

Smith D. J., and Garwood, S. J., 1992. *The Application of Fracture Mechanics to Assess the Significance of Proof Loading.* Fracture Mechanics: Twenty Second Symposium (Volume I) ASTM STP 1131, H. A. Ernst, A Saxena, and L. McDowell, Eds., American Society for Testing and Materials, Philadelphia, pp 833-849.

Smith, D. J., Bourke, M. A. M., Hodgson, A. P., Webster, G. A., and Webster, P. J., 1992. *Interpretation of Residual Stress Distributions in Previously Loaded Cracked Beams.* Journal of Strain Analysis, Vol. 27, No. 2, pp 77 – 83.

Steigerwald, E. A., 1961. *Influence of Warm Prestressing on the Notch Properties of Several High —Strength Alloys.* Transactions of the American Society of Metals, Vol. 54, pp 445 – 455.

Succop, L. N., Pense, A. W., and Stout, R. D., *The Effects if Warm Overstressing on Pressure Vessel Steel Properties.* Welding Research Supplement, pp 345S –364S.

Sugino, S., Pense, A. W., and Stout, R. D., 1979. *The Warm Overstressing of Pressure Vessel Steels.* Application of Materials for Pressure Vessels and Piping. American Society of Mechanical Engineers.

Tracey, D. M., 1976. Transactions of the ASME, Journal of Engineering Materials and Technology, Vol. 98, pp 146 –151.

Wallin, K., 1984. *The Scatter in Klc Results.* Engineering Fracture Mechanics, Vol. 19, No. 6. No 1085 – 1093.

Wallin, K., 1985. *The Size Effect in Klc Results.* Engineering Fracture Mechanics, Vol. 22, No. 1. No 149 – 163.

Wallin, K., 1989. *The Effect Of Ligament Size on Cleavage Fracture Toughness.* Engineering Fracture Mechanics, Vol. 32, No. 3, pp 449-457.

Wallin, K., 1989b. *The Effect Of Ductile Tearing on Cleavage Fracture Probability in Fracture Toughness Testing.* Engineering Fracture Mechanics, Vol. 32, No. 4. No 523-531.

Wallin, K., 1991. *Statistical Modelling of Fracture in the Ductile – to – Brittle Transition Region.* Defect Assessment in Components – Fundamentals and Applications, ESIS / EGF 9, (Edited by J. G. Blauel and K. H. Schwalbe) Mechanical Engineering Publications, London.

Wallin, K., Saario, T., and Törrönen, K., 1984. *Statistical Model for Carbide Induced Brittle Fracture in Steel.* Metal Science, Vol. 18, pp 13 – 16.

Wallin, K., Saario, T., and Törrönen, K., 1987. *Fracture of Brittle Particles In A Ductile Matrix.* International Journal of Fracture, Vol. 32, pp 201 – 209.

Weibull, W., 1951. *A Statistical Distribution Function of Wide Applicability.* Journal of Applied Mechanics, Vol. 18, pp 293 - 296, American Society of Mechanical Engineers.

Yukawa, S., 1969. *Evaluation of Periodic Proof Testing and Warm Prestressing Procedures for Nuclear Reactor Vessels.* General Electric Report HSSTP-TR-1.

TABLE 3.1. Chemical Analysis of BS1501 490Gr B LT50 C-Mn pressure vessel steel.

	C	S	P	Si	Mn	Ni	Cr	Mo	V
BS1501	0.18	0.01	0.015	0.32	1.12	0.02	0.02	<0.005	0.01
	Cu	**Nb**	**Ti**	**Al**	**B**	**Sn**	**Co**	**As**	**C.E.***
BS1501	0.02	0.031	<0.002	0.03	<0.0003	<0.005	0.01	0.005	0.38

*C.E..= carbon equivalent

TABLE 3.2. Chemical Analysis of A533B Class 1 pressure vessel steel.

	C	S	P	Si	Mn	Ni	Cr	Mo	V
A533B	0.18	0.005	0.006	0.24	1.41	0.56	0.18	0.48	<0.002
	Cu	**Nb**	**Ti**	**Al**	**B**	**Sn**	**Co**	**As**	**C.E.**
A533B	0.12	<0.002	<0.018	0.03	<0.0003	0.01	0.01	0.005	0.59

TABLE 4.1. Uniaxial Tensile Properties of BS1501

temp	E (GPa)	σ_y ^{upper} (MPa)	σ_y ^{lower} (MPa)	σ_{UTS} (MPa)
20°C	203	507	421	421
-70°C	223.5	542	445	445
-120°C	207.3	610	470	470

TABLE 4.2. BS1501 As-Received Fracture Test Details .

specimen	a (mm)	B (mm)	W (mm)	P_f (kN)	K_f (MPa√m)	temp
5a*	25.885	50	24.962	41.5	75.75	-120°C
5b*	25.837	50.001	24.972	32.25	58.66	-120°C
5c*	26.21	49.996	24.952	34.5	64.33	-120°C
6a§	25.54	50.002	25.02	41.7	97.4	-70°C
6b§	25.934	50.202	25.022	33.34	87.09	-70°C
6d§	24.67	49.936	24.968	40.38	95.85	-70°C

*: fatigue precracked; §: edm notched.

TABLE 4.3. BS1501 Single Proof Load Test Details For Fracture at -120°C.

specimen	a (mm)	B (mm)	W (mm)	P_1 (kN)	K_1 (MPa√m)	J_1 (N/mm)	P_f (kN)	K_f (MPa√m)
11c	25.44	49.84	24.97	58.82	105.09	340.60	62.00	110.77
13b	25.16	50.01	24.93	52.12	91.00	256.47	53.50	93.41
14c	28.63	50.00	25.10	37.35	81.65	210.23	43.75	95.63
15a	25.46	50.00	25.00	59.61	105.80	345.04	67.37	119.56
15b	25.66	50.16	24.96	59.41	106.23	343.23	57.71	103.18
15c	25.54	50.00	24.97	59.41	106.07	342.86	62.47	111.53
16a	23.99	49.98	24.95	56.50	91.94	268.43	64.00	104.15
16c	21.37	50.01	24.71	69.25	98.08	295.51	72.46	102.62
18a	25.56	49.94	24.99	59.63	106.82	343.75	63.64	114.01

TABLE 4.4. BS1501 Repeated Proof Load Test (displacement control) Details For Fracture at -120°C.

specimen	a (mm)	W (mm)	B (mm)	P_1 (kN)	K_1 (MPa√m)	J_1 (N/mm)	P_f (kN)	K_f (MPa√m)
13e	25.56	50.18	24.94	52.63	93.52	367.83	60.23	107.02
13f	23.87	49.98	24.92	58.95	95.40	391.95	71.95	116.43
18f	23.81	50.01	24.98	59.01	94.83	389.08	71.96	115.64
21a	25.87	49.96	24.99	59.77	109.09	433.25	54.91	100.22
21b	26.49	50.19	24.99	58.70	110.36	505.64	55.65	104.64
21c	25.90	50.00	24.96	58.87	107.61	391.08	61.04	111.57
22a	26.19	50.18	24.92	57.13	105.69	356.10	61.96	114.62
22b	26.02	50.20	24.93	58.04	106.12	359.32	60.93	111.40

TABLE 4.5. BS1501 Repeated Proof Load Test (load control) Details For Fracture at -120°C.

specimen	a (mm)	B (mm)	W (mm)	P_1 (kN)	K_1 (MPa√m)	J_1 (N/mm)	P_f (kN)	K_f (MPa√m)
13d	25.71	24.97	50.14	49.219	88.28	272.9	58.17	104.34
18b	26.21	24.96	50.11	58.749	108.97	389.9	61.25	113.61
18c	25.06	24.99	50.07	59.632	109.62	395.2	65.83	121.02
20a	26.12	24.97	50.10	59.476	109.71	398.0	58.47	107.84
20b	26.20	24.99	49.97	60.270	112.26	460.86	56.35	104.96
20c	25.96	24.98	50.01	58.695	107.56	419.09	68.18	124.95

TABLE 4.6. Uniaxial Tensile Properties of A533B.

temp	E (GPa)	σ_y^{upper} (MPa)	σ_y^{lower} (MPa)	σ_{UTS} (MPa)
20°C	202	561	500	668
-170°C	209	953	873	960

TABLE 4.7. A533B As-Received Fracture Test Details For Fracture at -170°C, B=25mm.

specimen	a (mm)	B (mm)	W (mm)	J_f (MPamm)	P_f (kN)	K_f (MPa√m)
ab1n	26.15	49.85	24.95	10.42	33.67	62.98
ab2n	25.22	49.94	24.91	9.79	24.83	43.66
ab3n	27.21	49.74	24.96	11.22	35.00	70.52
1596	25.12	49.90	24.99	9.74	41.96	73.23
2596	24.92	50.03	25.03	9.58	49.15	84.15
3596	24.89	49.86	24.92	9.62	49.15	84.97

TABLE 4.8. A533B Single Proof Load Test Details For Fracture at -170°C, B=25mm.

specimen	a (mm)	B (mm)	W (mm)	P_1 (kN)	K_1 (MPa√m)	J_1 (N/mm)	P_f (kN)	K_f (MPa√m)
ab4wps	26.48	49.83	24.95	68.00	130.05	119.18	40.57	77.58
ab5wps	25.70	49.88	24.91	60.49	109.90	15.78	61.57	111.86
ab7wps	25.99	50.08	25.00	60.31	110.27	17.41	44.79	81.90
a1spl	25.89	50.17	24.96	61.00	110.60	17.66	37.46	67.92
a3spl	27.37	50.11	24.94	60.32	120.88	48.47	32.75	65.63
a4spl	27.27	50.05	24.96	60.38	120.48	17.13	31.66	63.18
a5spl	26.00	49.88	24.99	60.91	112.47	20.15	28.18	52.03

TABLE 4.9. A533B Repeated Proof Load Test Details For Fracture at -170°C, B=25mm.

specimen	a (mm)	B (mm)	W (mm)	P_1 (kN)	K_1 (MPa√m)	J_1 (N/mm)	P_f (kN)	K_f (MPa√m)
a7rpd*	25.25	49.72	24.96	86.25	153.08	424	52.5	93.17
a8rpd*	26.43	49.964	24.978	77.5	146.7	398	46.25	87.52
a9rpl§	25.29	50.002	24.944	76.205	134.1	67	69.625	122.5
a10rpl§	28.95	50.09	24.97	55	123.2	83	55	123.16

*: displacement control; §: load control

TABLE 4.10. A533B Sub - Critical Crack Growth Test Details For Fracture at -170°C, B=25mm.

specimen	a (mm)	B (mm)	W (mm)	da (mm)	P_1 (kN)	K_1 (MPa√m)	J_1 (N/mm)	P_f (kN)	K_f (MPa√m)
4596	25.138	49.906	24.954	0.274	71.875	123.63	159.40	49.825	87.16
5596	25.502	49.842	24.976	0.528	70.625	122.51	202.92	52.381	93.90
6596	24.89	49.64	24.96	0.418	70.9375	120.39	188.68	65.016	113.21
7496	25.972	49.944	25.004	1.022	71.25	122.77	144.16	78.129	143.51
8596	25.94	49.926	24.994	1.072	71.25	122.29	180.99	69.018	126.67
9596	26.13	50.01	24.992	1.044	71.25	123.52	163.54	42.546	78.76
10596	27.366	49.96	24.994	2.446	70.625	121.44	195.10	56.475	113.69
11596	27.442	50.064	24.928	2.368	70.625	122.39	278.37	34.894	70.45
12596	27.65	50.06	24.966	2.57	71.25	123.35	221.17	50.855	104.01

TABLE 4.11. A533B As-Received Fracture Test Details For Fracture at -170°C, B = 6mm.

specimen	a (mm)	W (mm)	B (mm)	Pf (kN)	J_{Ic} (N/mm)	K_{Ic} (MPa√m)
1ar6	25	50	6	17	68.43	122.17
2ar6	25	50	6	13.25	39.85	95.22
3ar6	25	50	6	21	111.71	150.92
4ar6	25	50	6	14	44.5	100.61
5ar6	25	50	6	24.125	173.9	173.37

TABLE 4.12. A533B Single Proof Load Test Details For Fracture -170°C, B = 6mm.

specimen	a (mm)	W (mm)	B (mm)	P_1 (kN)	K_1 (MPa√m)	J_1 (N/mm)	P_f (kN)	K_f (MPa√m)	J_{crit} (N/mm)
1spl6	25	50	6	14.462	103.93	68	25.30	181.87	124.11
3spl6	25	50	6	14.52	104.45	*	23.75	170.67	*
5spl6	25	50	6	14.52	104.39	57	26.31	189.08	113.95
6spl6	25	50	6	14.39	103.44	62	23.02	165.45	118.50
7spl6	25	50	6	14.3	102.76	*	22	158.10	*
8spl6	25	50	6	14.46	103.93	60	25.07	180.23	117.17

* data not available.

TABLE 4.13. A533B Repeated Proof Load Test Details For Fracture -170°C, B = 6mm.

specimen	a (mm)	W (mm)	B (mm)	P_1 (kN)	K_1 (MPa√m)	J_1 (N/mm)	P_f (kN)	K_f (MPa√m)	J_{crit} (N/mm)
2rpl6 *	25	50	6	15.193	109.19	74	24.961	179.38	130
4rpl6 *	25	50	6	14.375	103.30	63	25.071	180.17	120
6rpl6 *	25	50	6	14.513	104.2	60	13.95	100.30	117
7rsp6 §	25	50	6	16.323	117.30	119	14.5	104.20	164
8rsp6 §	25	50	6	16.411	117.94	137	16.04	115.28	176
9rsp6 §	25	50	6	16.013	115.07	127	20.150	144.86	170

• load control; § displacement control.

TABLE 5.1. Loading conditions for specimens Ab1n and Ab5wps.

specimen	a (mm)	B (mm)	W (mm)	P_1 (kN)	K_1 (MPa√m)	J_1 (N/mm)	P_f (kN)	K_f (MPa√m)
ab1n	26.15	49.85	24.95	62.98	10.42	33.67	x	x
ab5wps	25.70	49.88	24.91	60.49	109.90	15.78	61.57	111.86

TABLE 5.2 Boundary Conditions Applied to Simulation of Fracture Following Warm Prestressing and Sub Critical Crack Growth Experiments.

K_{Ic} MPa√m	Δa (mm)	0.0	0.25	0.5	0.75	1	2	3	4
40		x	x	x	x	x	x	x	x
60		x	x	x	x	x	x	x	x
85		x	x	x	x	x	x	x	x

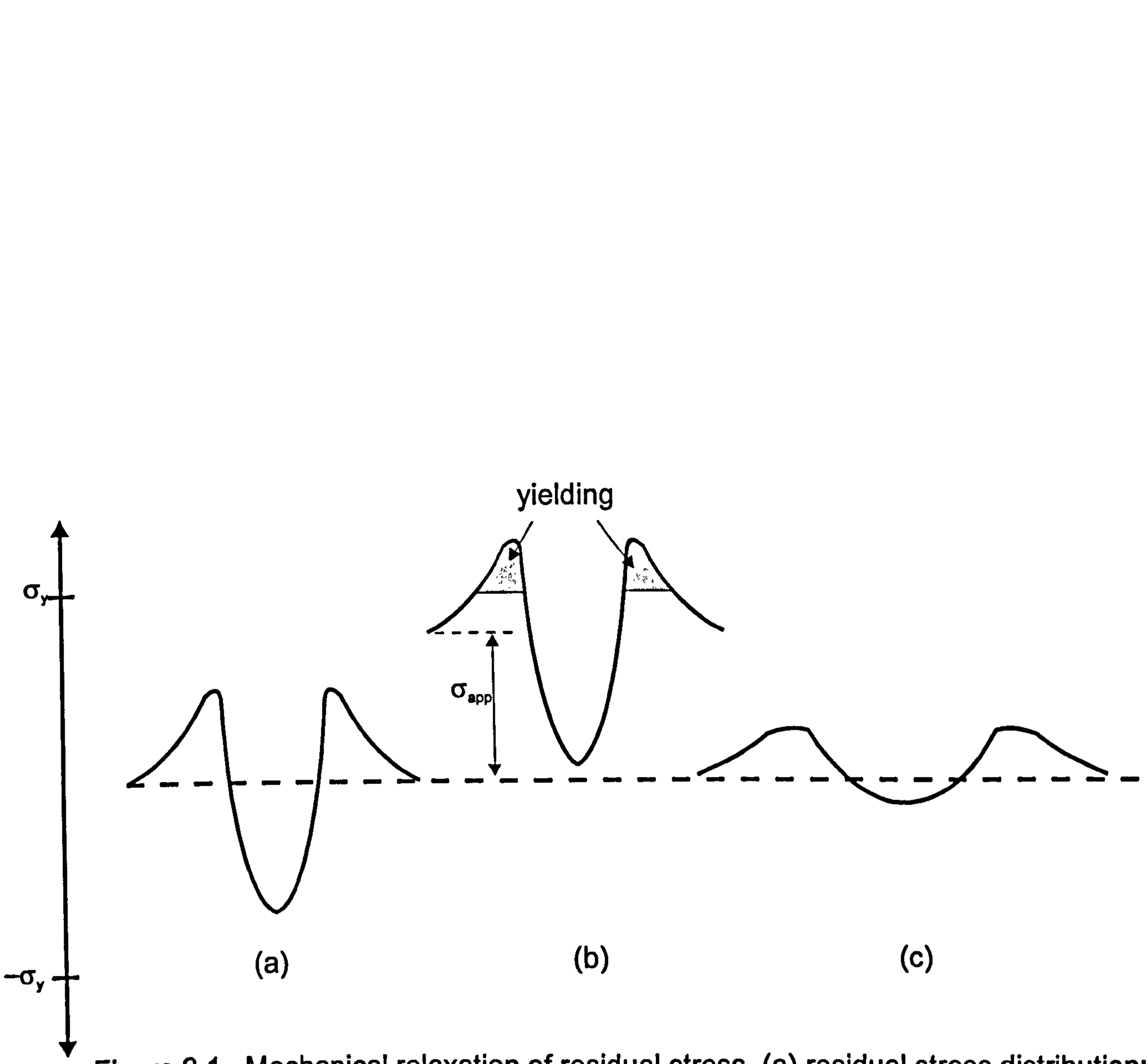

Figure 2.1. Mechanical relaxation of residual stress. (a) residual stress distribution; (b) application of uniform tensile stress; (c) final residual stress distribution after removal of tensile stress.

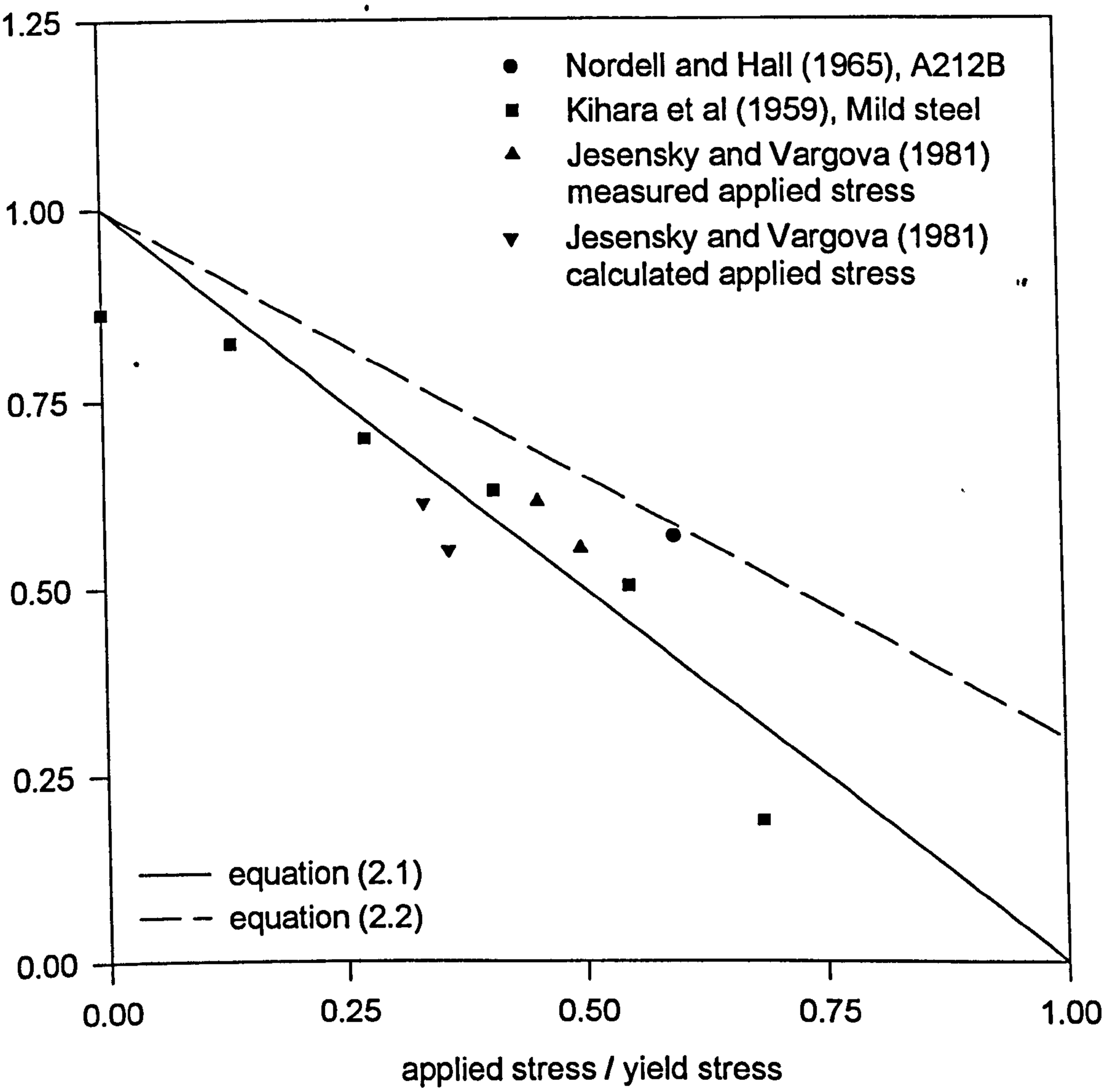

Figure 2.2. Variation of measured residual stress after overload with applied stress.

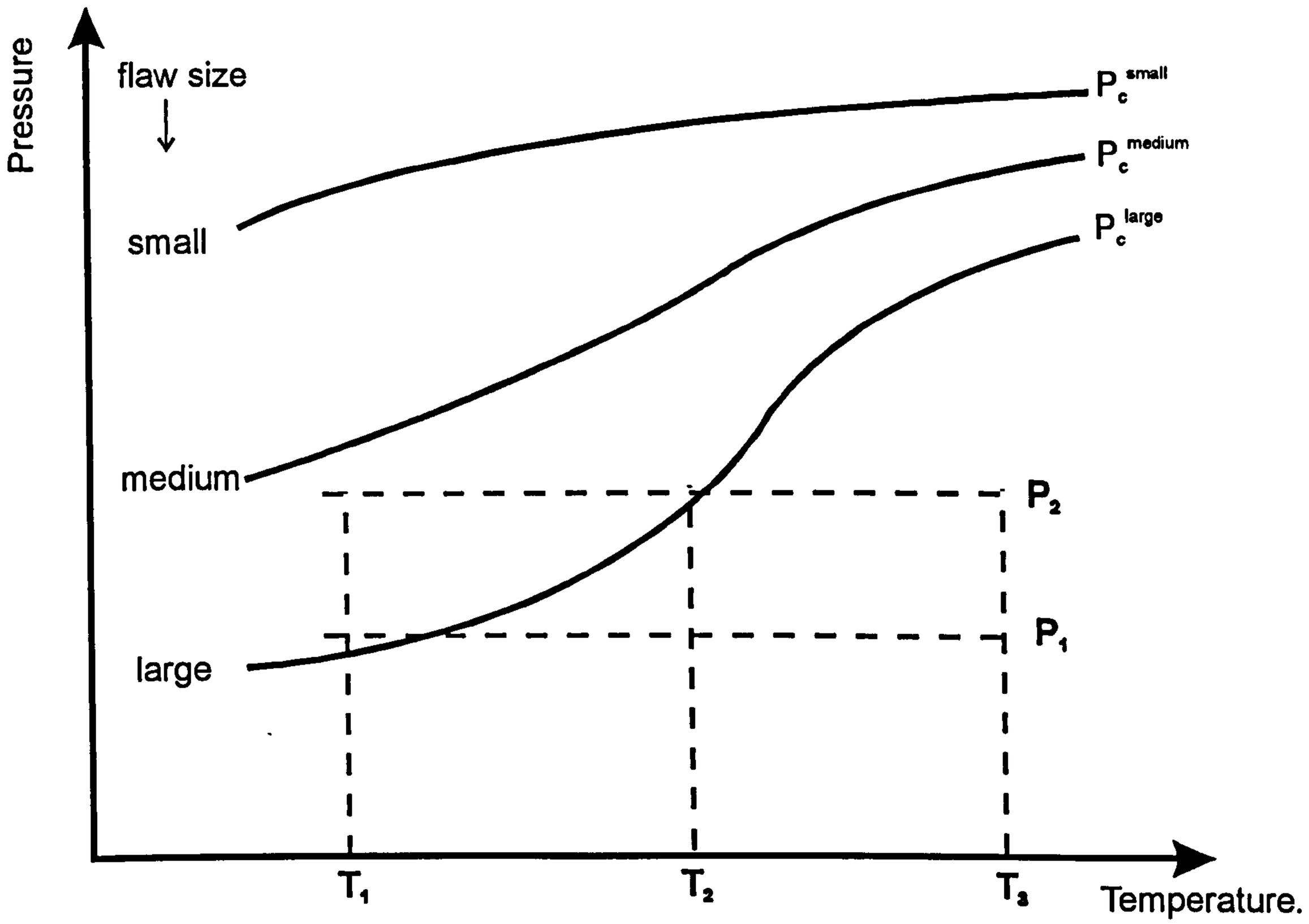

Figure 2.3. Warm Prestressing and Proof Loading Concepts. (After Yukawa, 1969).

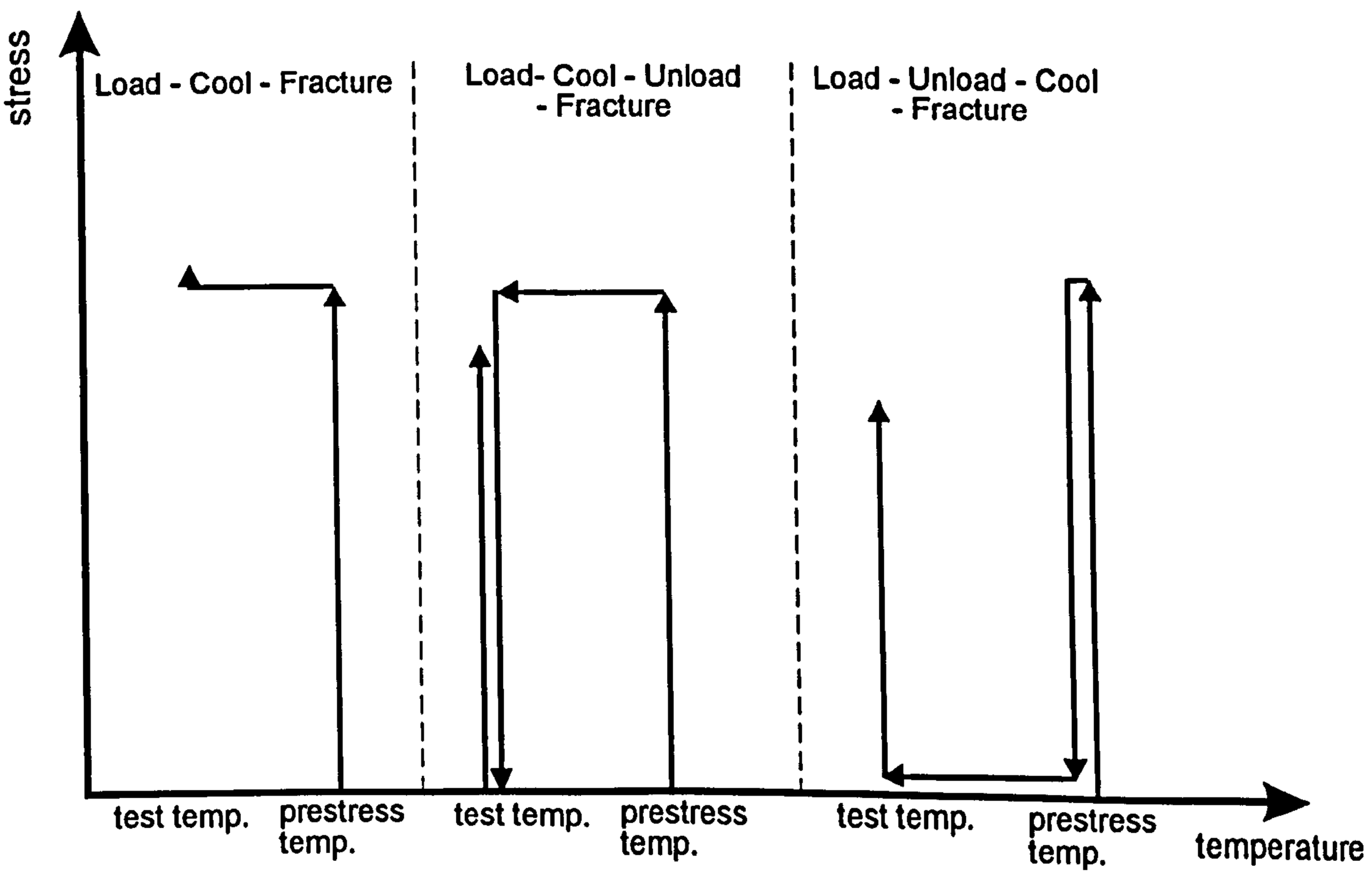

Figure 2.4. Idealisation of Warm Prestress Load Histories.
(After Smith and Garwood, 1990a).

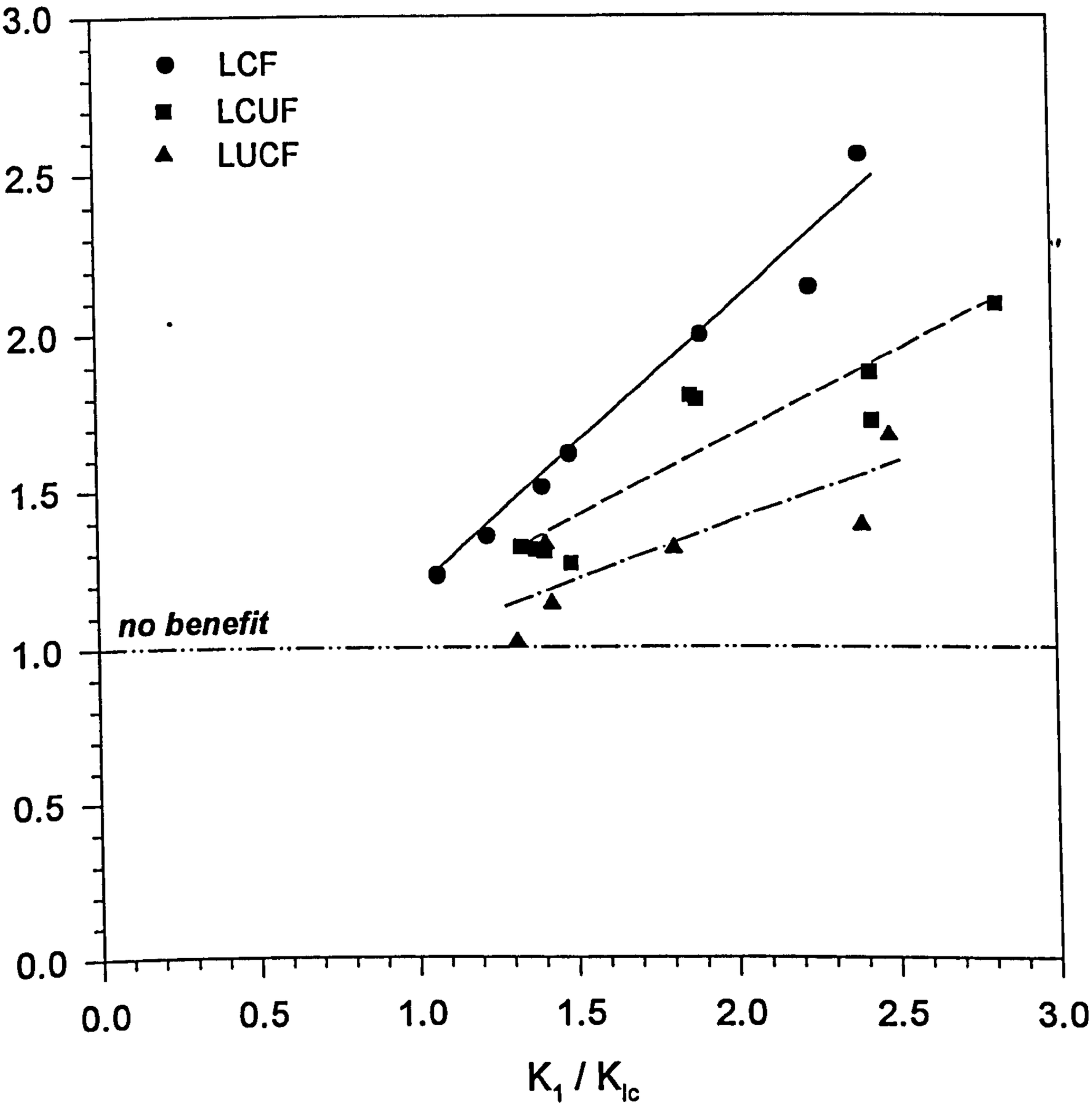

Figure 2.5. Influence of load history on the warm prestress effect.

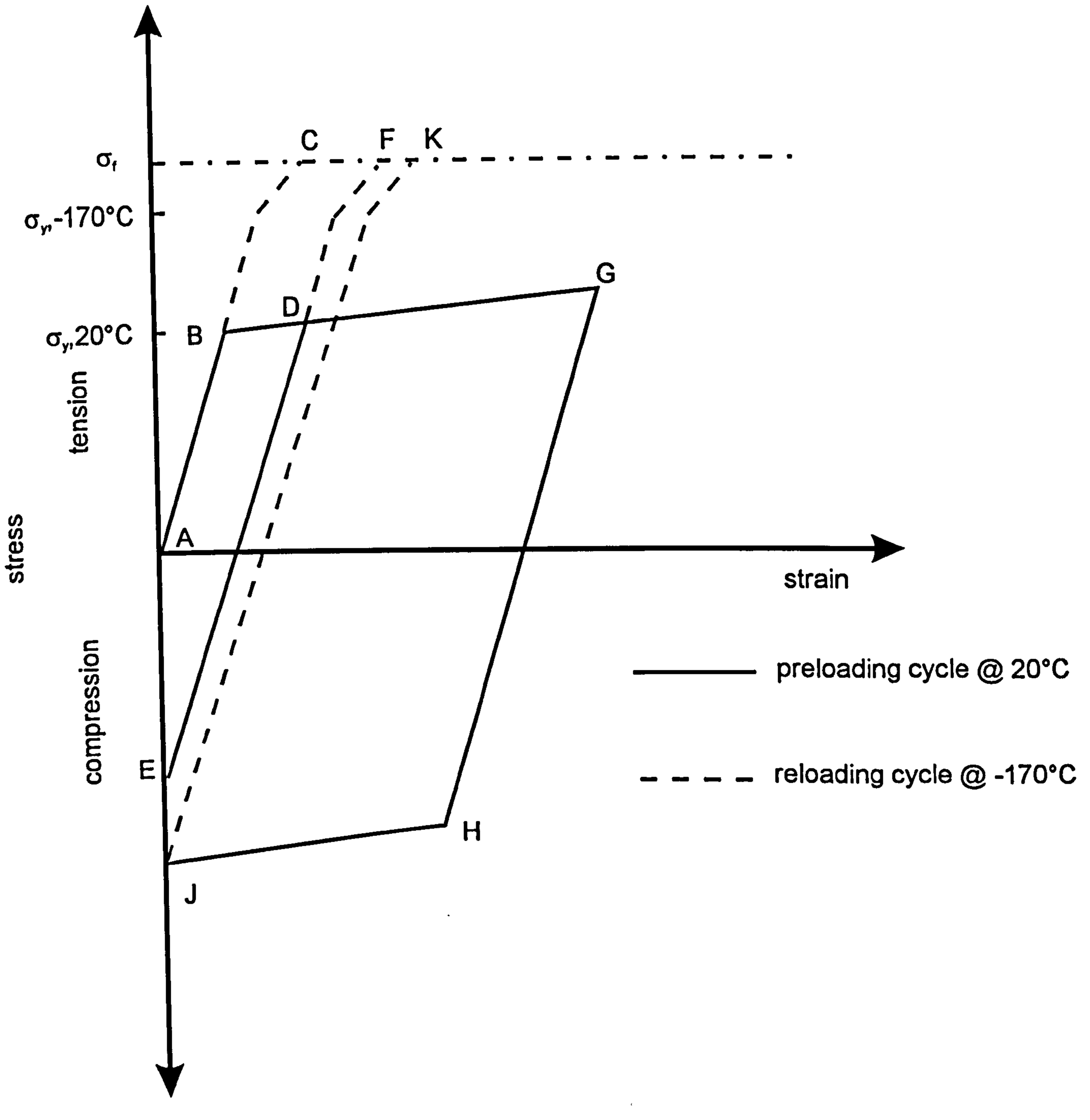

Figure 2.6. Stress - strain behaviour at the notch root.

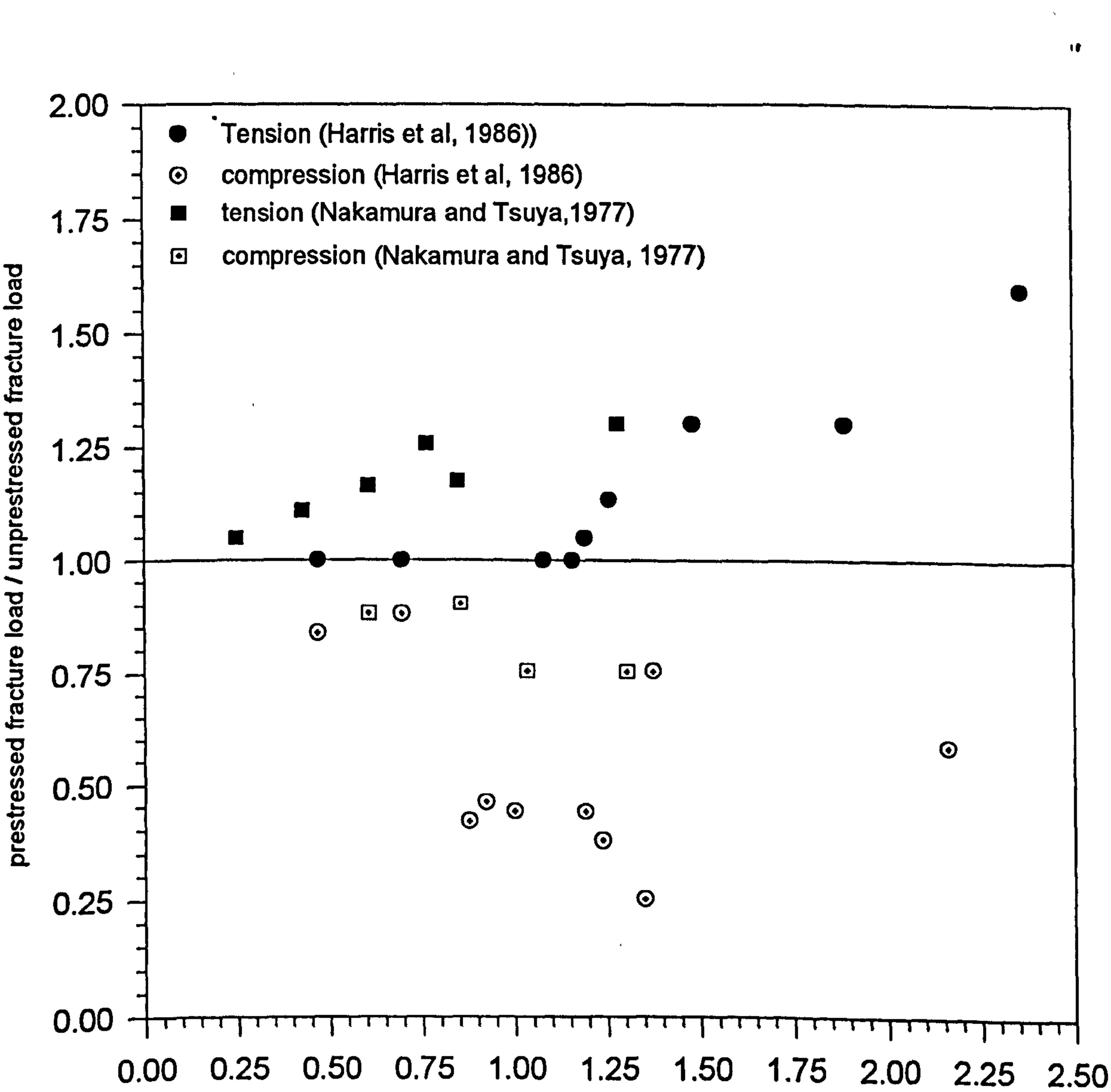

Figure 2.7. Influence of direction of preloading on warm prestress benefit

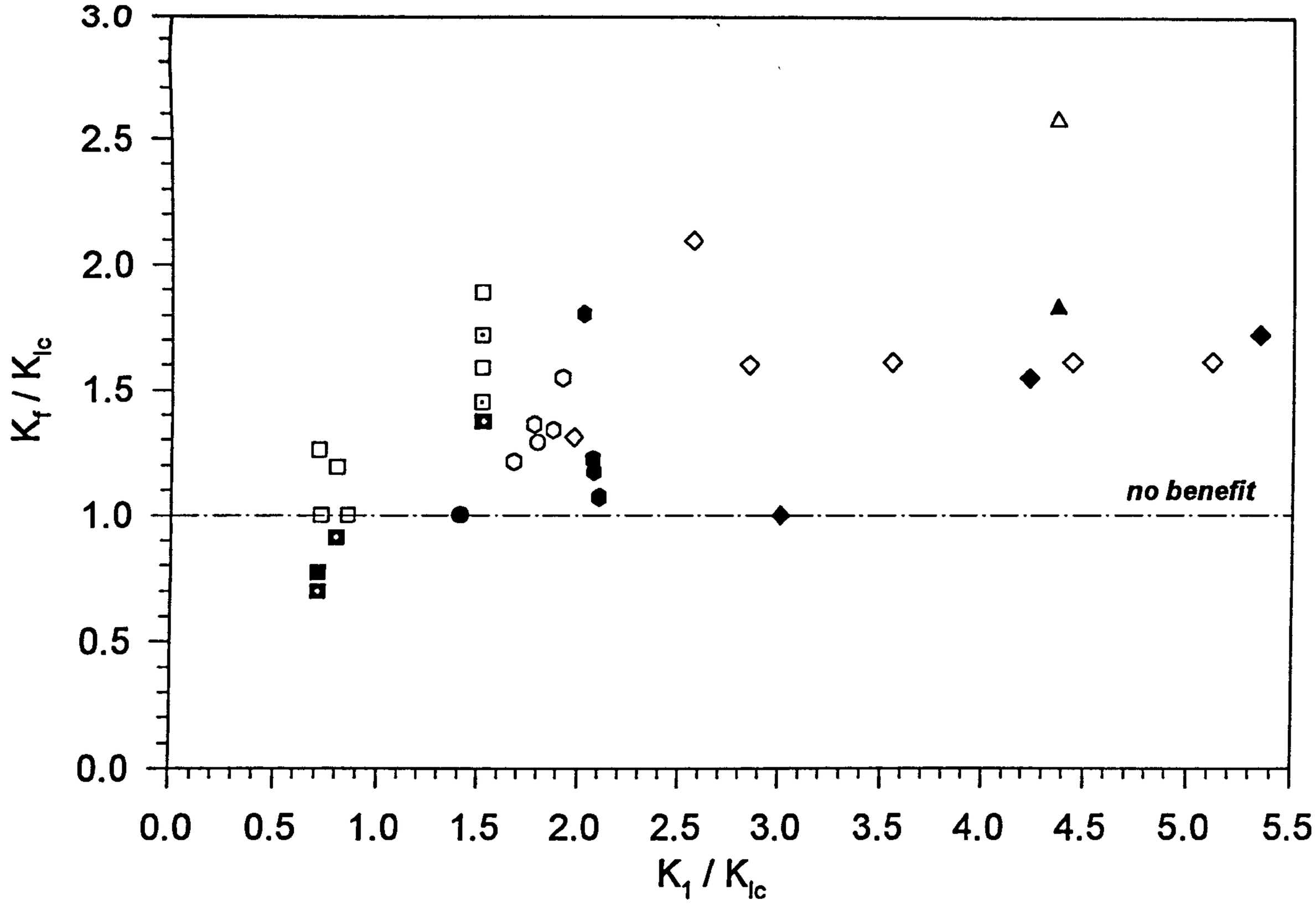

- ○ Andrews, (1970) LUCF
- ● Andrews, (1970), LUCF, aged 260°C 1 hr.
- □ Succop et al (1970), LUCF.
- ■ Succop et al (1970), LUCF, aged 343°C, 1000 hr
- ⊡ Succop et al (1970), LUCF, SR 593°C 8hr
- ◘ Succop et al (1970), LUCF aged 343°C, SR
- △ Beremin (1981), LUCF
- ▲ Beremin (1981), LUCF SR 600°C 2 hr
- ◇ Nakamura et al (1977), LUCF
- ◆ Nakamura et al (1977), LUCF SR 650°C 1.5 hr
- ○ Reed and Knott (1992), LUCF
- ● Reed and Knott (1992), LUCF, SR 650°C

Figure 2.8. Influence of stress relief and ageing on warm prestress effect

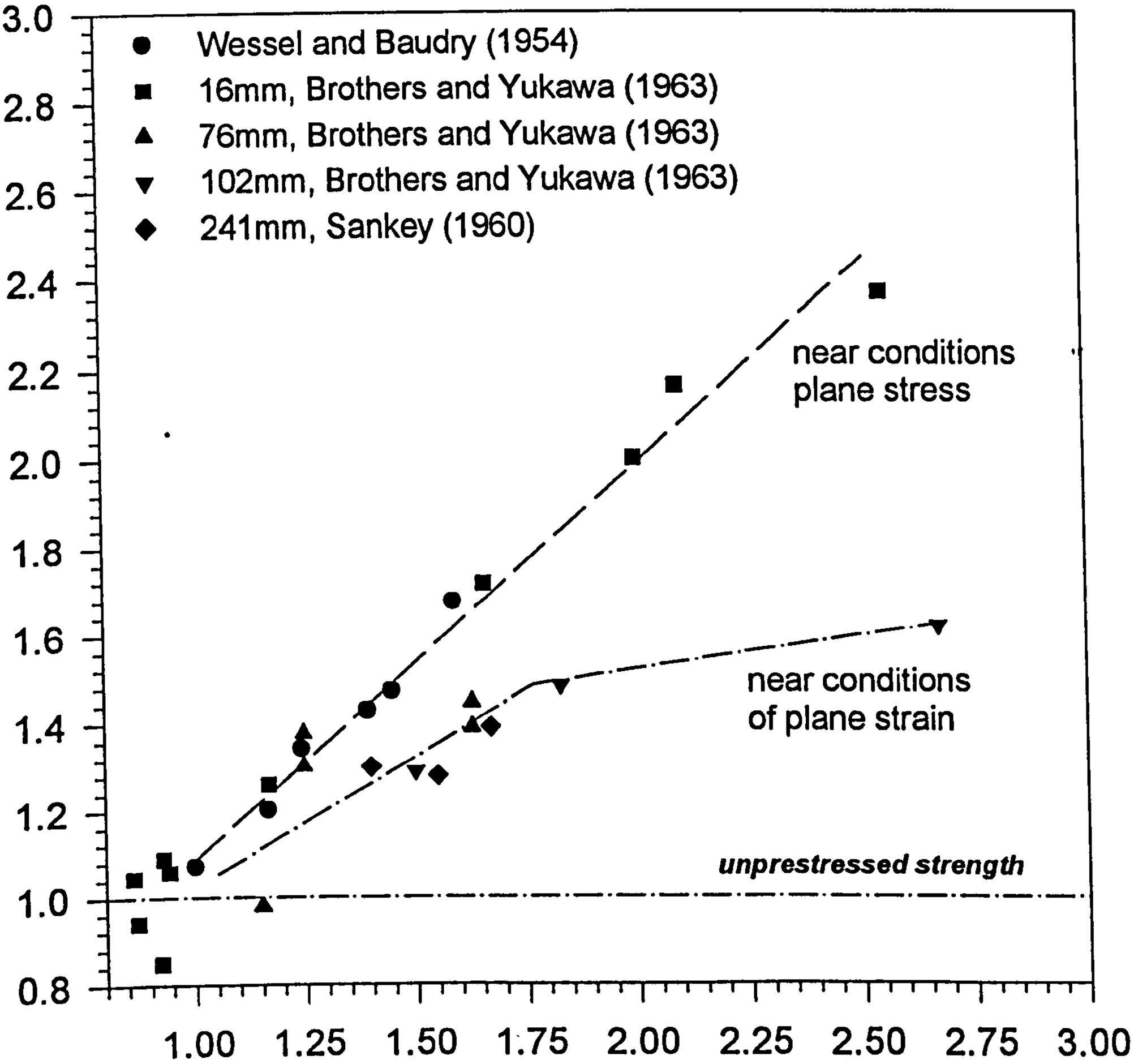

Figure 2.9. Influence of stress state on the warm prestress effect.

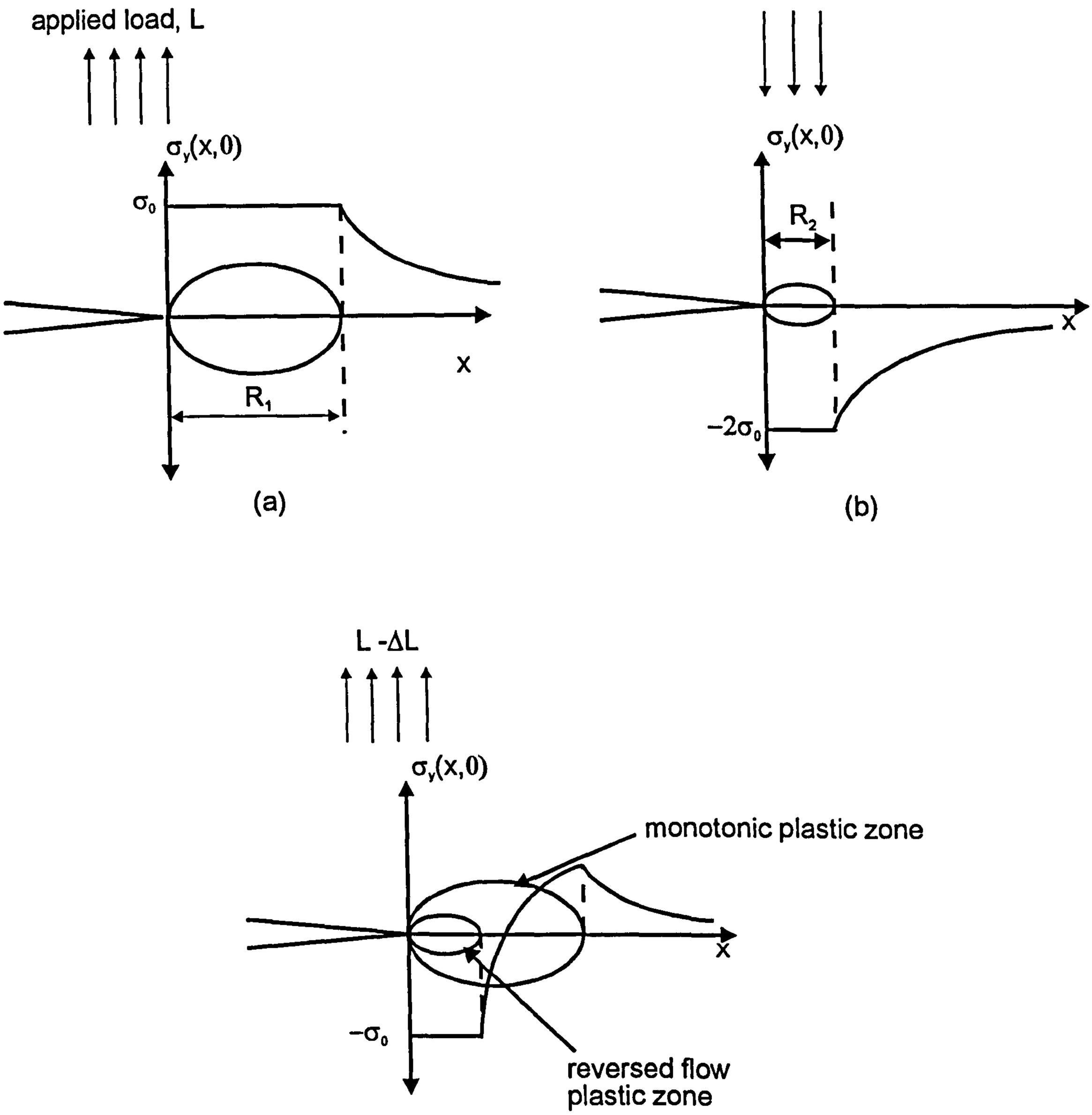

Figure 2.10. Plastic superposition for unloading.
Adding (b) for load -ΔL with a doubled yield stress to (a) gives the solution (c) resulting after unloading from L to L-ΔL. Reloading L-ΔL to Lrestores condition (a).

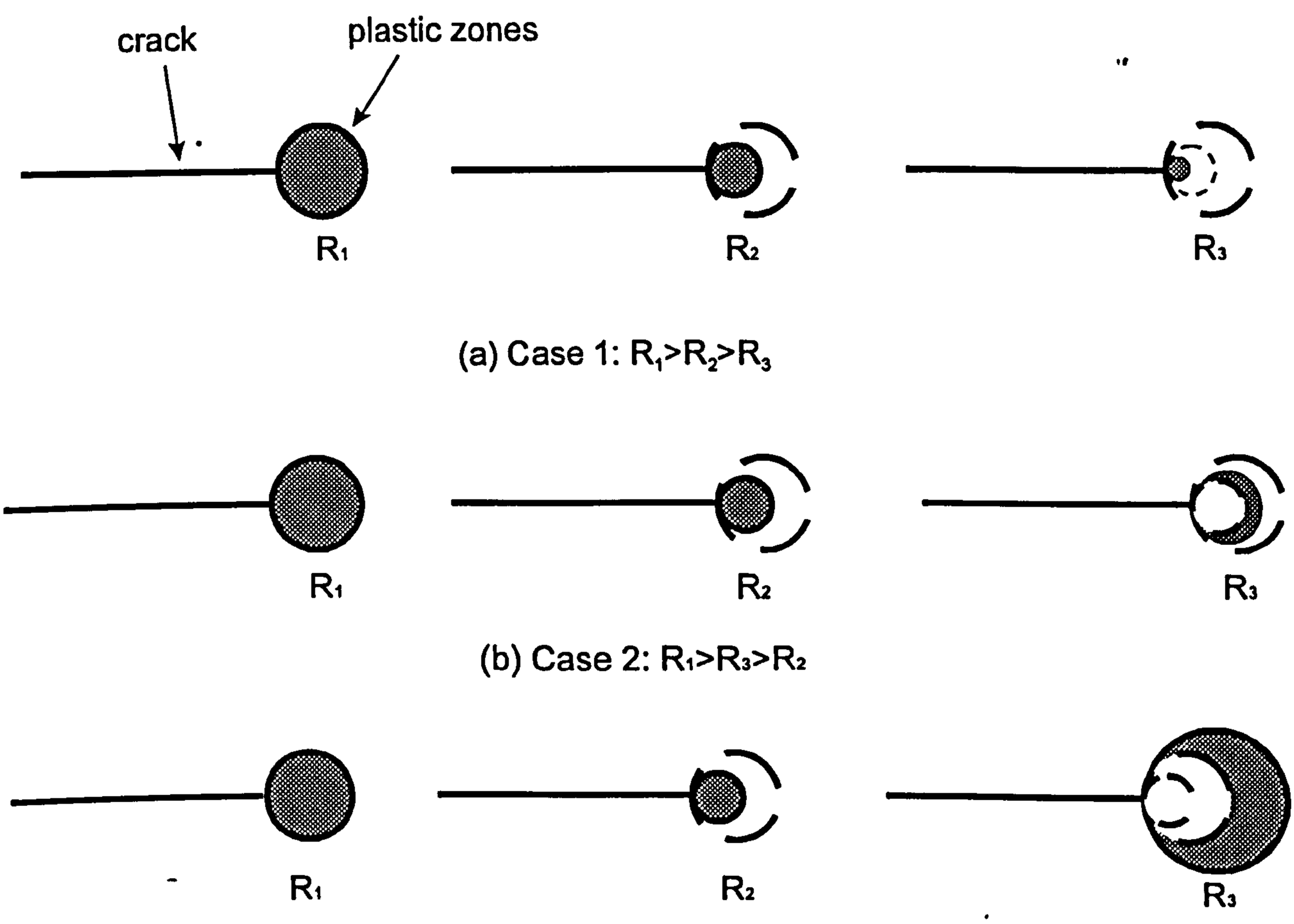

Figure 2.11 Formation of plastic zones for three LUCF cases.

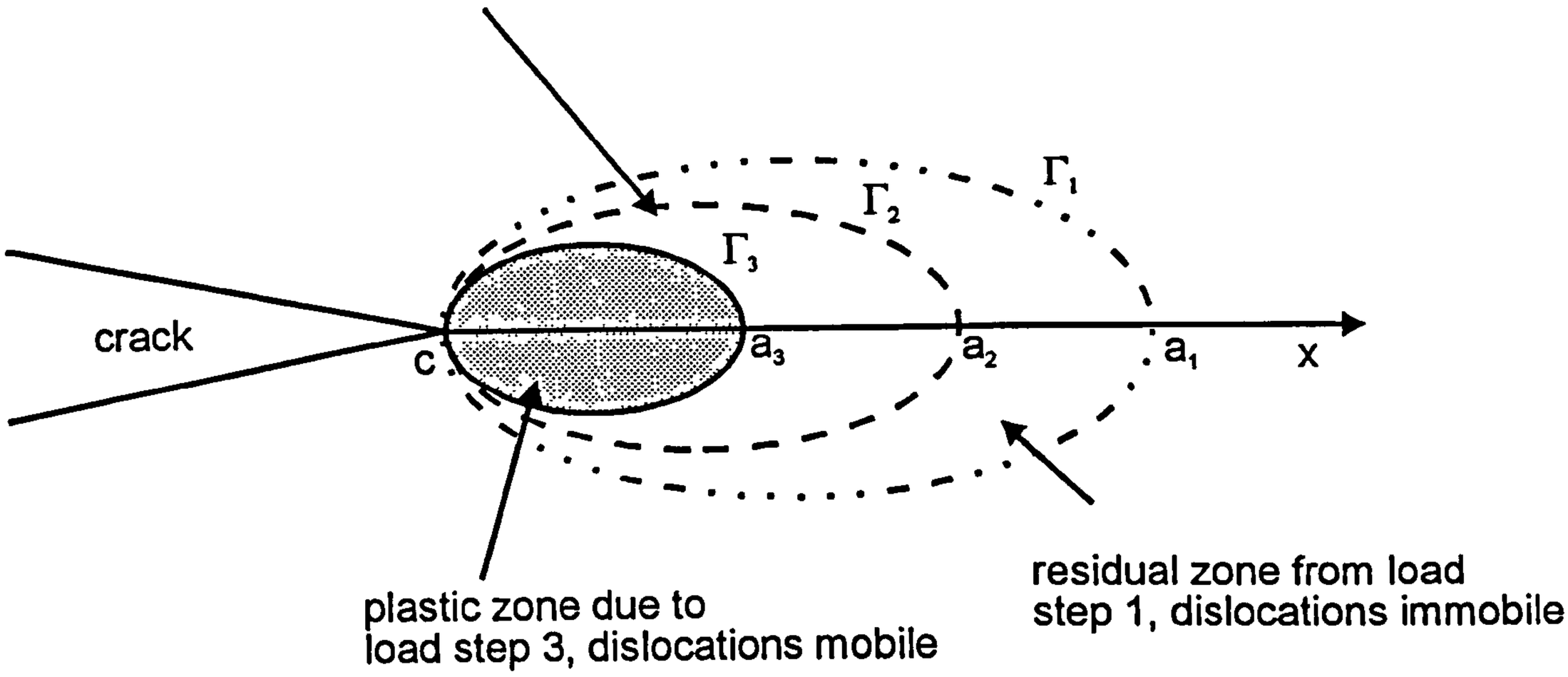

Figure 2.12. Case 1 plastic and residual deformation zones following warm prestressing.

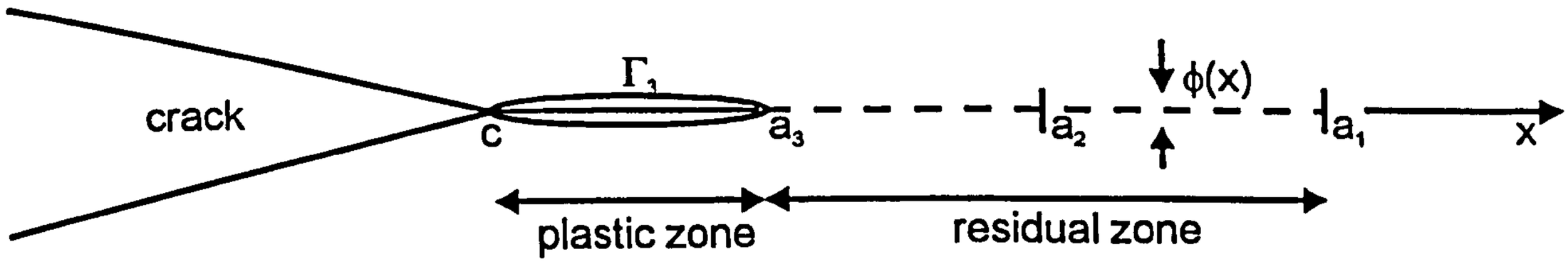

Figure 2.13. Strip Yield Model representation of case 1.

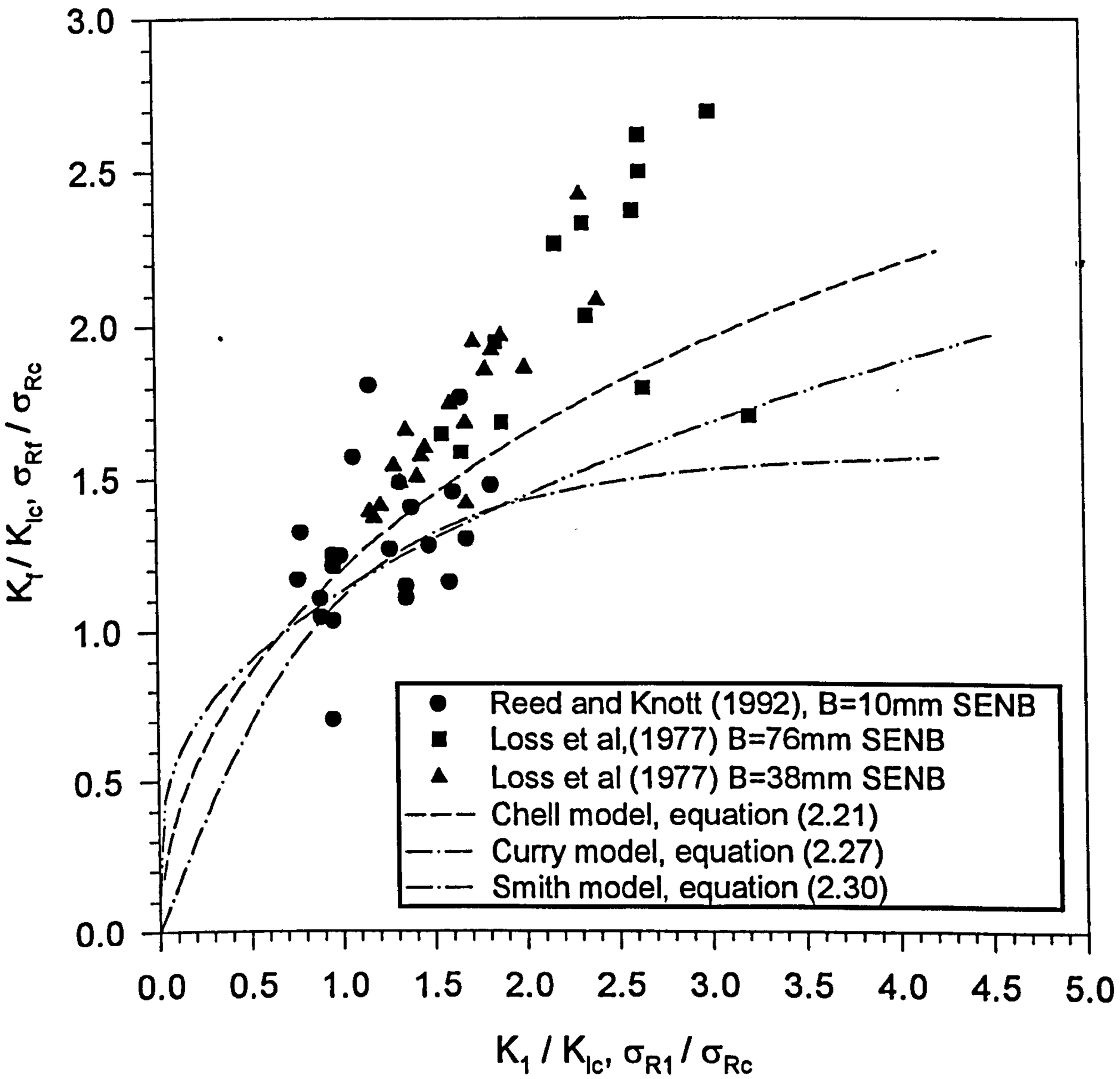

Figure 2.14. Comparison between experimental warm prestress data and theoretical predictions for A533B overloaded at 20°C and fractured at -170°C.

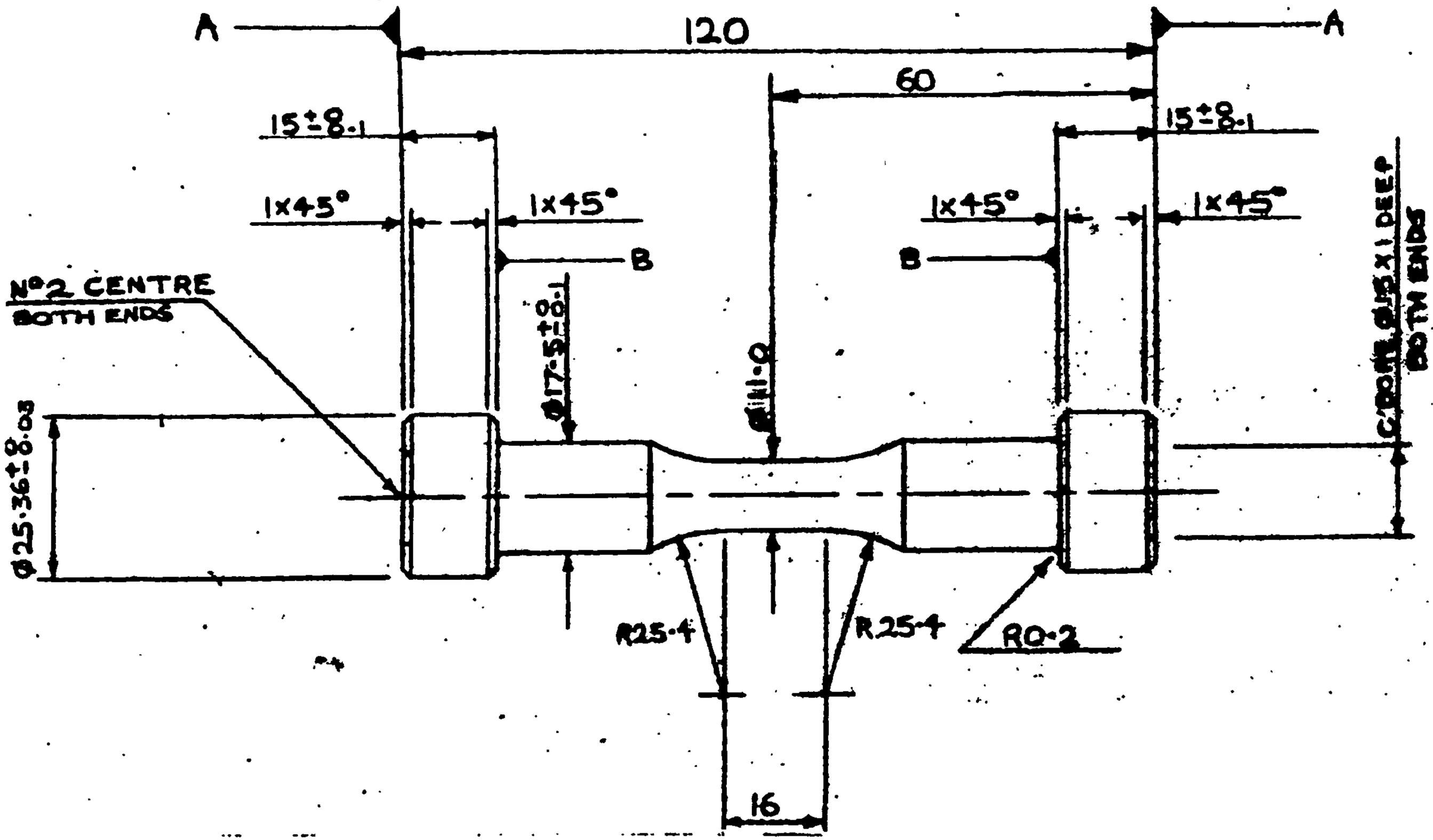

Figure 3.1. Button Ended Tensile Specimen Geometry

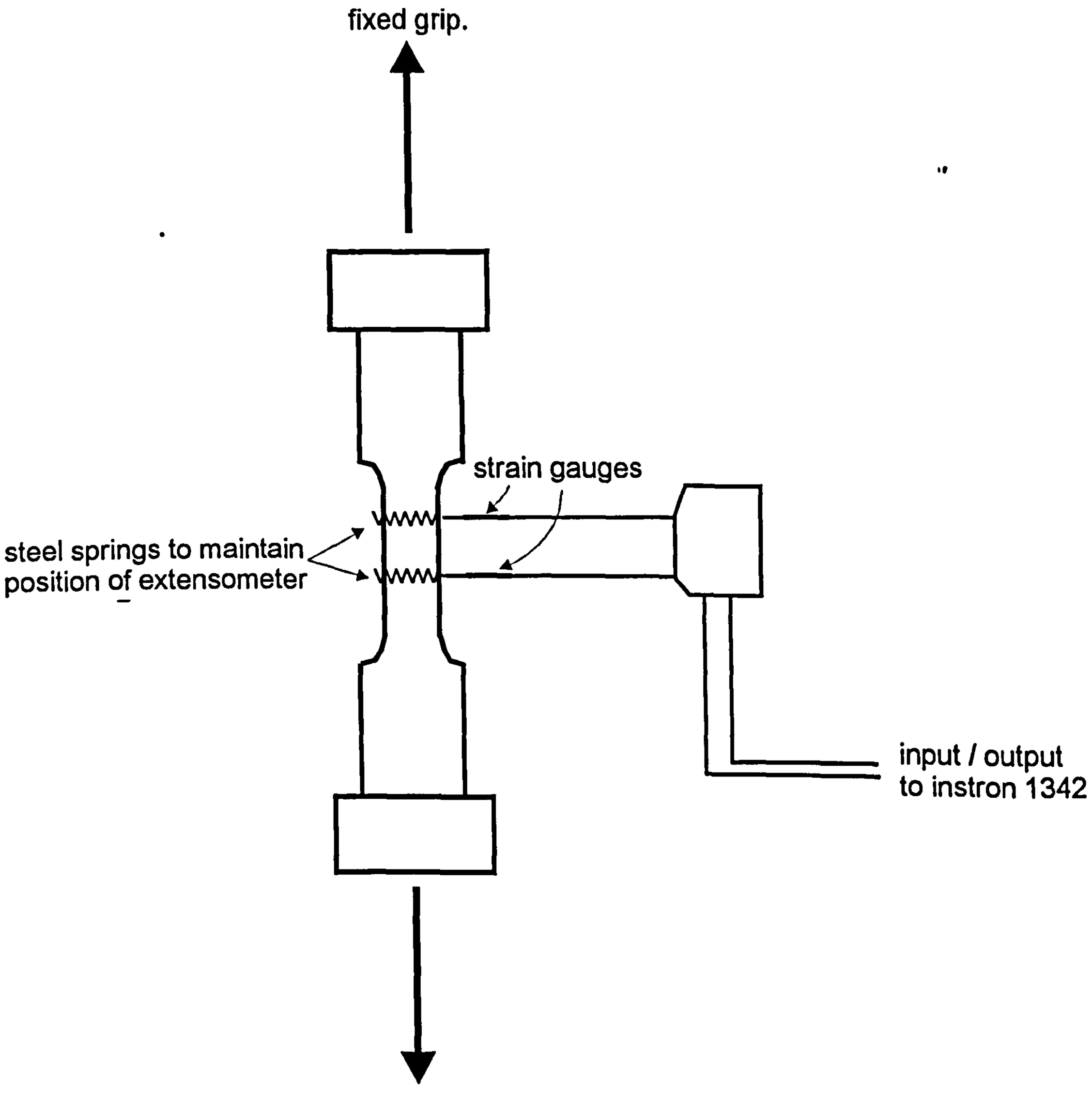

Figure 3.2 Extensometer arrangement during tensile testing.

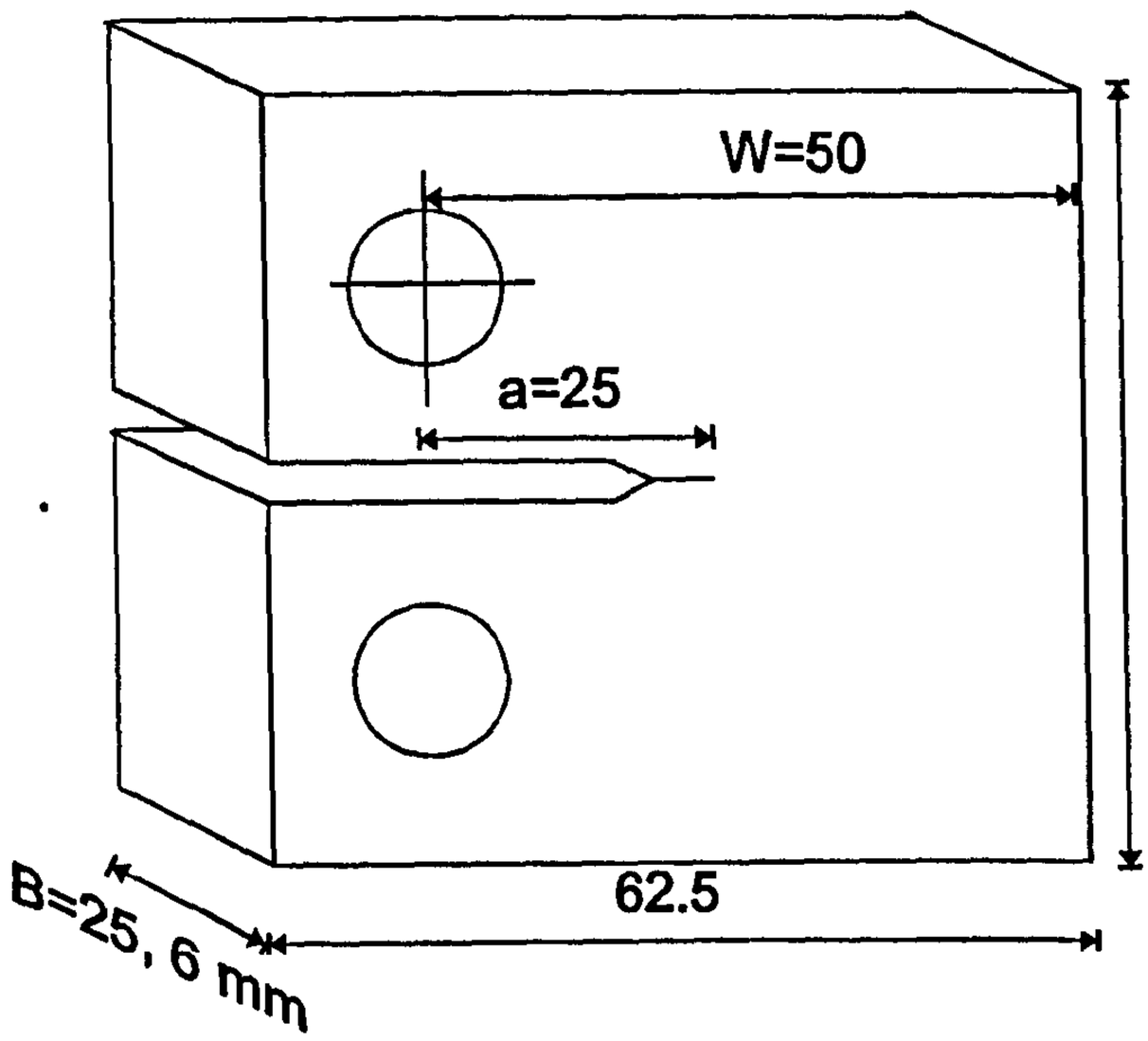

Figure 3.3. Compact tension specimen geometry.

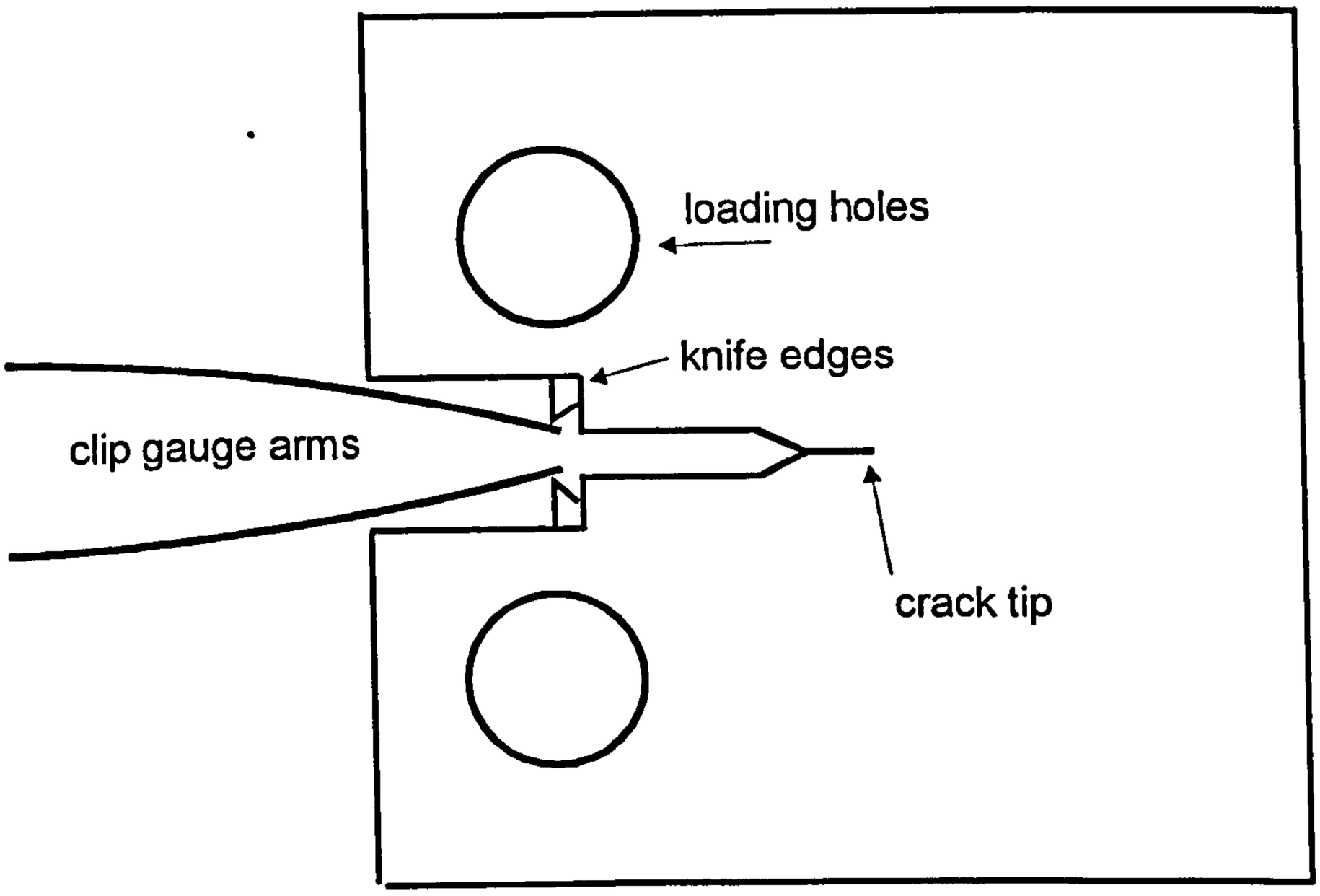

Figure 3.4. Compact Tension specimen extensometer arrangement for fracture toughness testing

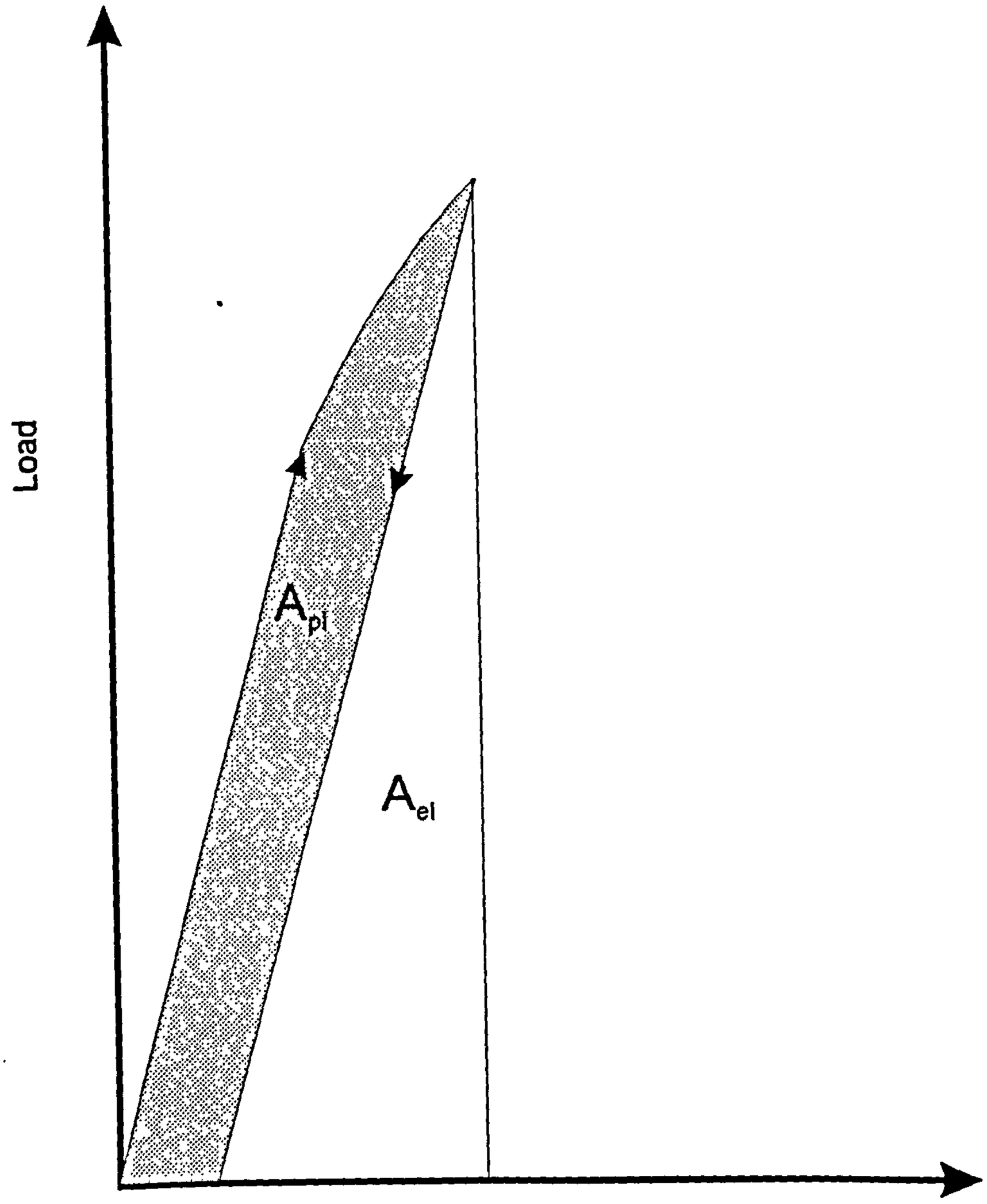

Figure 3.5. Schematic illustration of the area under the load displacement curves used in the evaluation of J_{wpe} and J_t

Figure 4.1. Monotonic Response of BS1501 Steel at 20°C, -70°C and -120°C

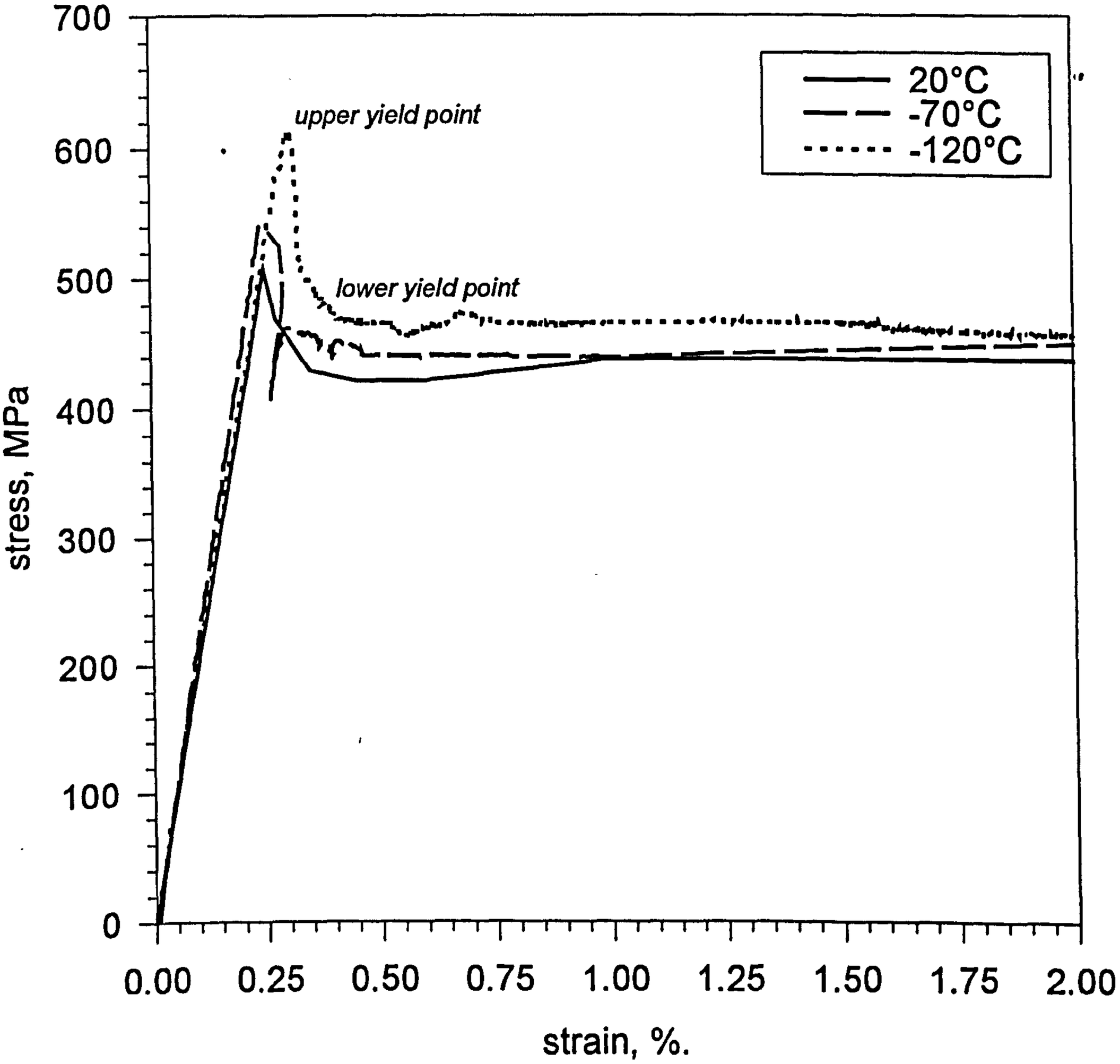

Figure 4.2a Cyclic Response of BS1501 Steel at 20°C

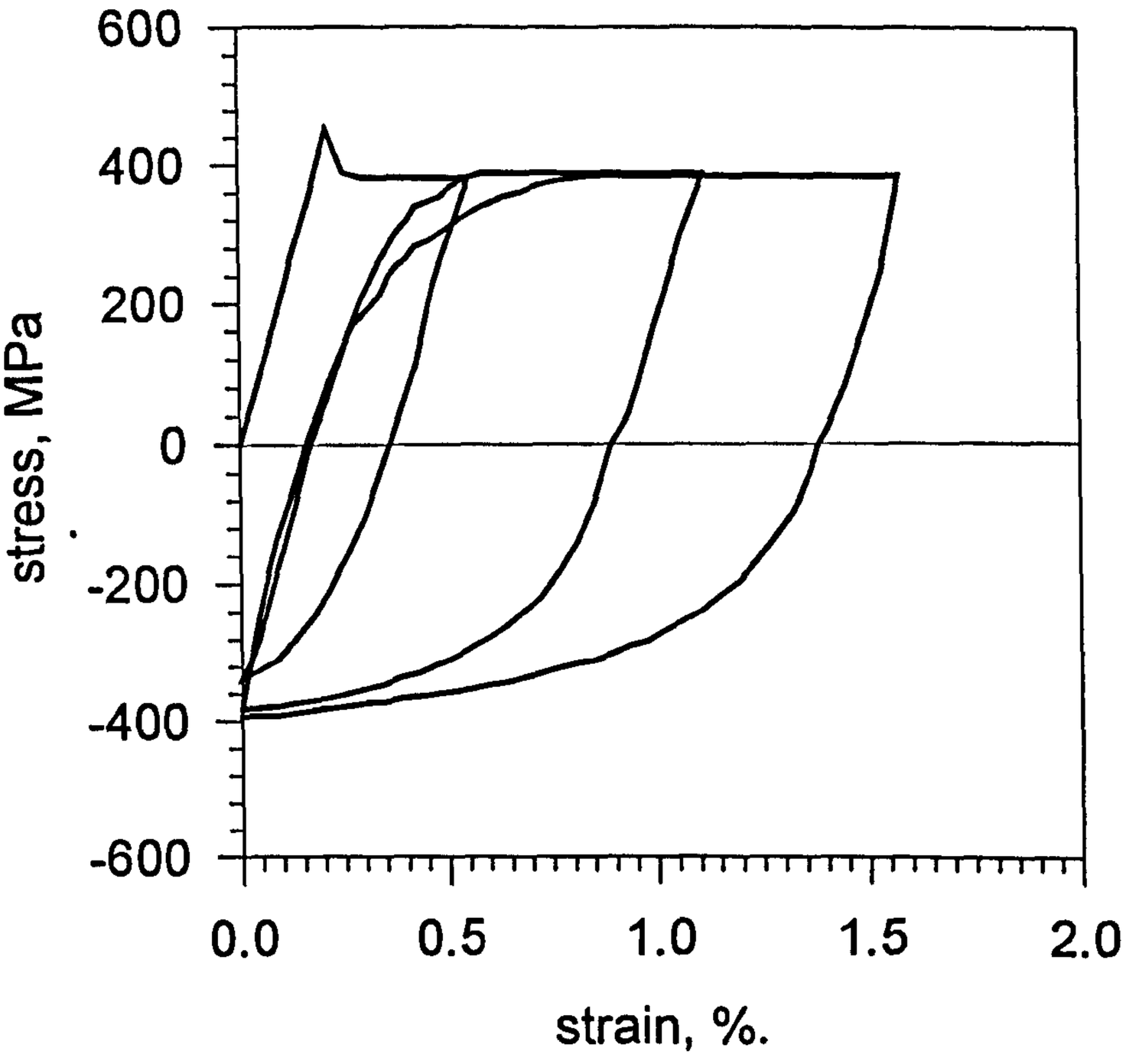

Figure 4.2b Cyclic Response of BS1501 Steel at -70°C.

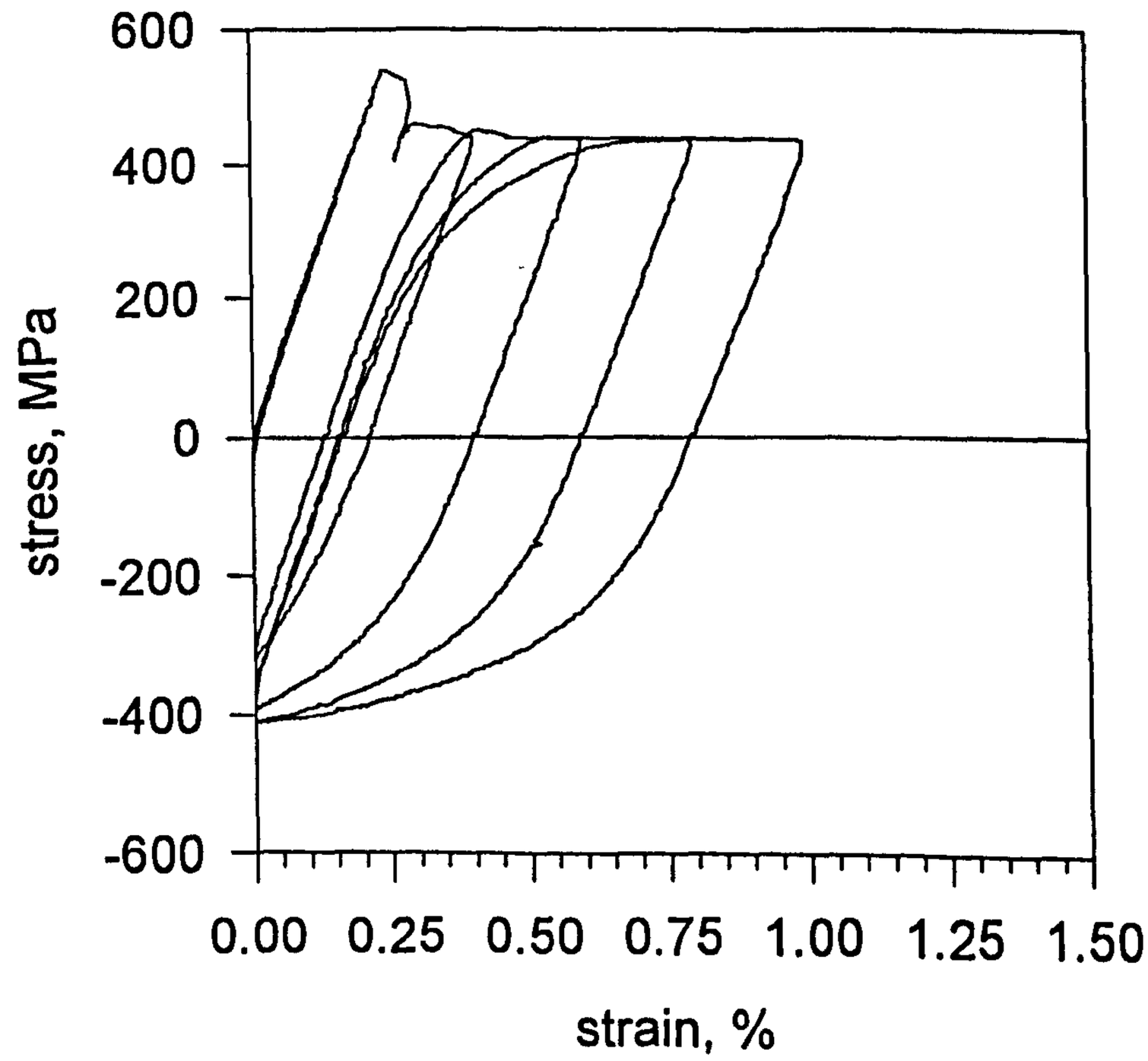

Figure 4.2c. Cyclic response of BS1501 Steel at -120°C.

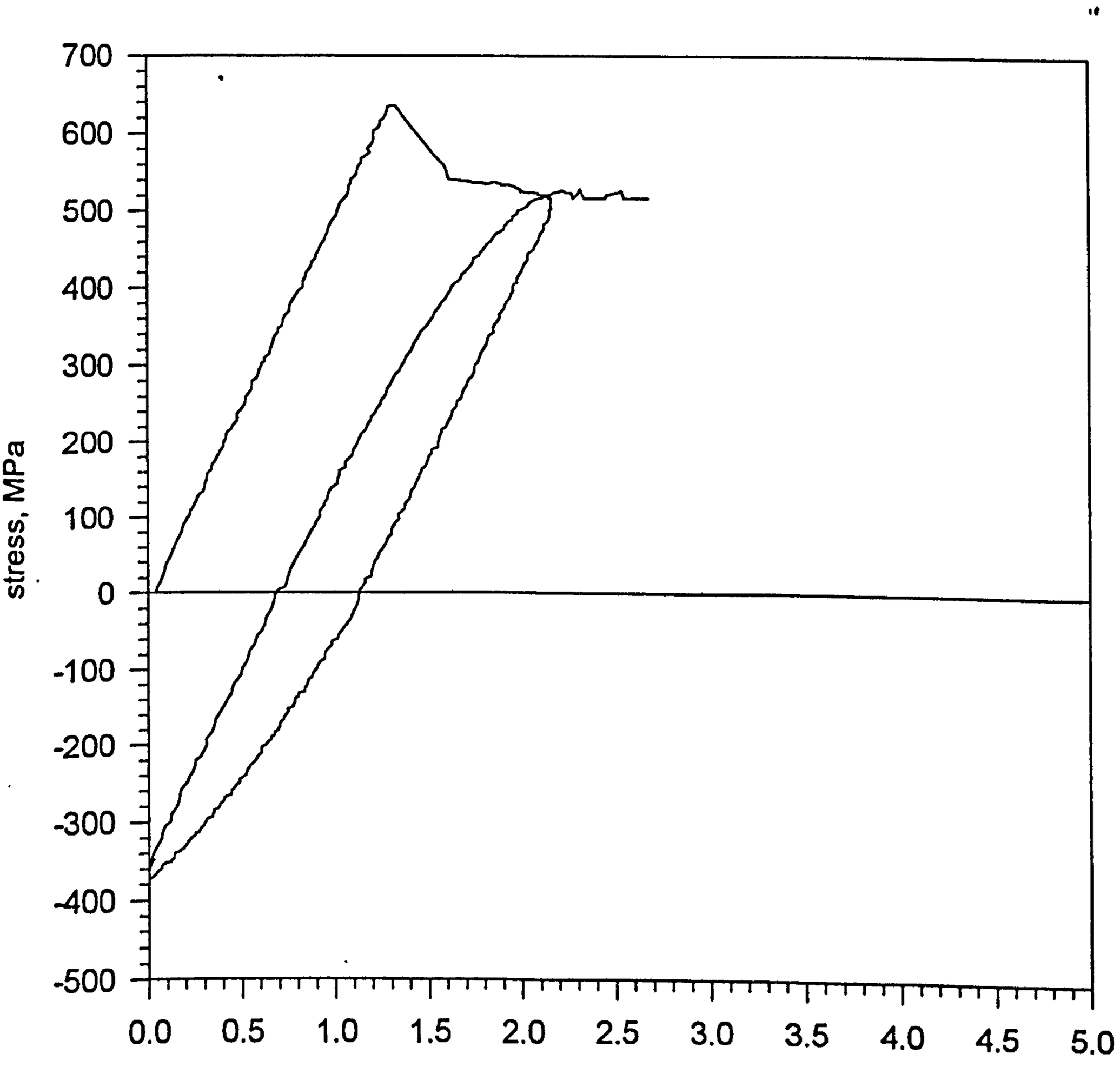

Figure 4.3. Definition of Bauschinger Effect Factor.

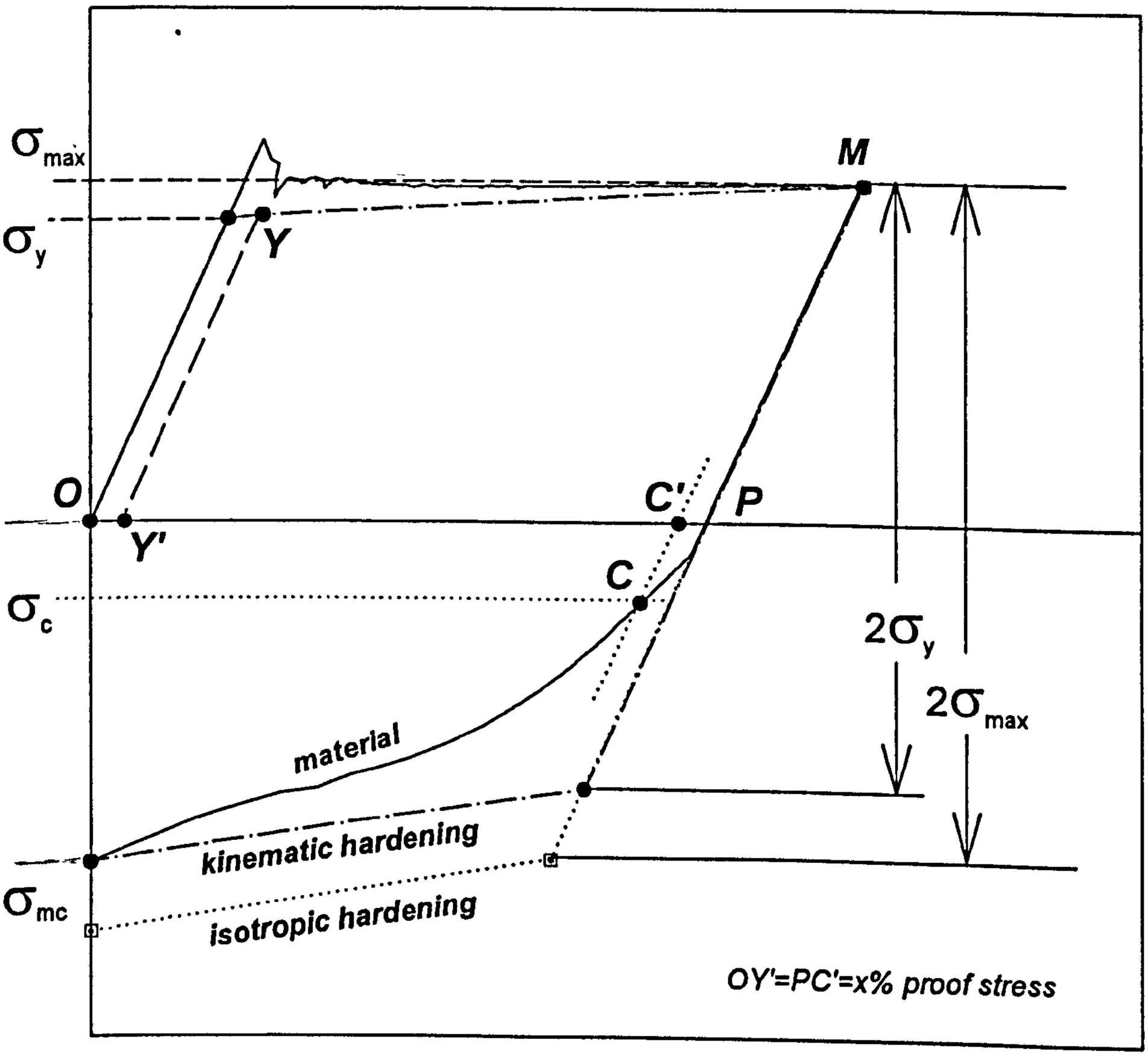

Figure 4.4. Influence of prior plastic deformation on subsequent compressive yielding behaviour of BS1501.

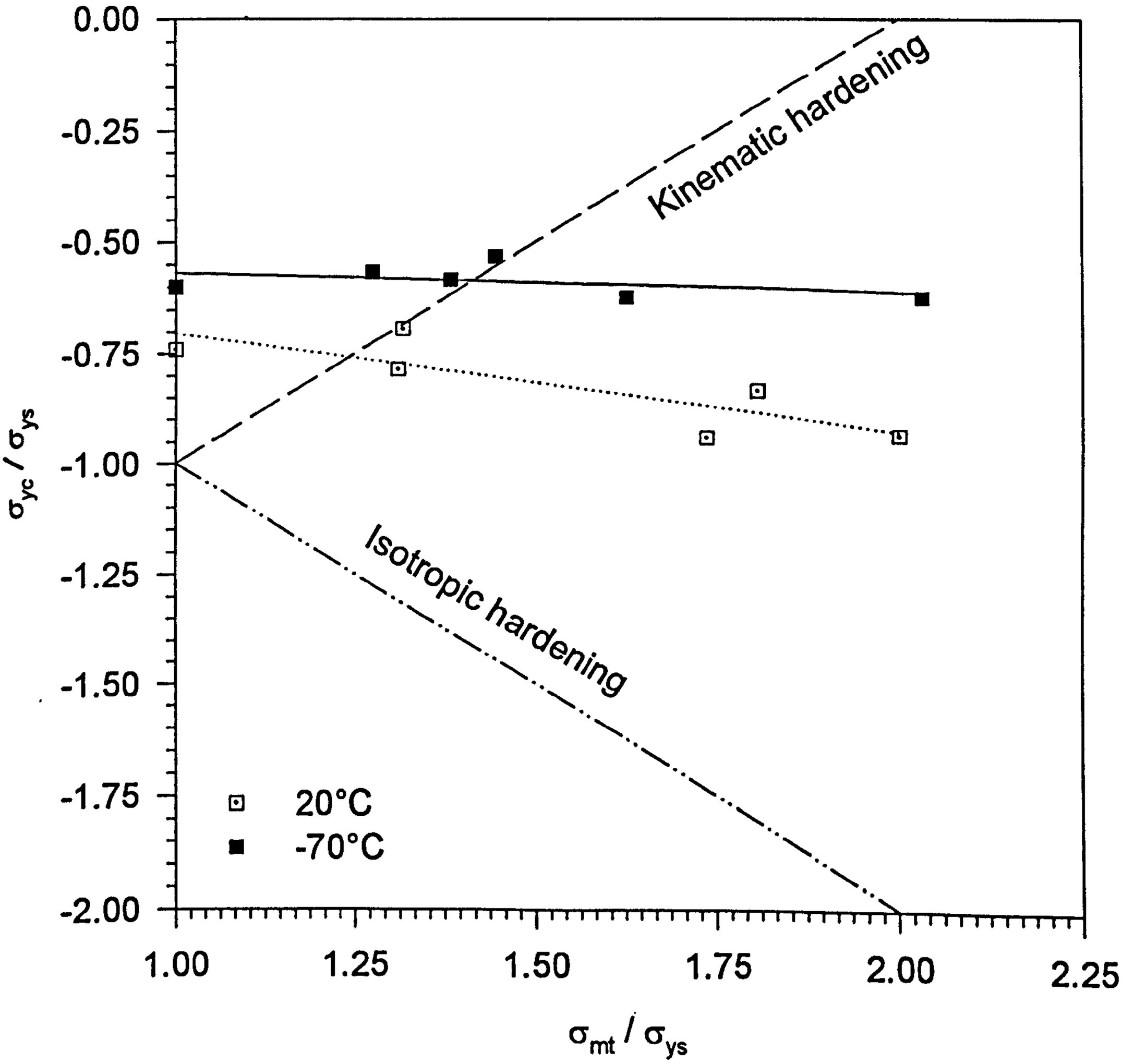

Figure 4.5. Uniaxial response of BS1501 at -120°C following a 5% preload at room temperature.

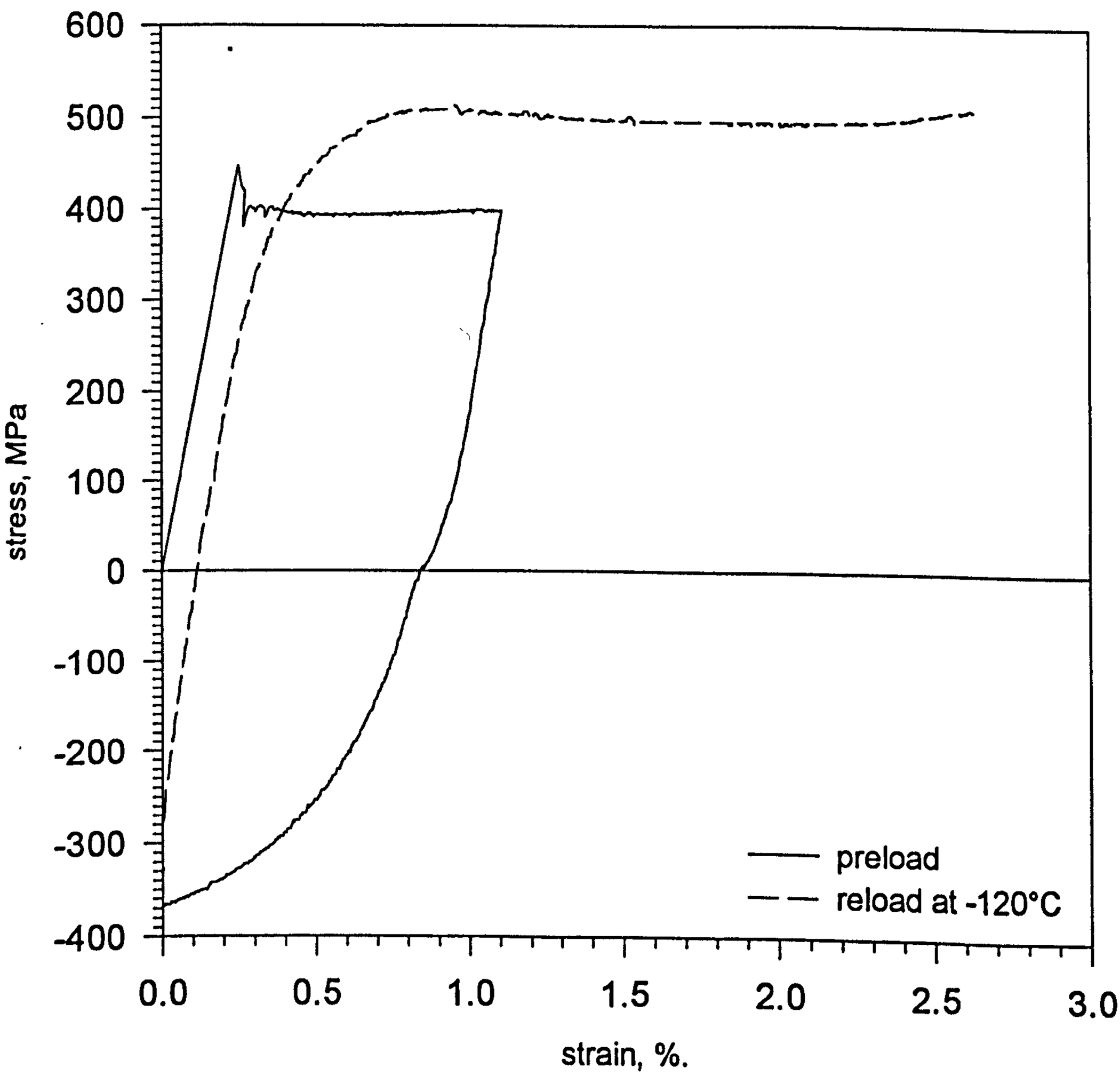

Figure 4.6. As-Received Fracture Toughness at -120°C and -70°C for 50mm SENB and 25 mm CT specimens.

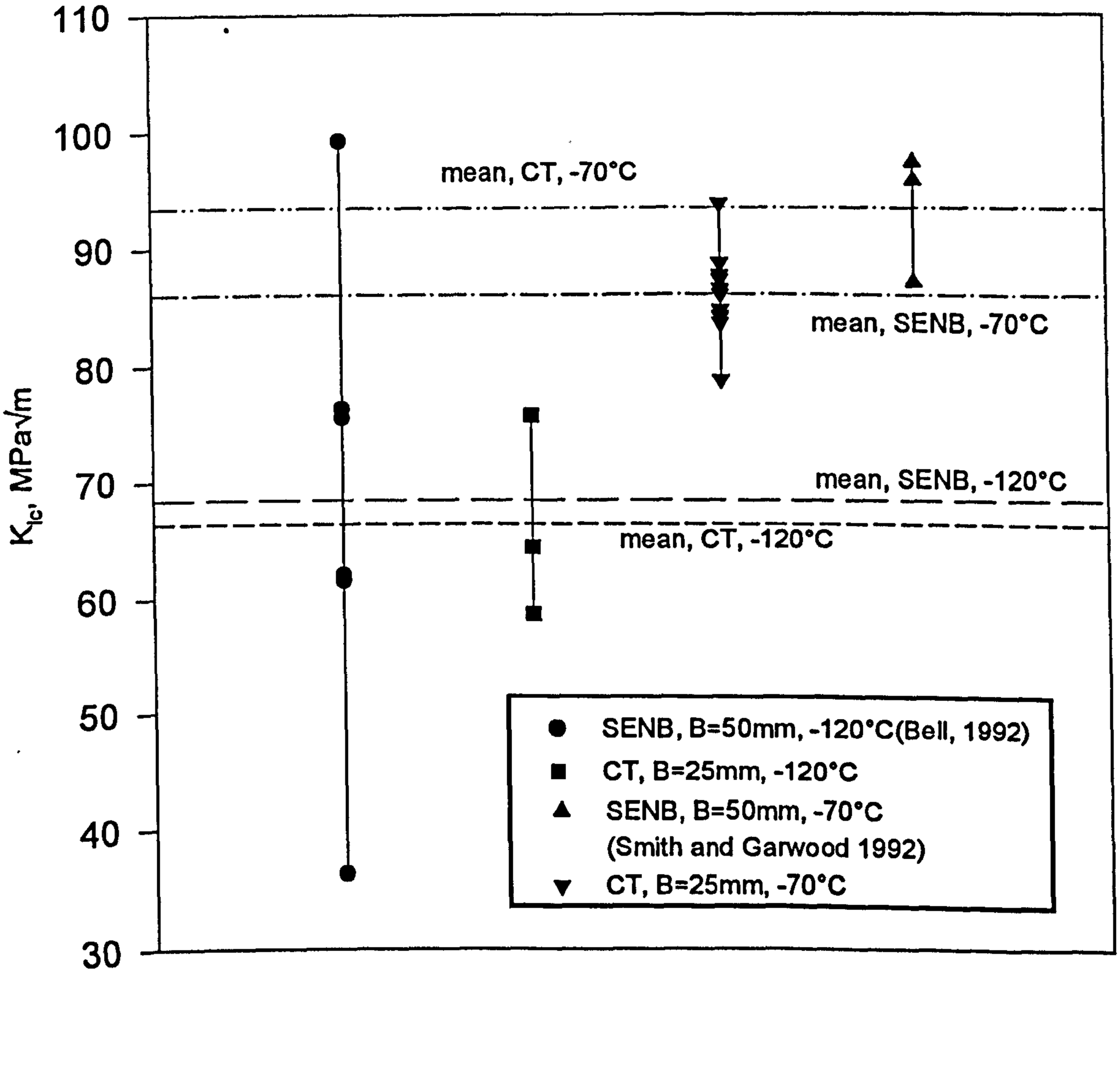

Figure 4.7. Load - Displacement trace for room temperature fracture of BS1501, illustrating proof load levels in terms of collapse load.

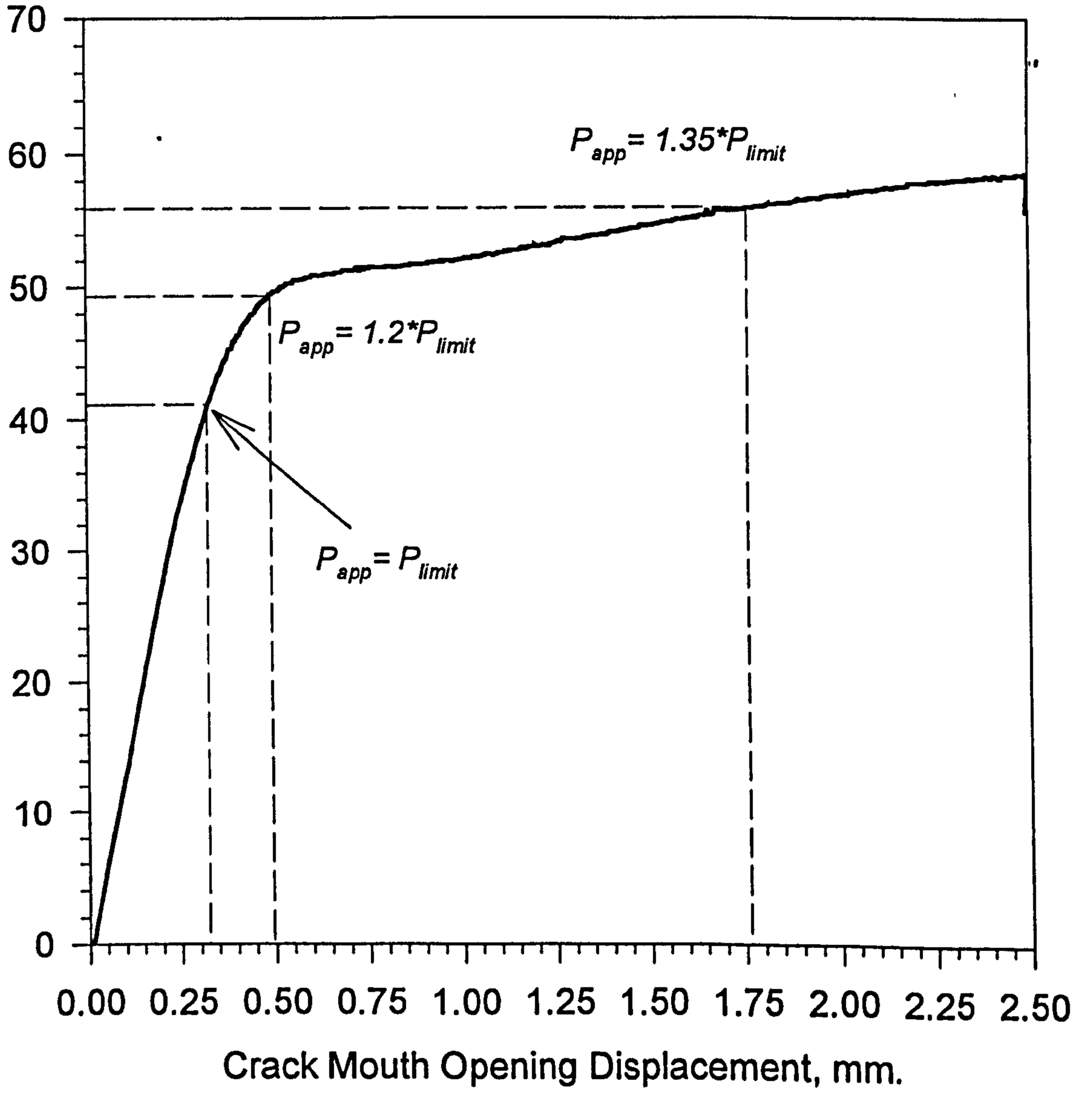

Figure 4.8. Proof Loaded Fracture Toughness Compared to As-Received Toughness at -120°C

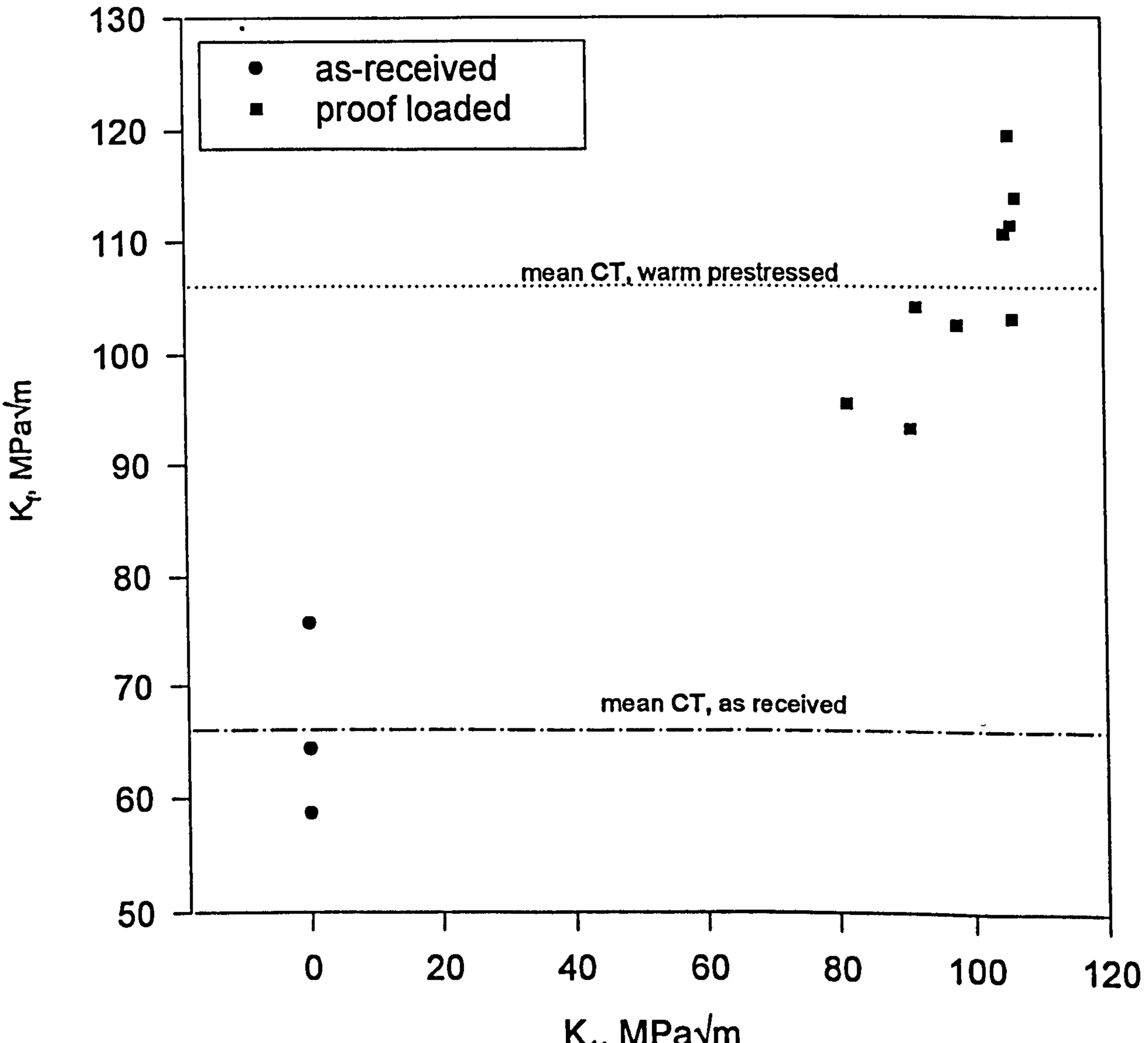

Figure 4.9. Warm Prestress Effect on BS1501 at -70°C.

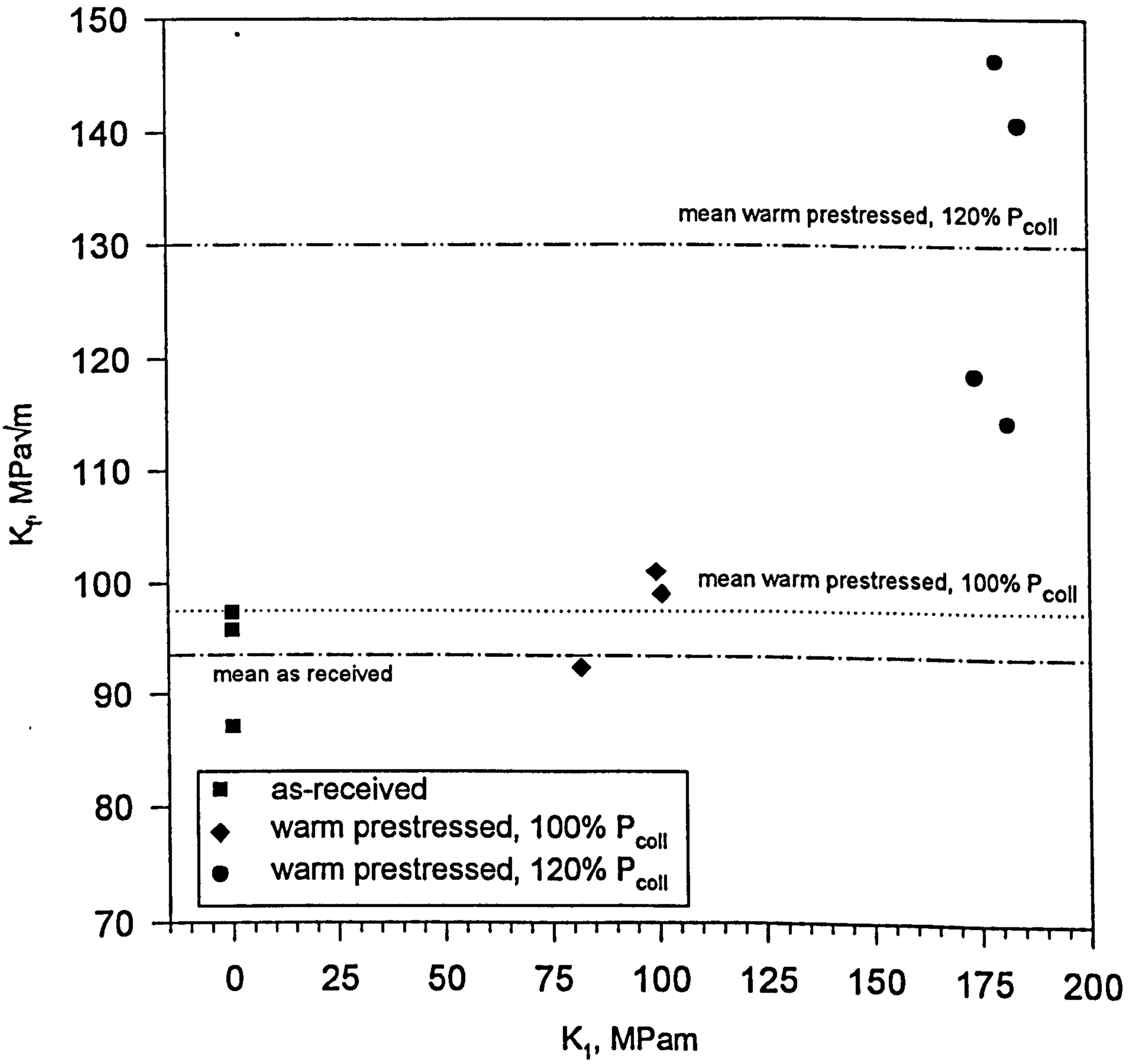

Figure 4.10. Typical Load - Displacement History of a Repeated Proof Load Cycle in Displacement Control (BS1501 specimen 1,3e).

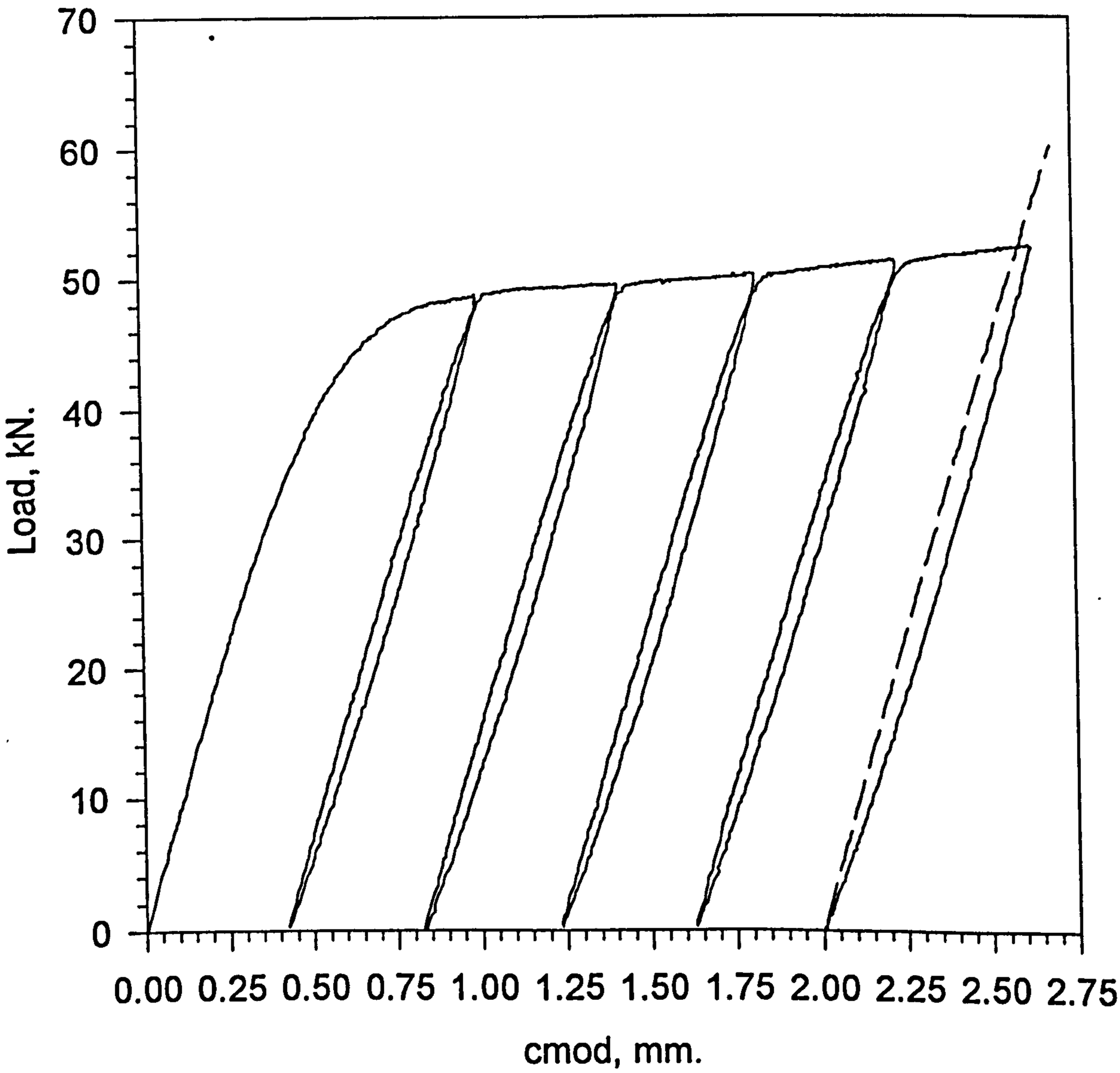

Figure 4.11. Typical Load - Displacement Trace For a Repeated Proof Load in Load Control (BS1501 specimen 20a).

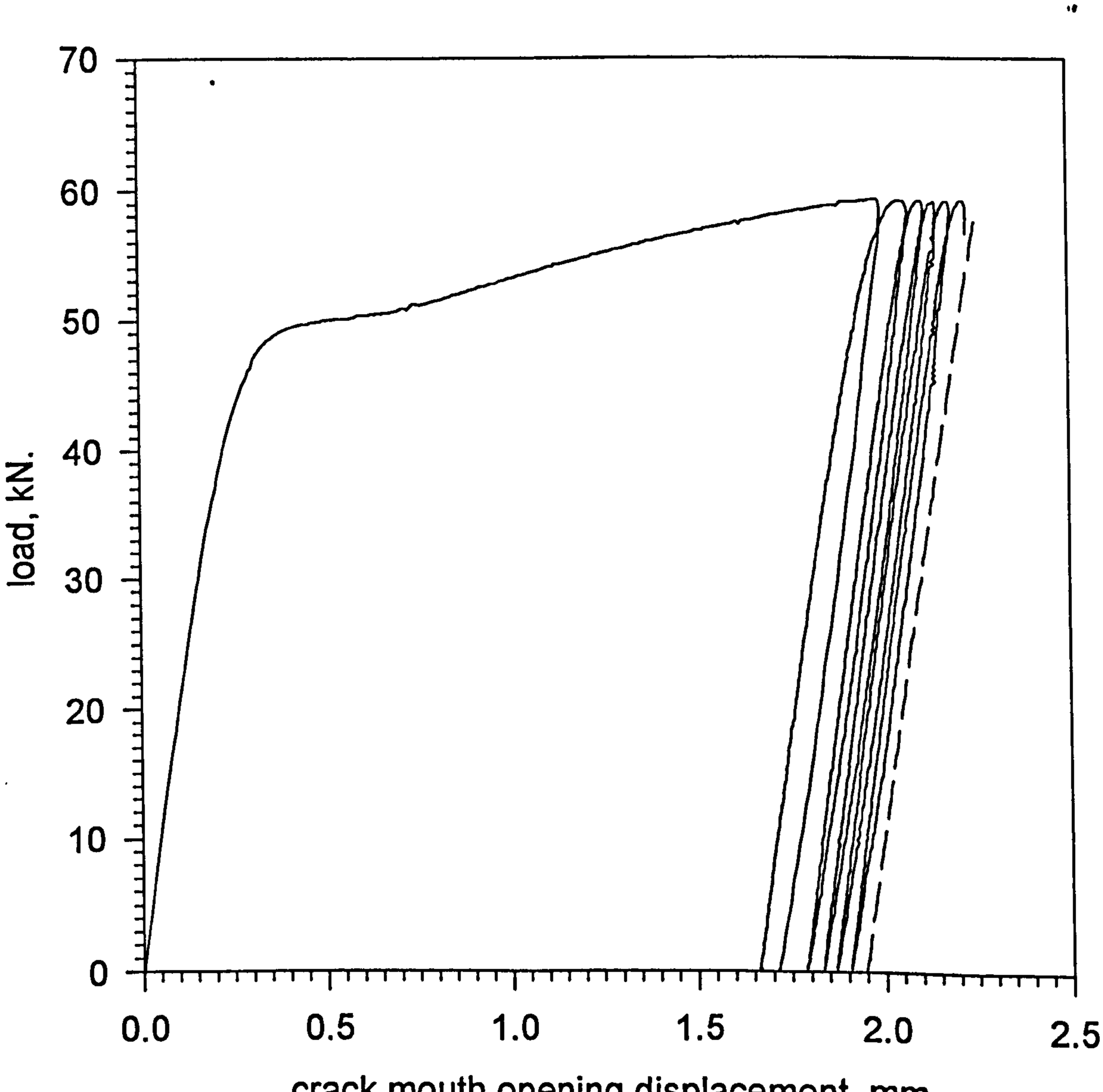

Figure 4.12. Influence of Repeated Proof Loading on Cleavage Toughness of BS1501 at -120°C.

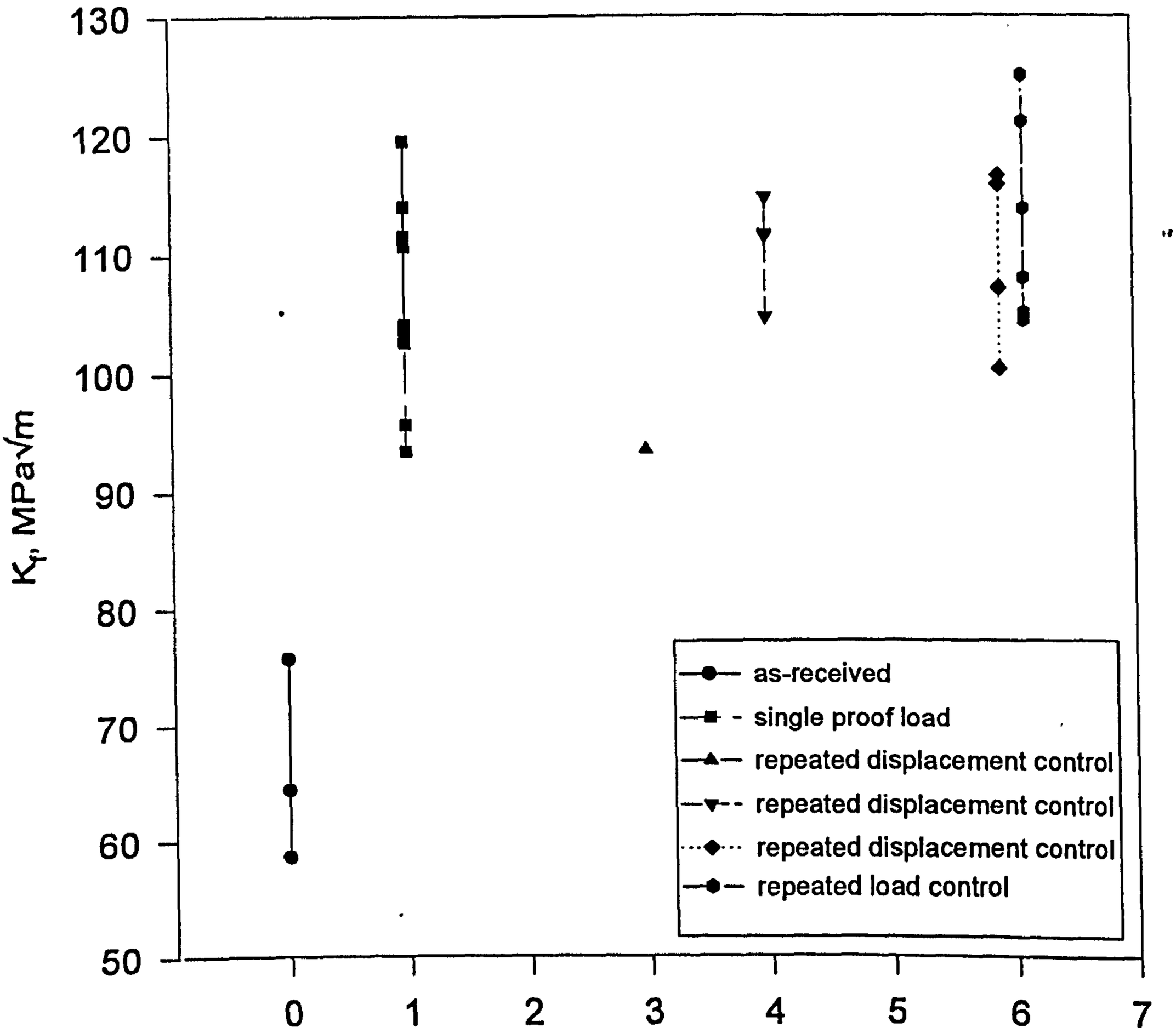

Figure 4.13. Tensile Properties of A533B at 20°C and -170°C.

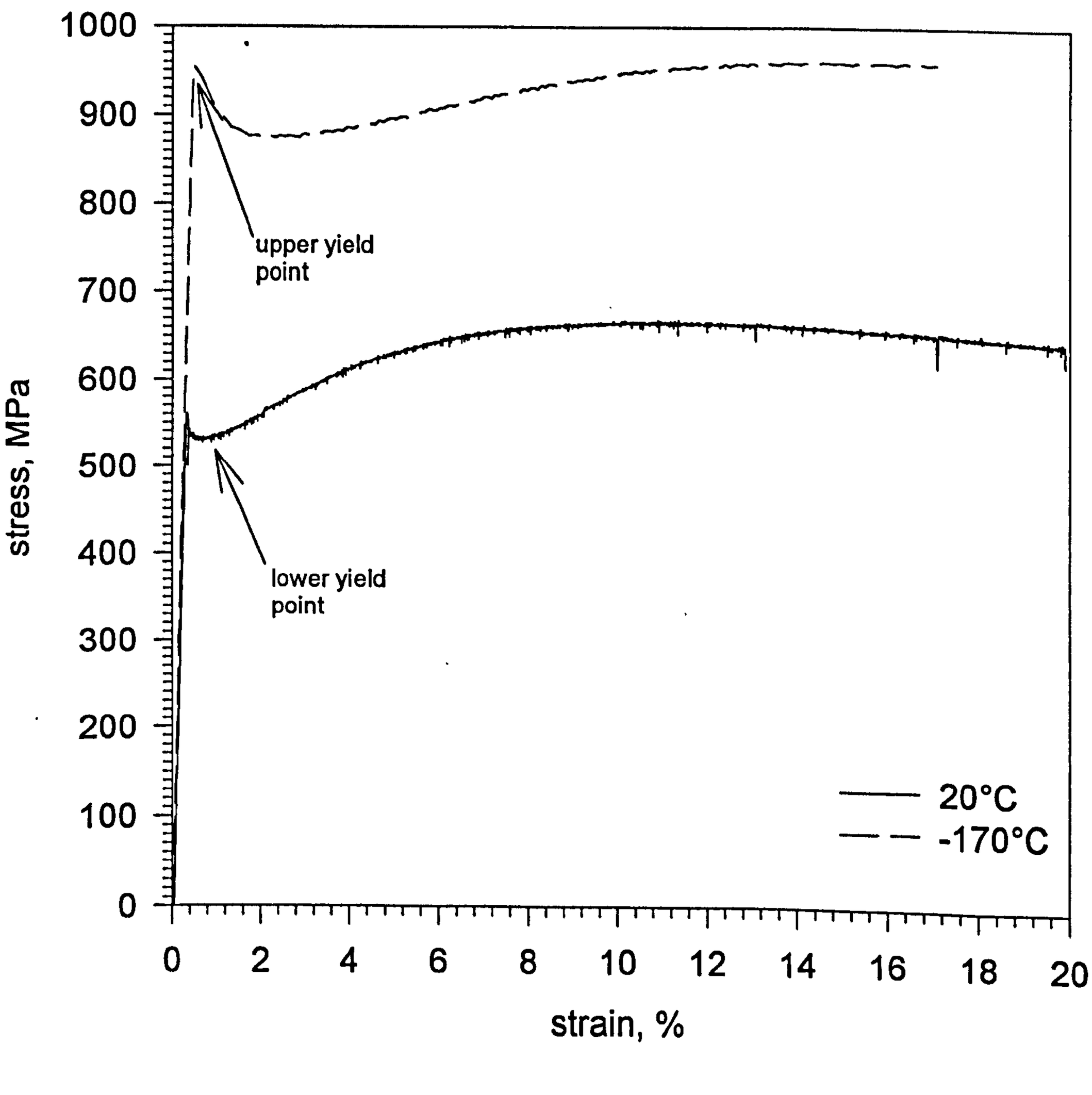

Figure 4.14. Comparison Between Edm Notched, Fatigue Precracked CT Specimens and SENB Toughness Data at -170°C

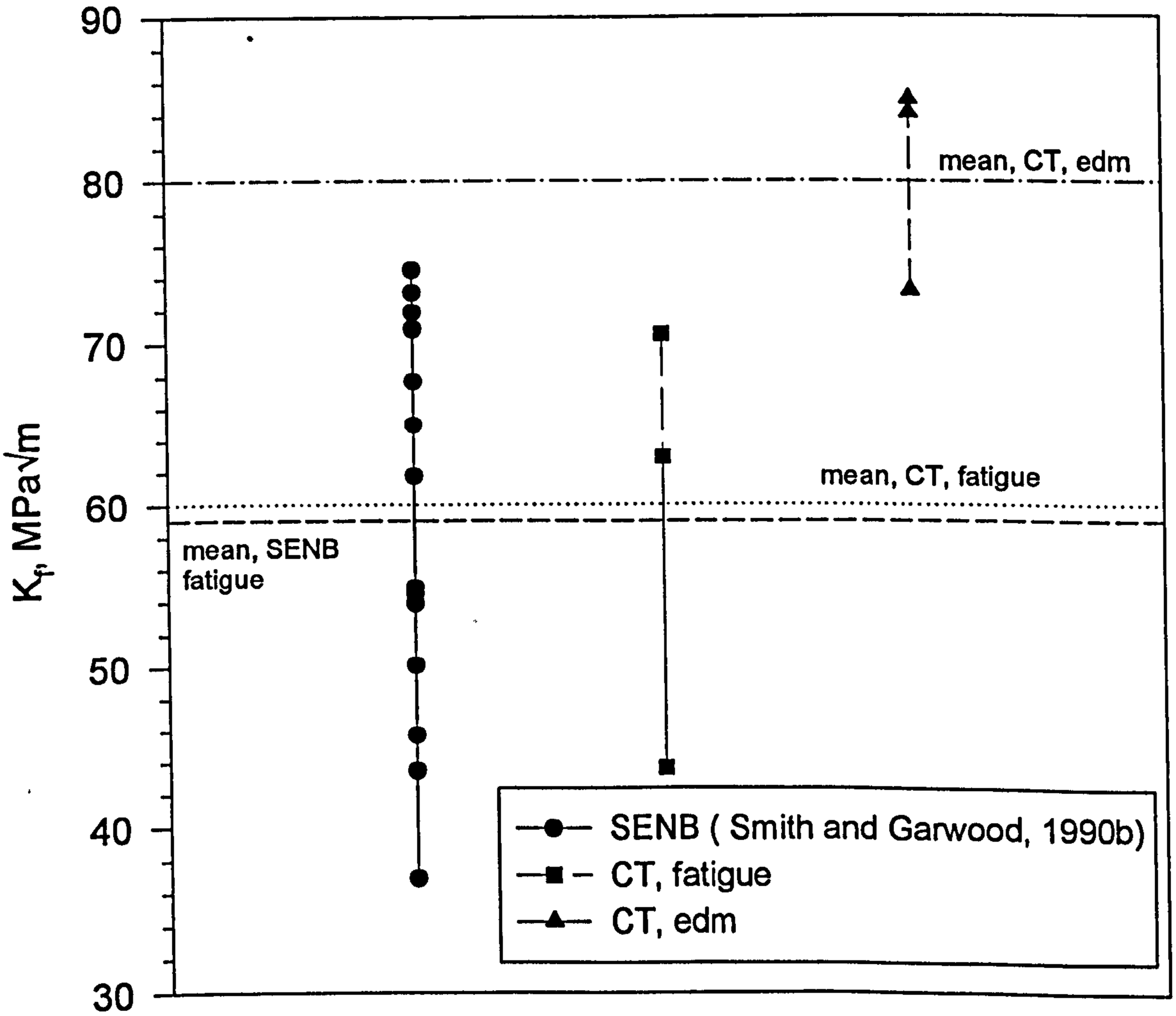

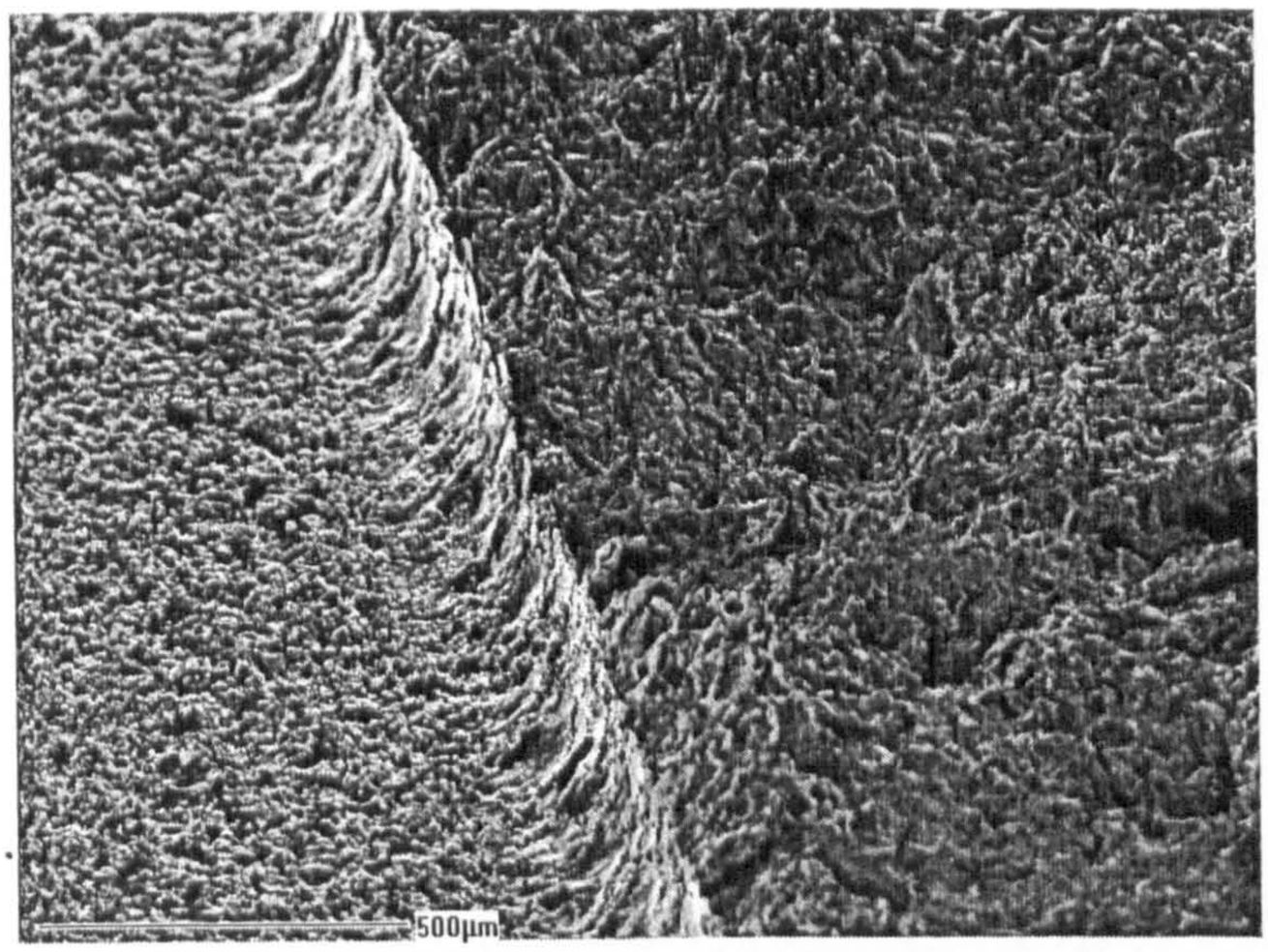

Figure 4.15. Fracture surface for as-recieved edm notched A533B showing brittle fracture initiation sites at tip

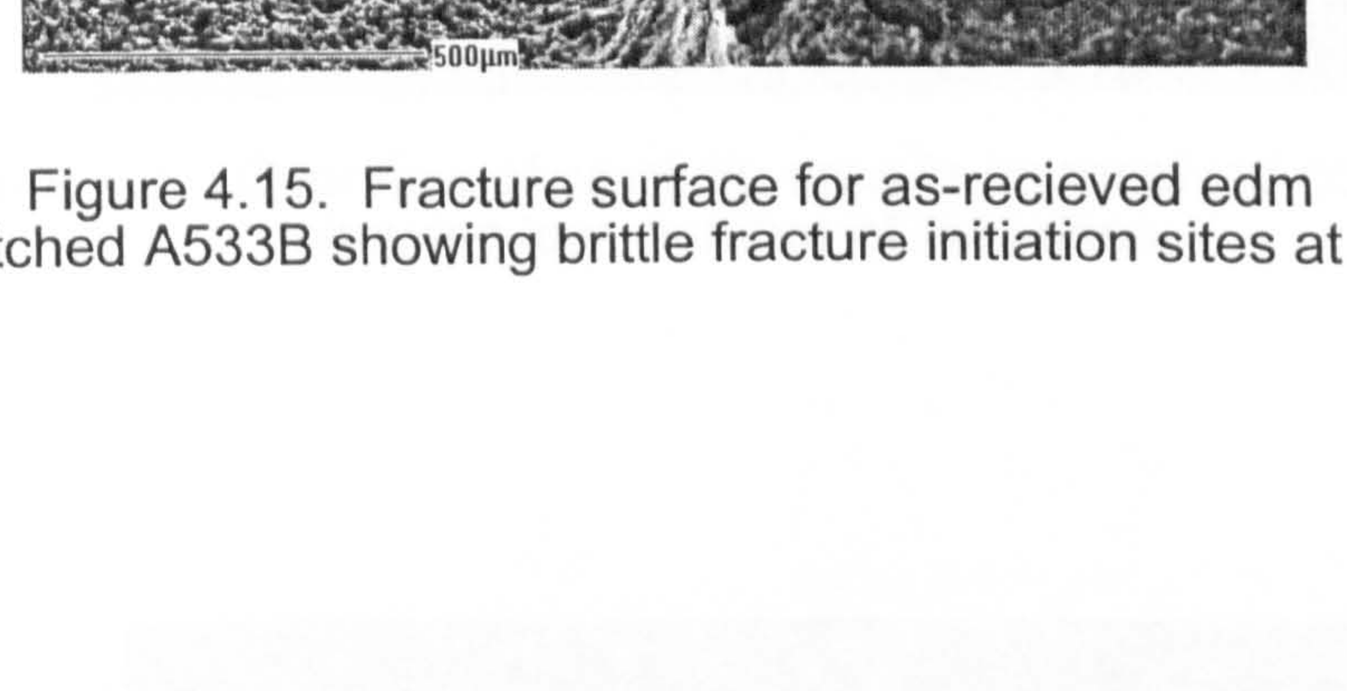

Figure 4.16. Pure cleavage of as received specimen showing slip induced initiation and extensive microcracking

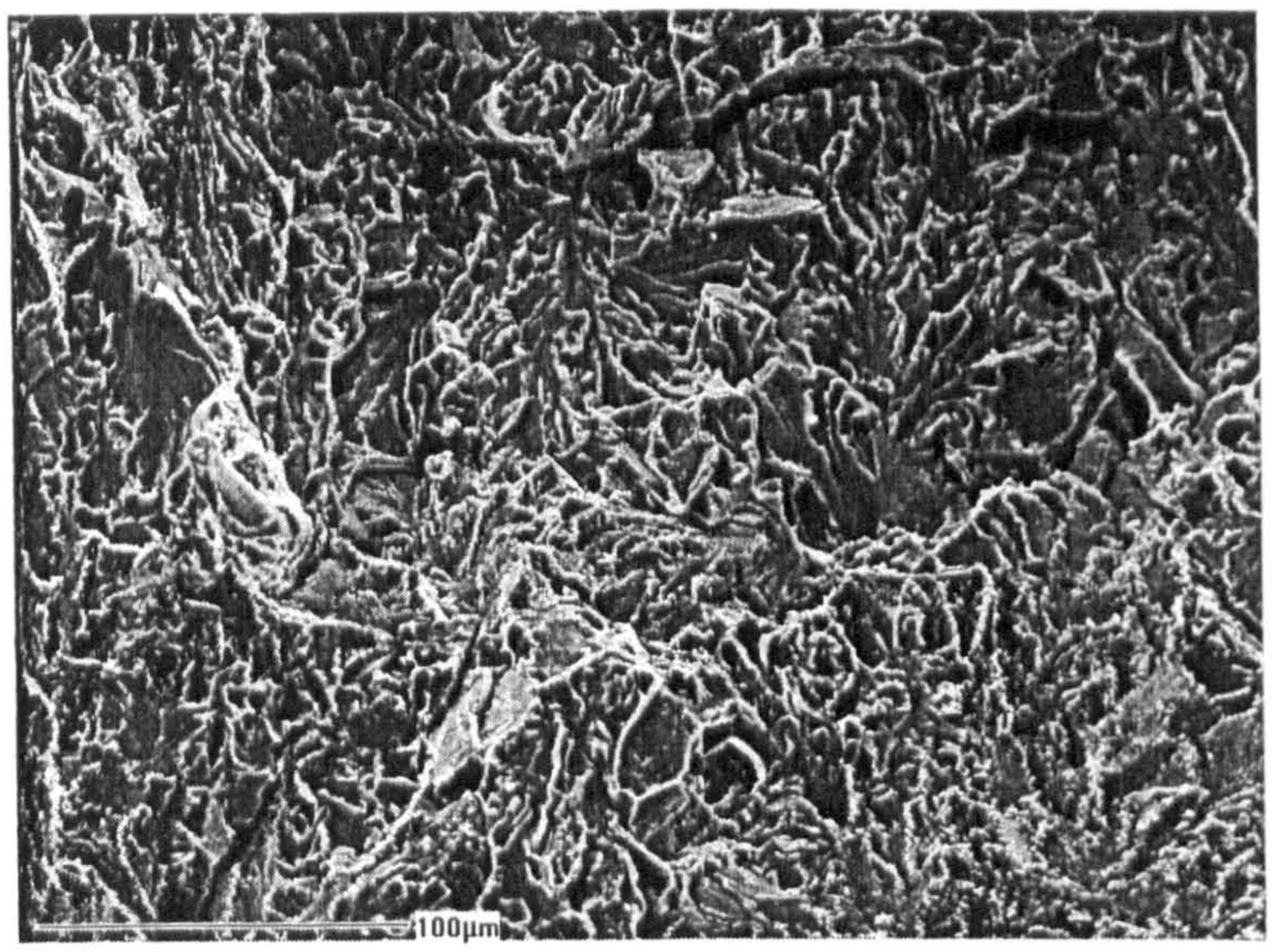

Figure 4.17. Overview of crack tip area in as received condition, showing low number of void sites.

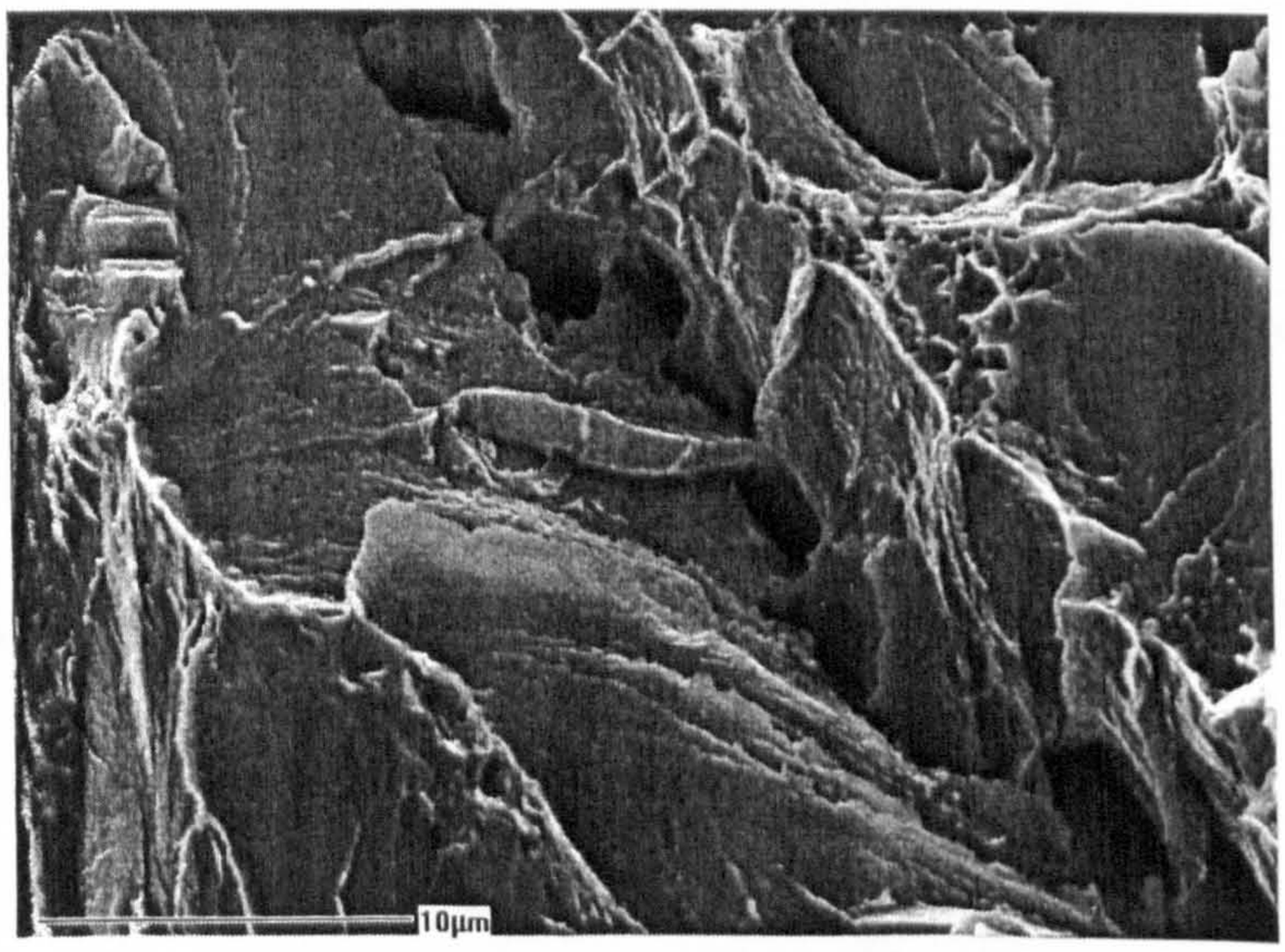

Figure 4.18. Microcrack formed in as-received specimens through void coalesence prior to fracture.

Figure 4.19. Influence of Repeated Proof Testing On Cleavage Toughness of A533B at -170°C.

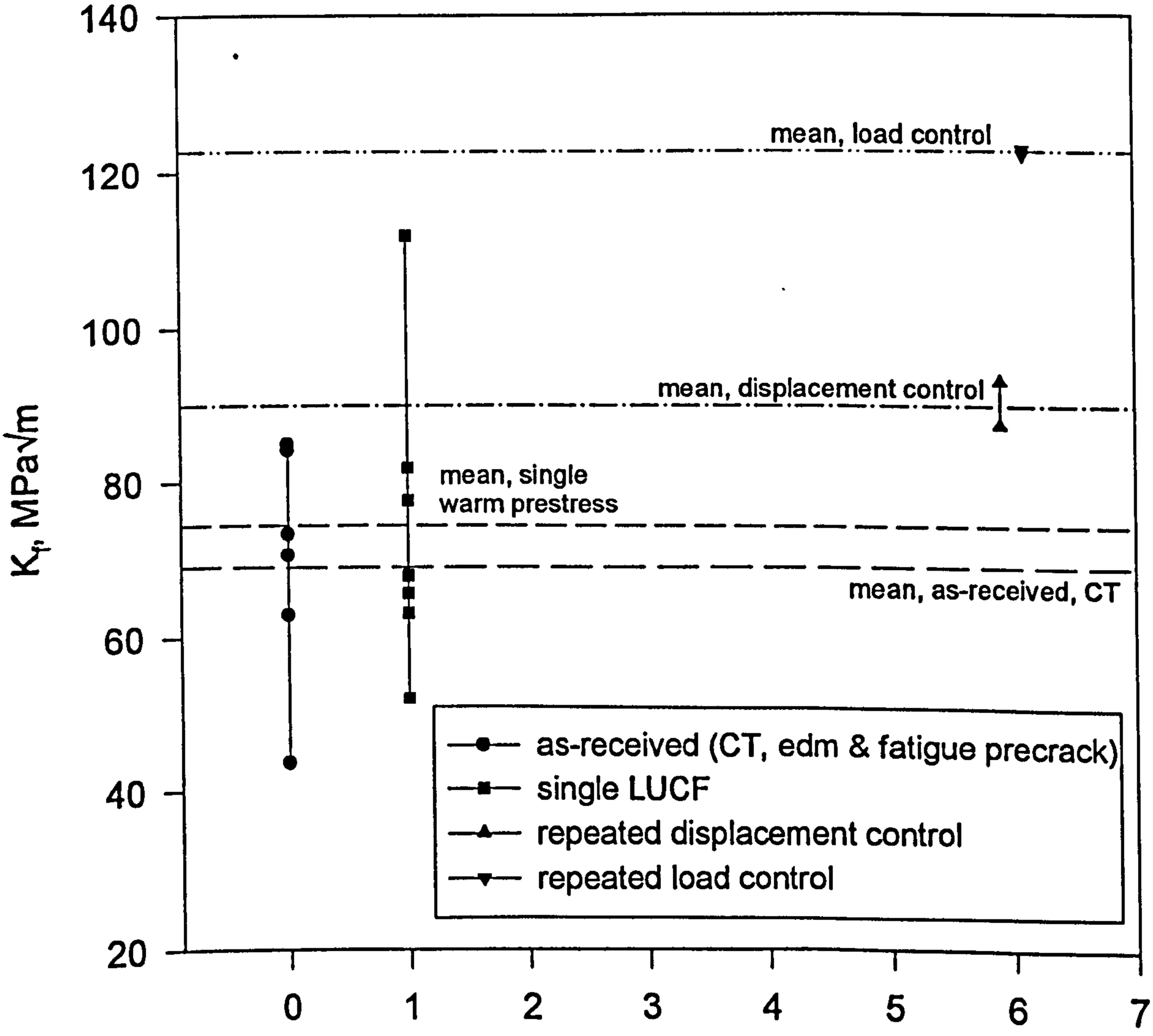

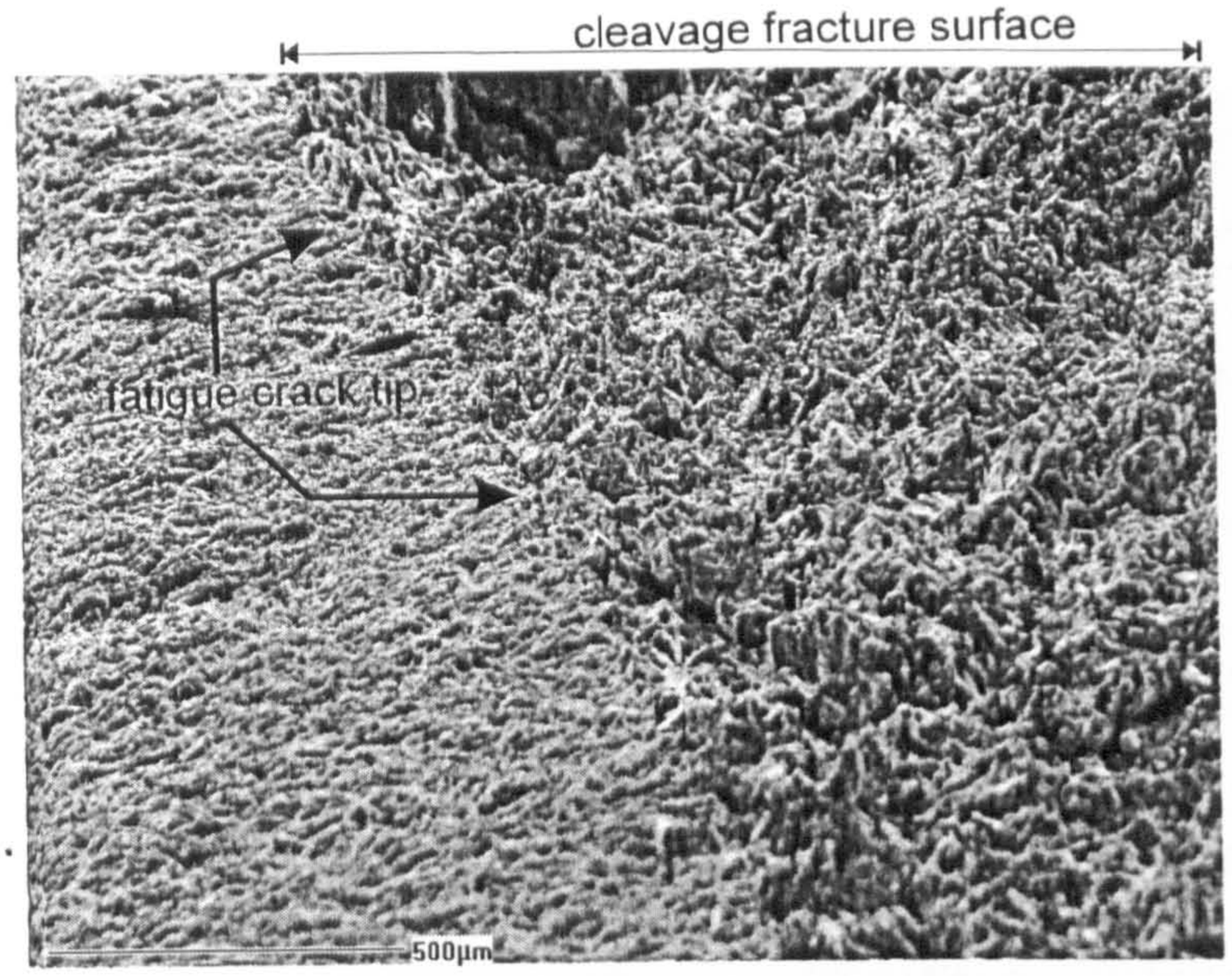

Figure 4.20. Low proof load specimen, fatigue precracked showing no blunting with pure cleavage from crack tip.

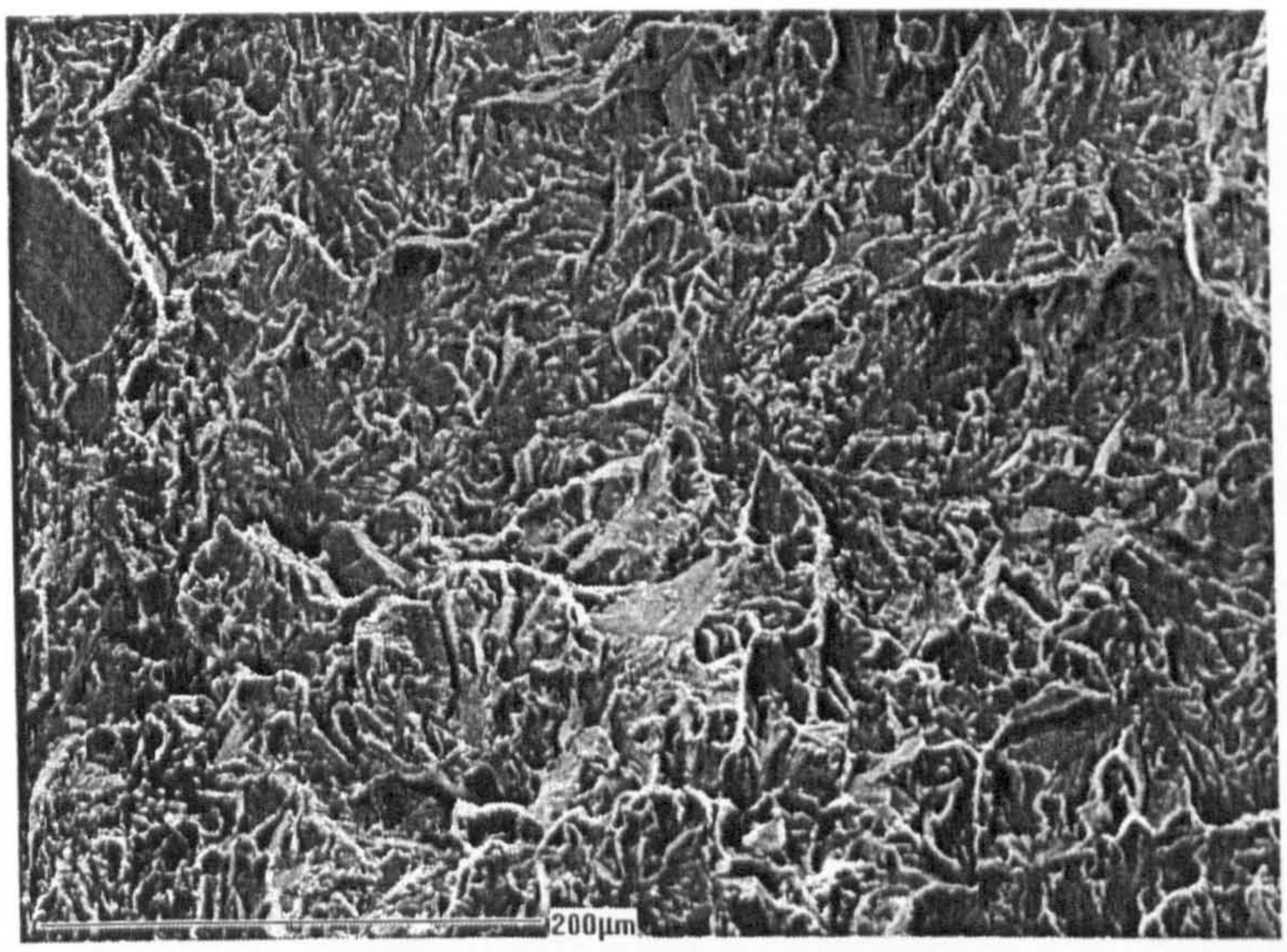

Figure 4.21. Fracture following low proof load.
Small number of voids with cleavage initiation sites between voids.

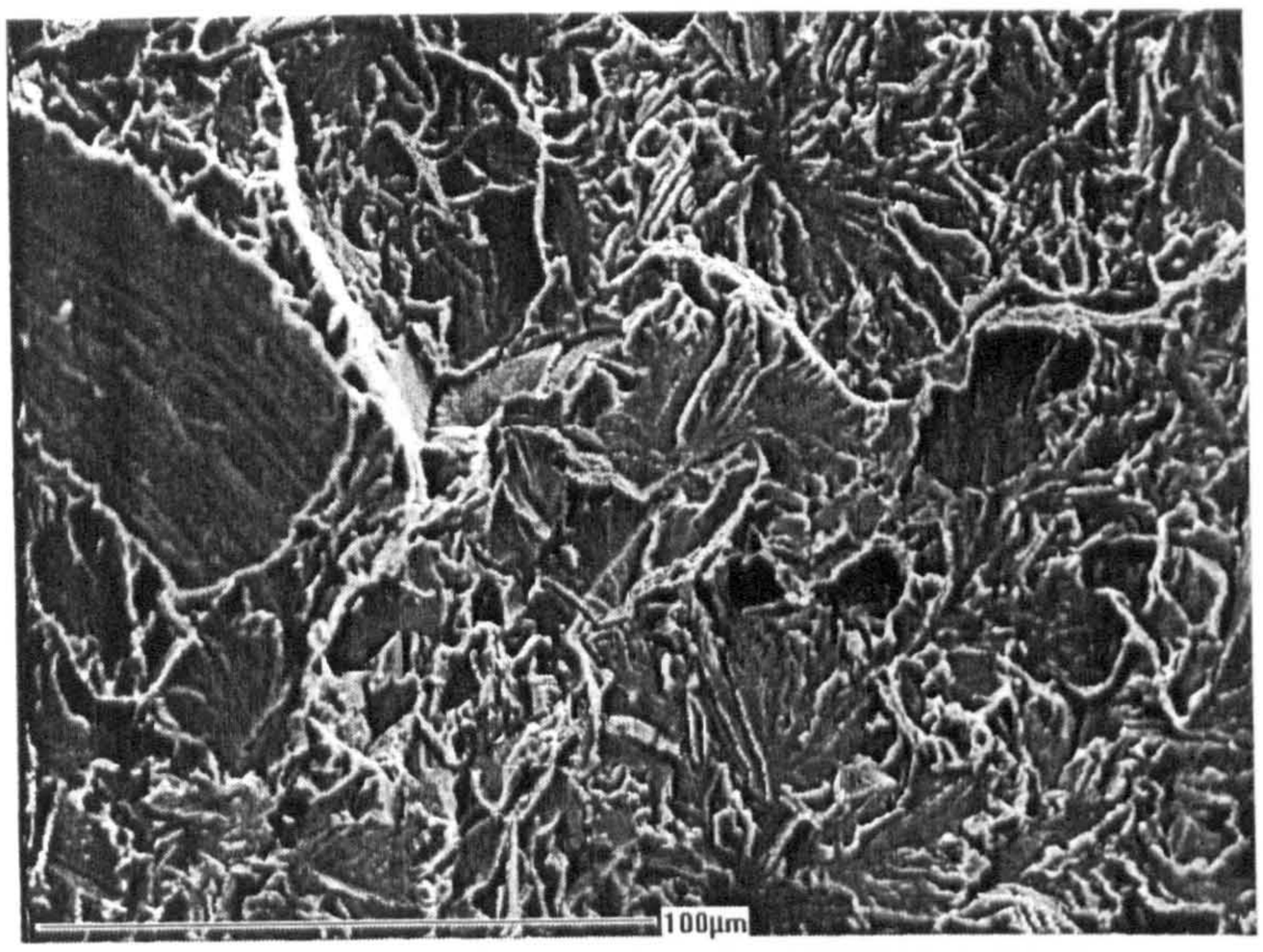

Figure 4.22. Higher mag. showing small voids nucleated during proof loading with fracture initiating between the voids.

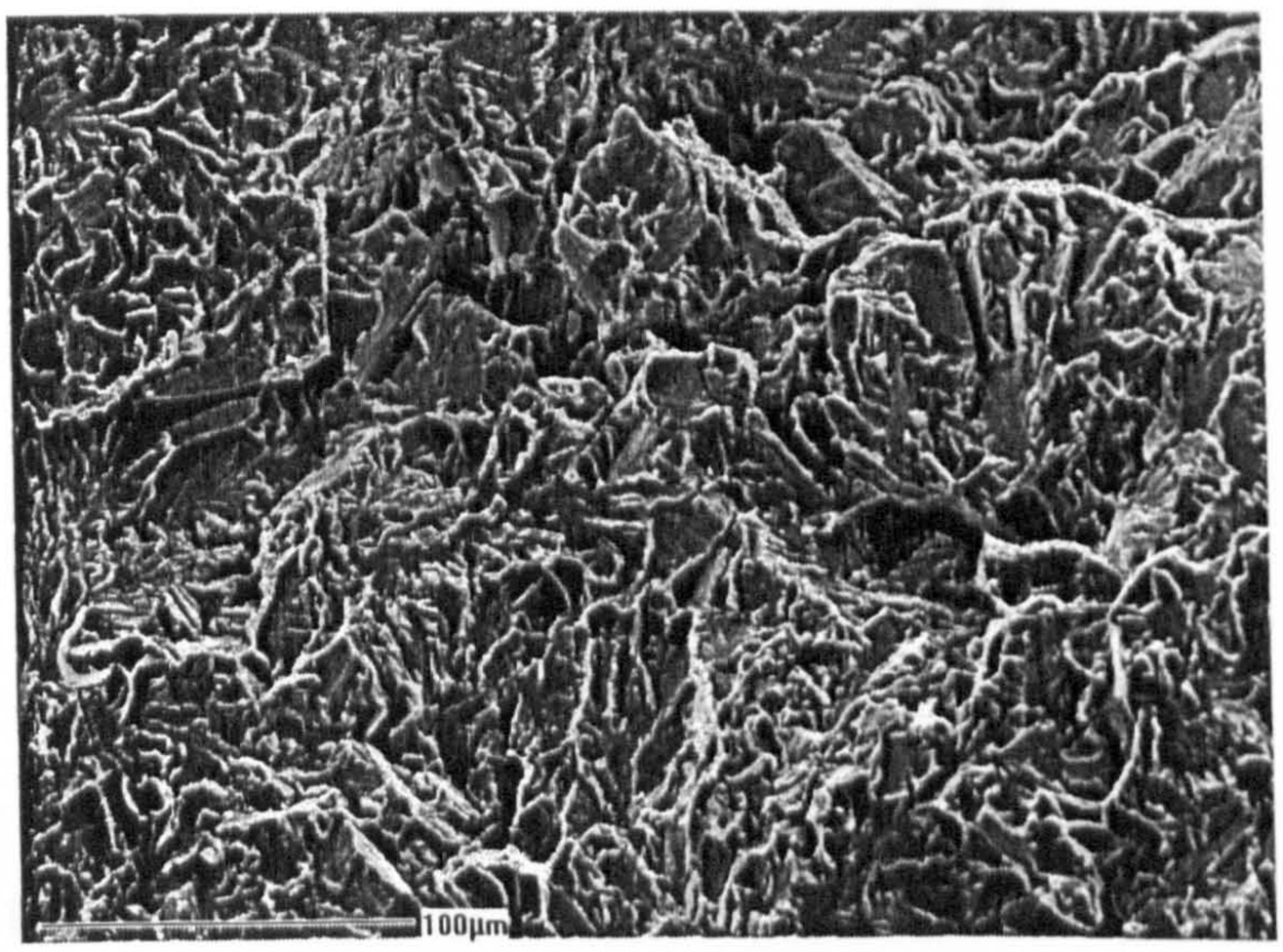

Figure 4.23. Overview of crack tip area showing low numbers of voids in low proof load specimen.

Figure 4.24. Load - Displacement Trace of Specimen A9rpl.
Repeated Proof Load Under Load Control.

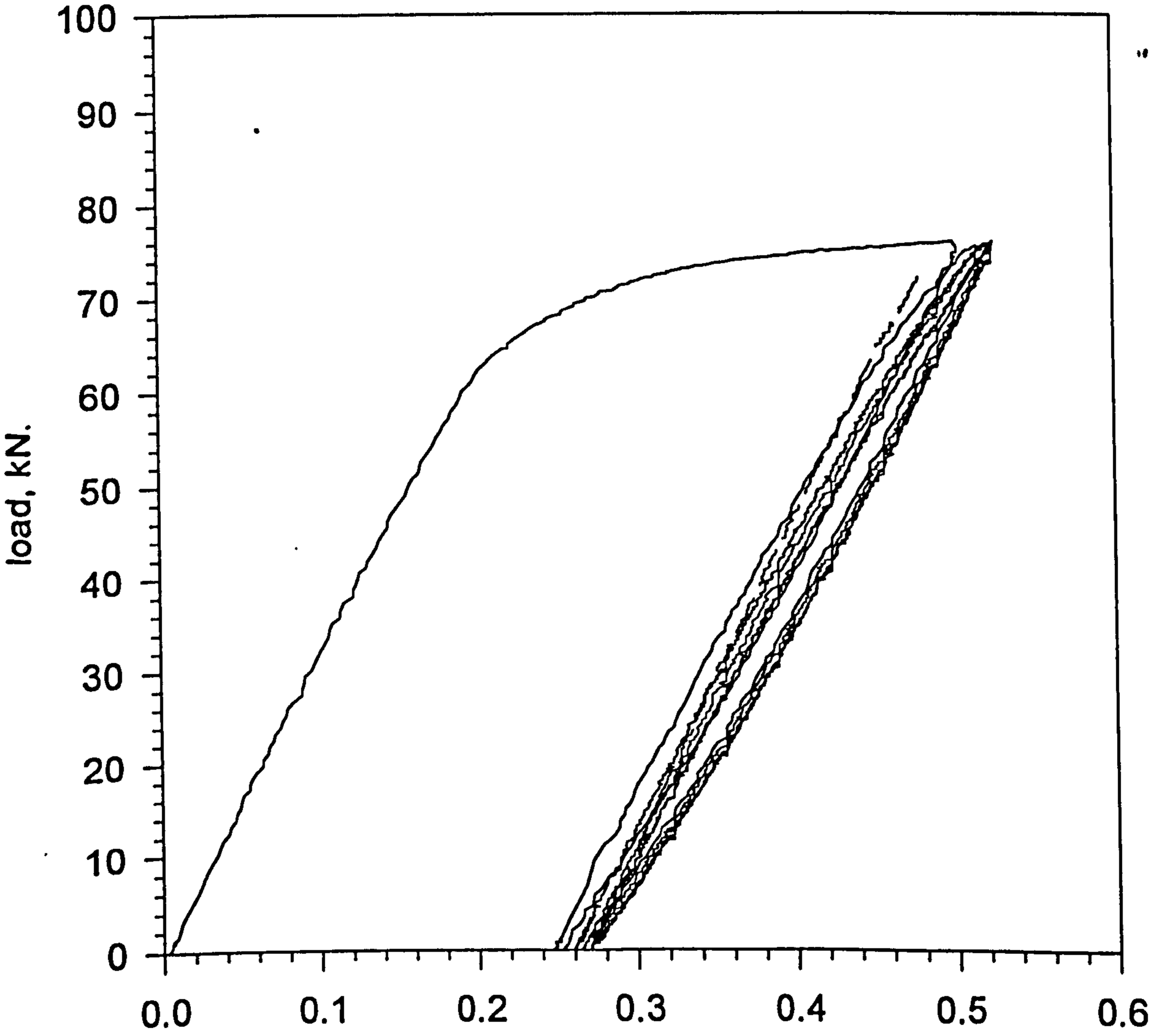

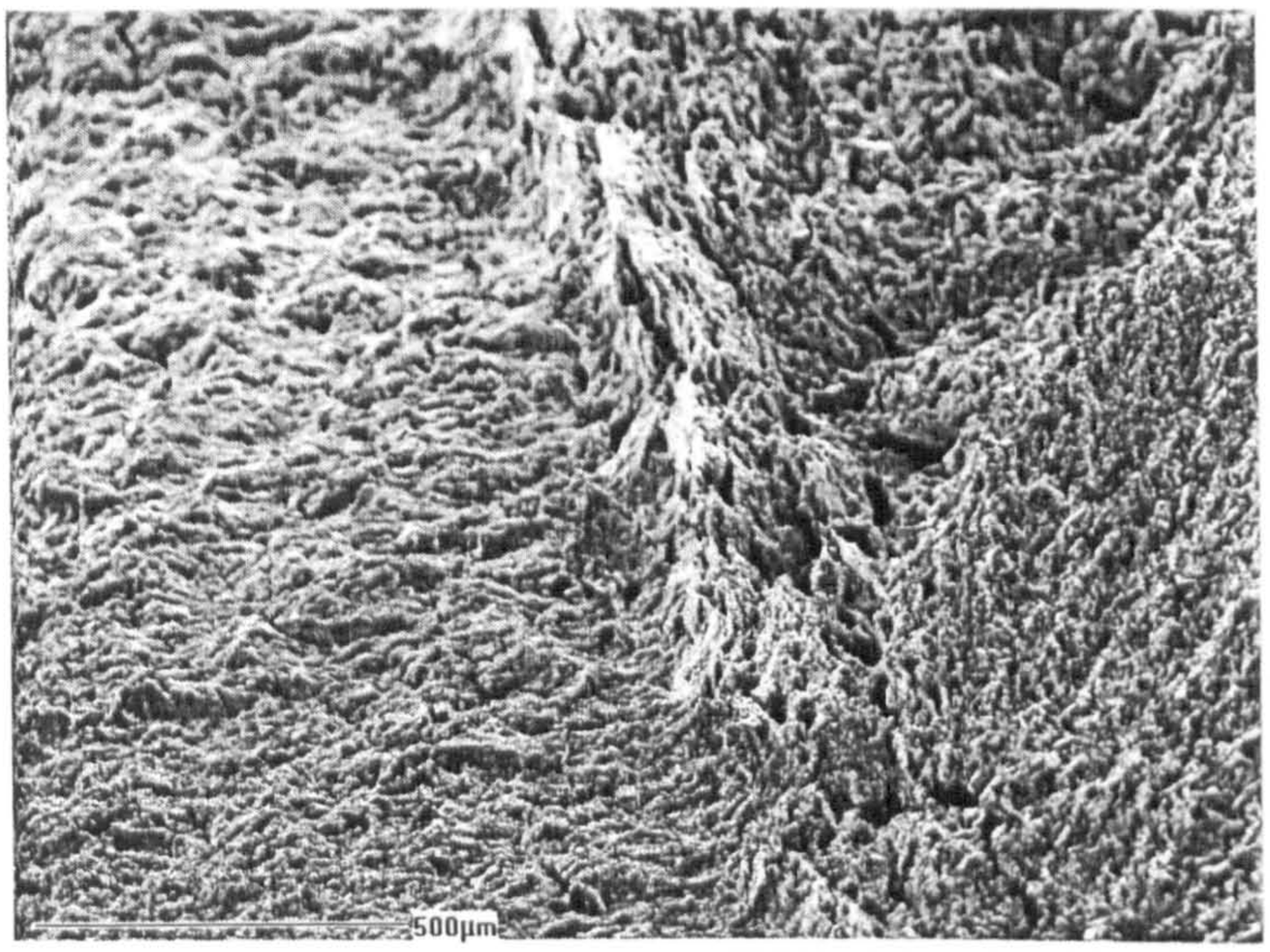

Figure 4.25. Fatigue precracked specimen, subjected to repeated load control testing showing voids at crack tip with cleavage fracture beyond damaged zone.

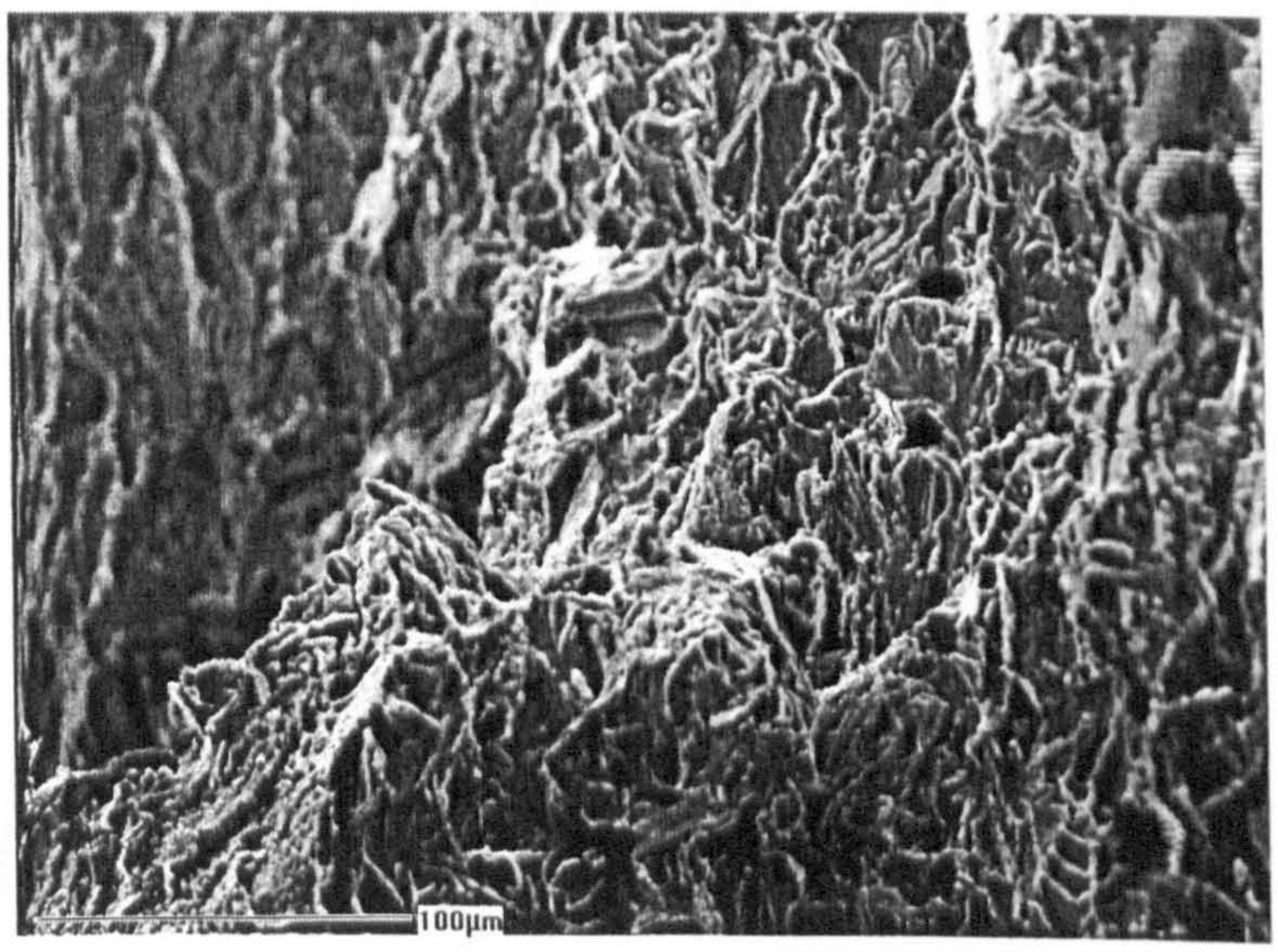

Figure 4.26. Crack tip area with small voids and cleavage sites.

Figure 4.27. Load - Displacement Trace For Specimen A8rpd, Repeated Proof Load In Displacement Control.

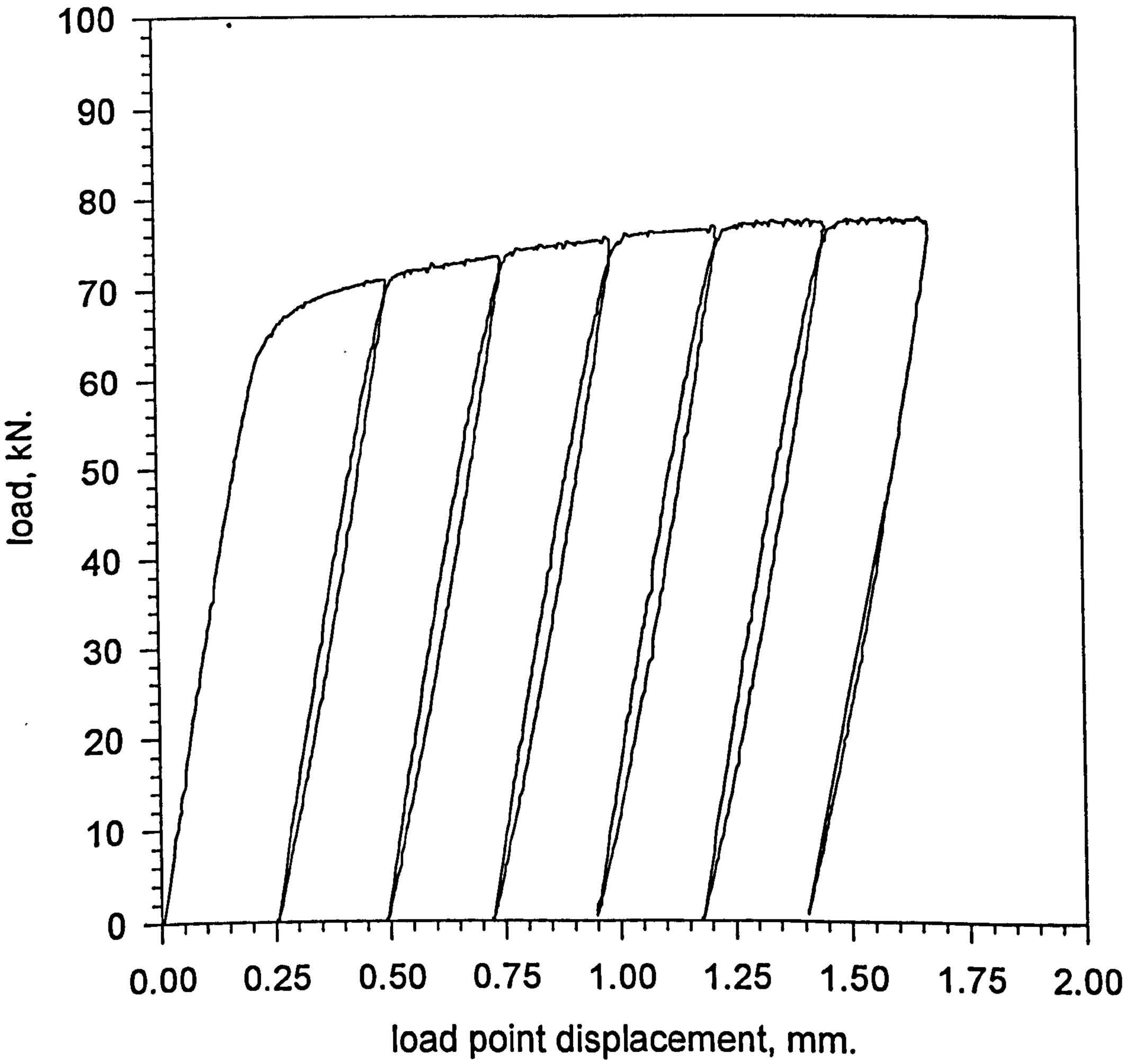

Figure 4.28. Repeated displacement controlled proof loaded specimen showing high degree of blunting and tearing.

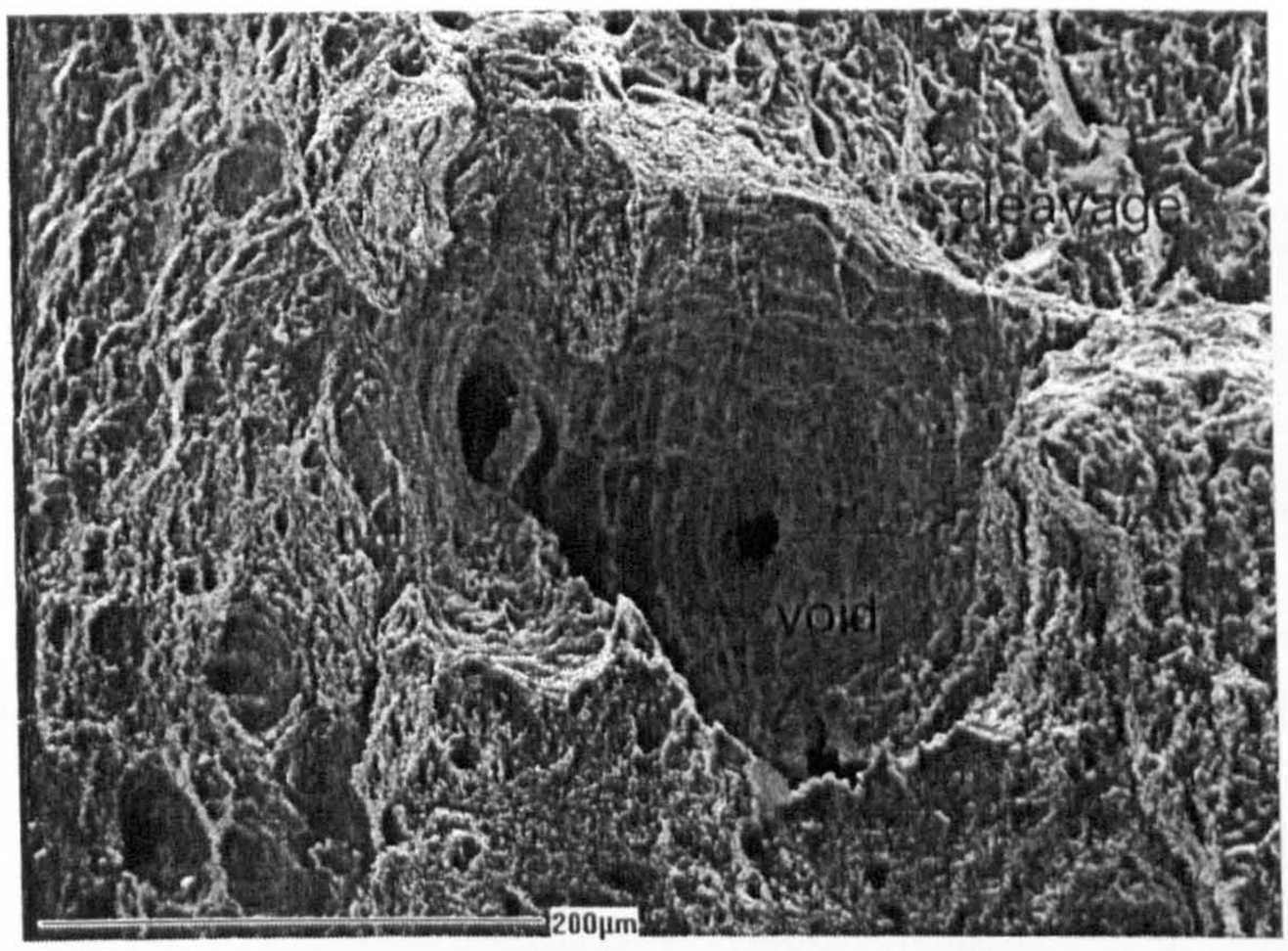

Figure 4.29. Large voids nucleated within cleavage fracture area, fracture initiated from small inclusions.

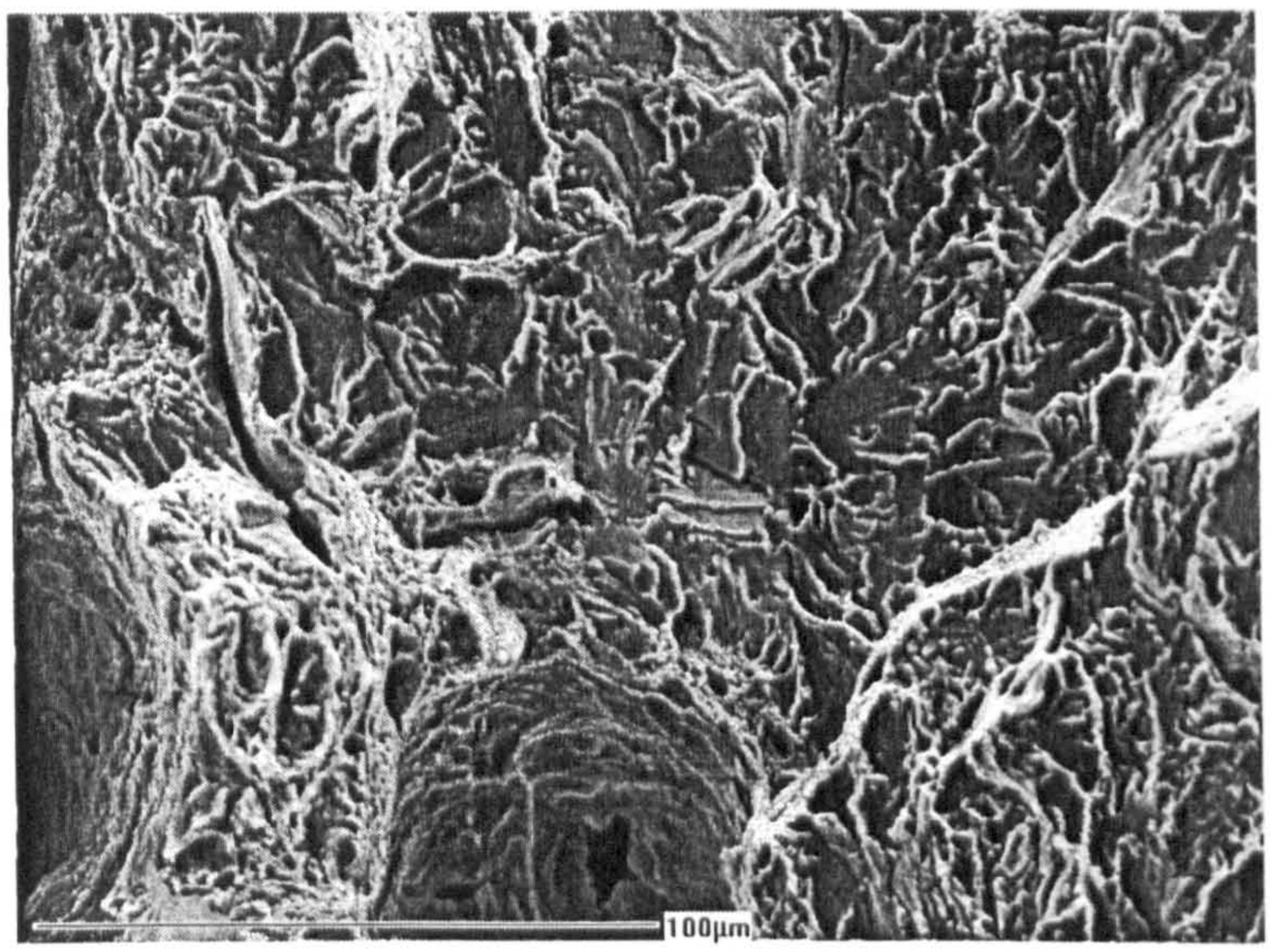

Figure 4.30. Initiation sites by small voids, with large voids not influencing fracture initiation.

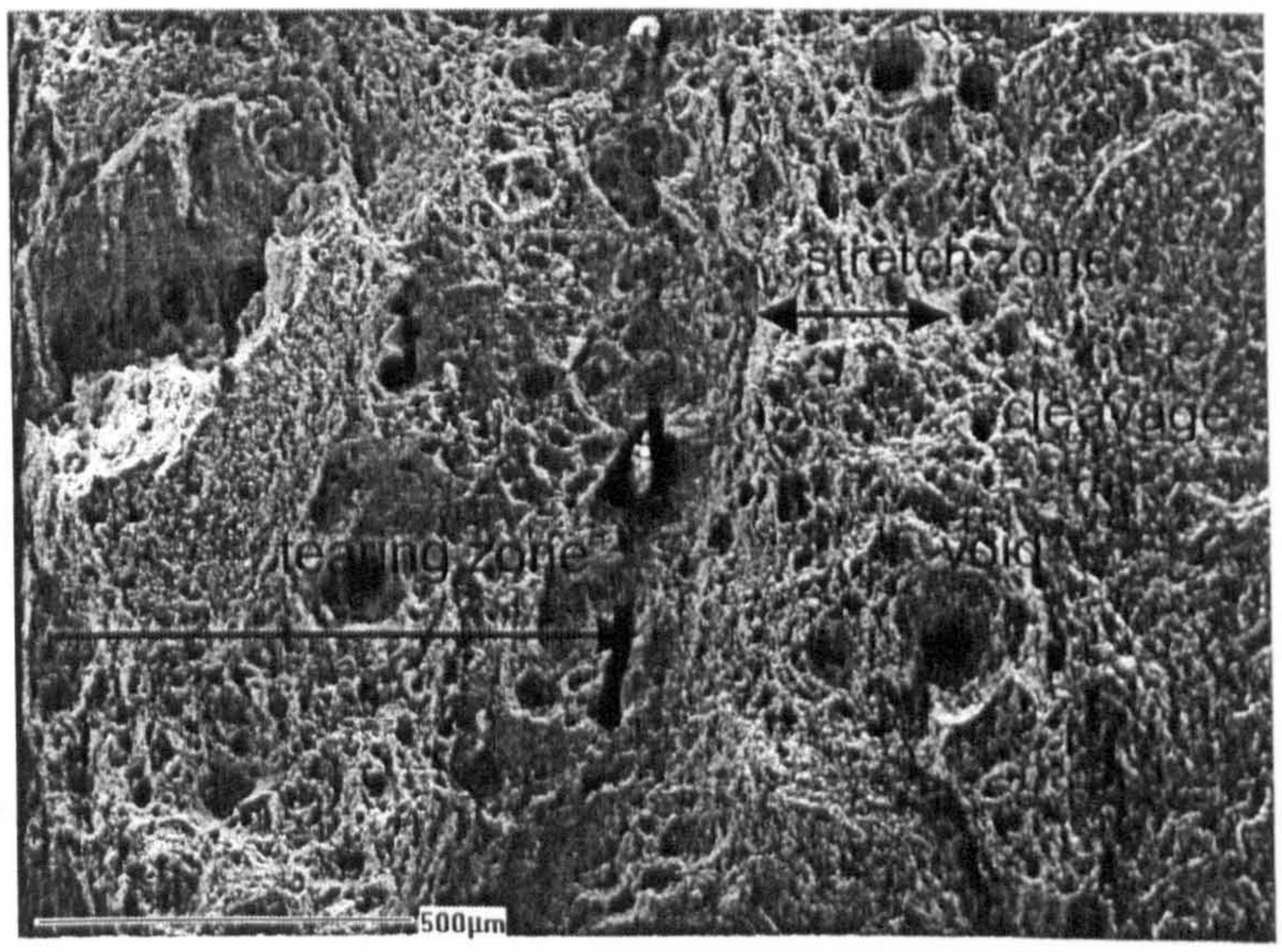

Figure 4.31. Overview of crack tip area showing large numbers of voids with brittle fracture

Figure 4.32. Variation in Failure Stress Intensity With Sub Critical Crack Growth Increment

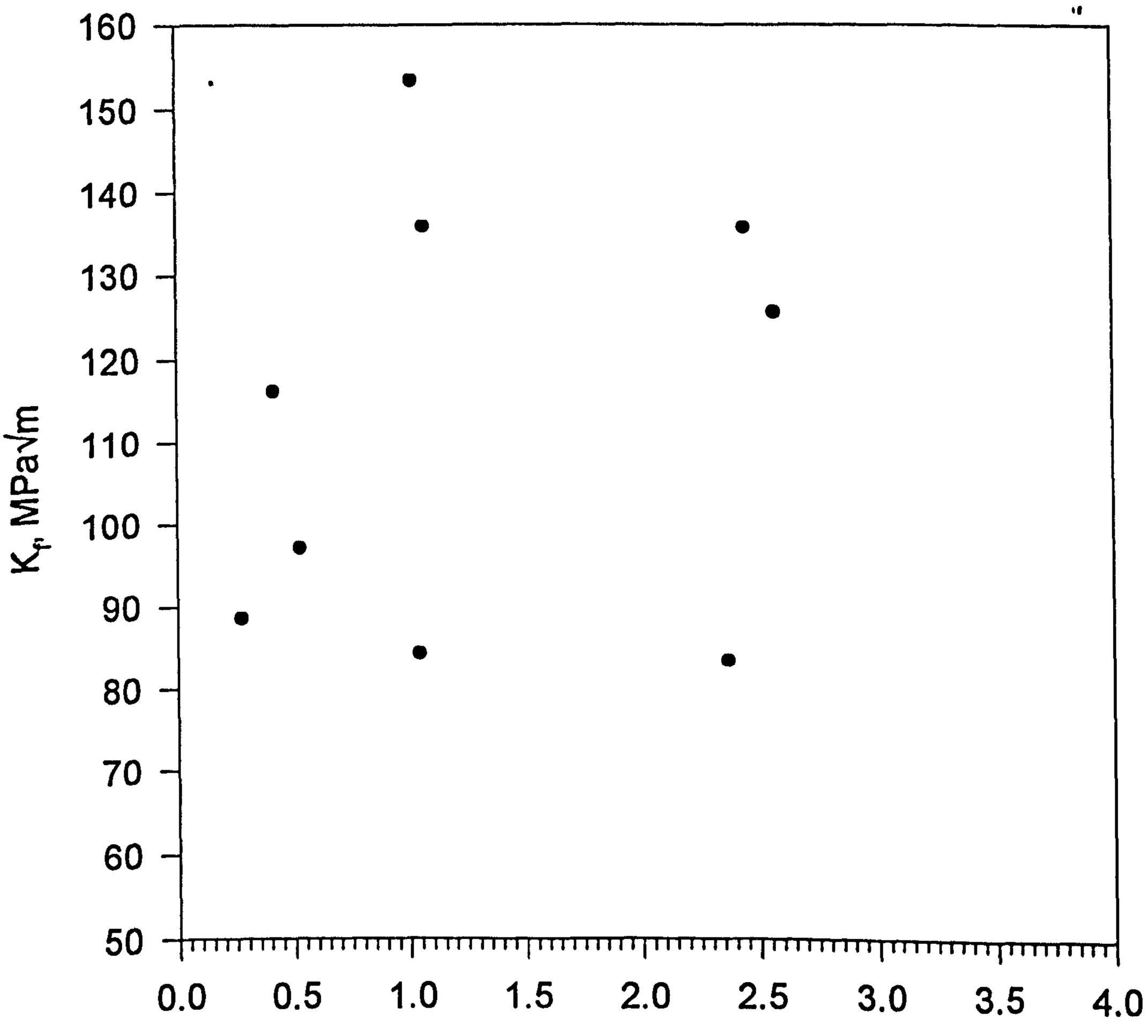

Figure 4.33. Effect of warm prestressing on Kf,
(based on maximum load) for 6mm thick A533B specimens.

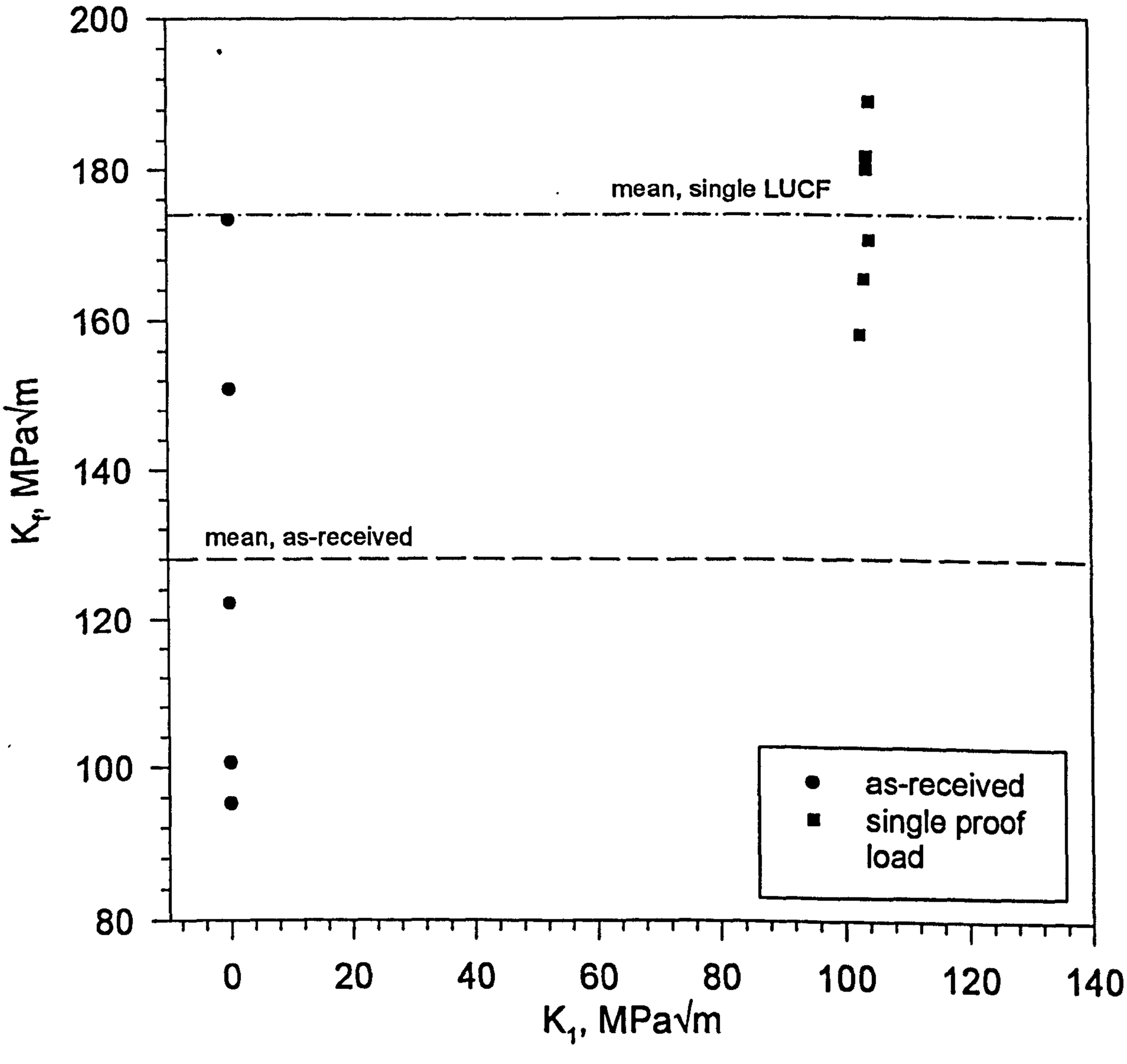

Figure 4.34. Load - Displacement Trace for Specimens ab5wps and 5sp6.

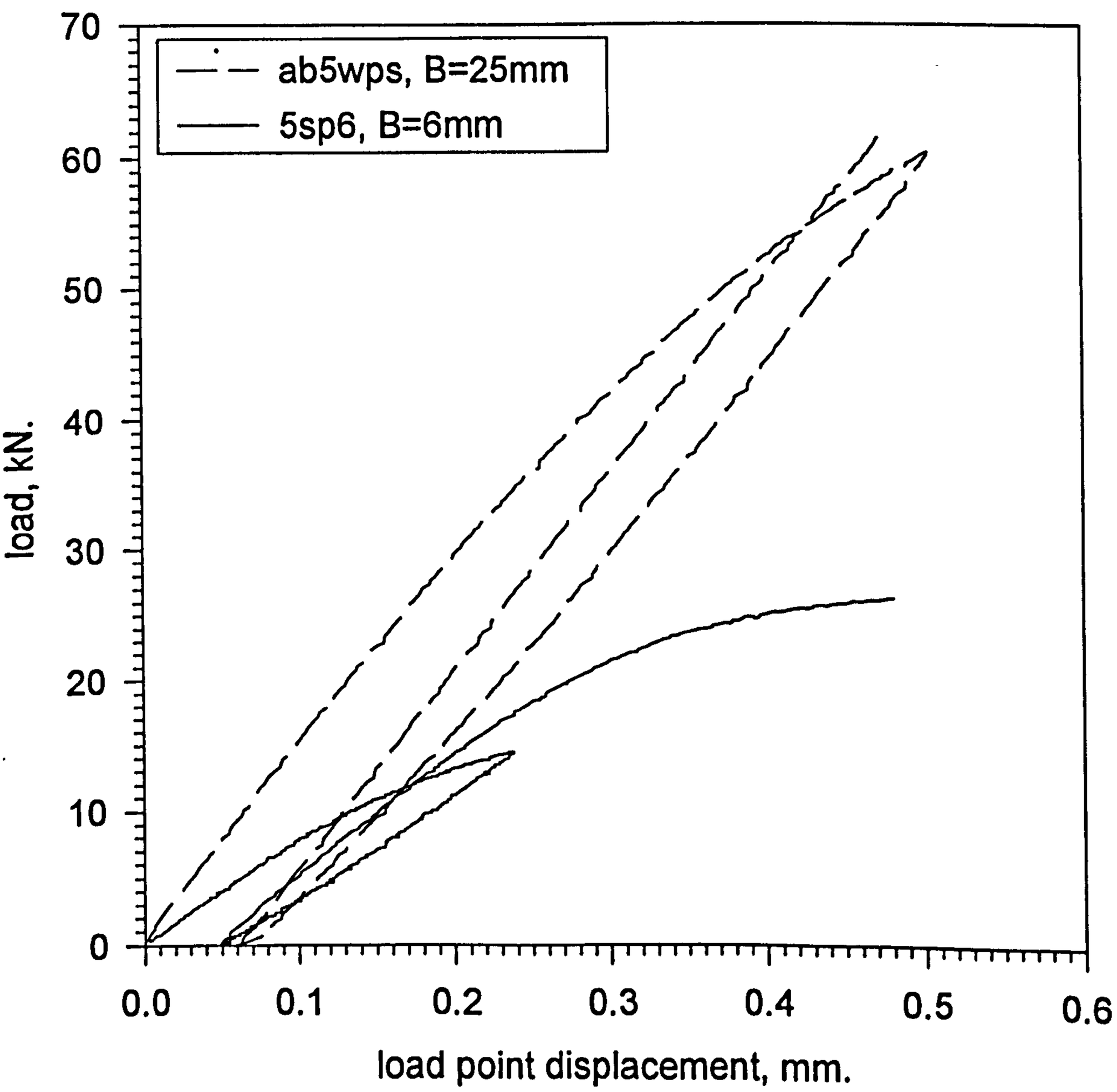

Figure 4.35. Critical equivalent stress intensity factors evaluated using experimental *J* Integrals.

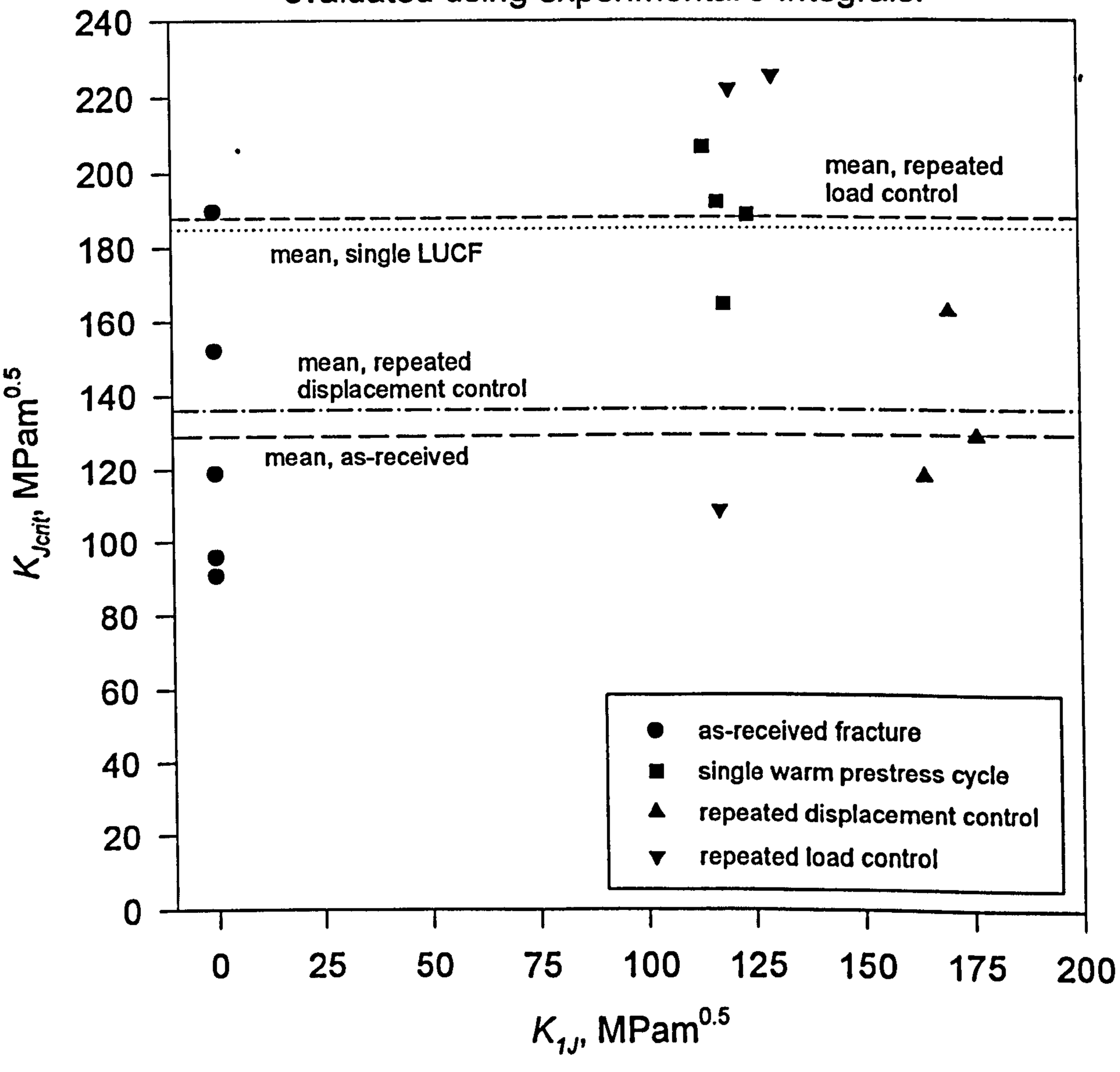

Figure 4.36. Effect of Repeated Proof Loading on Cleavage Toughness 6mm Thick A533B Specimens, based on maximum load.

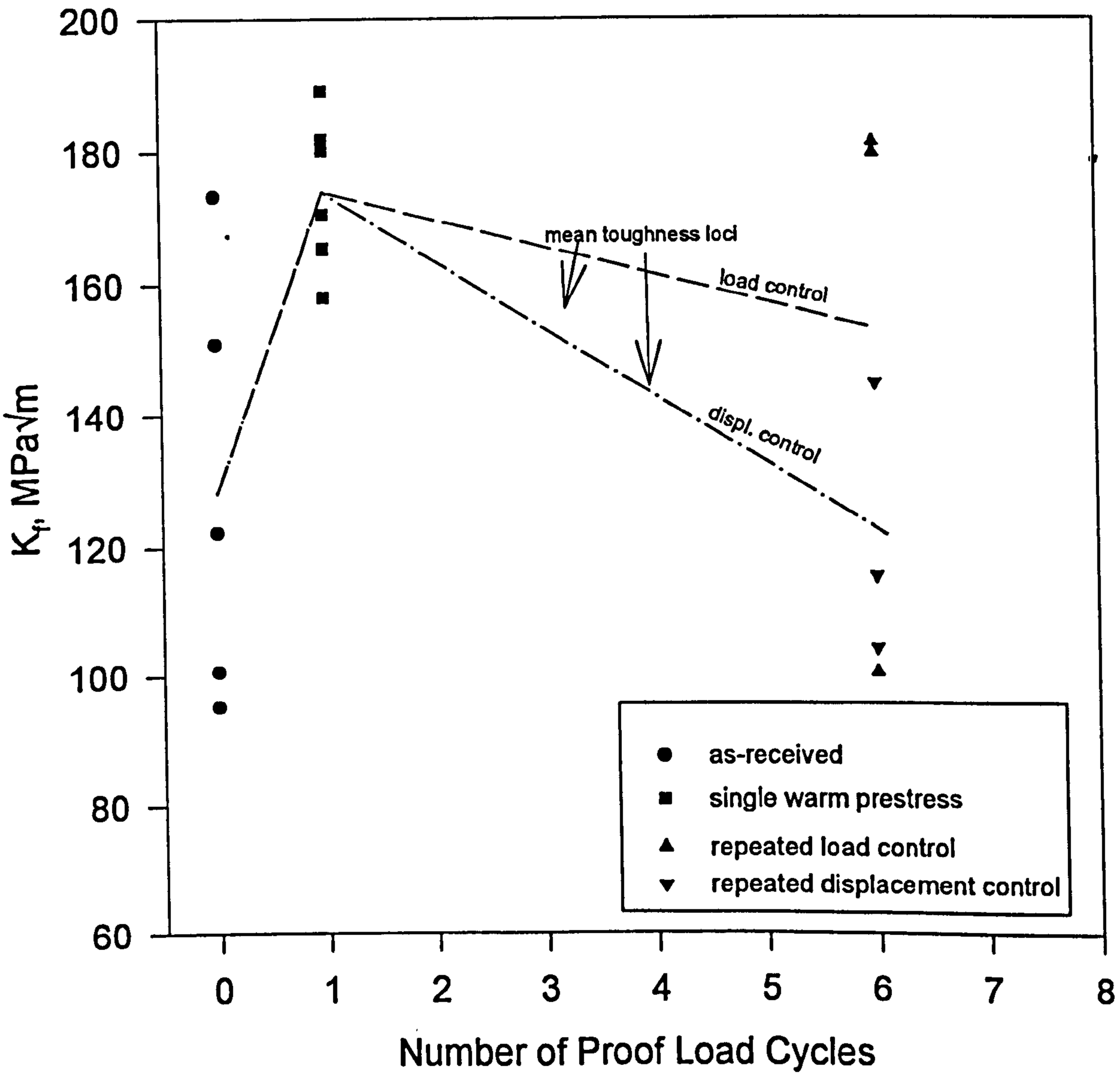

Figure 5.1. Comparison Between Uniaxial Response and Isotropic Hardening Response of A533B at 20°C and -170°C, as implemented in ABAQUS

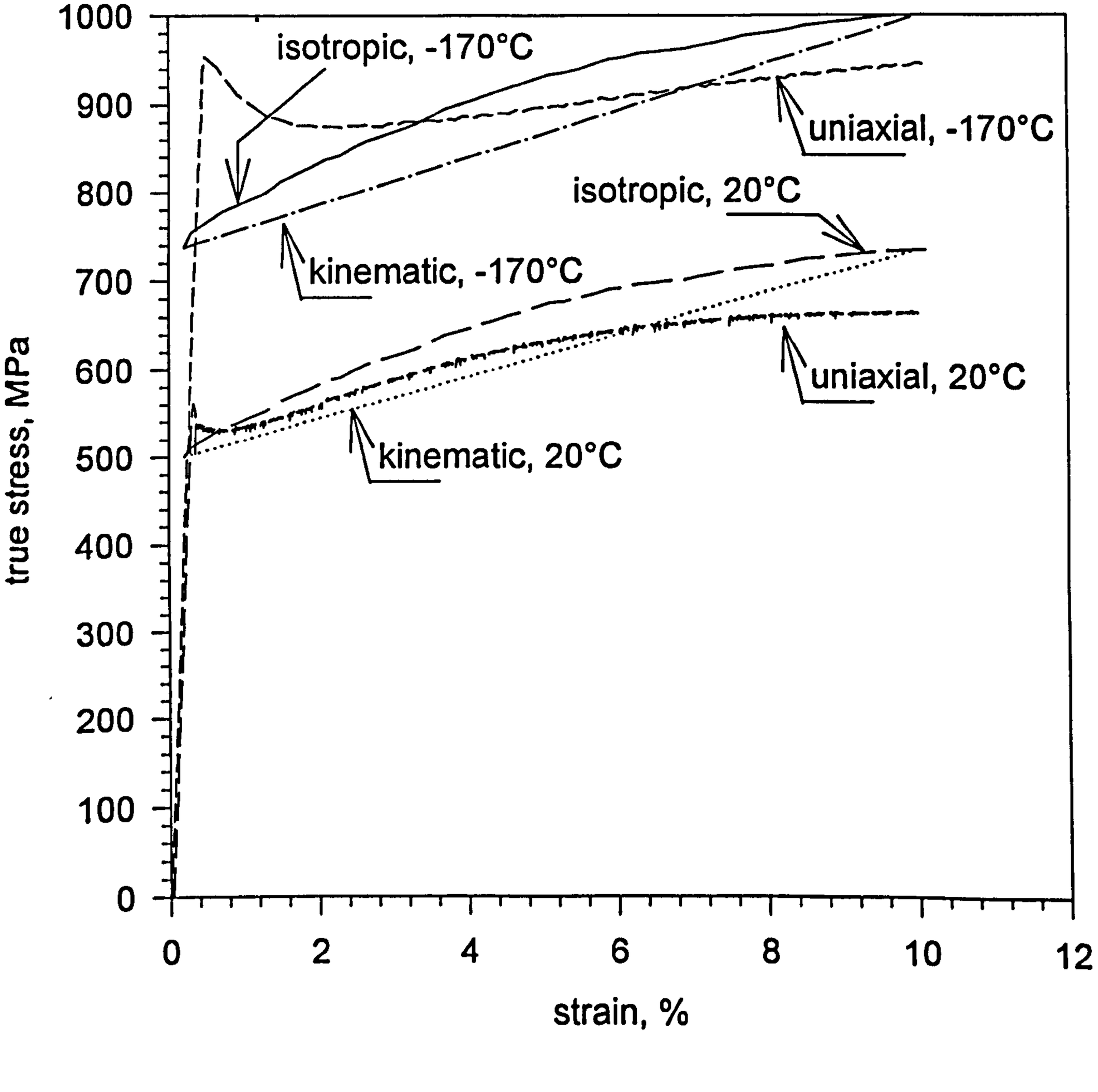

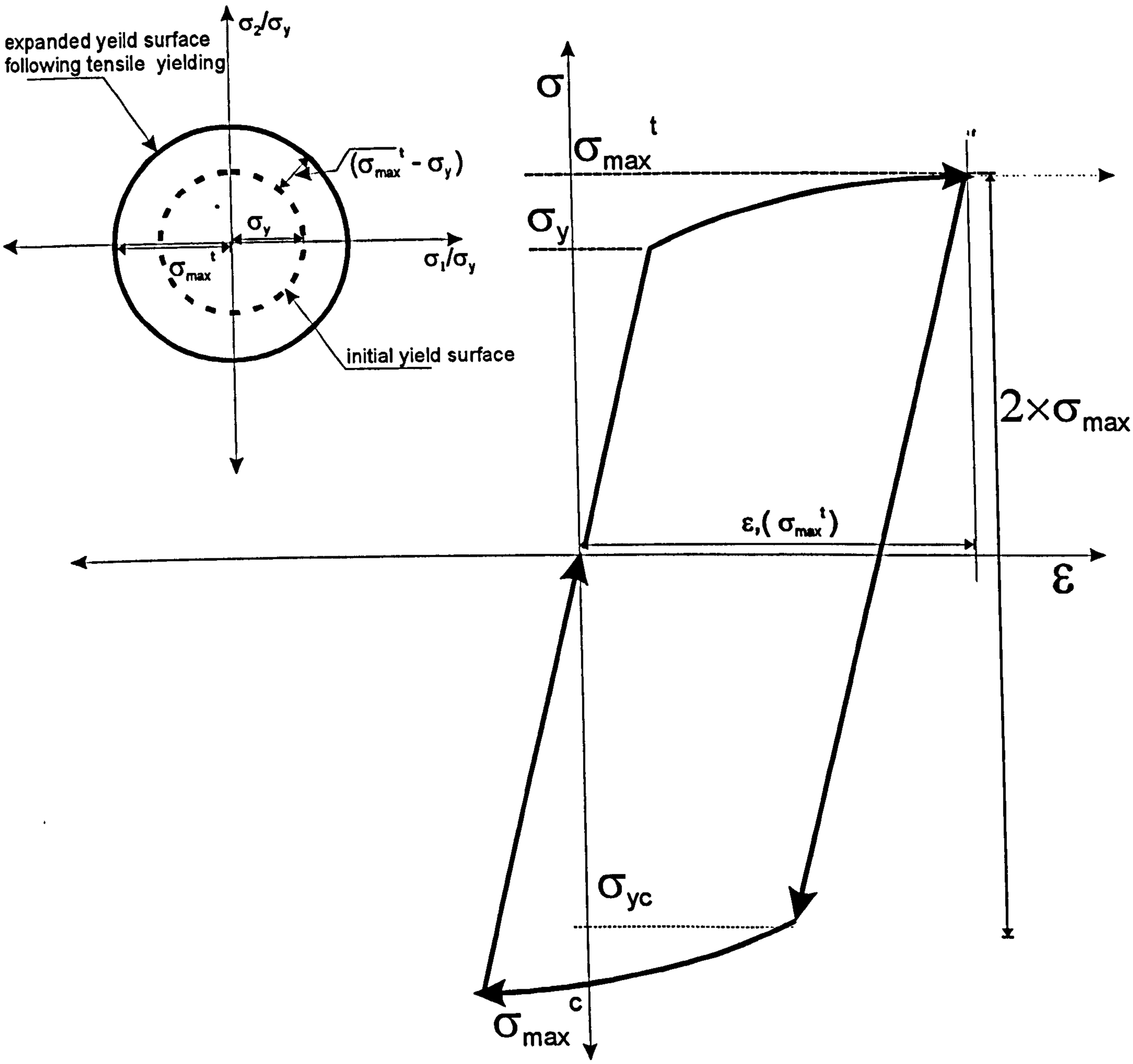

Figure 5.2. Isotropic hardening law illustrated in stress - strain diagram

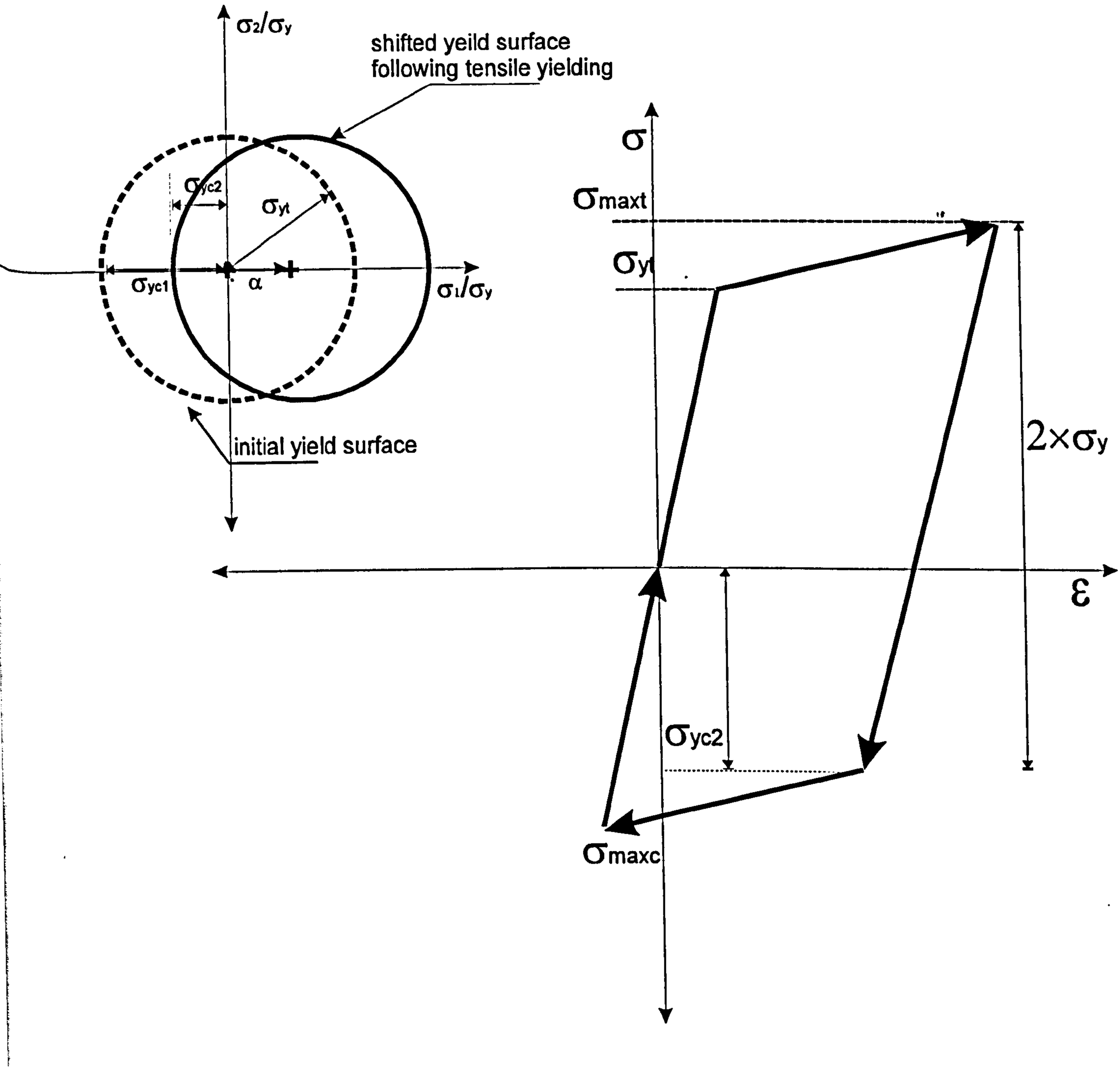

Figure 5.3. Kinematic hardening law illustrated in stress - strain diagram

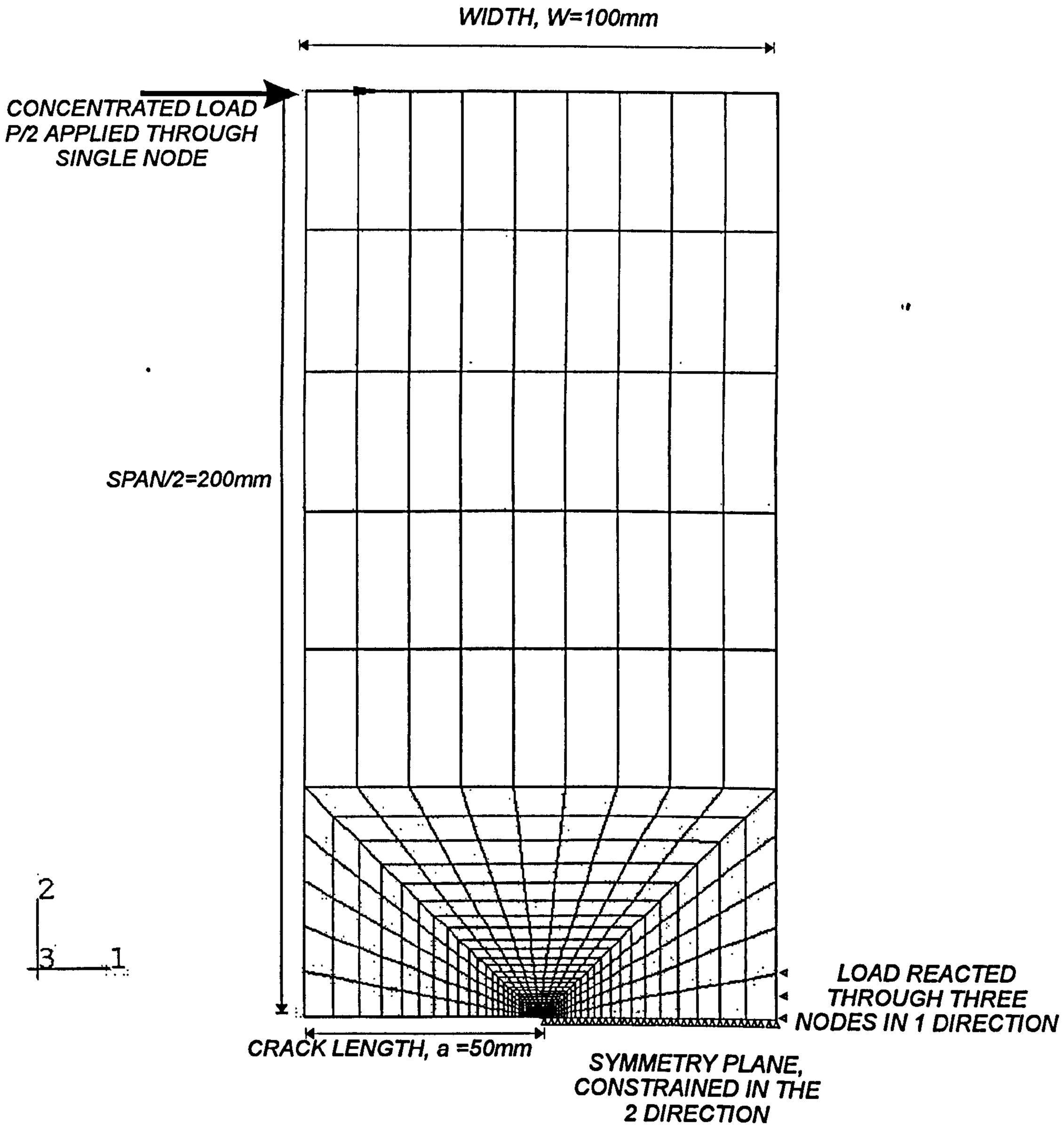

Figure 5.4. Overiview of Single Edge Notch Bend Specimen Finite Element Model showing constraints and loading points.

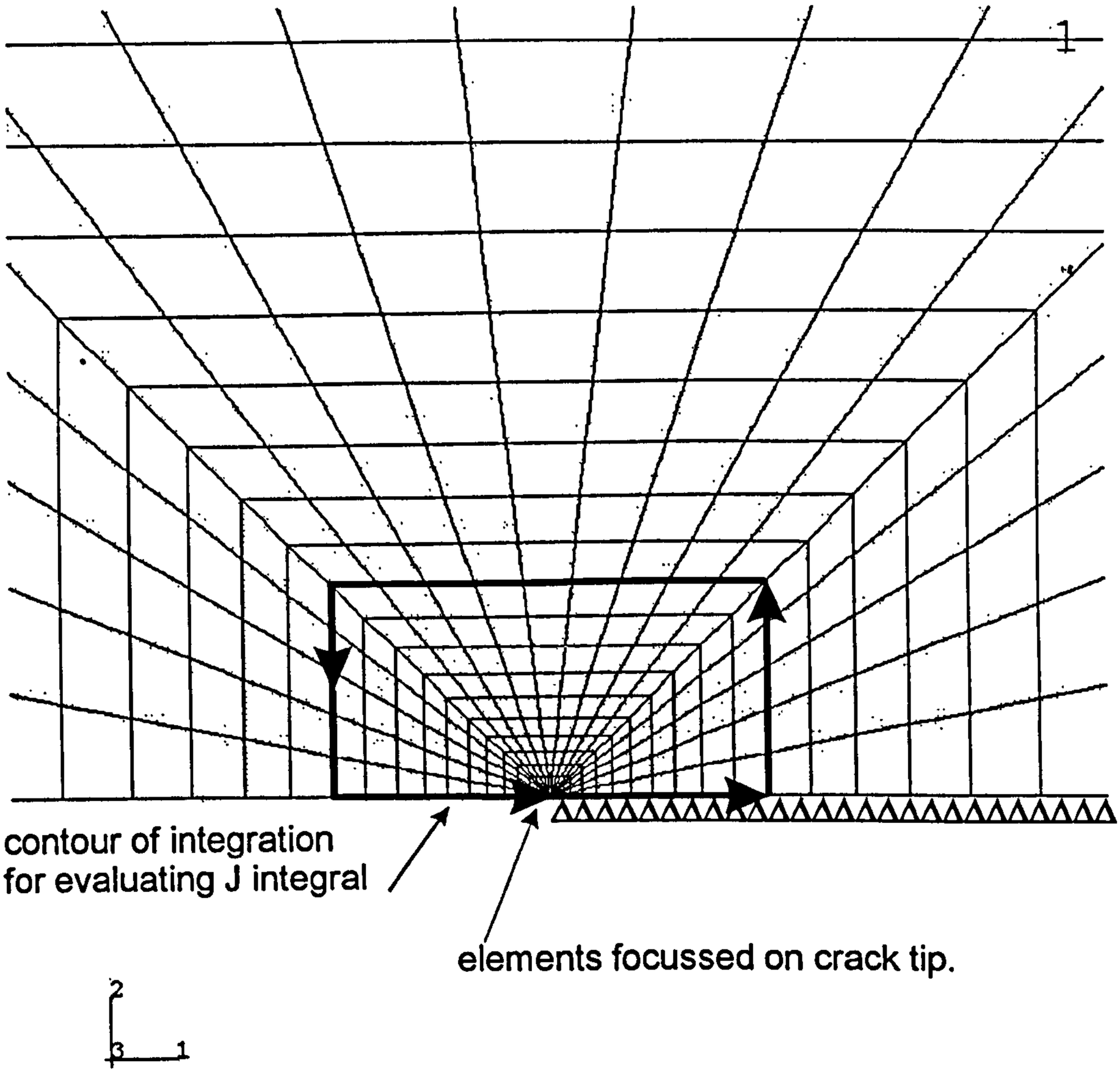

Figure 5.5. Crack tip detail used in Single Edge Notch Bend specimens with sharp crack tip.

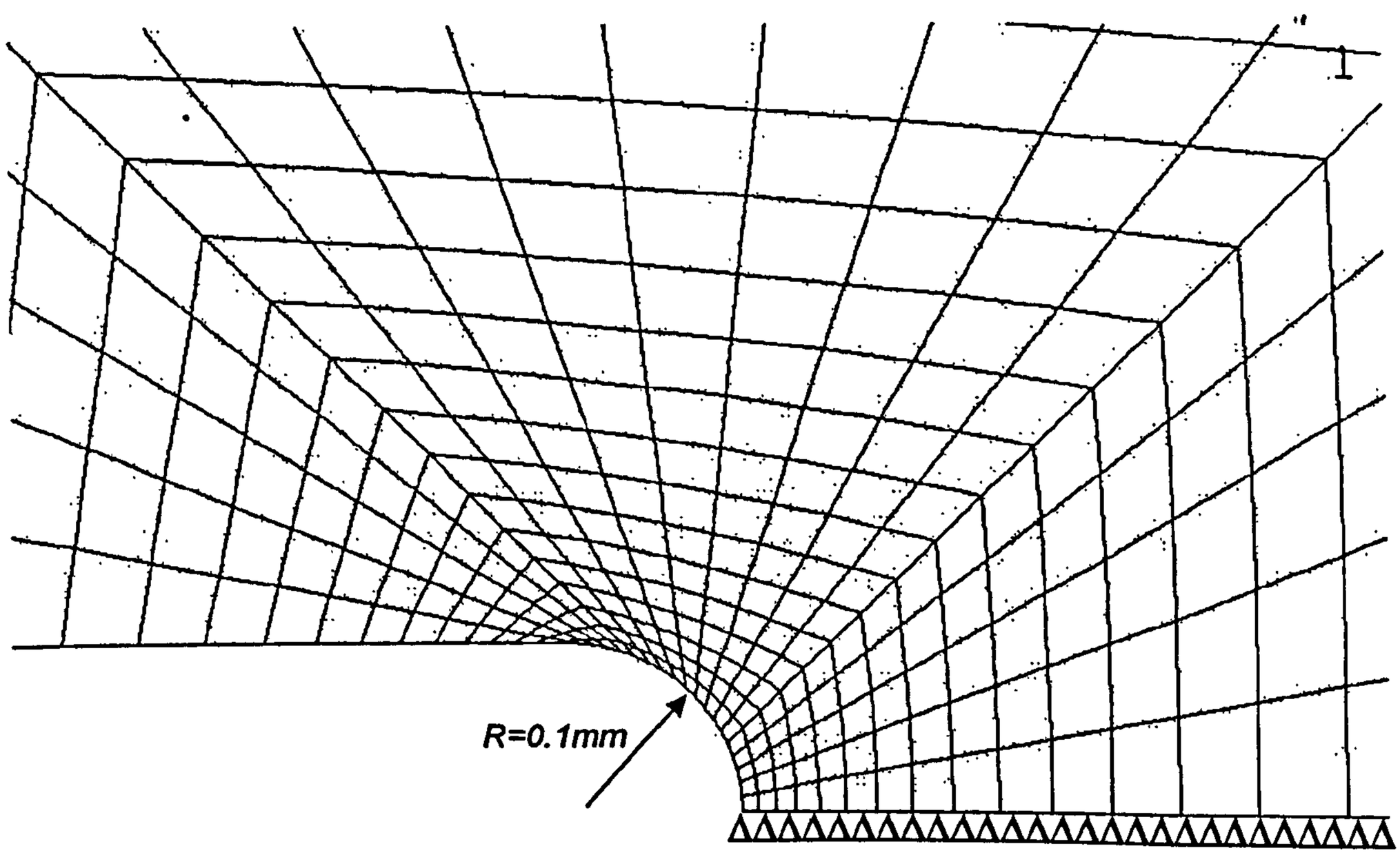

Detail of crack tip of finite radius = 0.1mm. crack tip element size=0.005mm

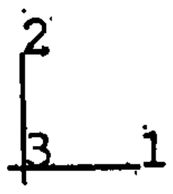

Figure 5.6. Detail of SENB blunt notch crack tip showing finite radius and element size at crack tip.

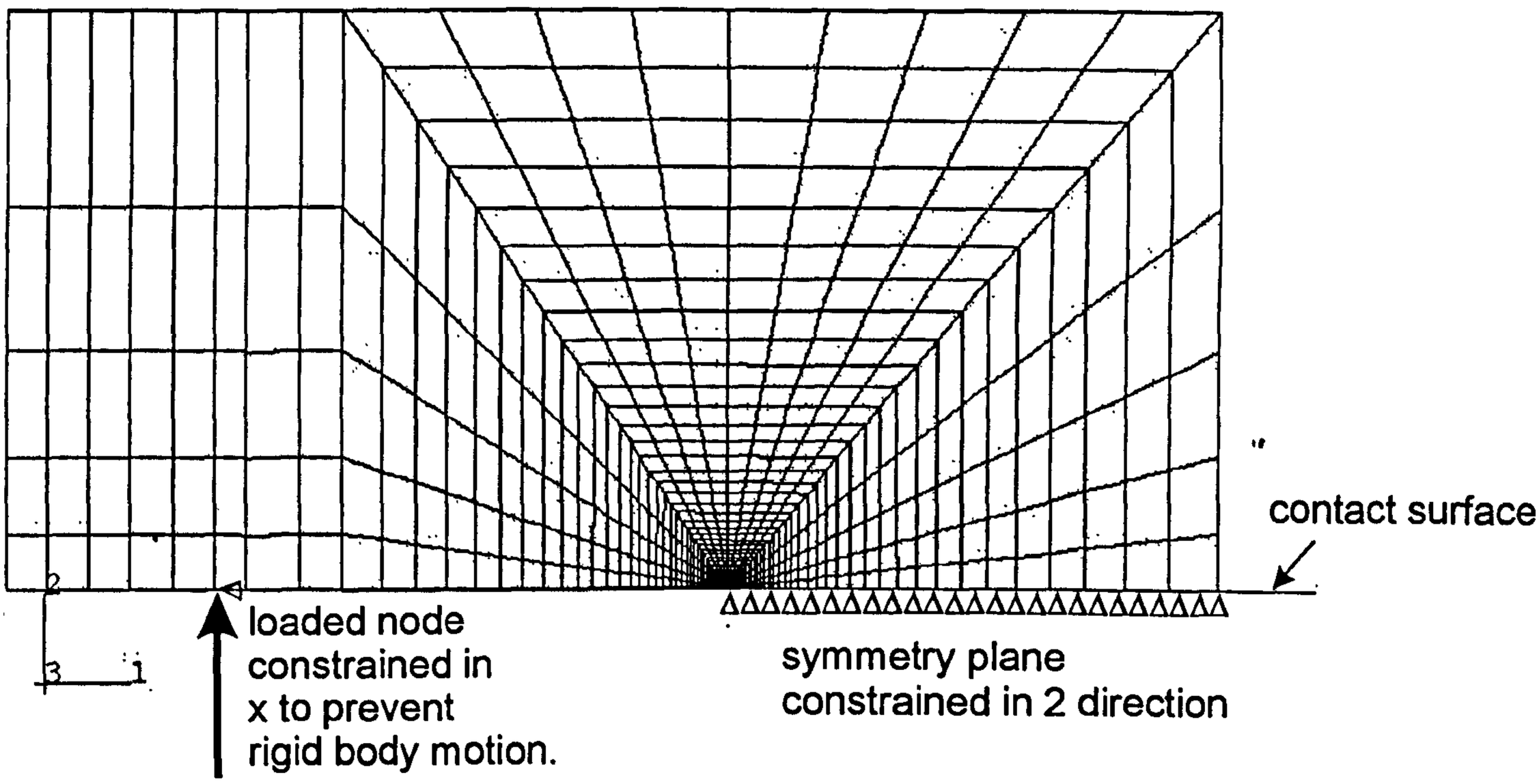

Figure 5.7. Overview of Compact Tension Specimen Finite Element model showing constraints and loading points.

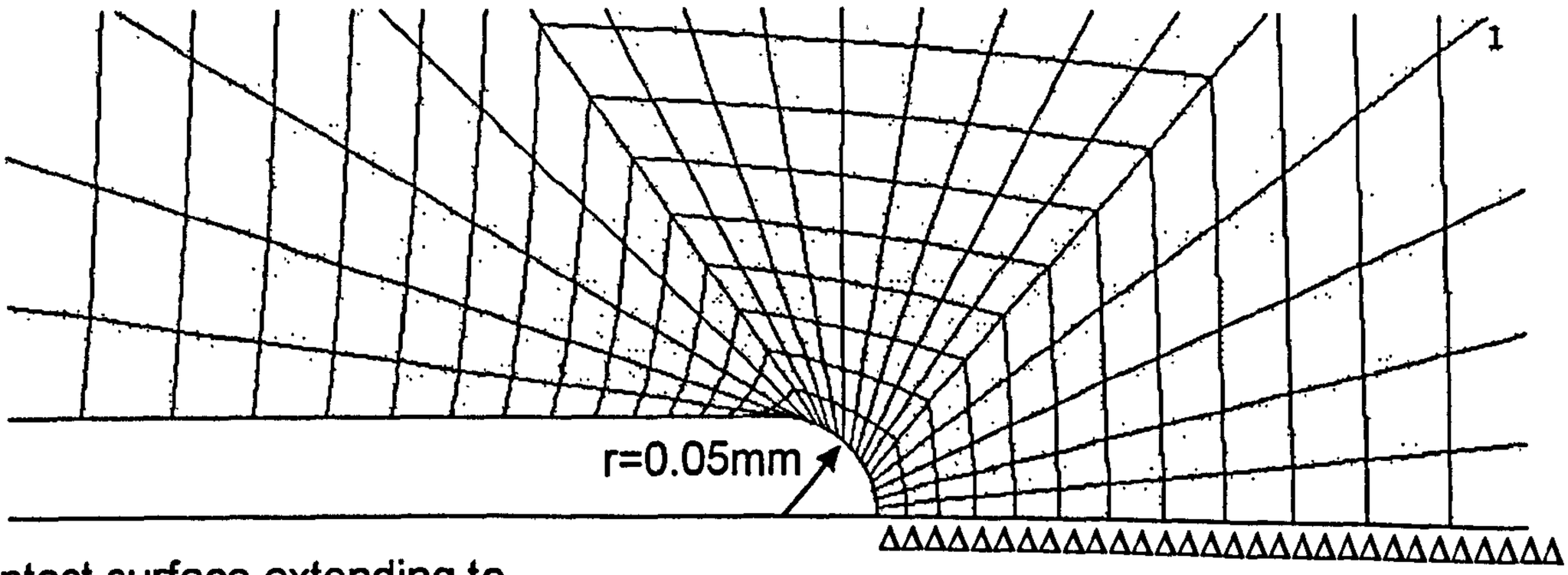

Figure 5.8. Detail of crack tip area of blunt notched CT specimen.

Figure 5.9. Plane strain, Isotropic σ_{22} at maximum load, compared to the HRR prediction and WIFES prediction.

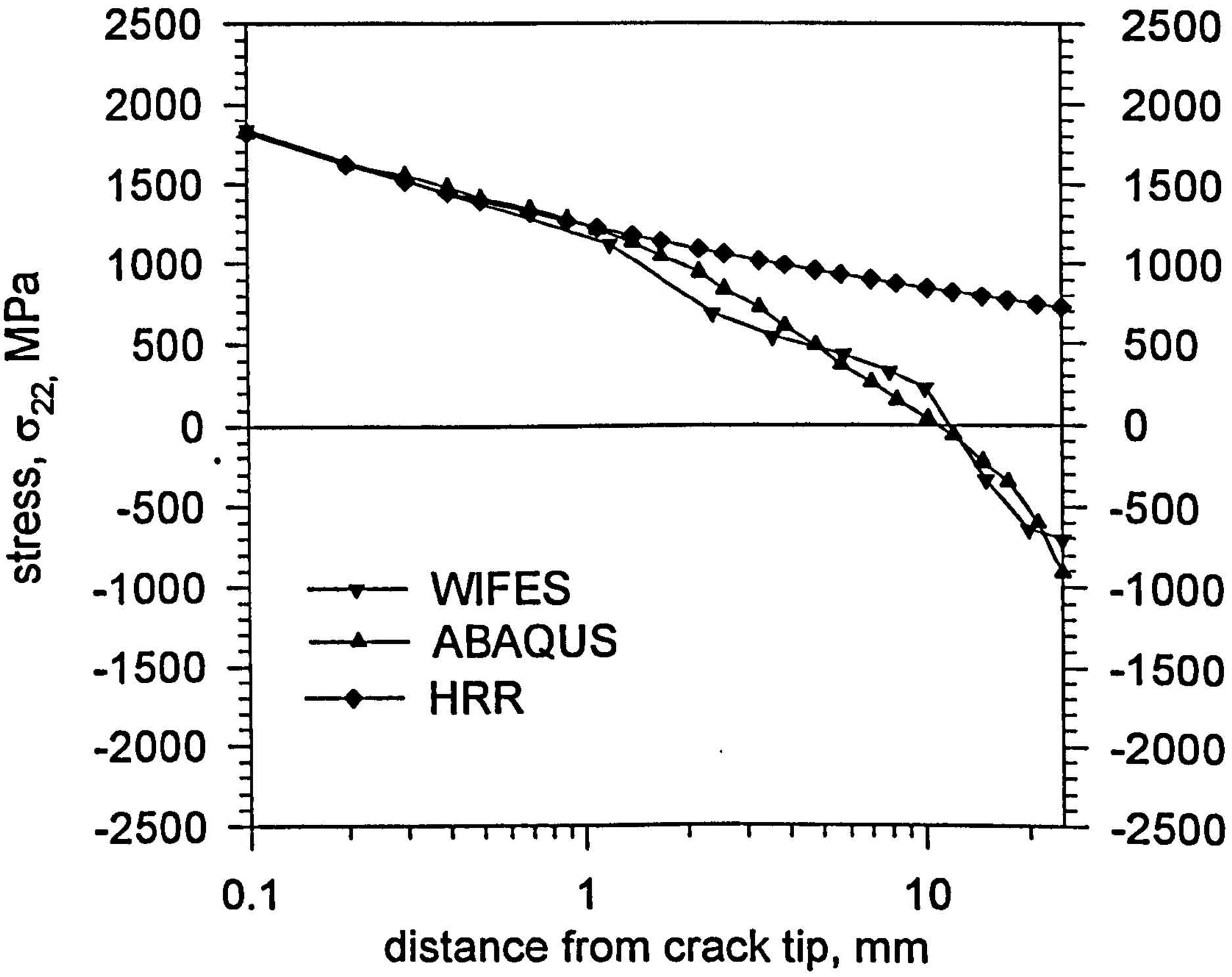

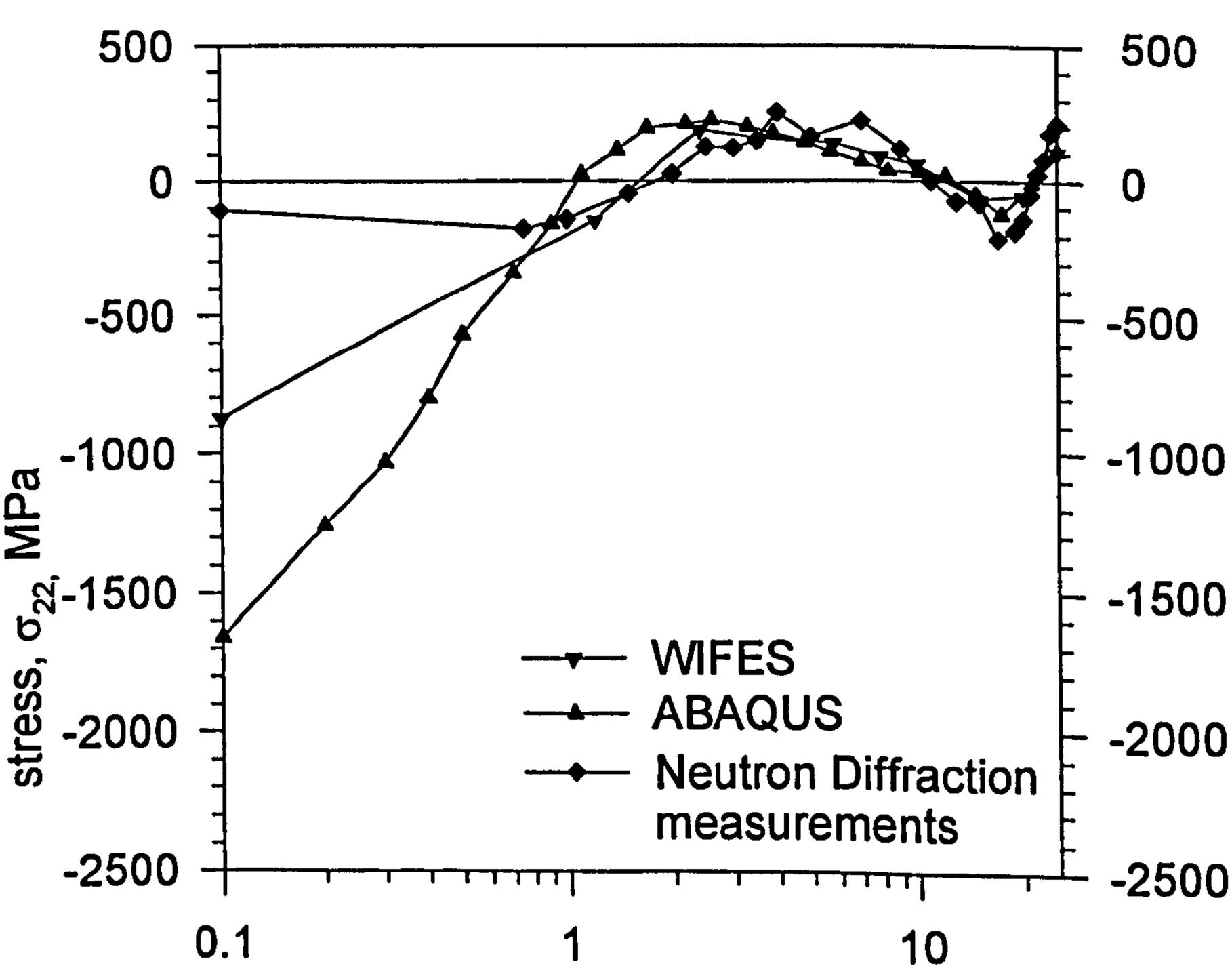

Figure 5.10. Plane strain, Isotropic σ_{22} at zero load, following unloading, compared to Neutron Diffraction (ND) Measurements

Figure 5.11. Comparison Between Isotropic and Kinematic Stress Distributions at Maximum Load.

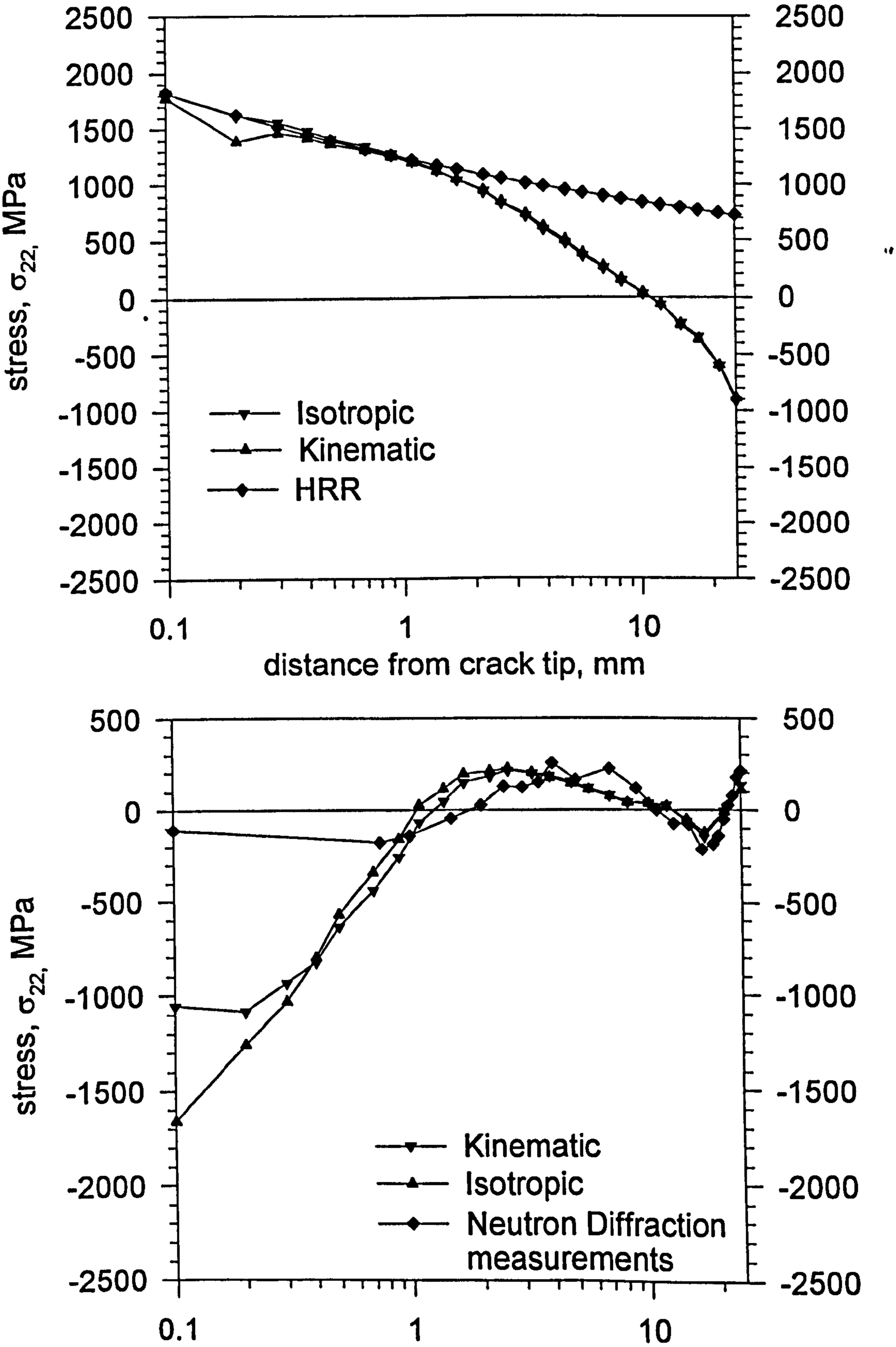

Figure 5.12. Comparison between Isotropic, Kinematic and ND residual stress distributions.

Figure 5.13. Plane stress, σ_{22} at maximum CMOD, compared to HRR prediction for plane stress.

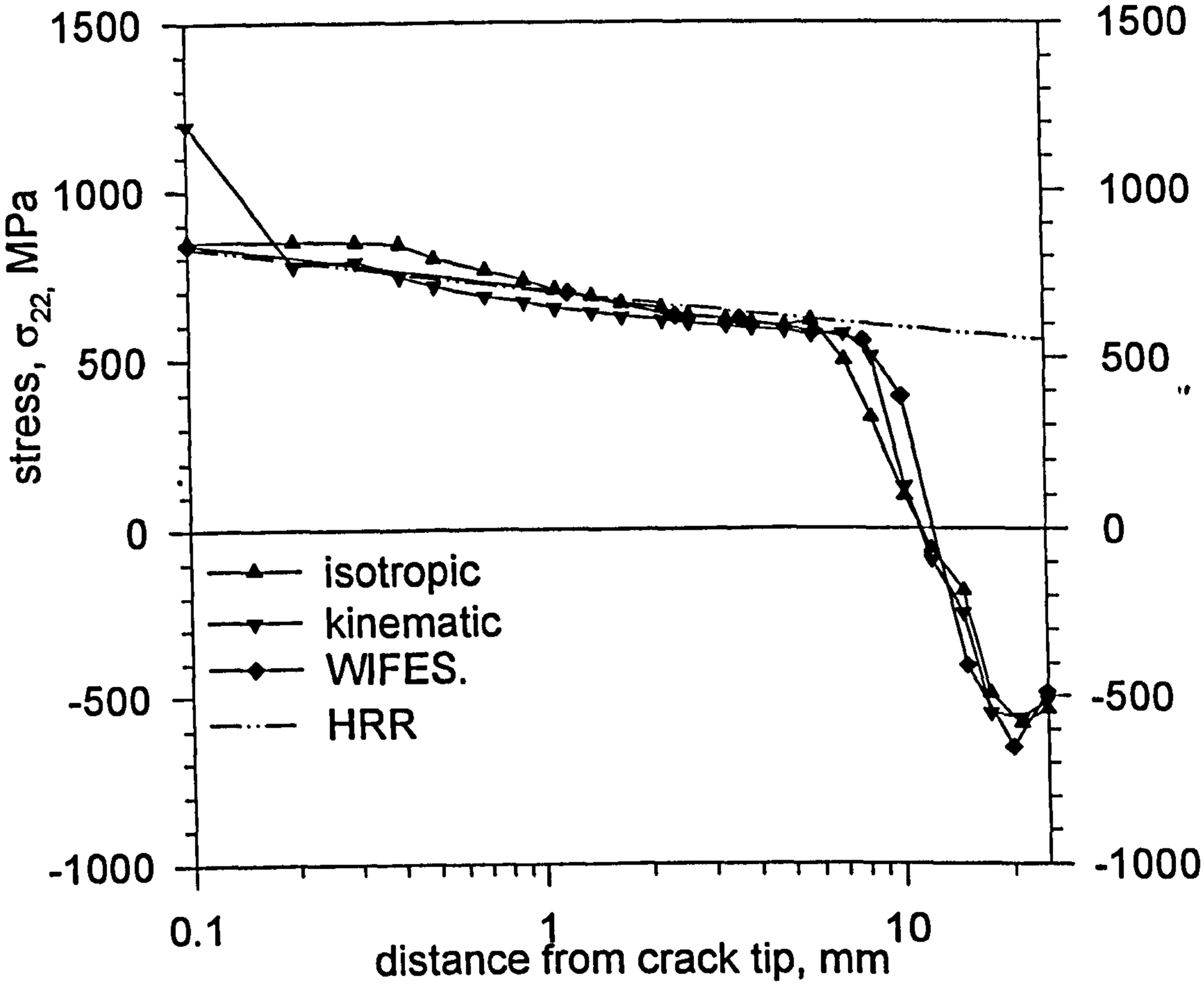

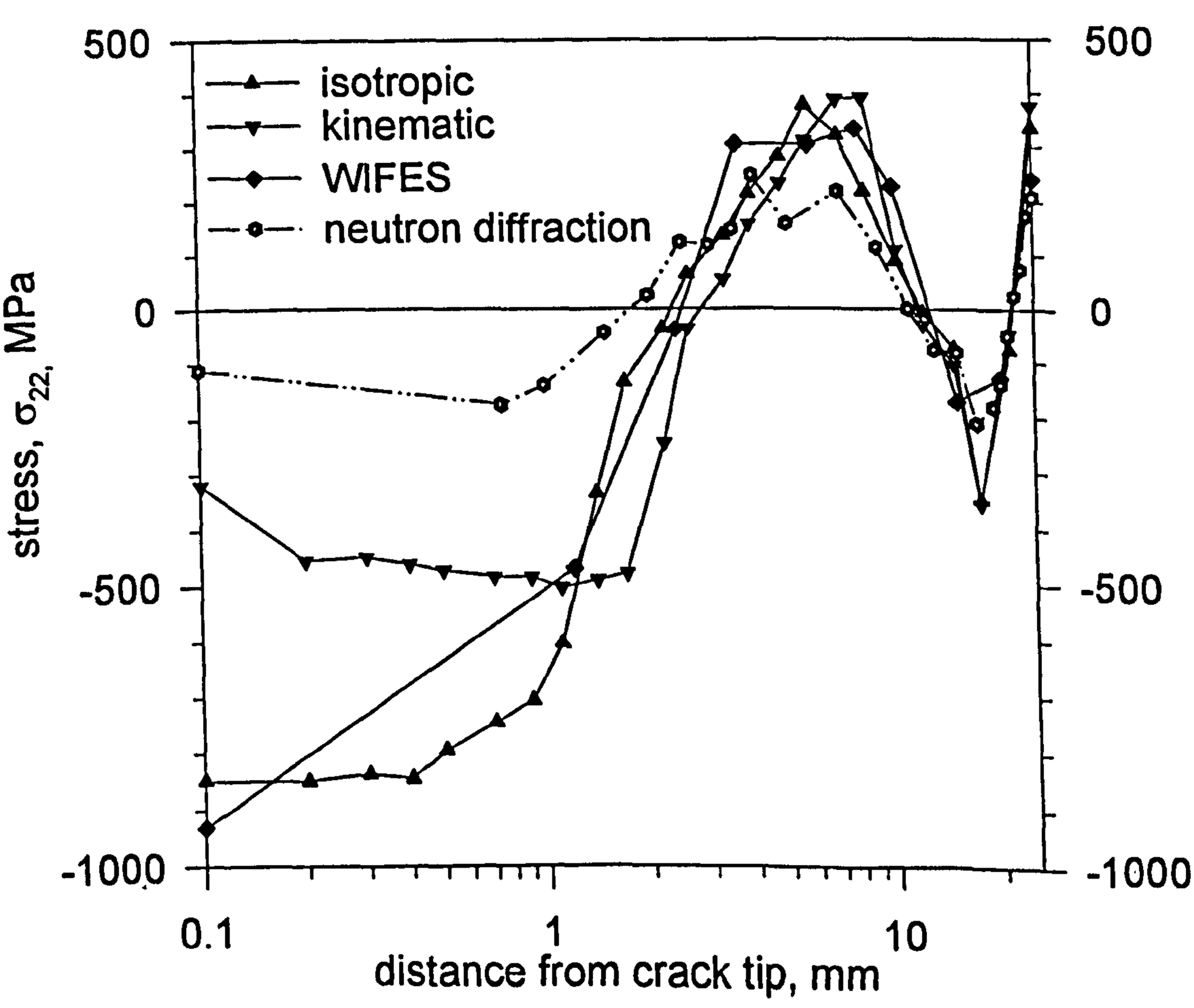

Figure 5.14. Plane stress, residual stress distributions, compared to neutron diffraction measured residual stresses.

Figure 5.15. As-Received fracture stress distribution and HRR field.

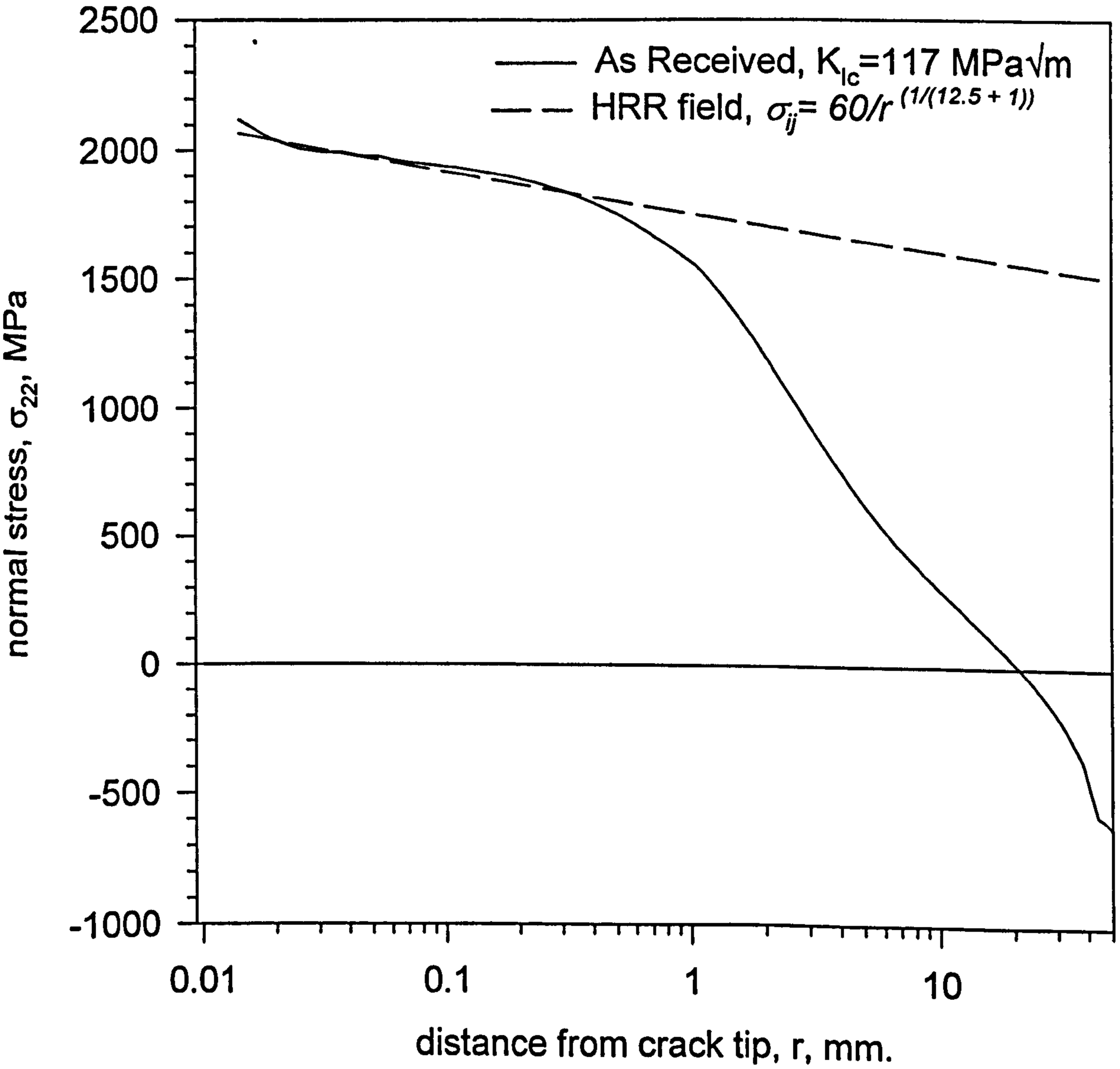

Figure 5.16. Path independent *J* integrals obtained for as - received fracture in 50mm thick SENB specimen.

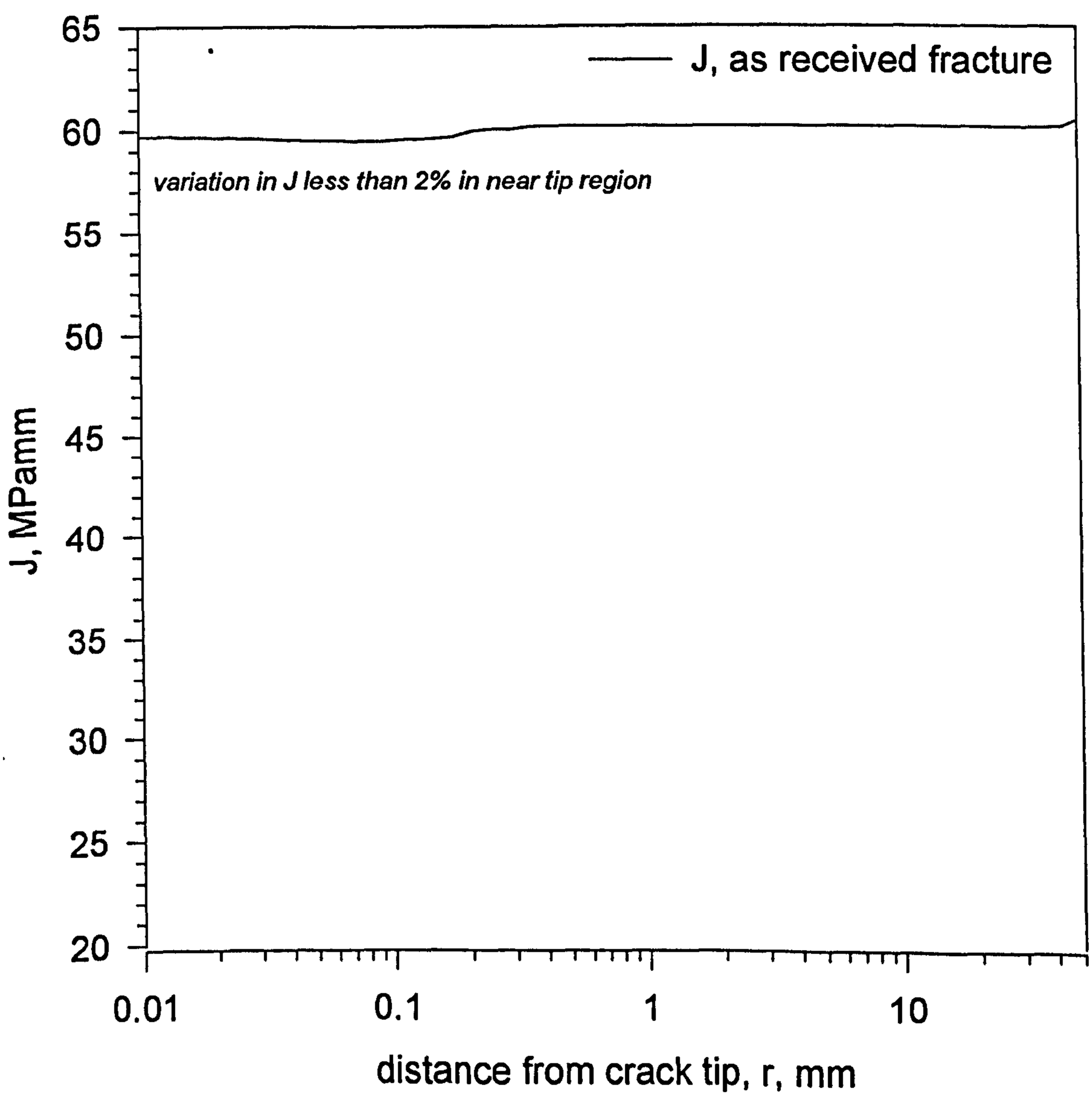

Figure 5.17. Proof load normal stress distributions for load cases *A* and *B*.

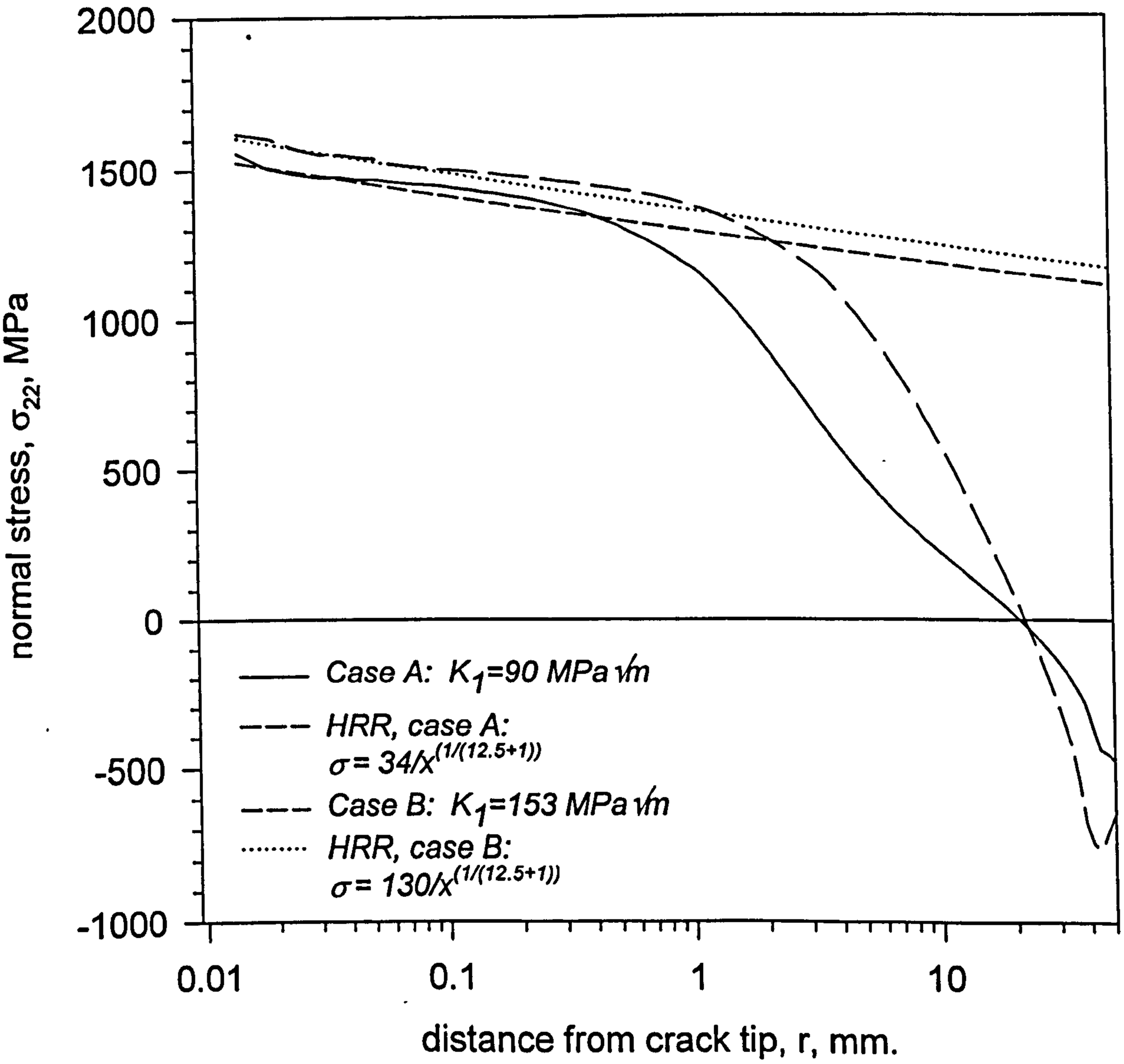

Figure 5.18. Plastic zones sizes at maximum preload, zero load following unloading and fracture for case A.

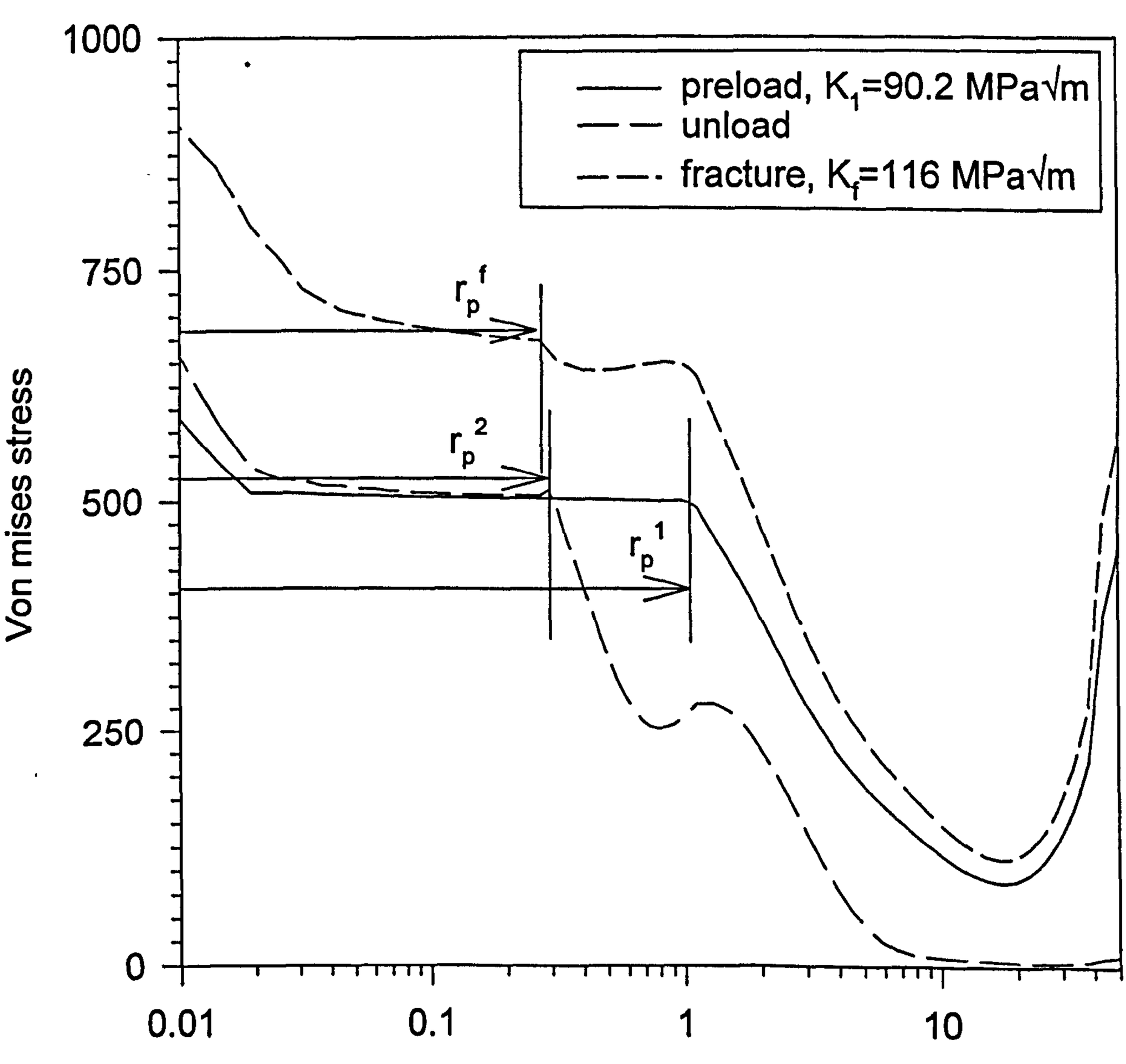

Figure 5.19. Plastic zones sizes at maximum preload, zero load following unloading and fracture for case B.

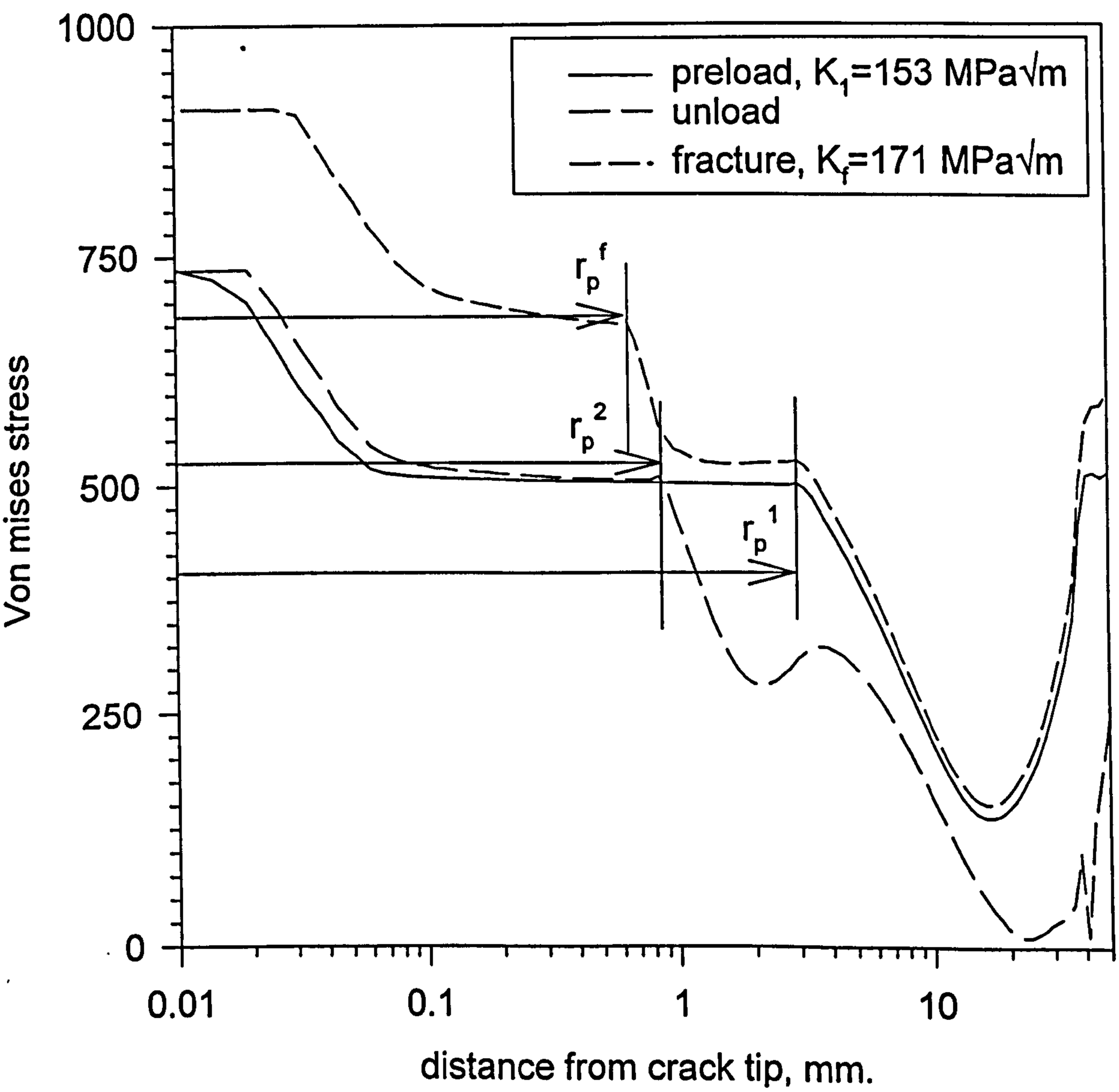

Figure 5.20. Comparison between residual stress states for different preload levels *A* and *B*.

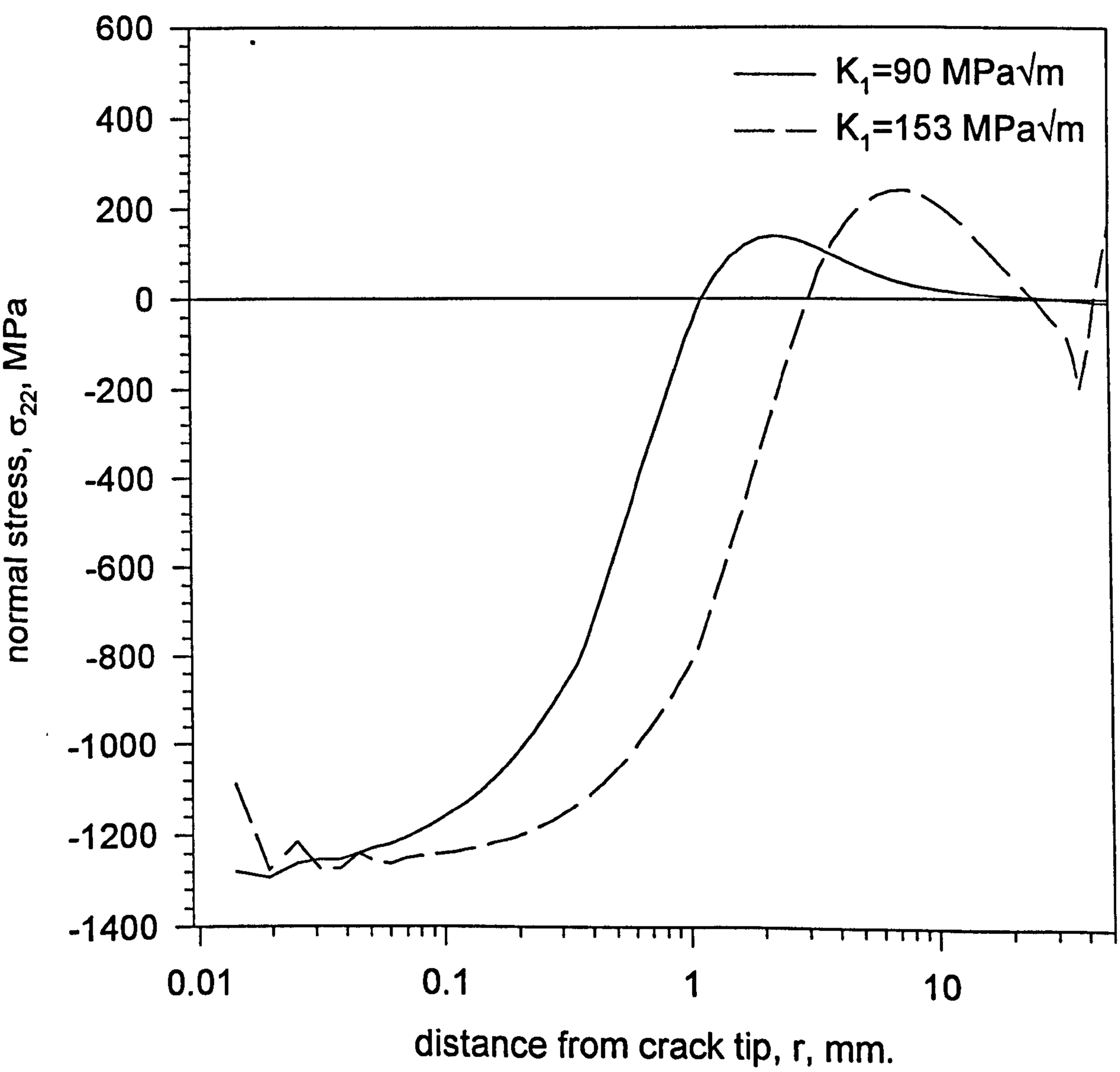

distance from crack tip, r, mm.

Figure 5.21. As-received and warm prestressed fracture stress fields compared with analytical HRR stress fields.

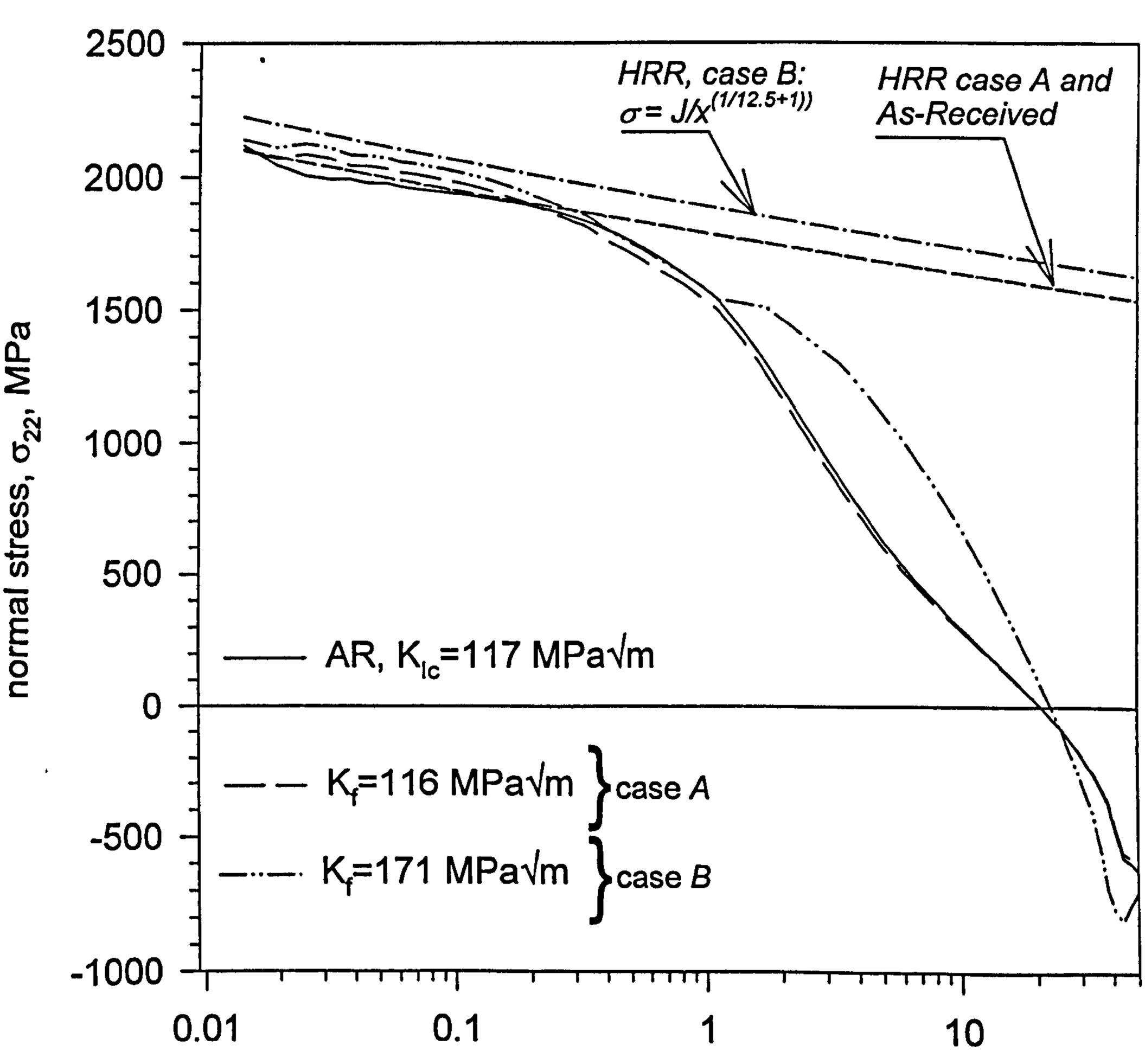

distance from crack tip, r, mm.

Figure 5.22. *J* Integral estimates as a function of contour distance from crack tip showing regions of path dependence and path independence due to residual stresses.

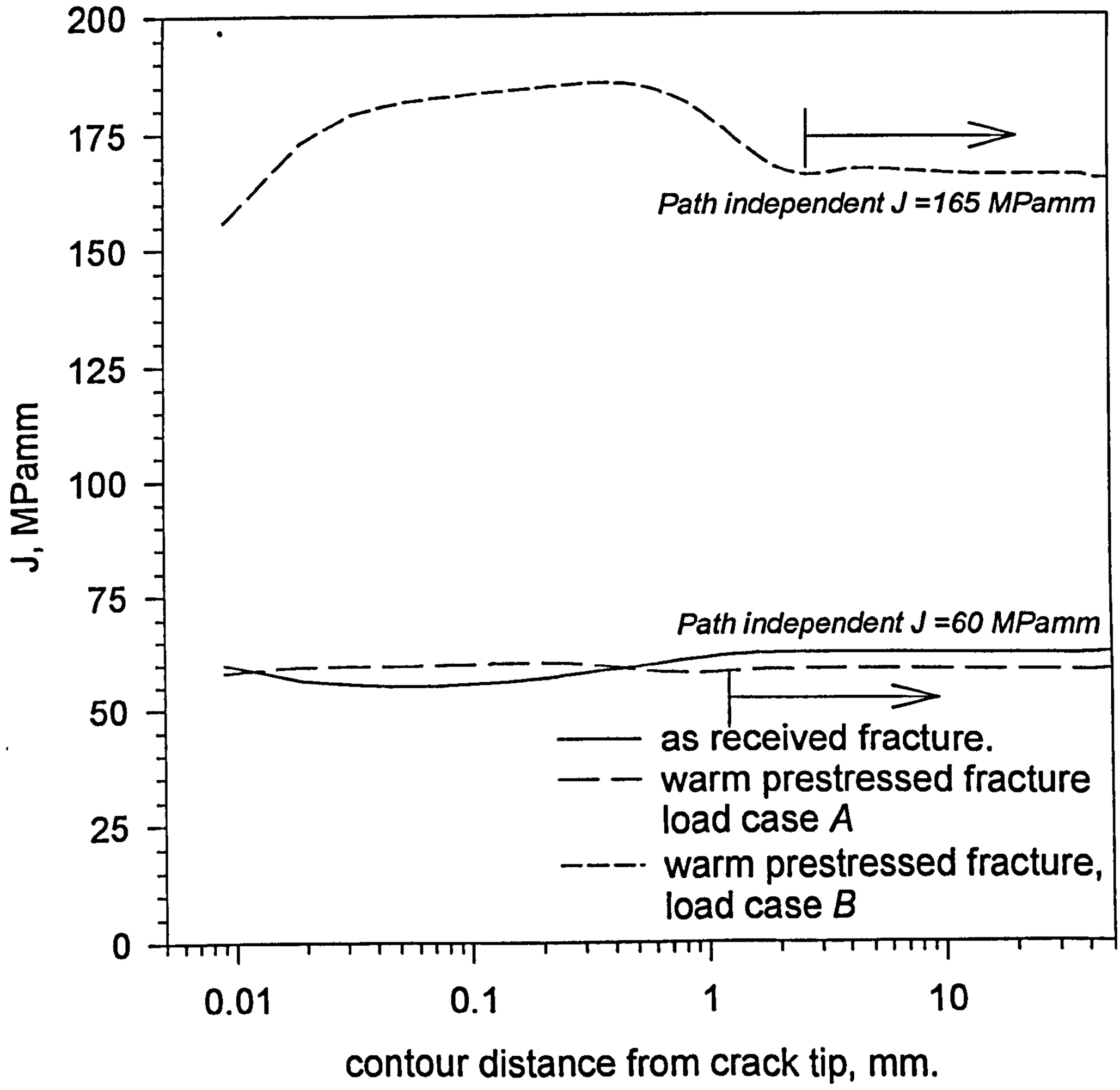

Figure 5.23. Normal stress distribution of load case B at experimental fracture load and at as-received fracture load, compared to the as-received stress distribution.

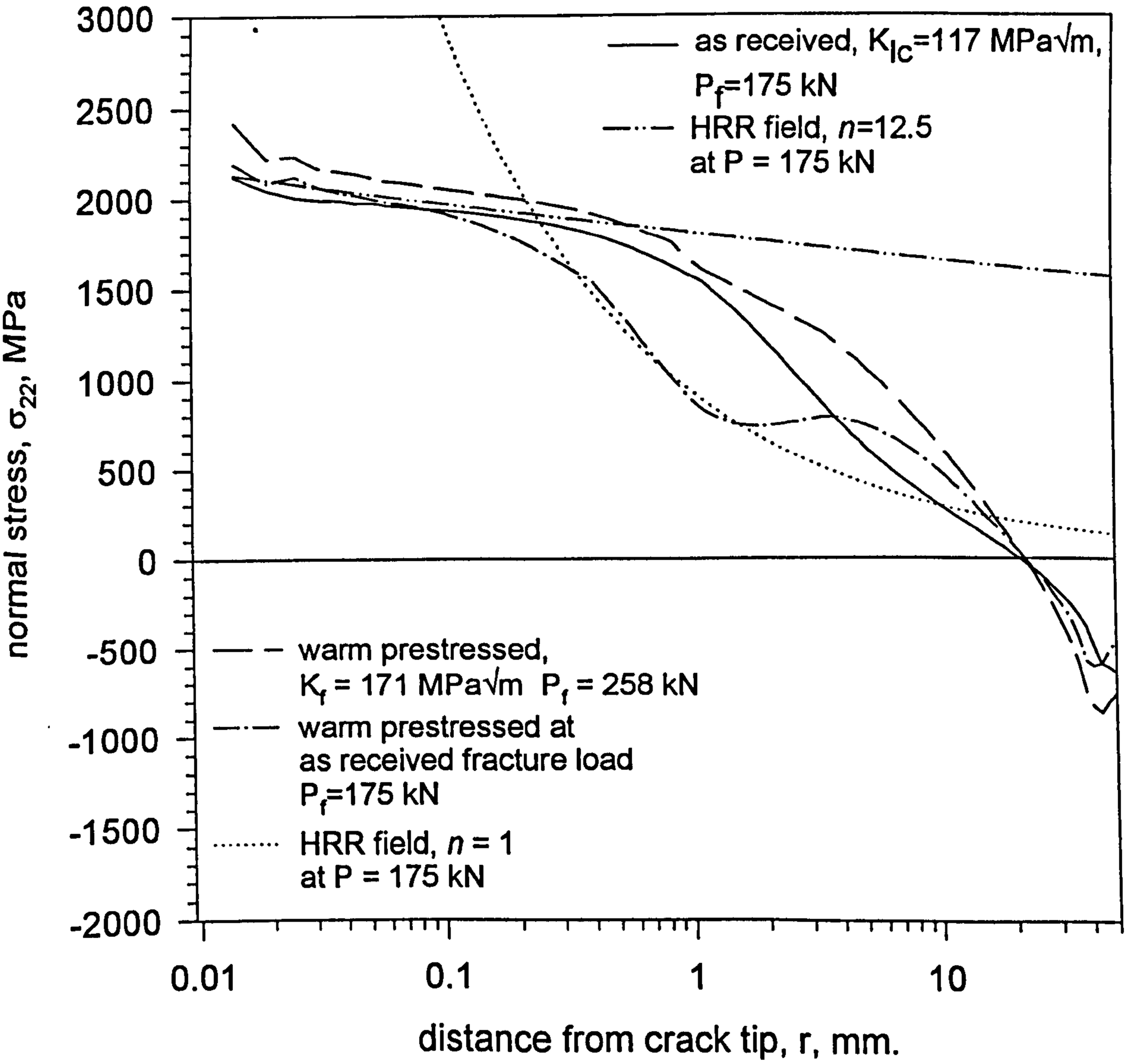

Figure 5.24. Residual stress distributions following preloads of 63.2, 95, 126.5 and 158 MPa√m.

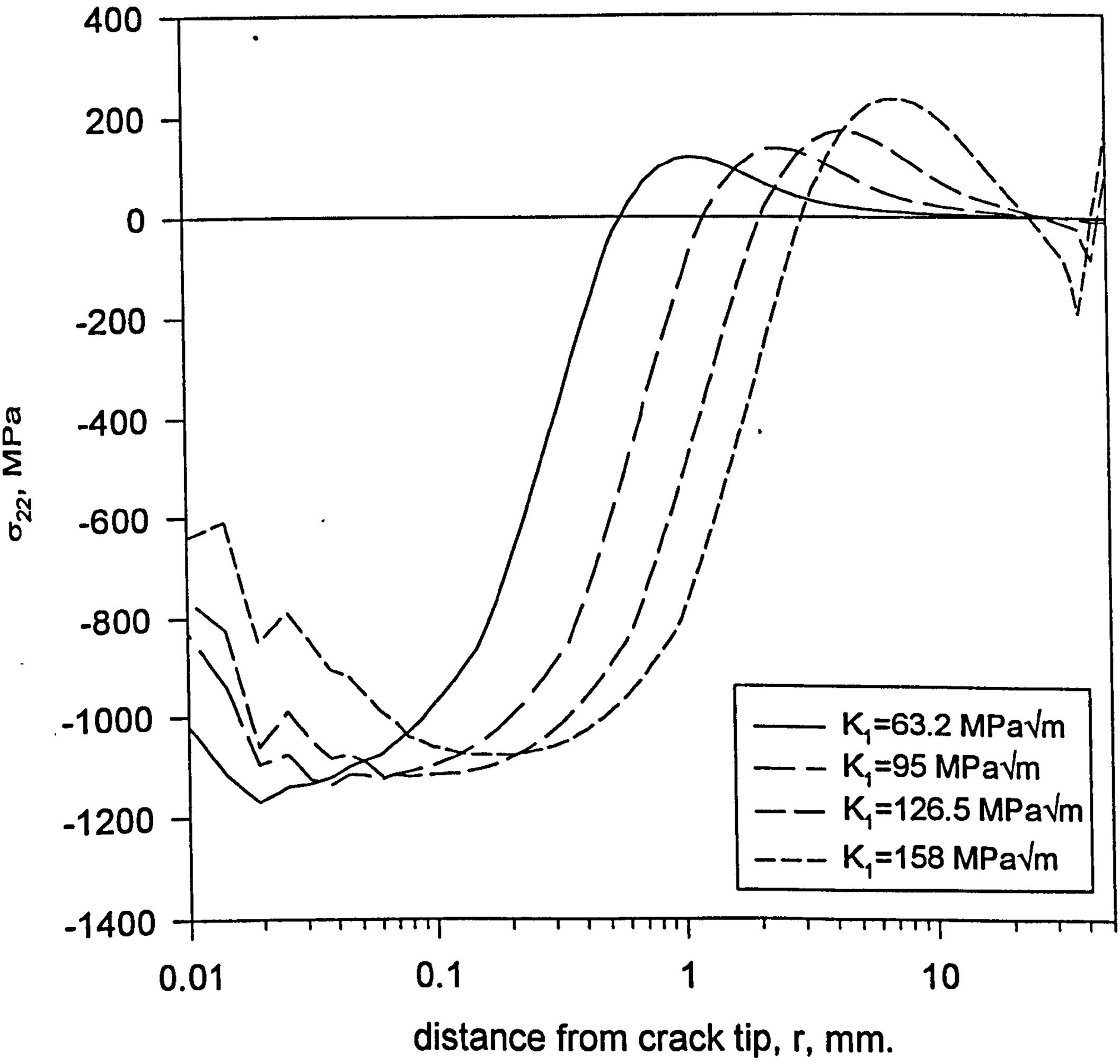

Figure 5.25. Normalised residual stress distributions following preloads of 63.2, 95, 126.5 and 158 MPa√m.

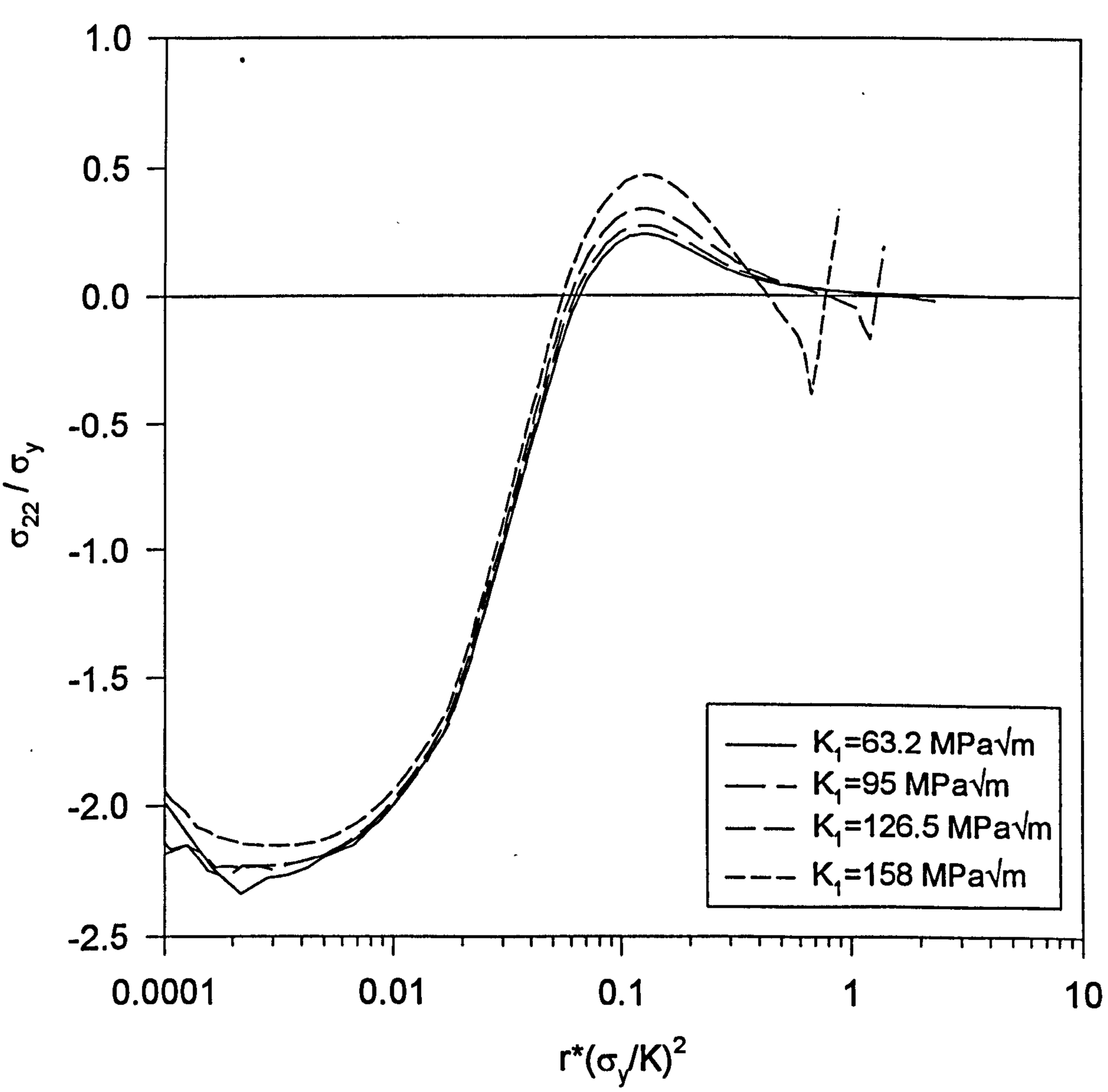

Figure 5.26. Stress distribution on reloading to fracture compared to critical stress distribution defined by K_{1c} (= 47.4 MPam)
Proof load K_1 =63.2 MPam, K_f=66 MPam

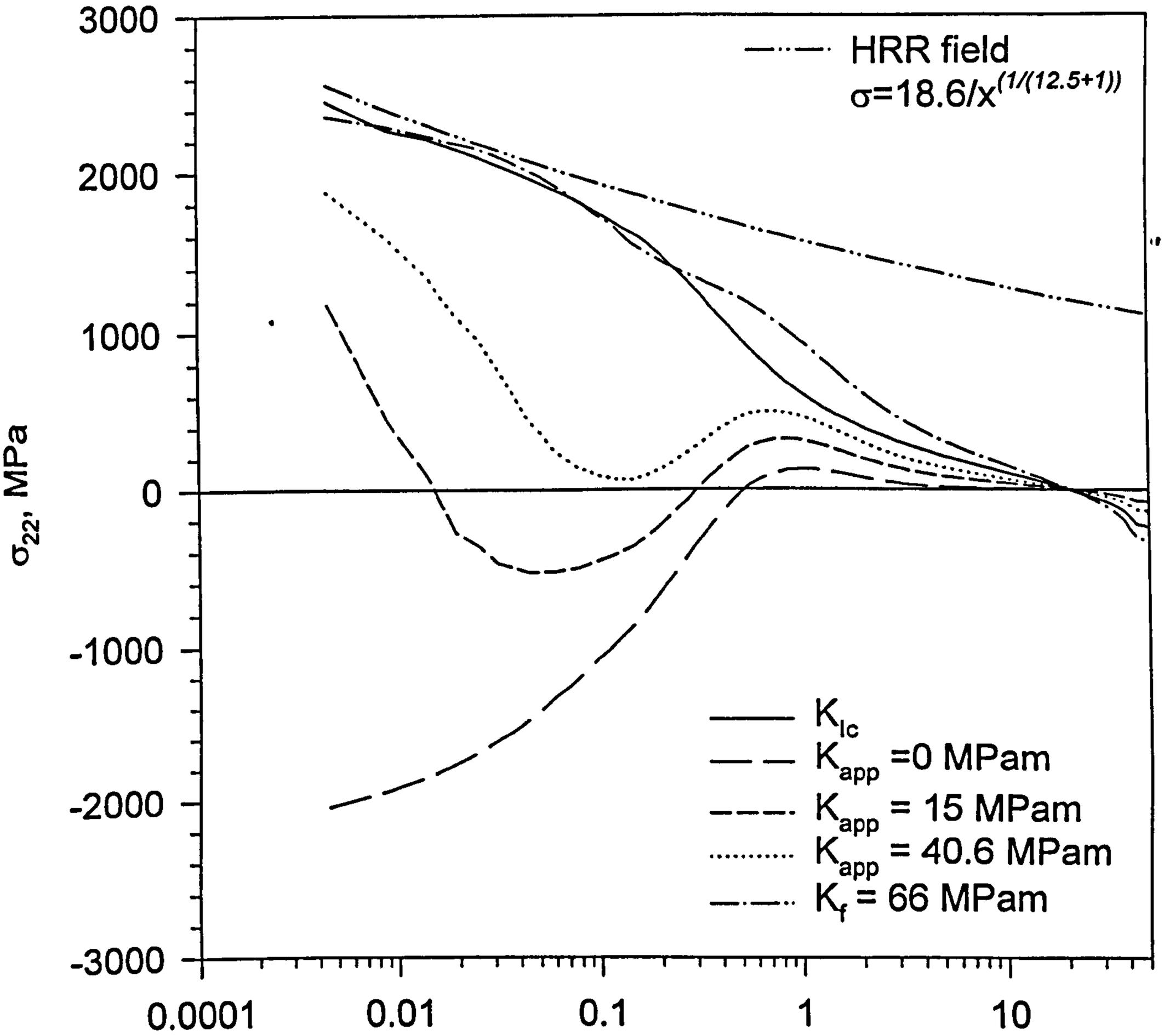

Figure 5.27. Comparison between failure stress intensity factors based on load and *J* integral estimates obtained from FEA.

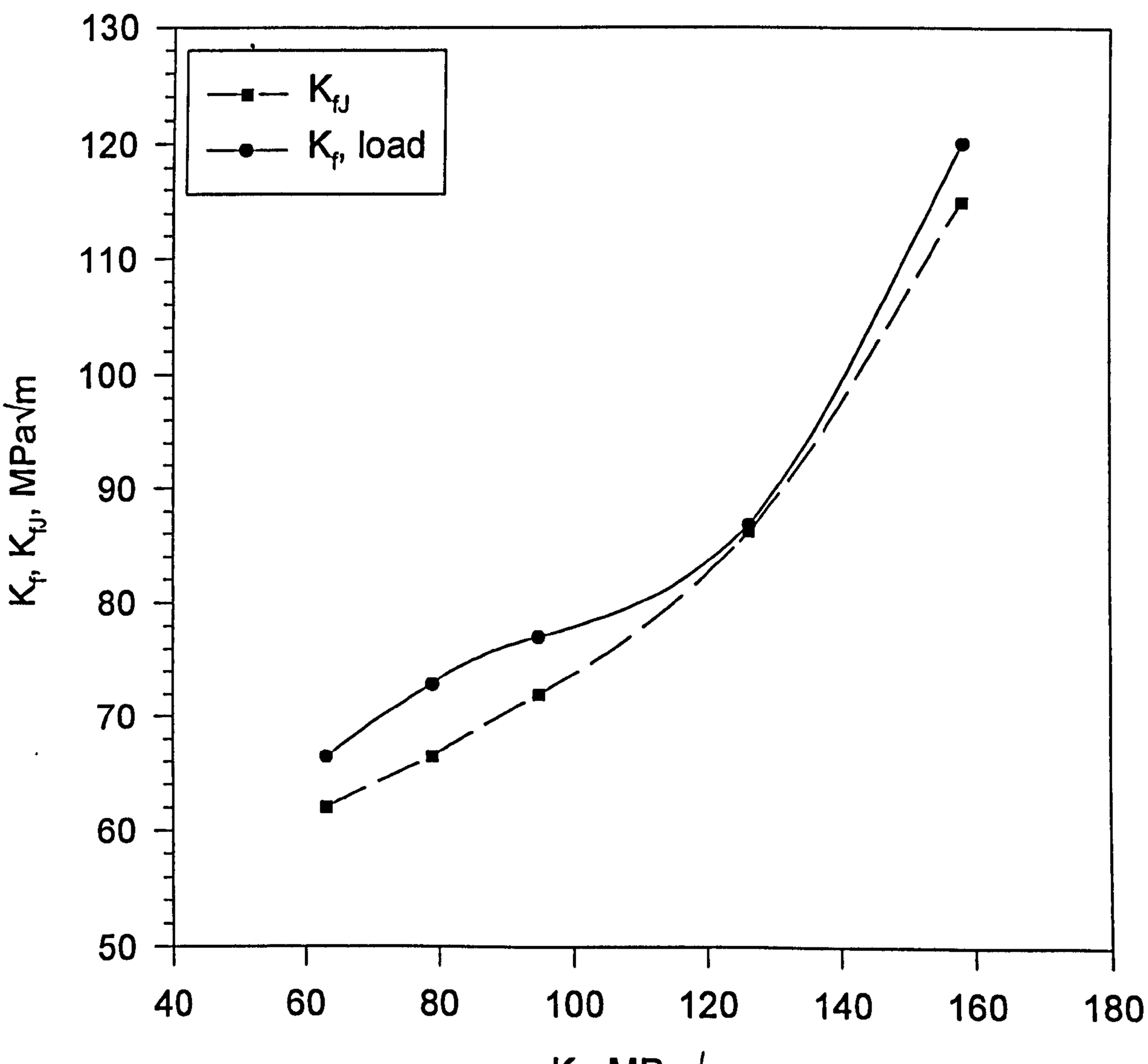

Figure 5.28. K_f predictions obtained using stress matching technique for different toughness's at a single temperature, -120°C.

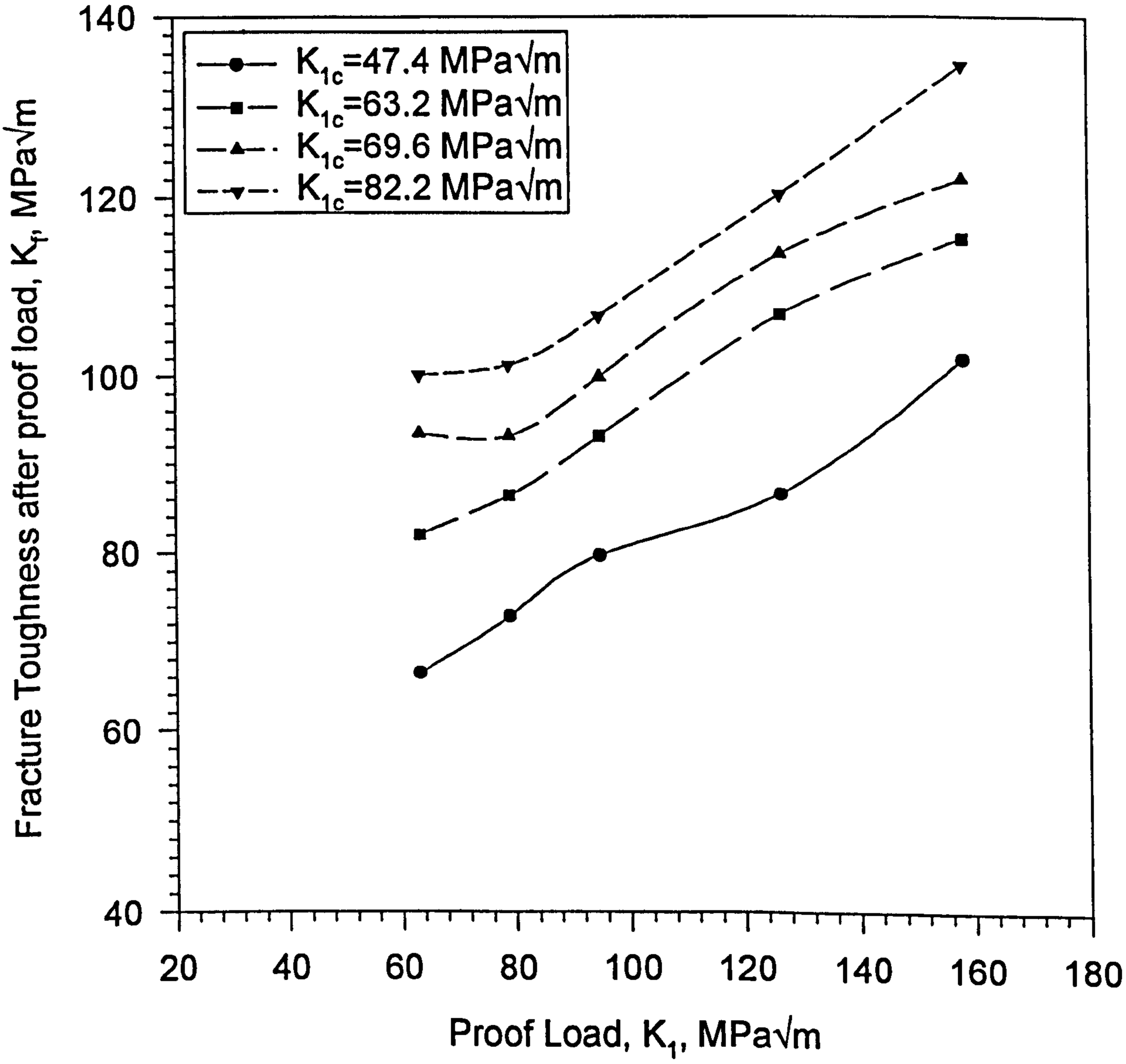

Figure 5.29. Comparison Between Isotropic and Kinematic Finite Element predictions of fracture for K_{1c}=47.4 MPa√m.

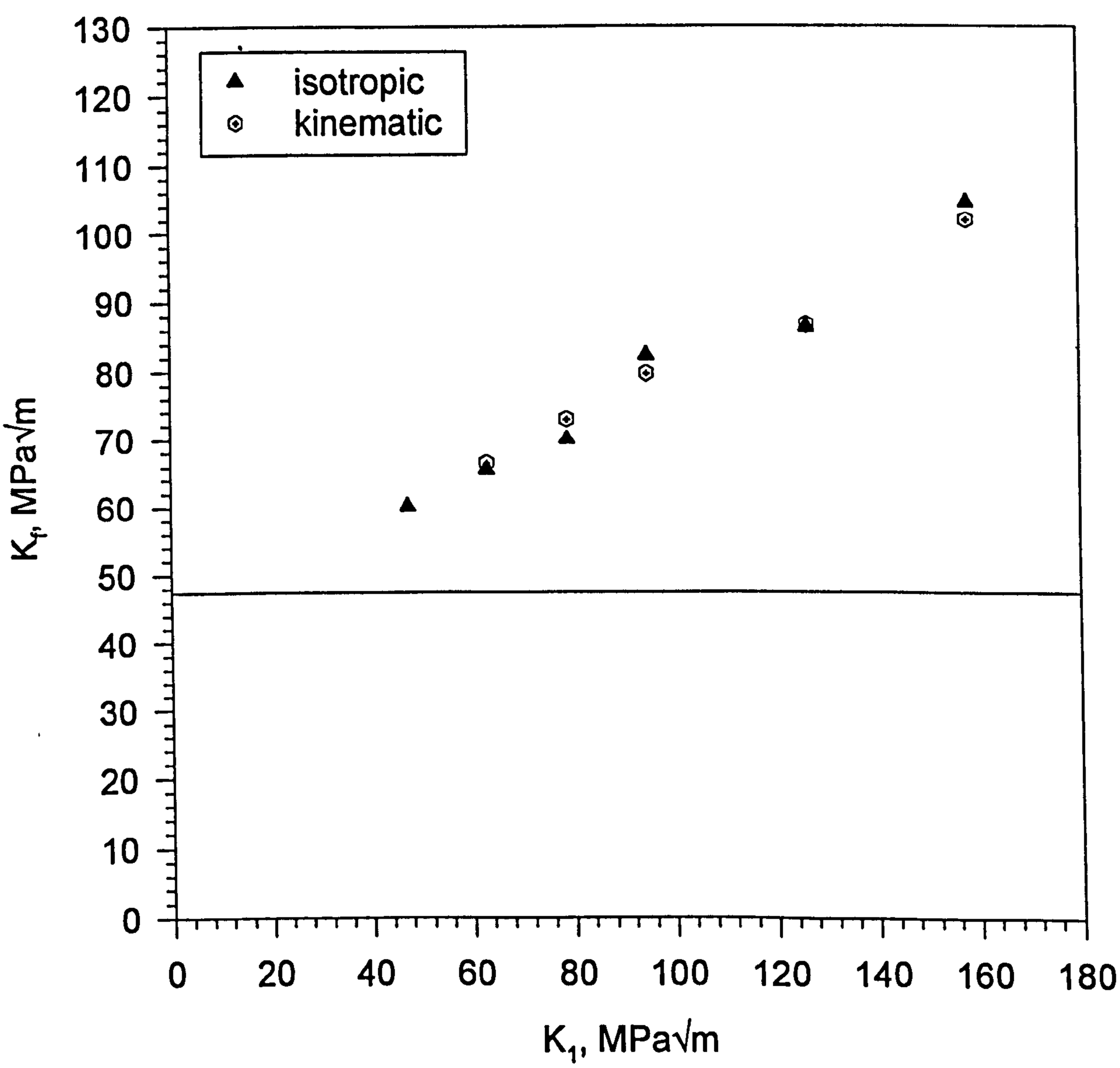

Figure 5.30. Influence of crack tip blunting on near tip fracture stress field.

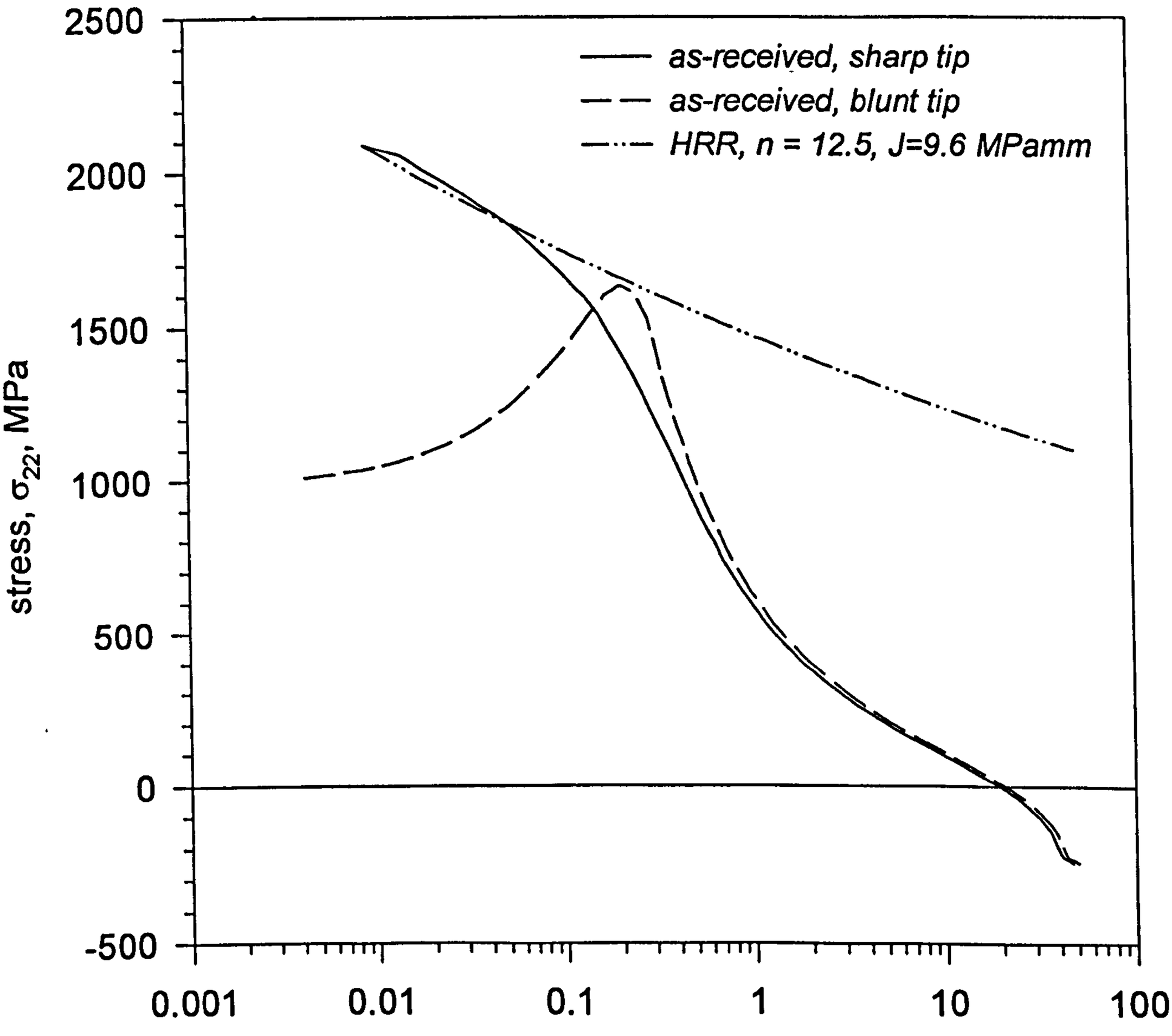

Figure 5.31. Path independent *J* integrals obtained for sharp and blunt crack tip fracture models.

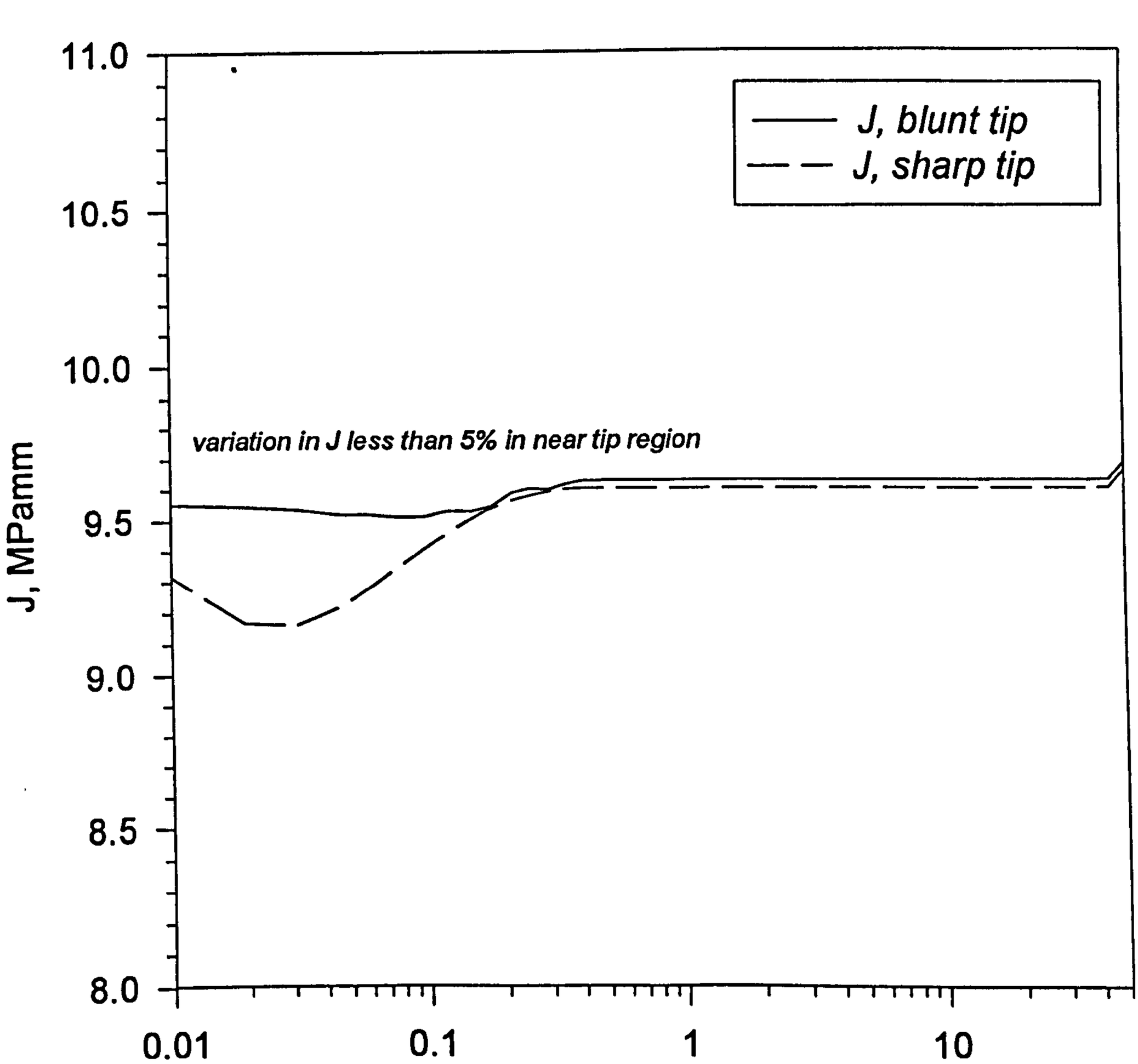

Figure 5.32. Influence of crack tip blunting on near tip fracture stress field.

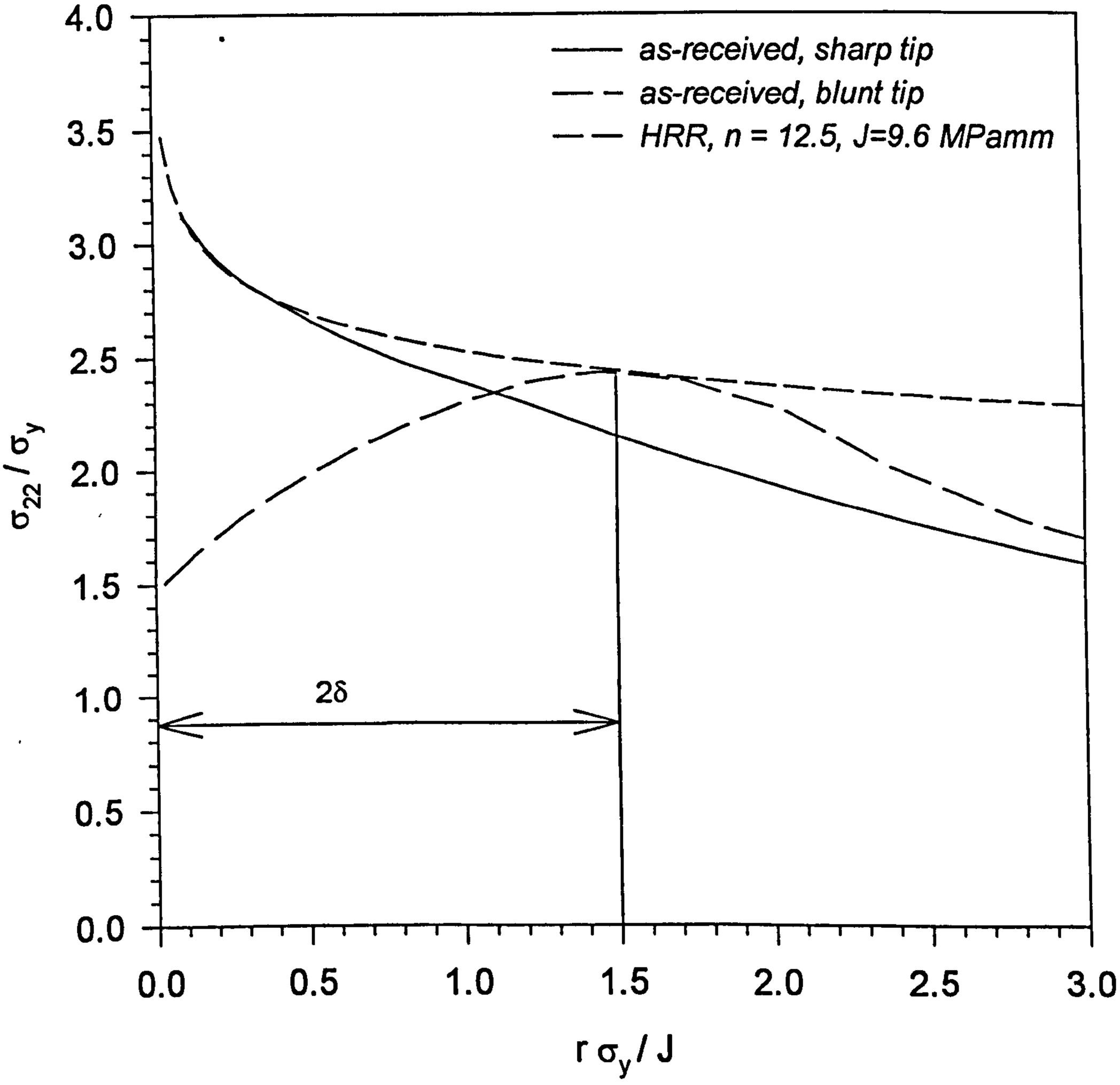

Figure 5.33. Stress distribution at maximum preload (K_1=63.2 MPam) and zero load following unloading

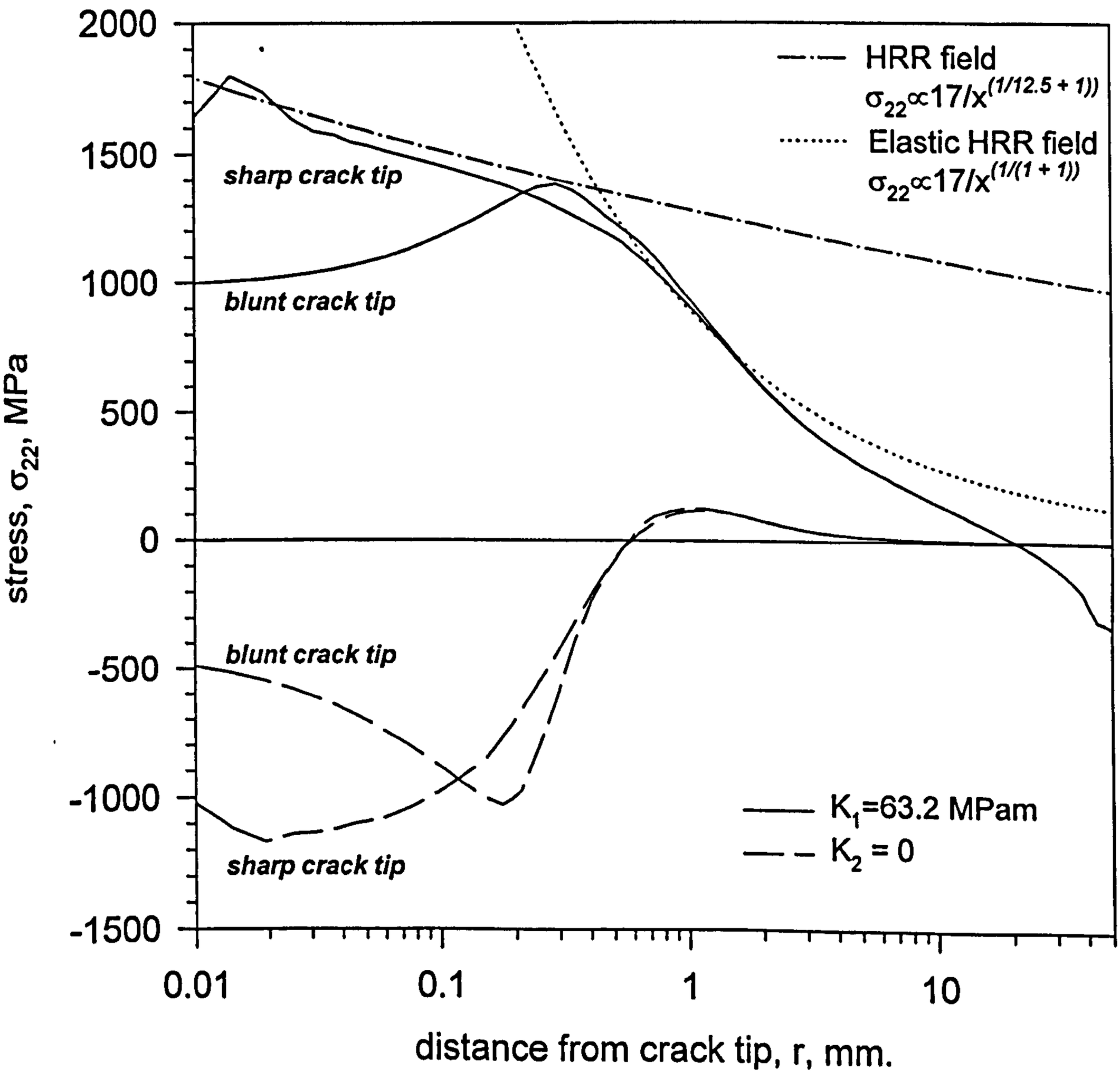

distance from crack tip, r, mm.

Figure 5.34. Stress distribution at fracture in blunt and sharp notched specimens

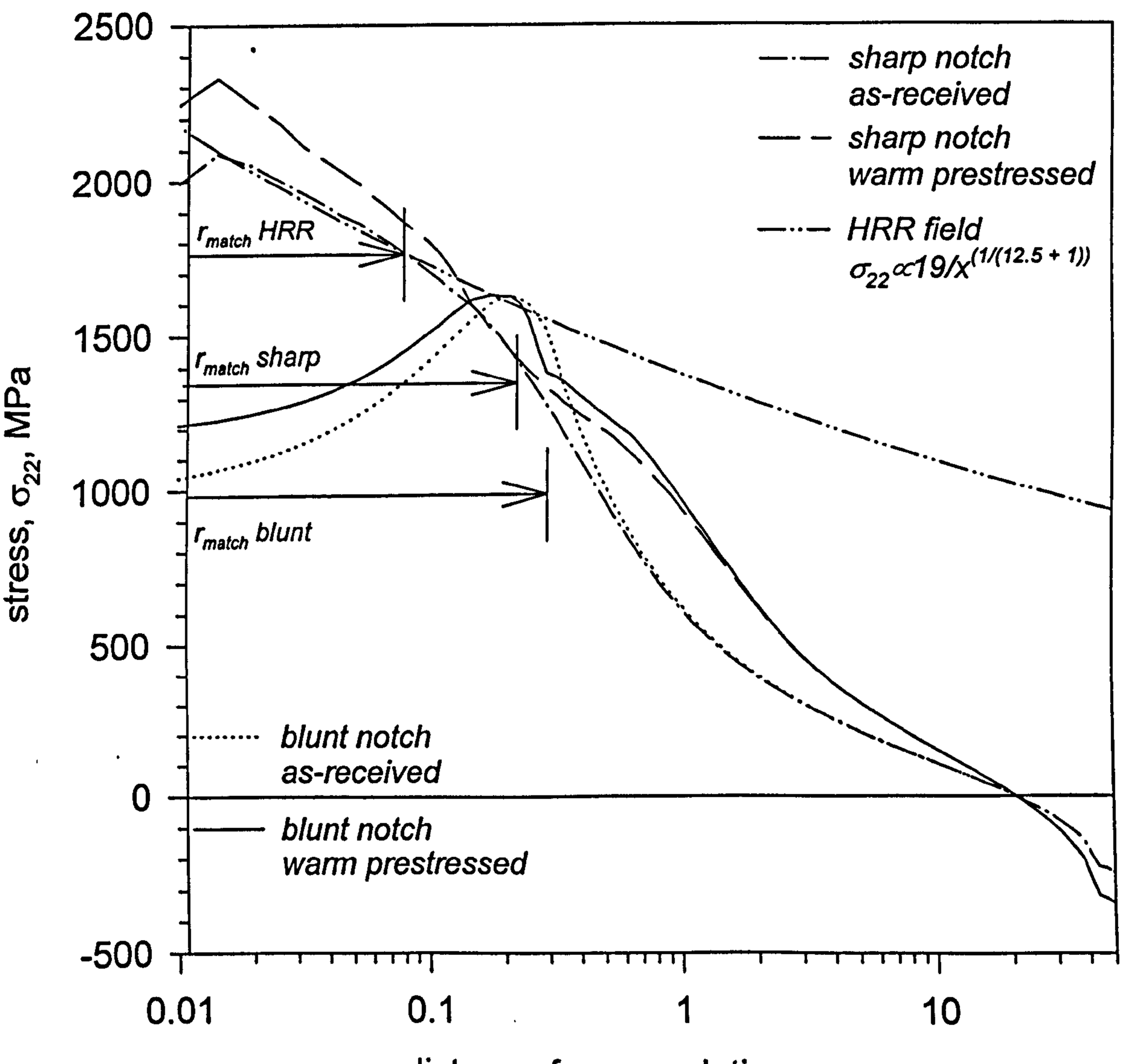

r_{match} HRR =0.12mm r_{match} sharp =0.21mm r_{match} blunt =0.3mm

Figure 5.35. Stress distribution obtained from blunt notched CT specimen in as received condition compared to HRR solution.

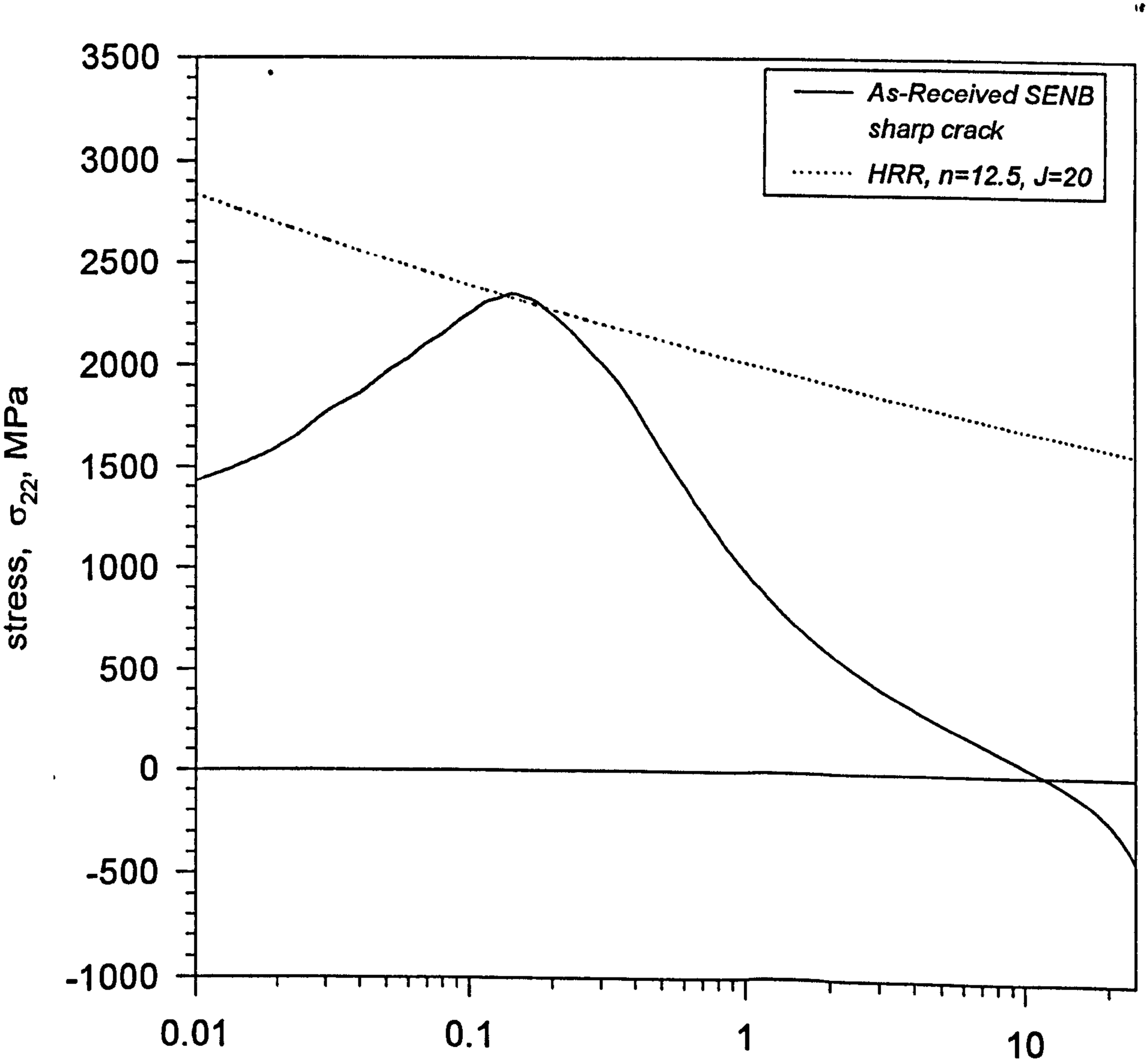

Figure 5.36. Normalised stress distribution obtained from specimen ab1n, compared to HRR solution.

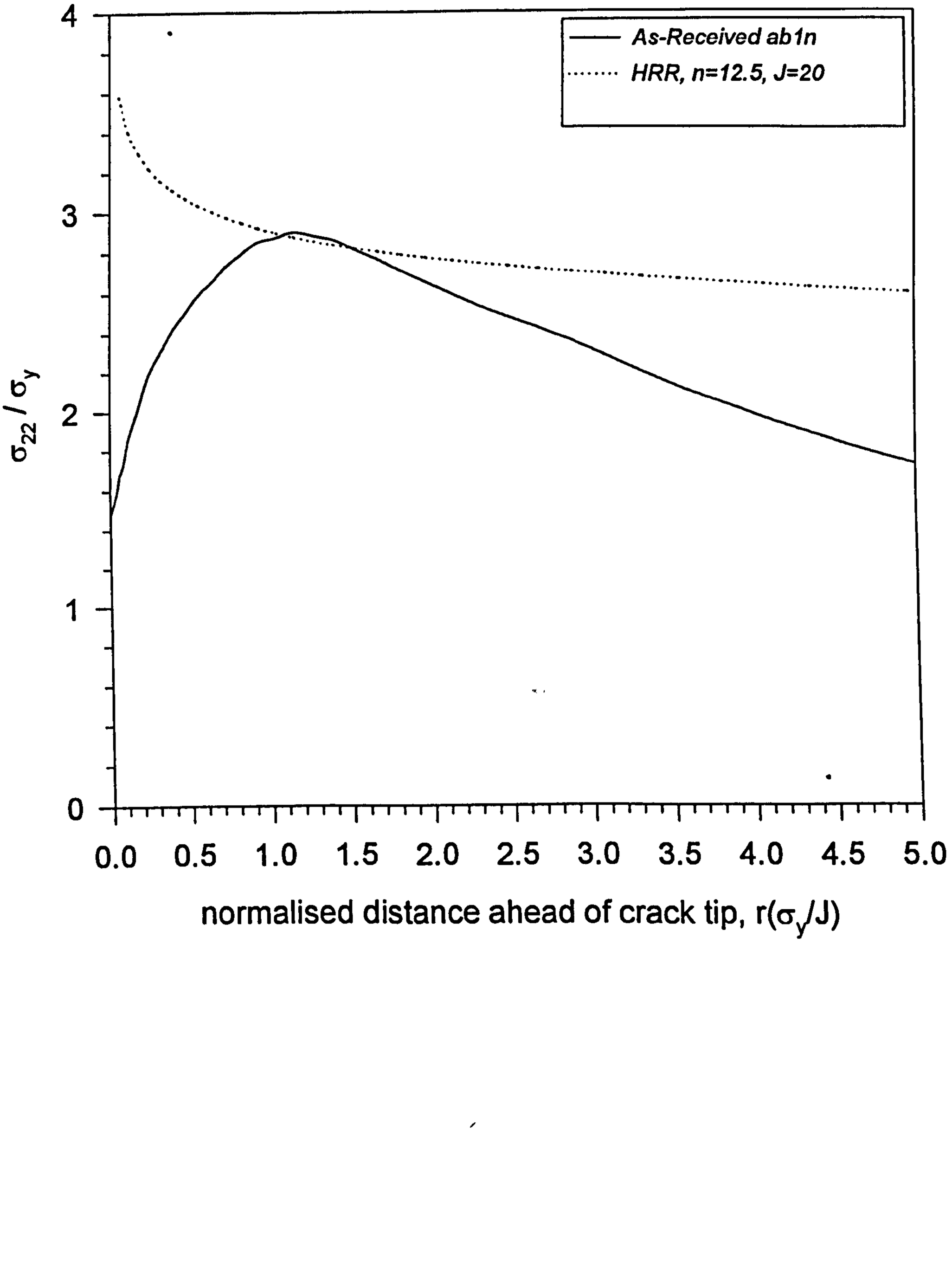

Figure 5.37. Stress distribution obtained from specimens ab1n and ab5wps, compared to HRR solution.

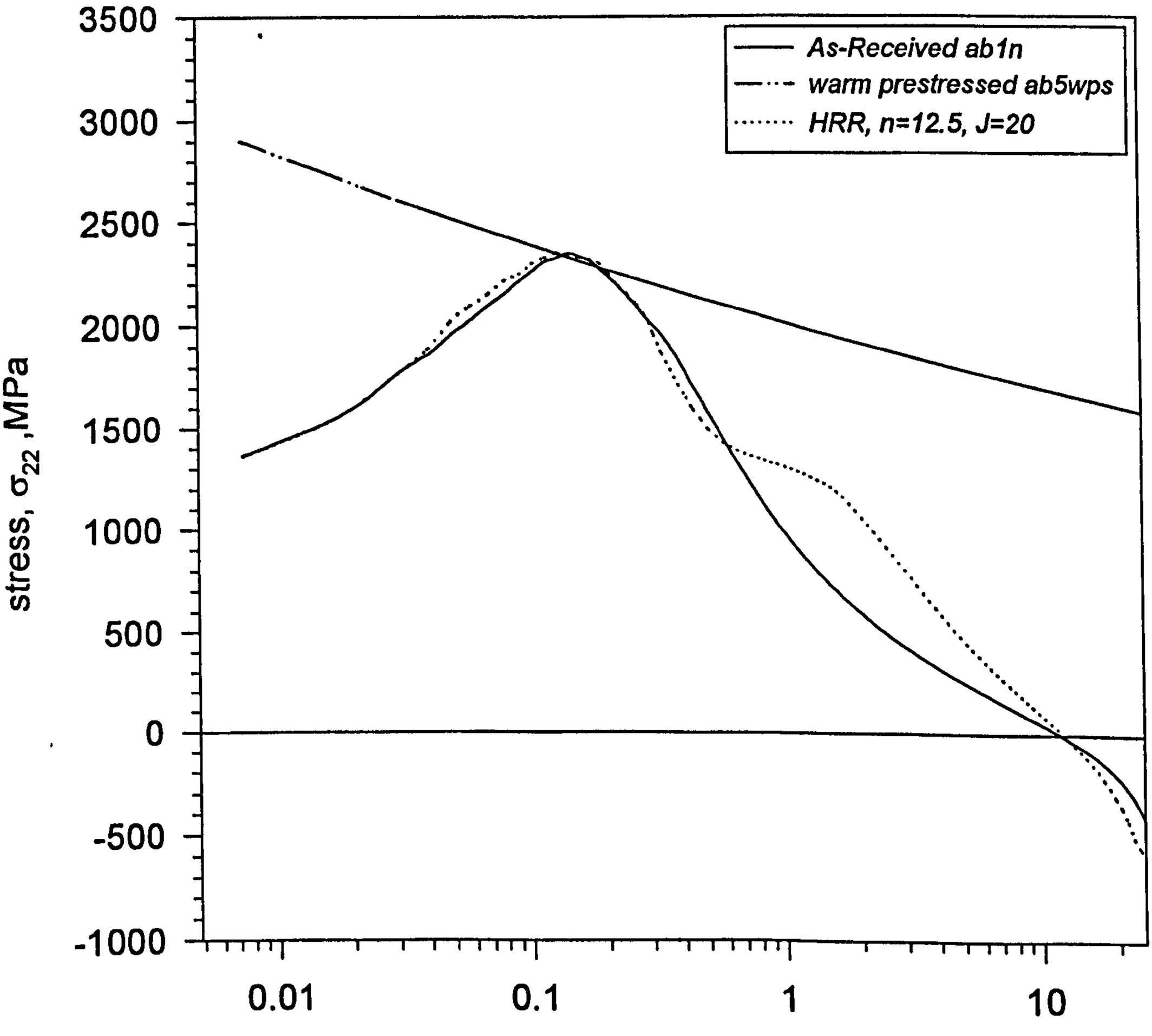

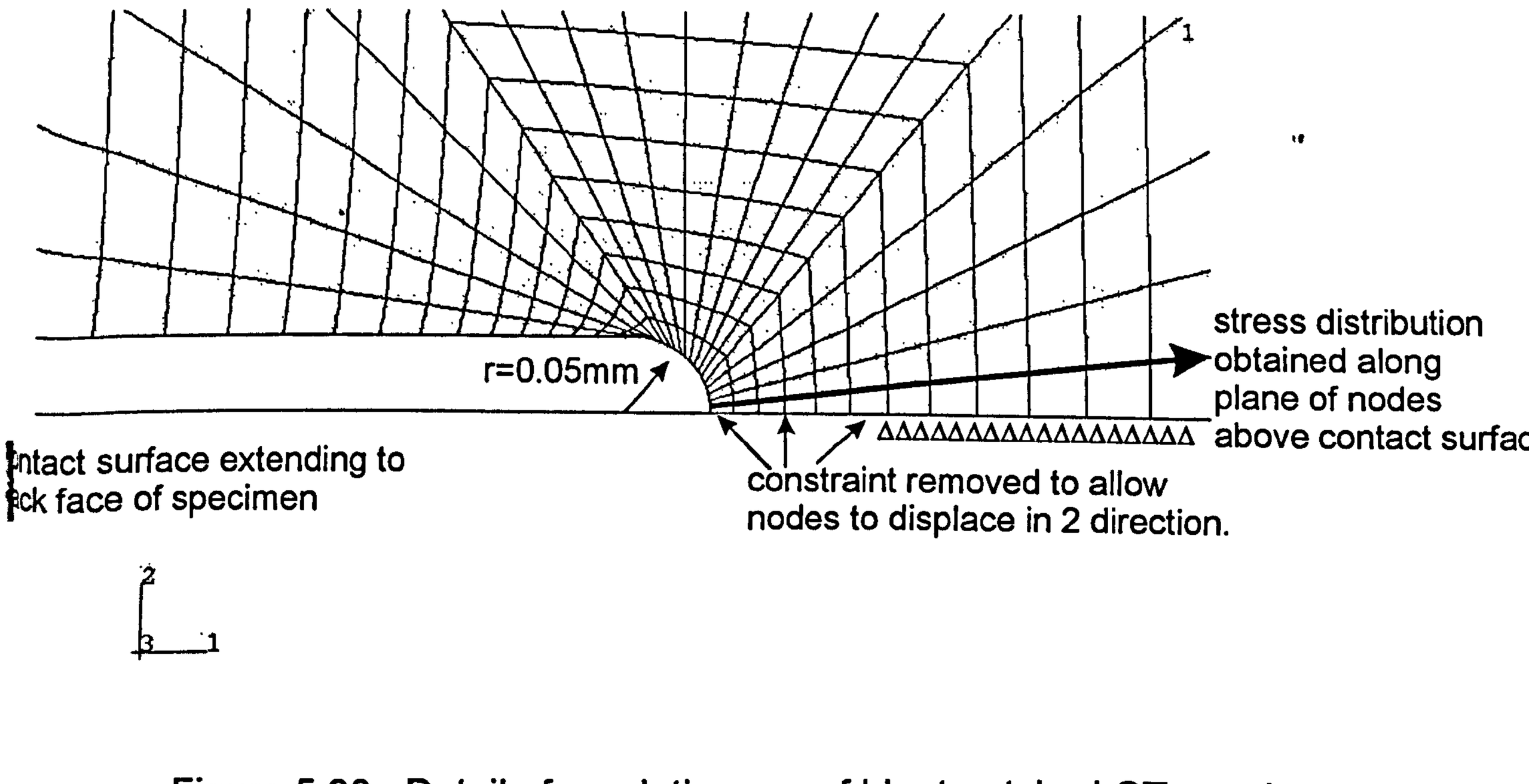

Figure 5.38. Detail of crack tip area of blunt notched CT specimen with released nodal constraint simulating sub critical crack extension following unloading.

Figure 5.39. Residual normal stress distribution following a proof load of 120 MPa√m.

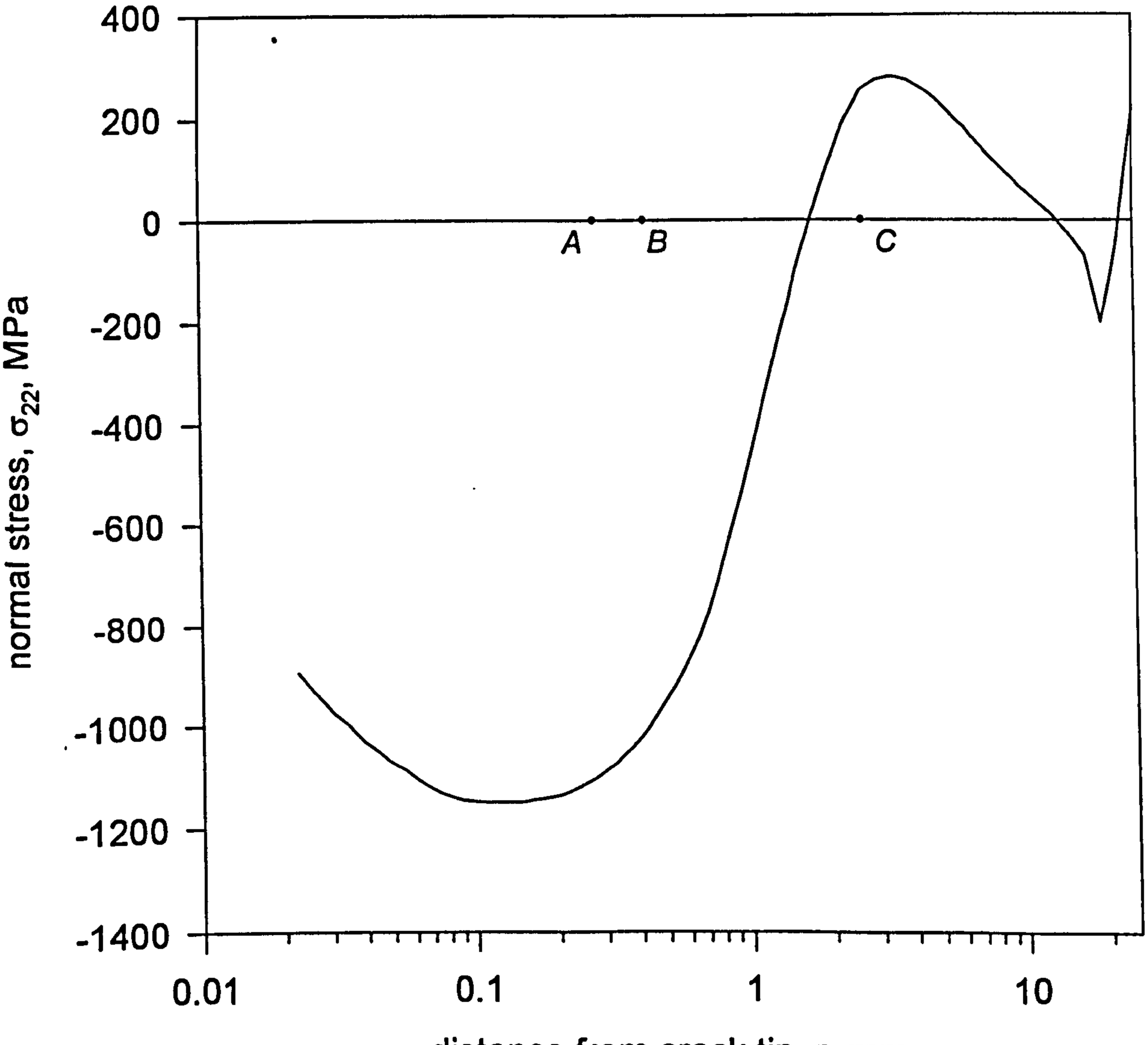

A: position of extended crack tip for specimen 4596
B: position of extended crack tip for specimen 6596
C: position of extended crack tip for specimen 12596

Figure 5.40. Fracture stress distribution of specimen 4596 compared to the as received fracture stress distribution of a specimen with a blunt notch of the same final length with toughness 40 MPa√m

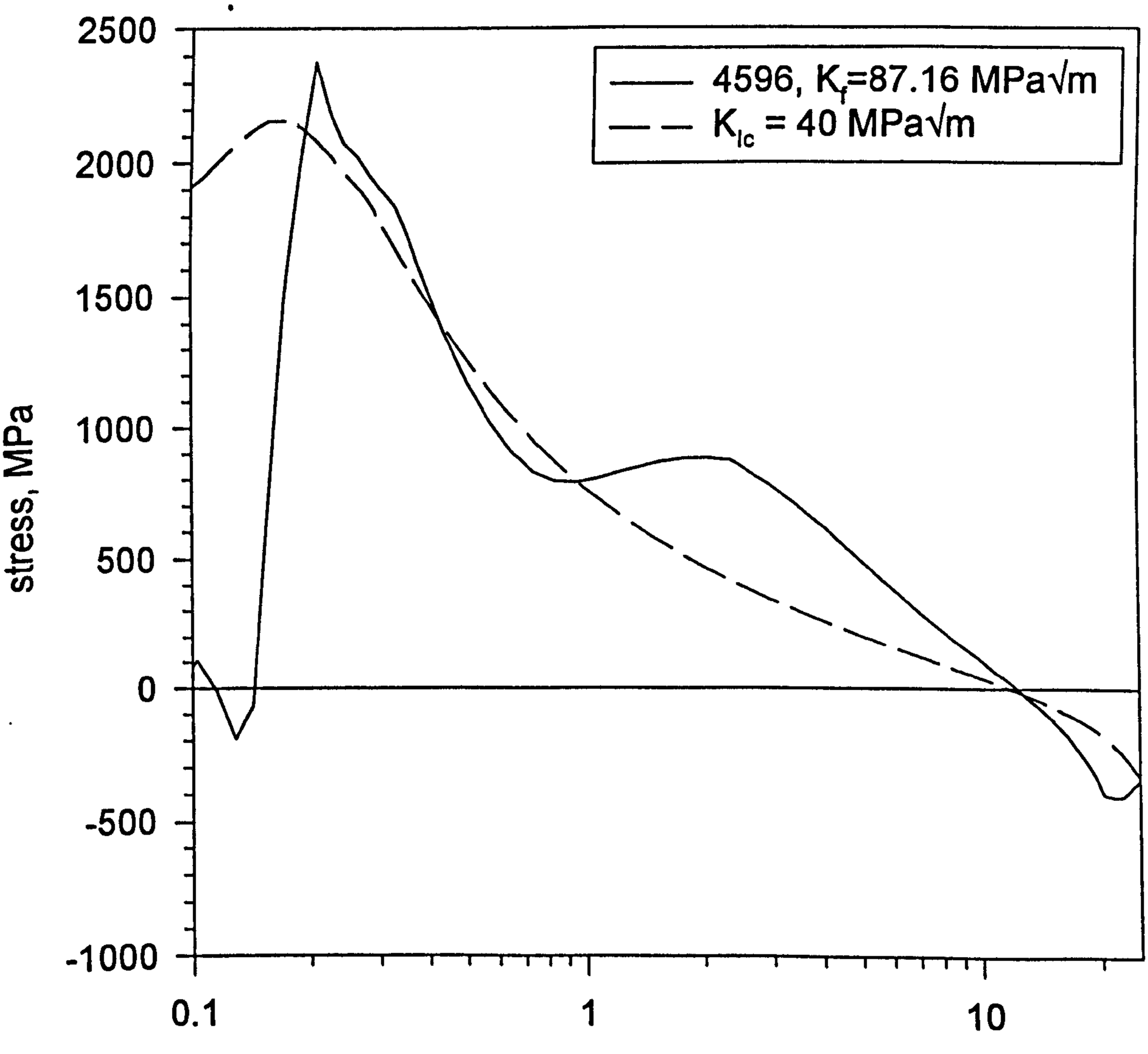

Figure 5.41. Fracture stress distribution of specimen 6596 compared to the as received fracture stress distribution of a specimen with a blunt notch of the same final length with toughness 85 MPa$\sqrt{m}$

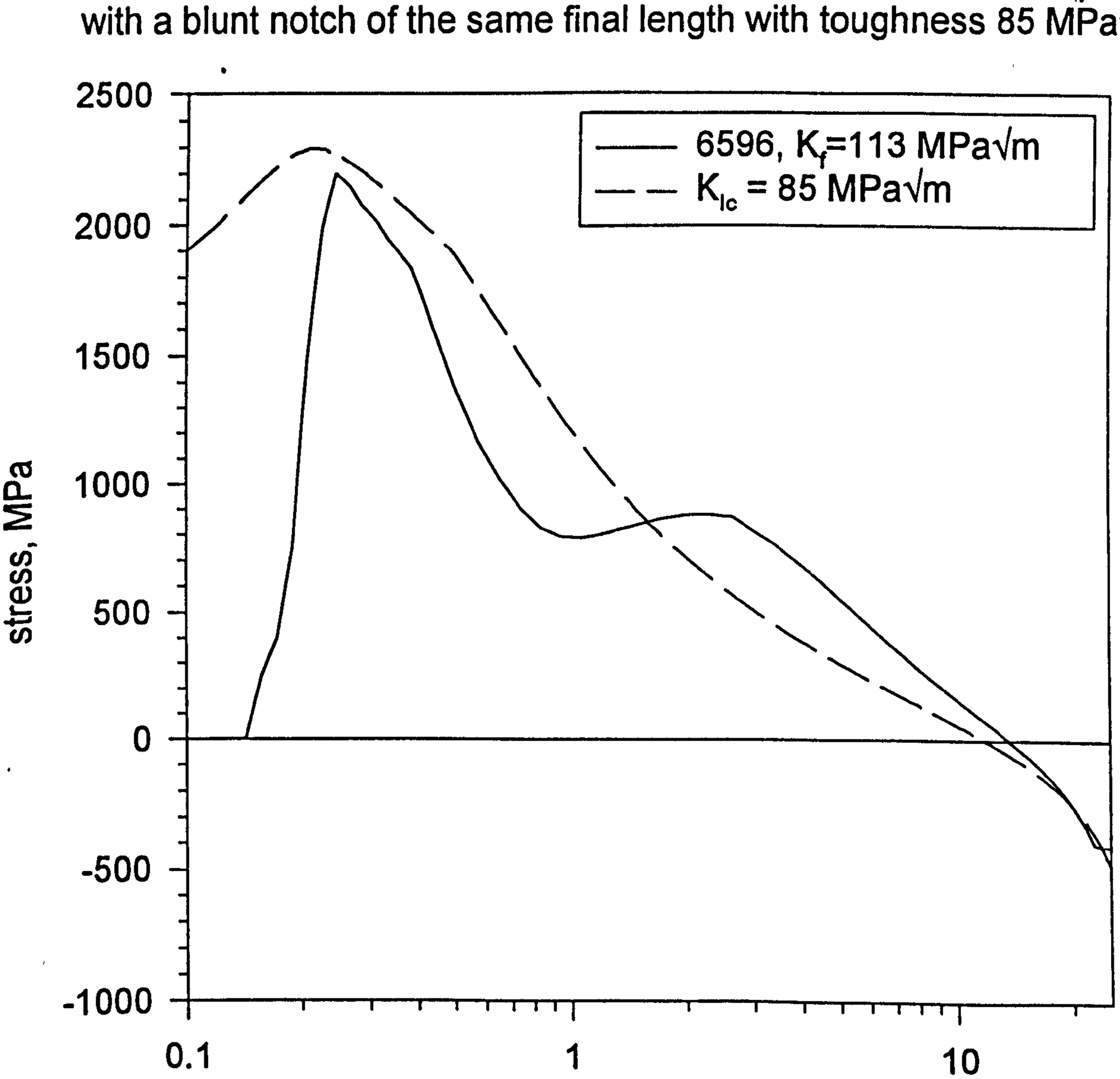

Figure 5.42. Finite element simulation of specimen 12596 compared to as-received fracture stress distribution for K_{Ic}=85 MPa√m and 113 MPa√m

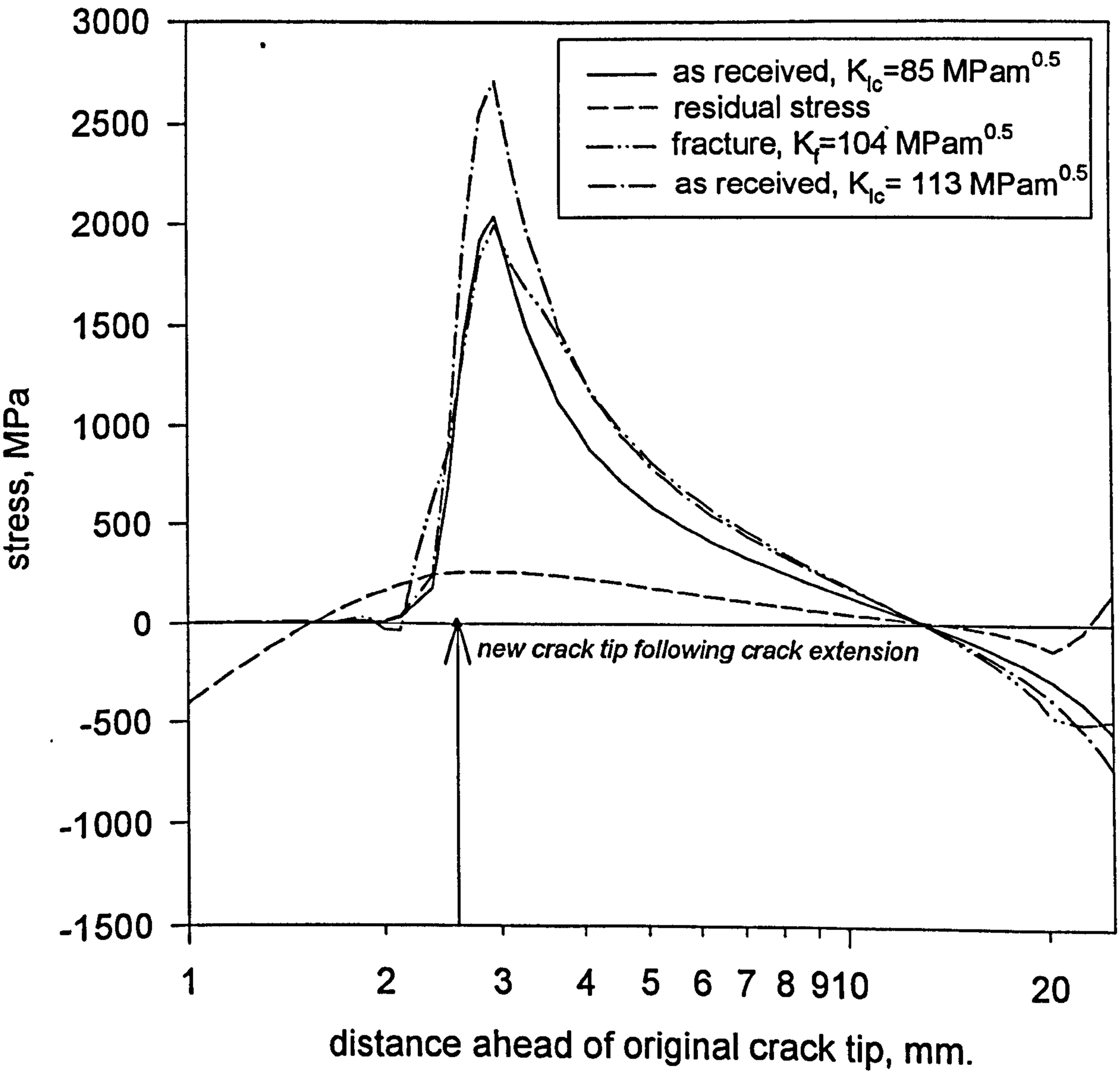

Figure 5.43. As received cleavage toughness distributions for specimens with various crack extensions increments. K_{Ic} = 85 MPa√m

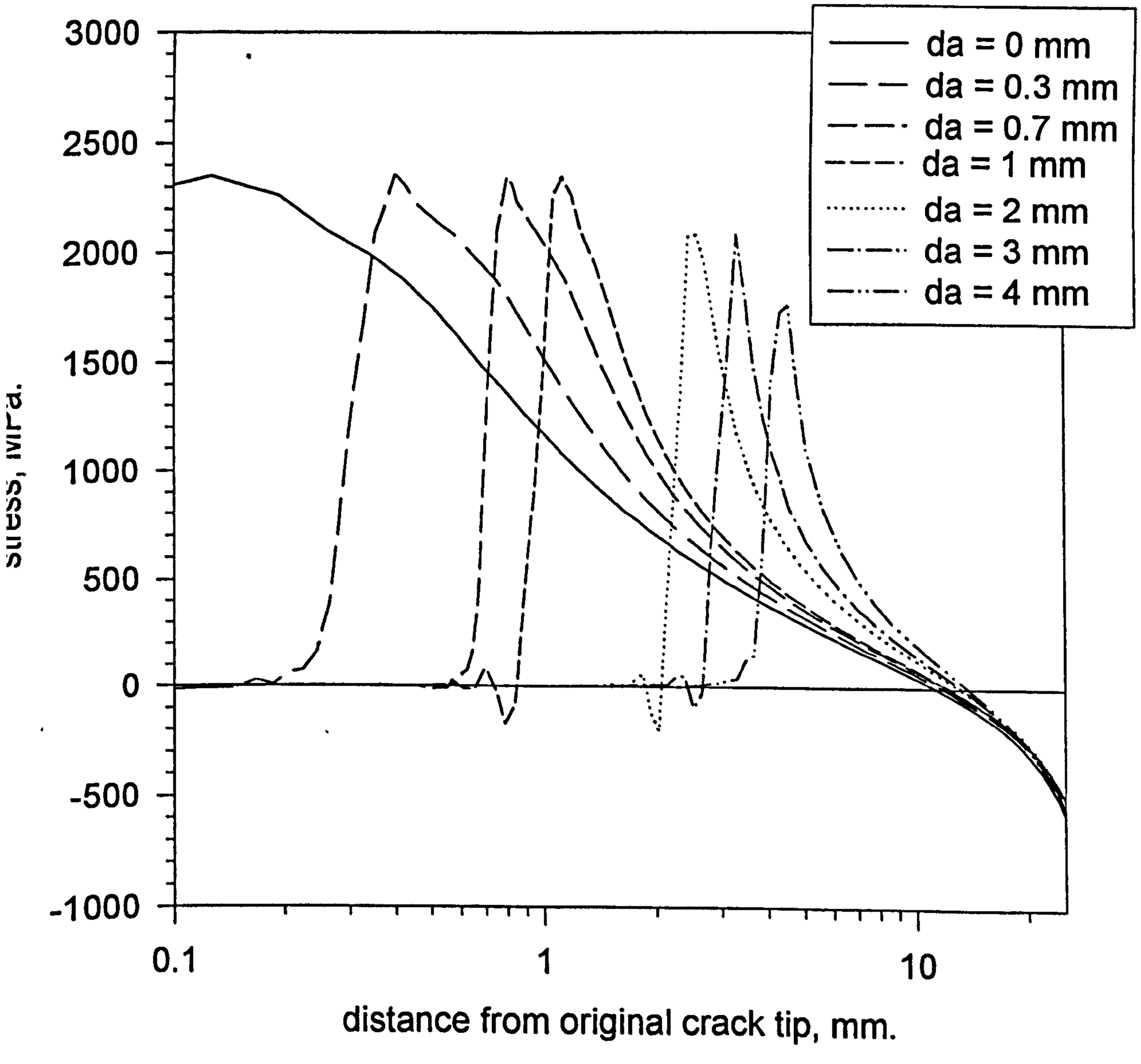

Figure 5.44. Normalised as received cleavage toughness distributions for specimens with various crack extensions increments. Distributions normalised with respect to the original crack length.
K_{Ic} = 85 MPa√m

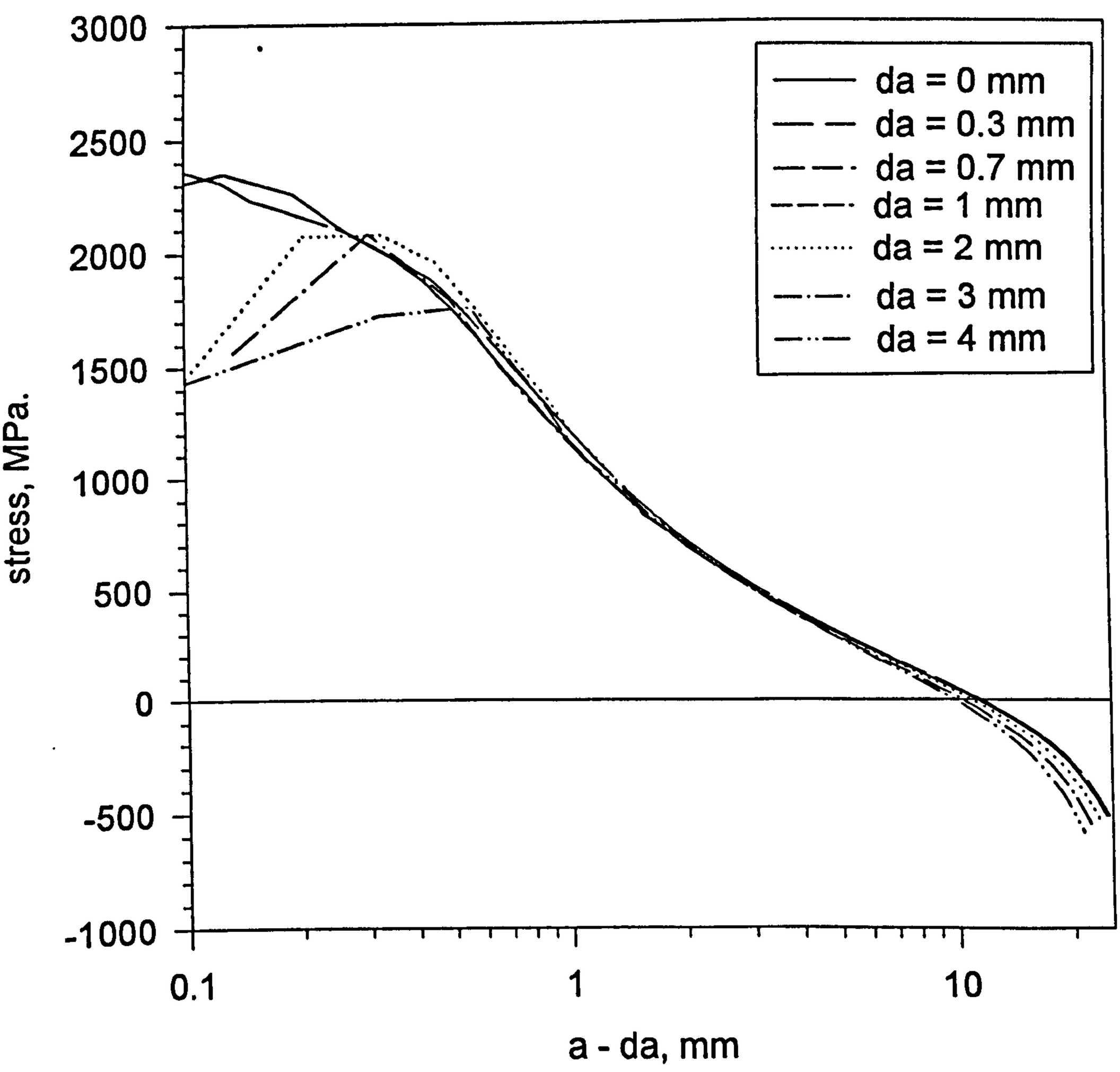

Figure 5.45. Normalised as received cleavage toughness distributions for specimens with various crack extensions increments. Distributions normalised with respect to the original crack length, yield strength and toughness.

K_{Ic} = 85 MPa$\sqrt{m}$, σ_y =810 MPa

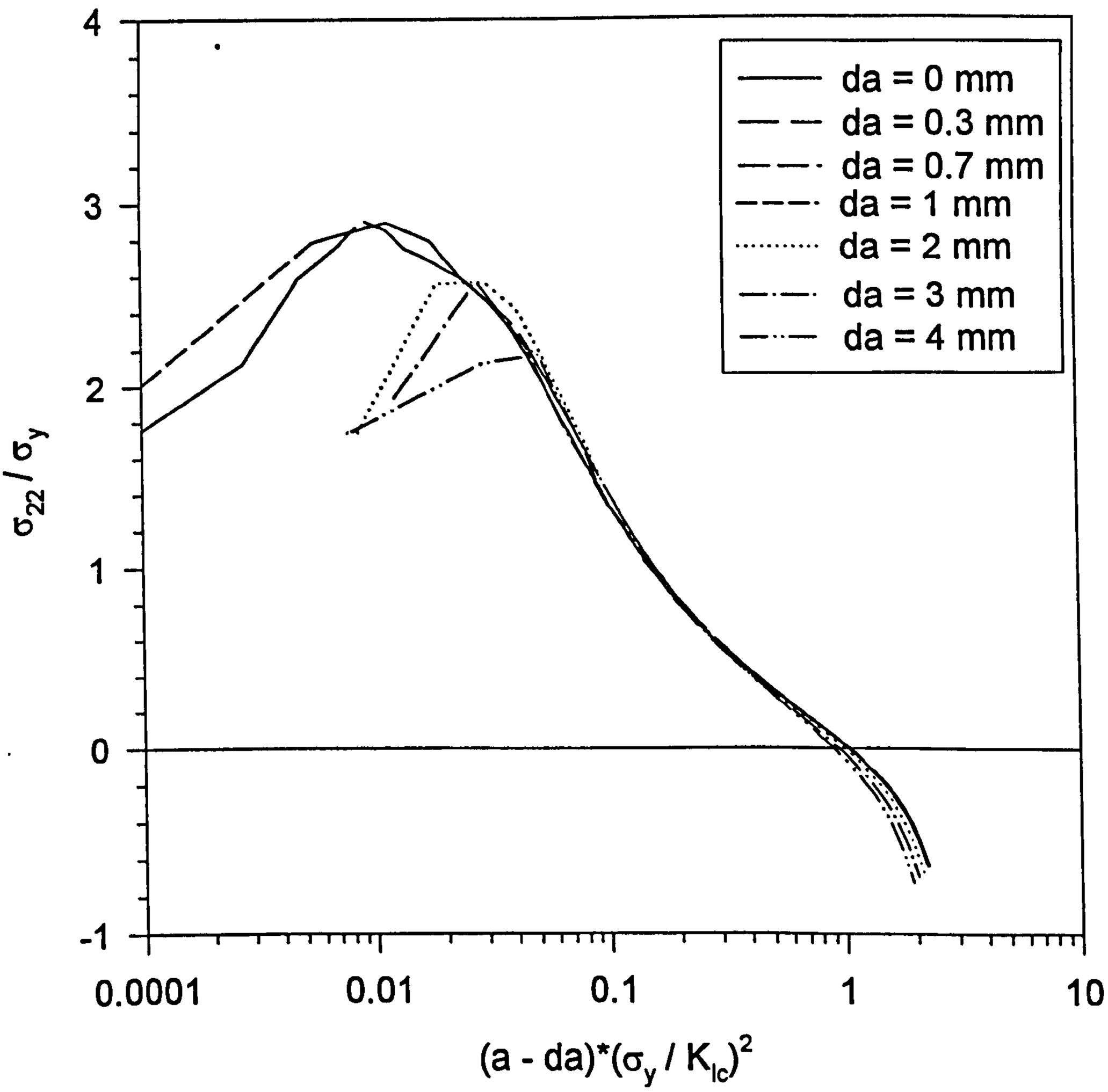

Figure 5.46. Predicted fracture stress distribution following warm prestress K_1= 120 MPa√m and fractured with no crack growth.

Critical stress distribution for K_{Ic} = 85 MPa√m

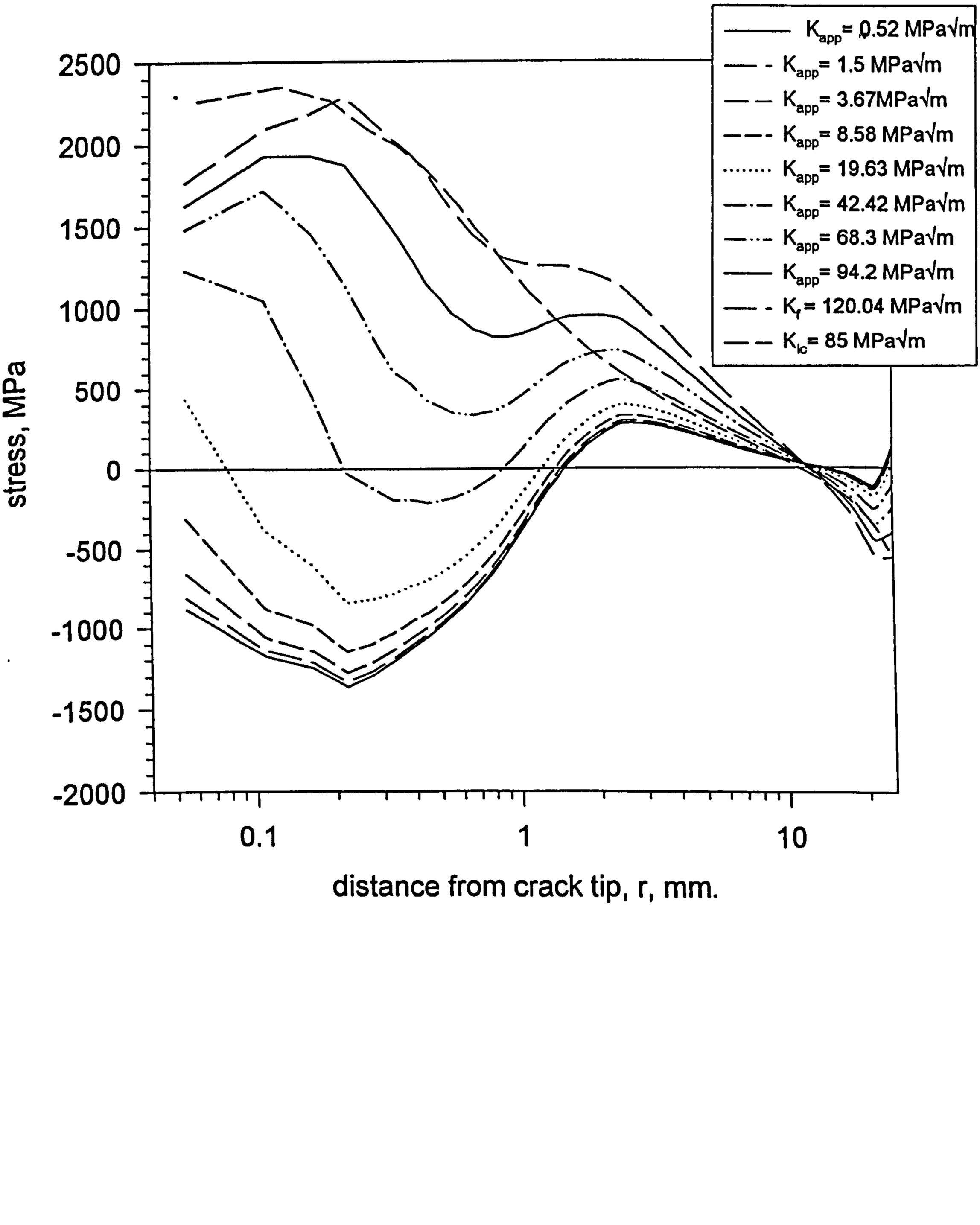

Figure 5.47. Predicted fracture stress distribution following warm prestressing to K_1 = 120 MPa√m and fracture following 0.3mm sub critical crack growth

Critical stress distribution for K_{1c} = 85 MPa√m

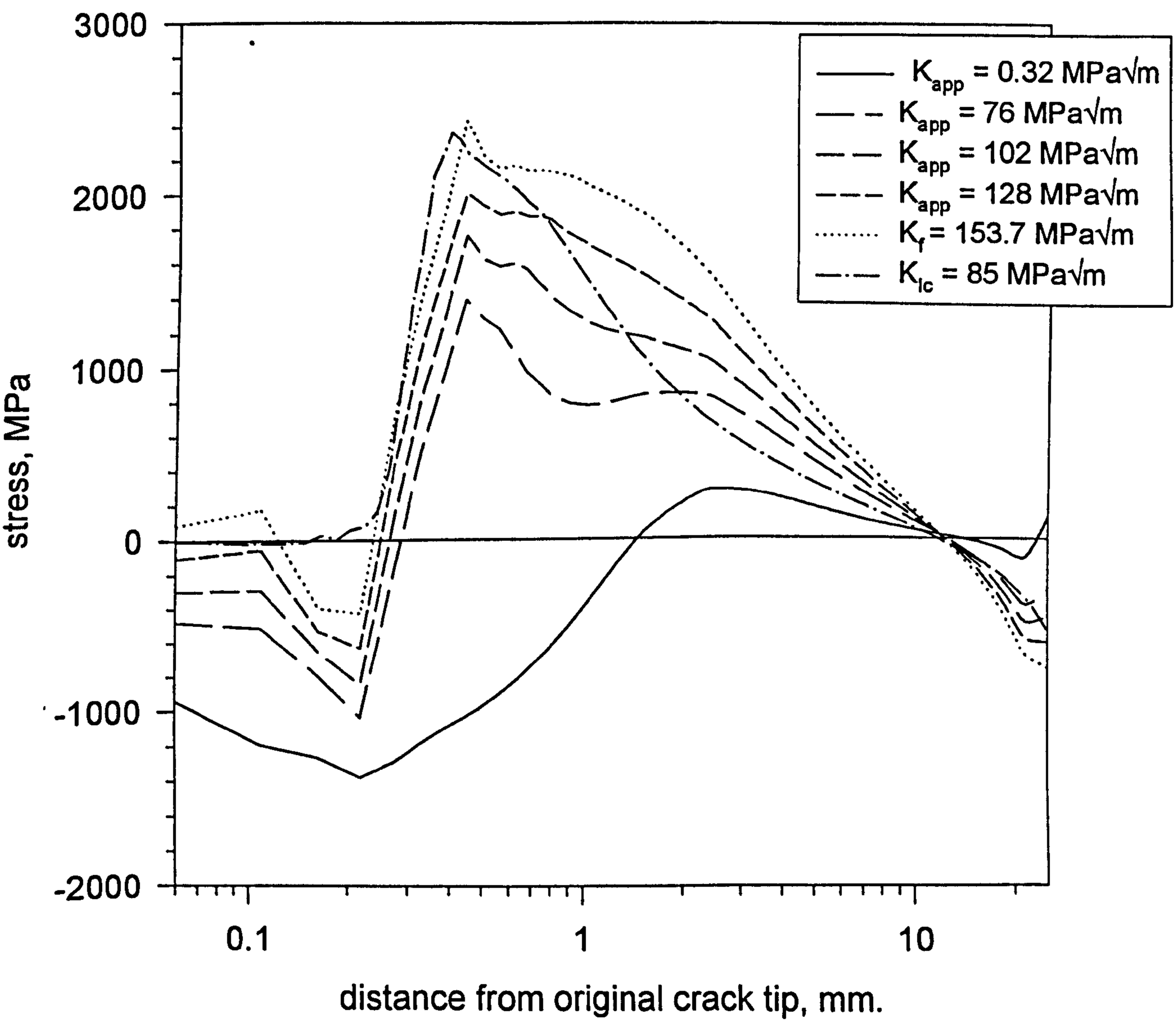

distance from original crack tip, mm.

ABAQUS

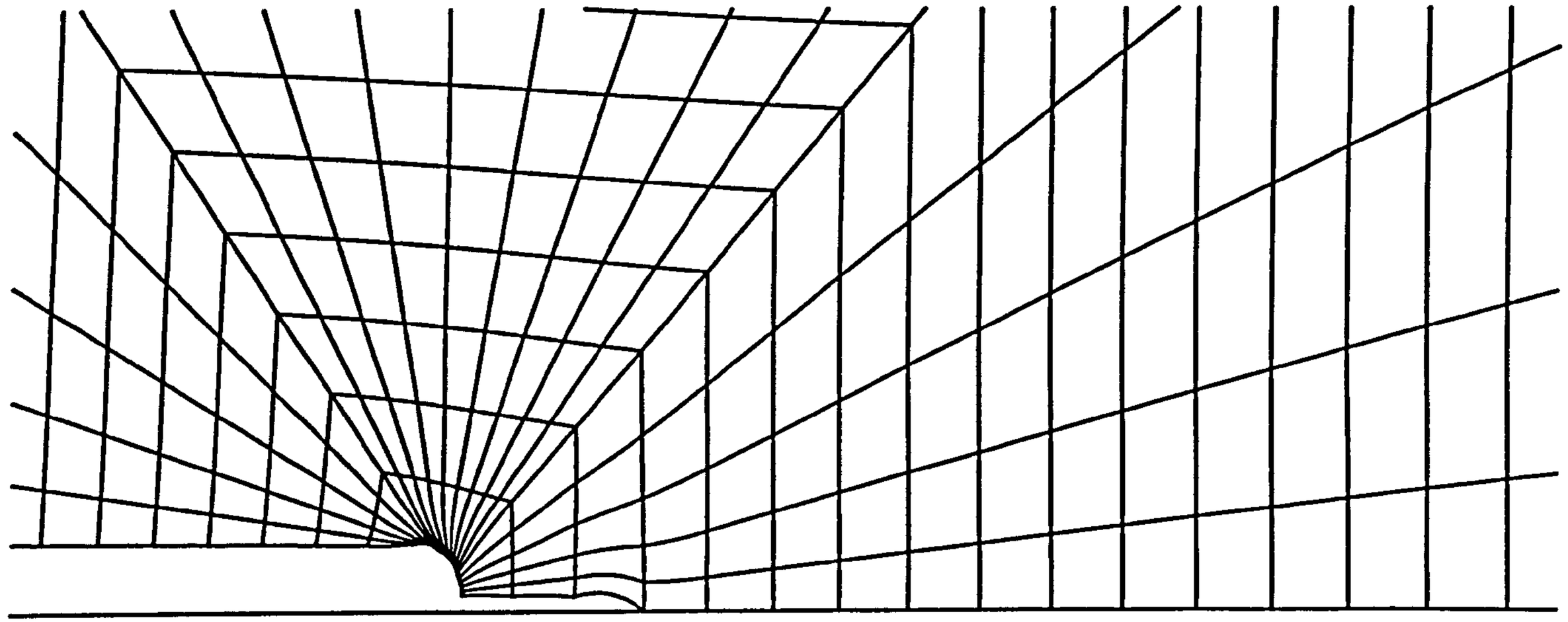

Figure 5.48. Displaced mesh plot of CT specimen at fracture following 0.3mm sub critical crack growth after warm prestressing.

Figure 5.49. Predicted fracture stress distribution following warm prestress to K_1=120 MPa√m and fracture following 0.7mm sub critical crack growth.
Critical stress distribution for K_{1c}=85 MPa√m

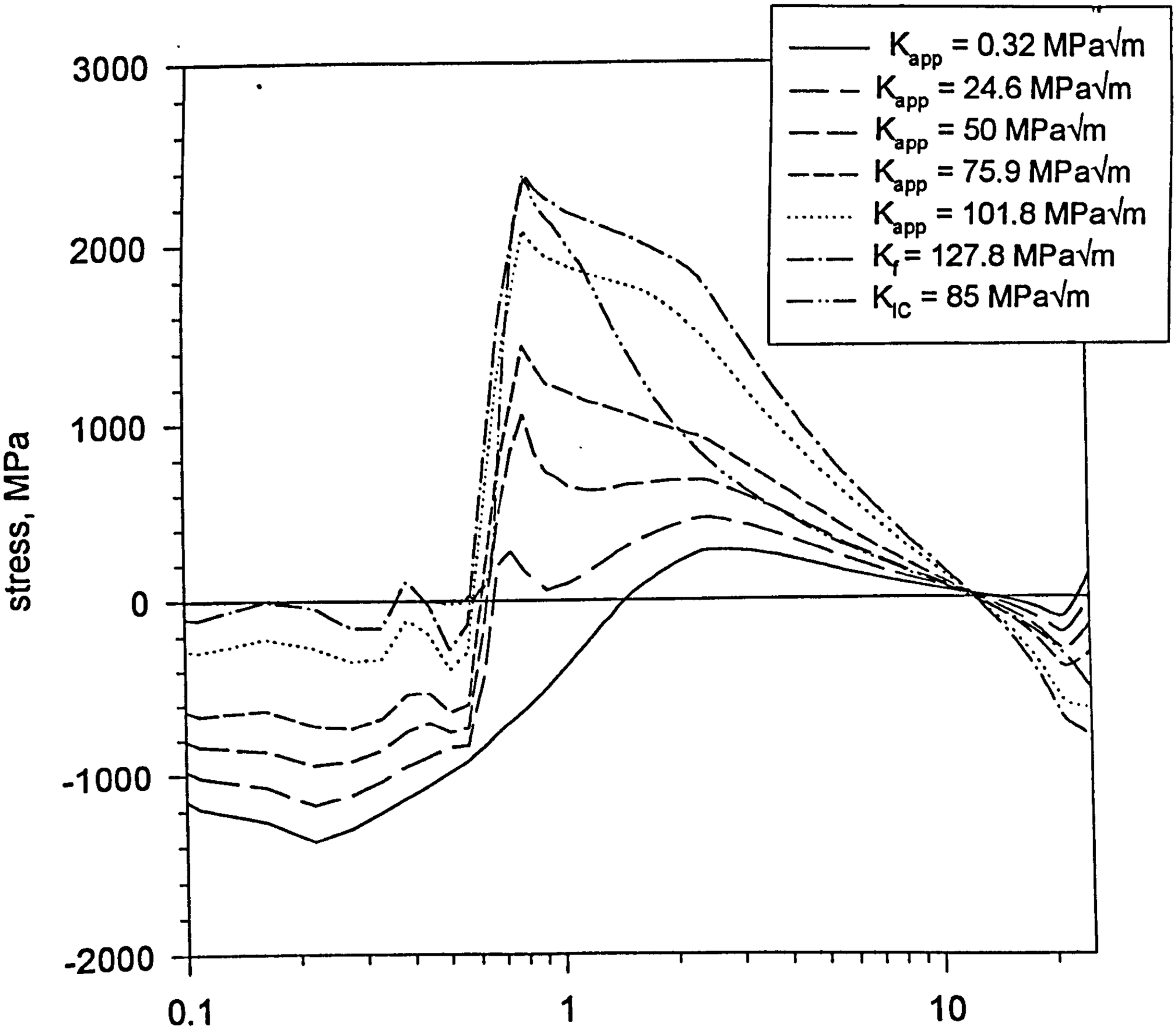

distance from original crack tip, mm.

Figure 5.50. Predicted fracture stress distribution following warm prestress K_1= 120 MPa√m and fractured following 1mm sub critical crack growth.

Critical stress distribution for K_{Ic}= 85 MPa√m

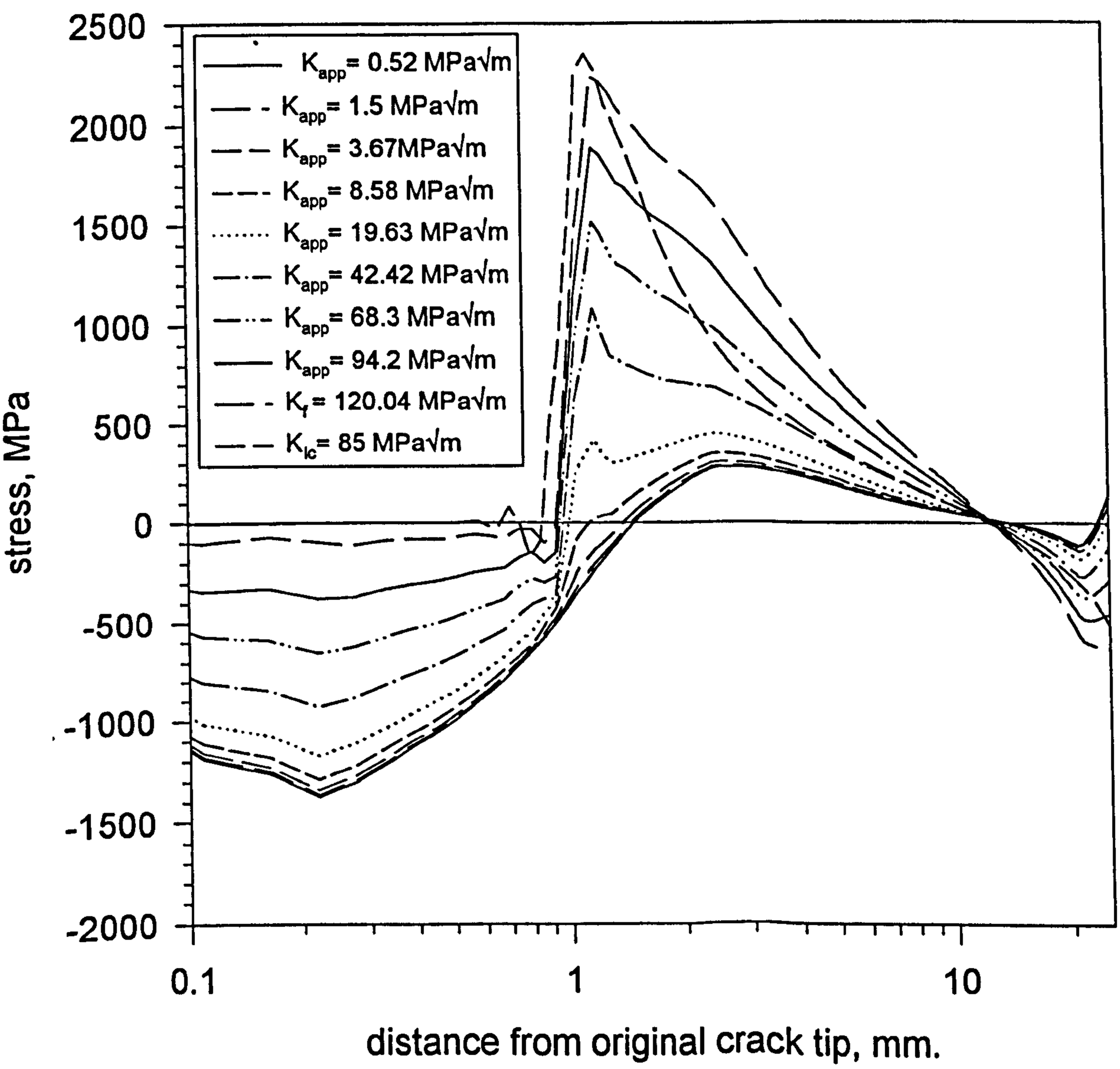

distance from original crack tip, mm.

Figure 5.51. Predicted fracture stress distribution following warm prestress K_1= 120 MPa√m and fractured following 2mm sub critical crack growth.

Critical stress distribution for K_{Ic}= 85 MPa√m

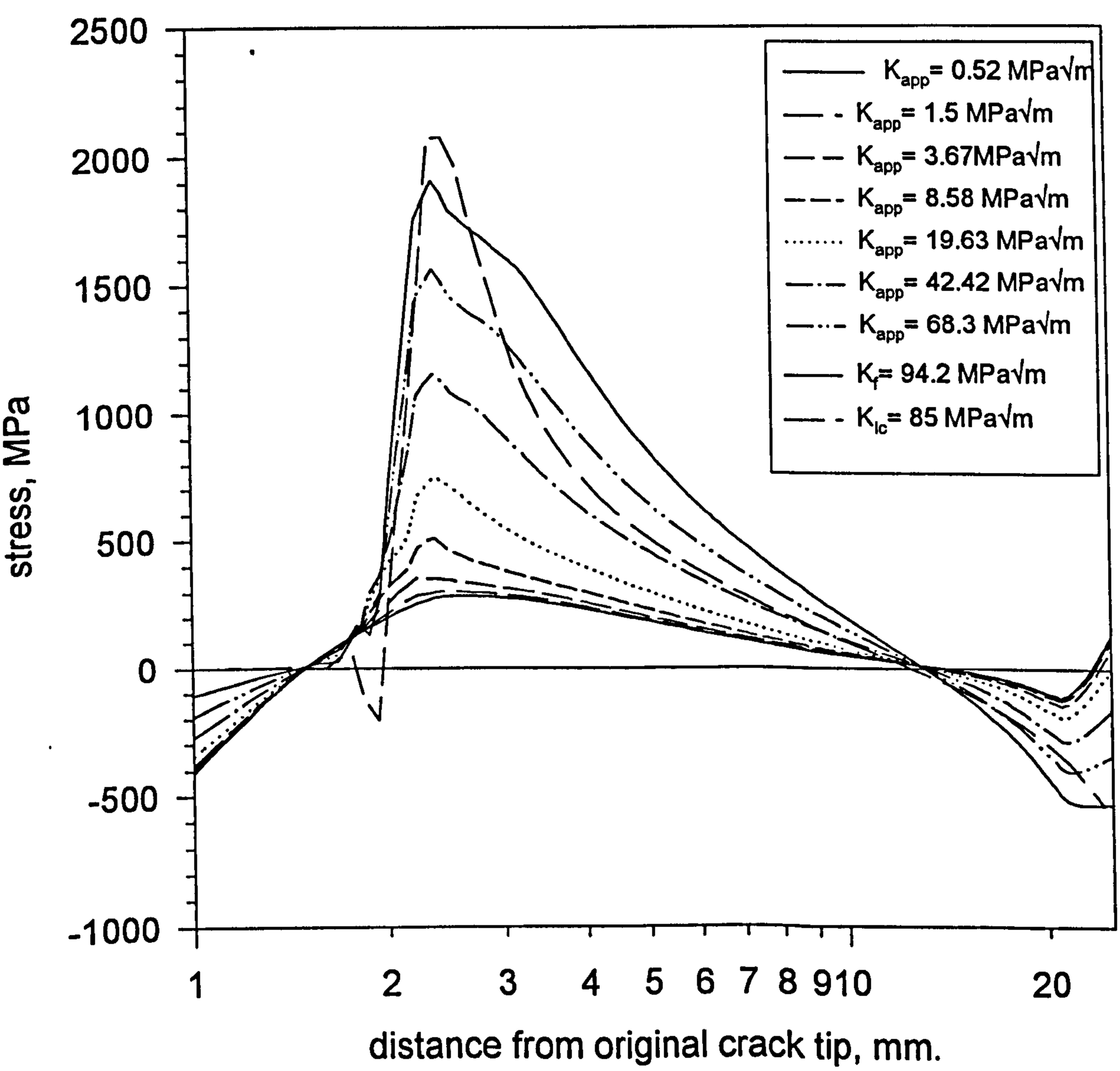

distance from original crack tip, mm.

Figure 5.52. Predicted fracture stress distribution following warm prestress K_1= 120 MPa√m and fractured following 3mm sub critical crack growth.

Critical stress distribution for K_{Ic}= 85 MPa√m

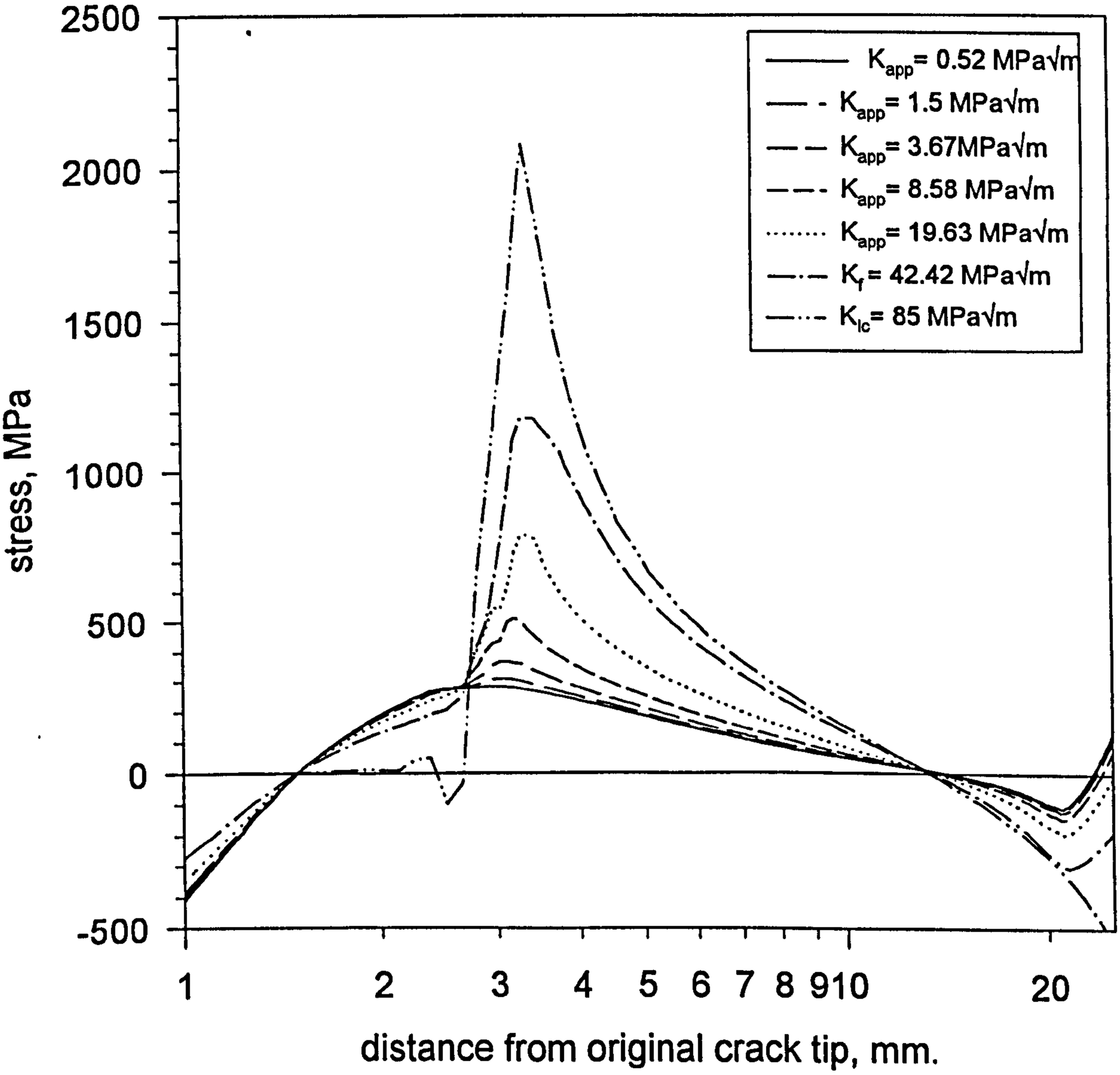

Figure 5.53. Predicted fracture stress distribution following warm prestress K_1= 120 MPa√m and fractured following 4 mm sub critical crack growth.

Critical stress distribution for K_{Ic}= 85 MPa√m

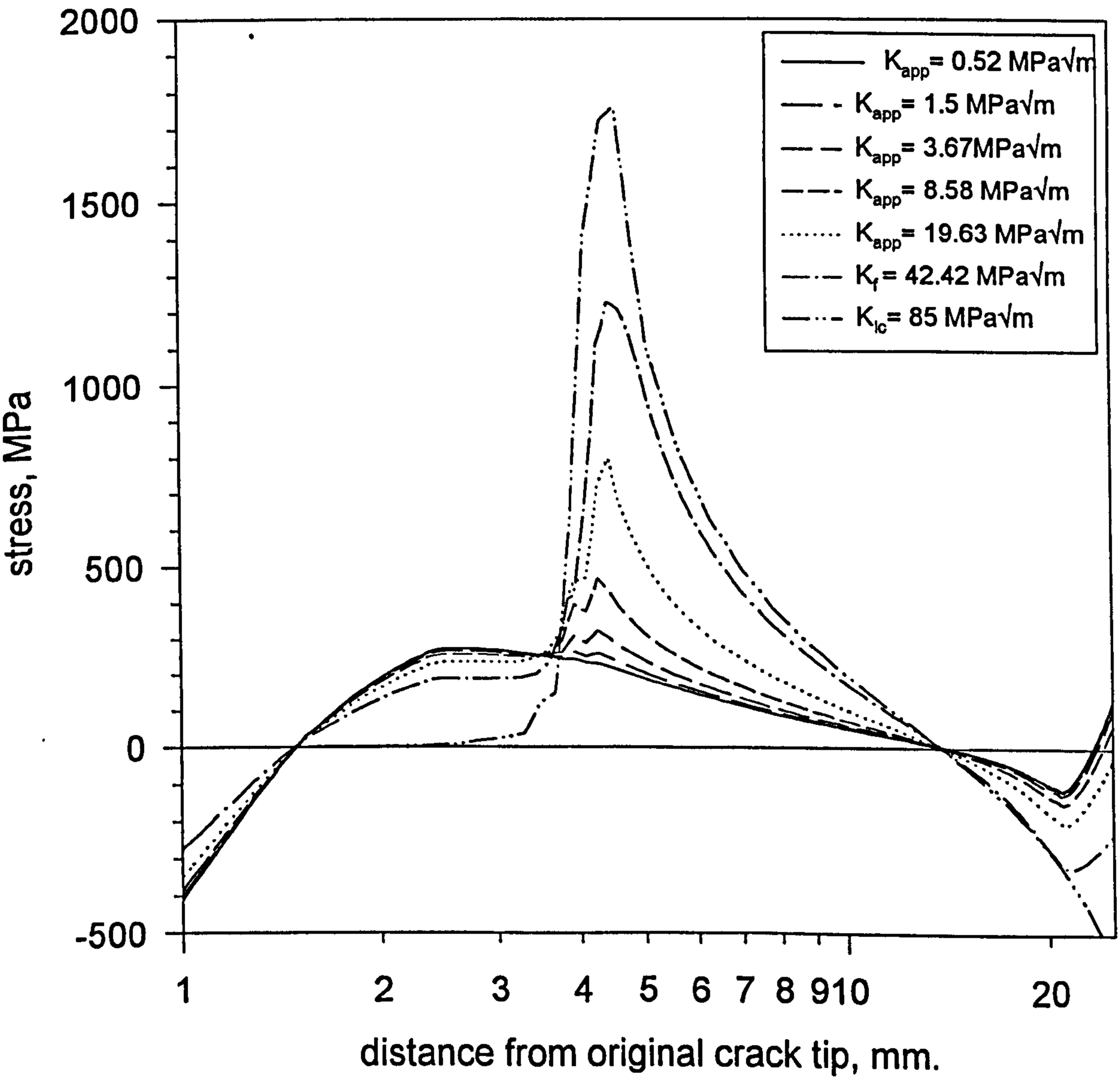

Figure 5.54. Finite element predictions of failure following sub-critical crack growth compared to experimental results.

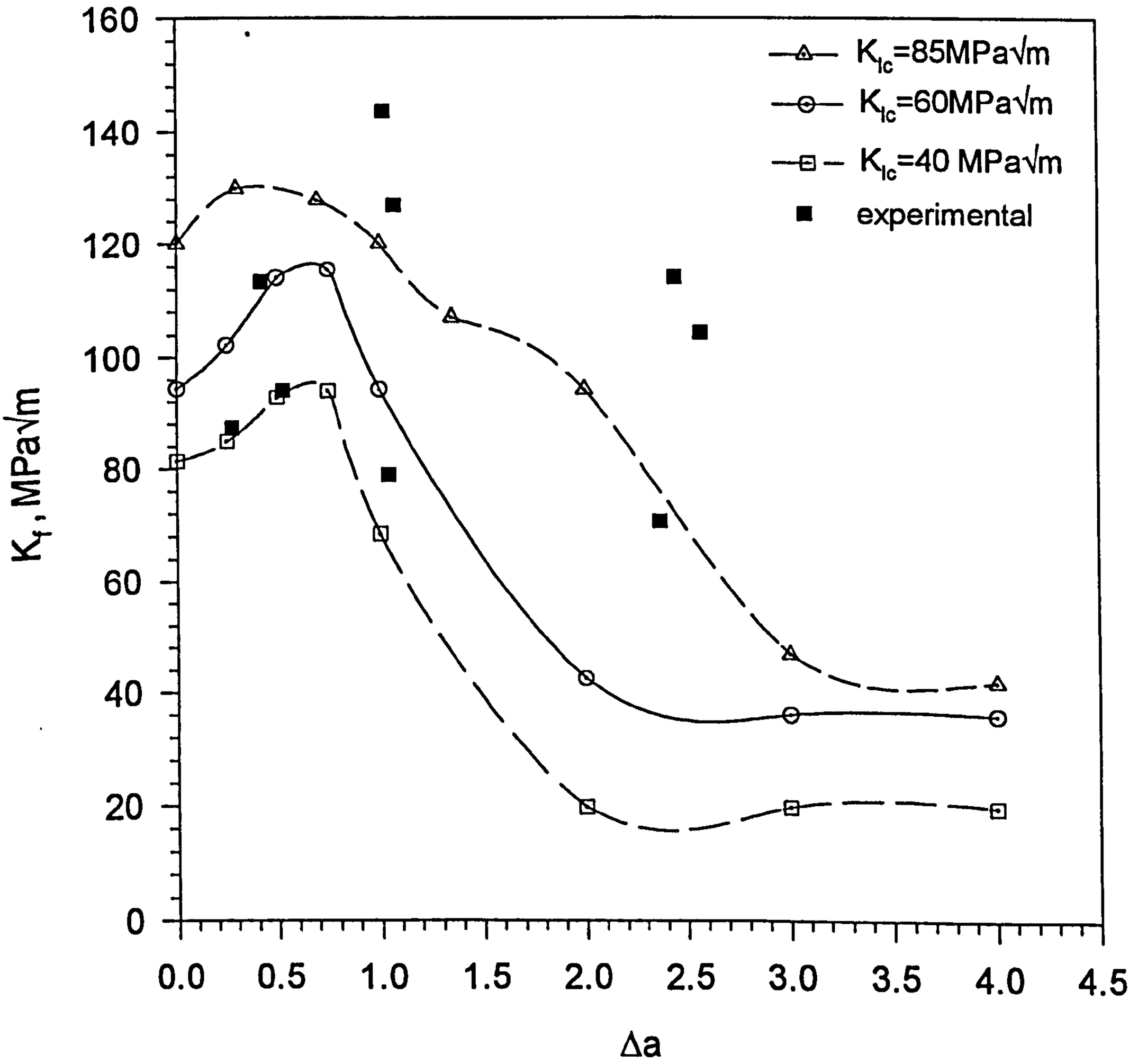

Figure 5.55. Predicted fracture stress distribution following warm prestress K_1= 120 MPa√m and fractured following 2mm sub critical crack growth. Matching peak stress at crack tip. Critical stress distribution for K_{Ic}= 85 MPa√m

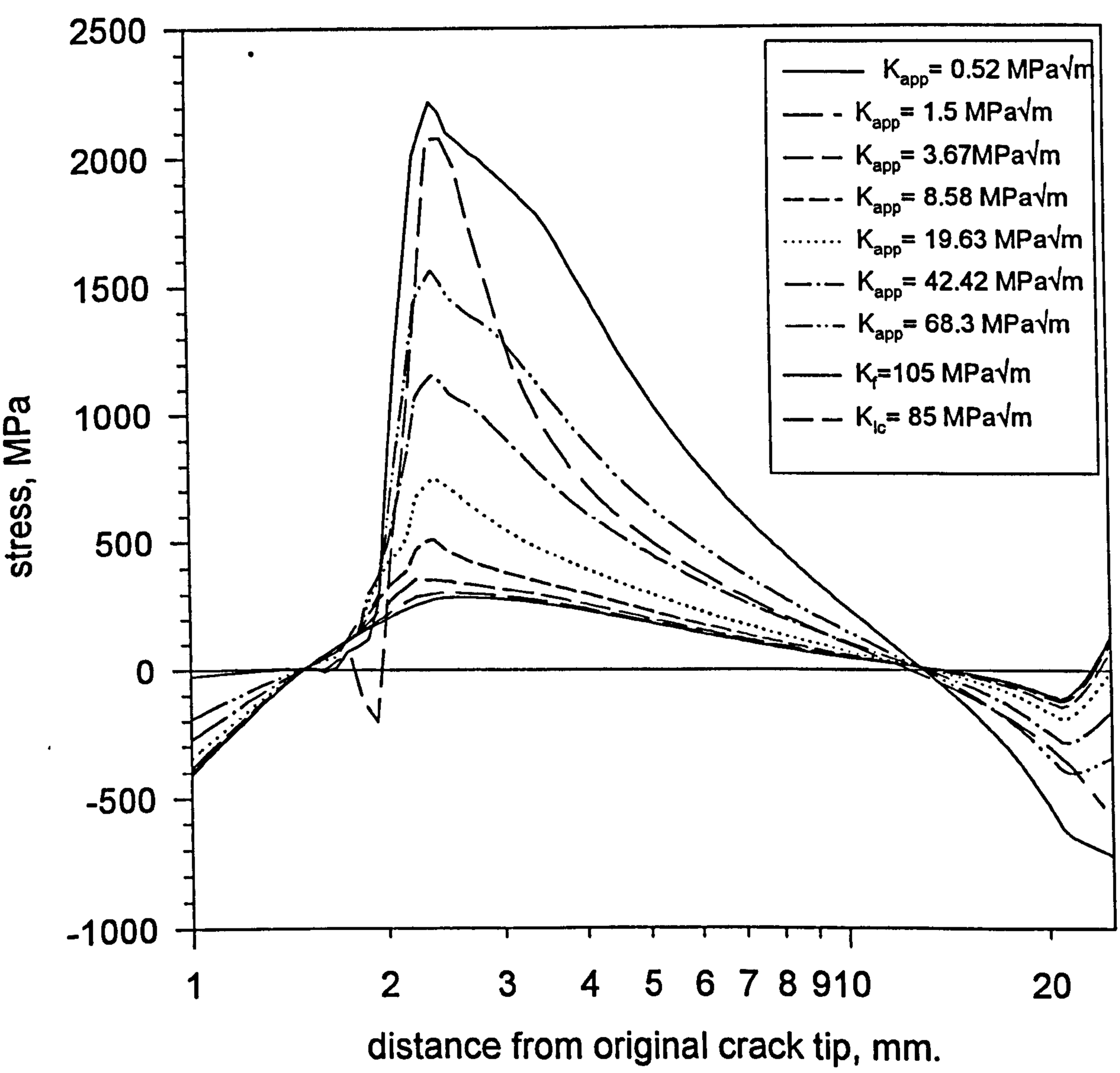

Figure 5.56. Finite element predictions of failure following sub-critical crack growth obtained by matching the peak stress for $\Delta a > 1mm$ compared to experimental results.

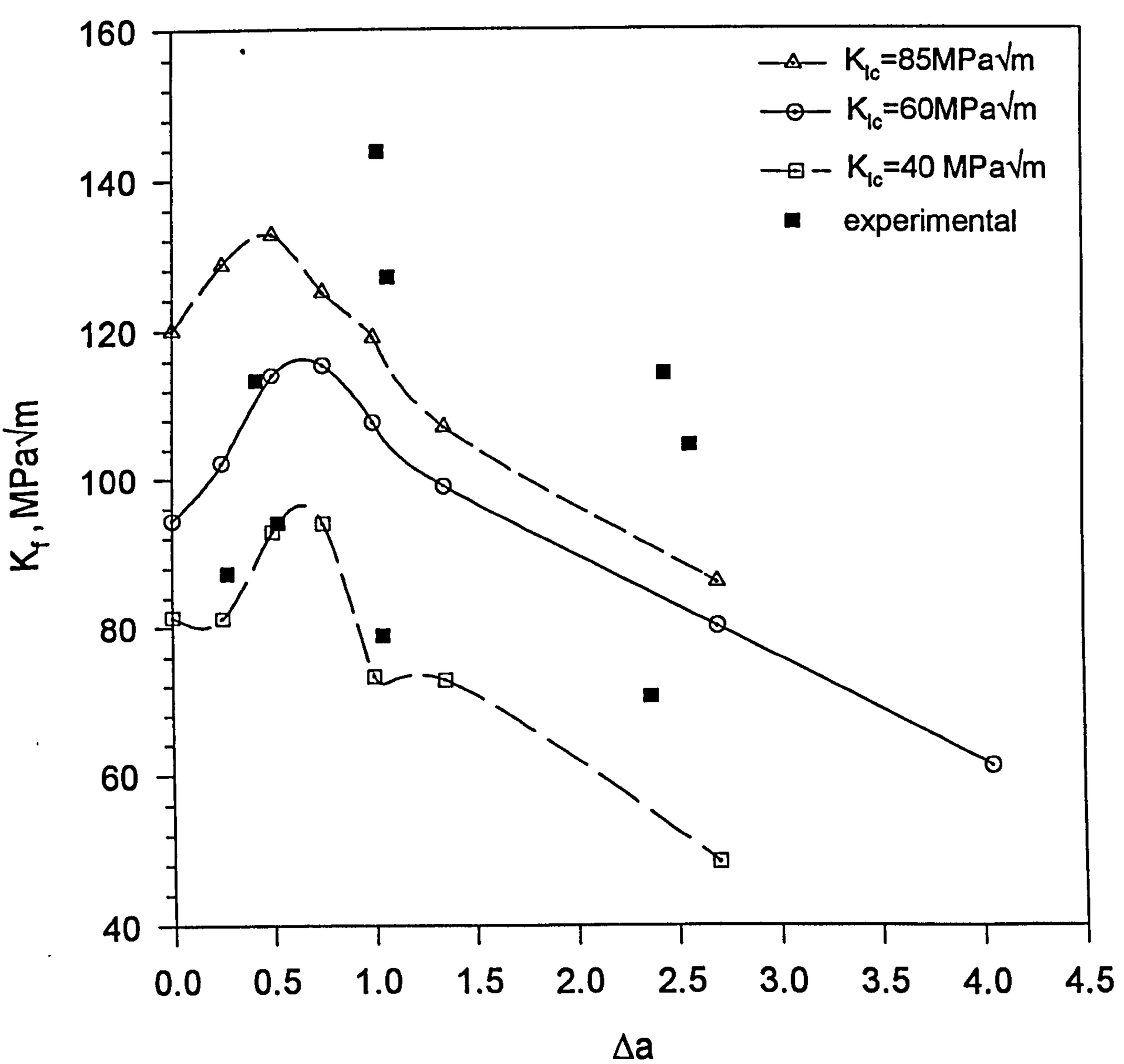

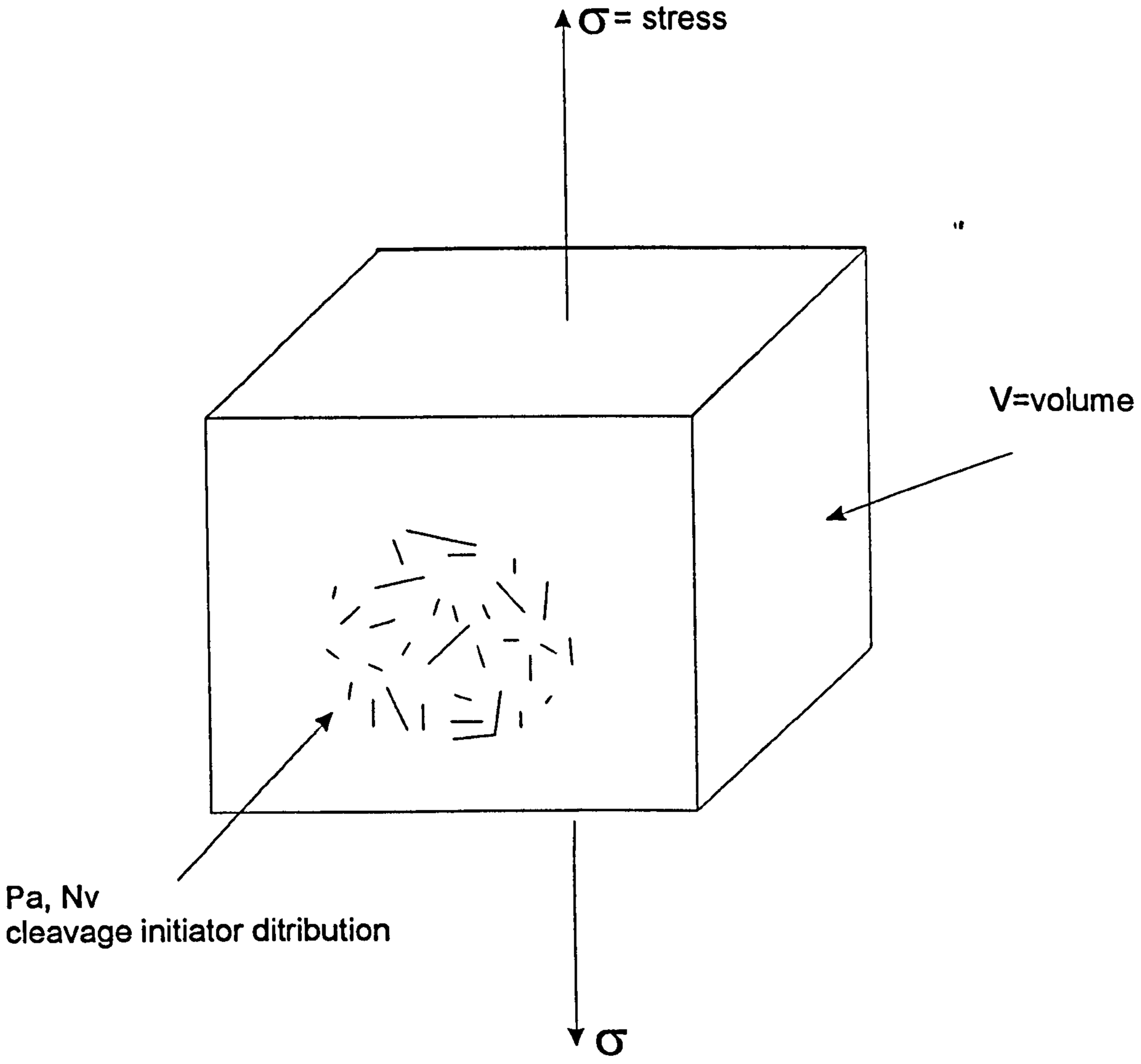

Figure 6.1. Basis of the general statistical model (after Wallin, 1991)

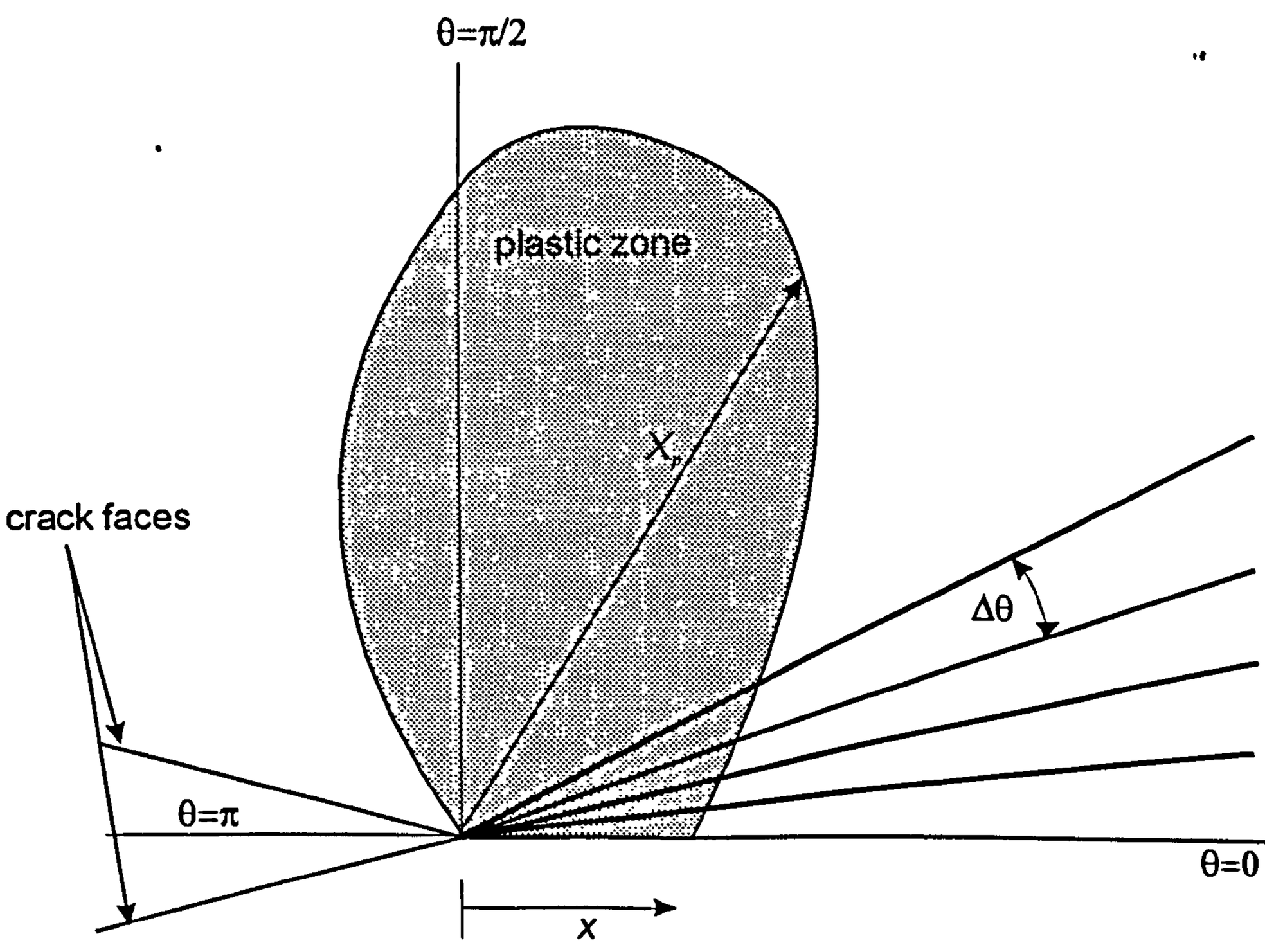

Figure 6.2. Implementation of HRR expression in General Statistical Model

Figure 6.3. Cumulative Distribution Functions for As -Received Cleavage Toughness Data Obtained at -170°C and -100°C in A533B specimens

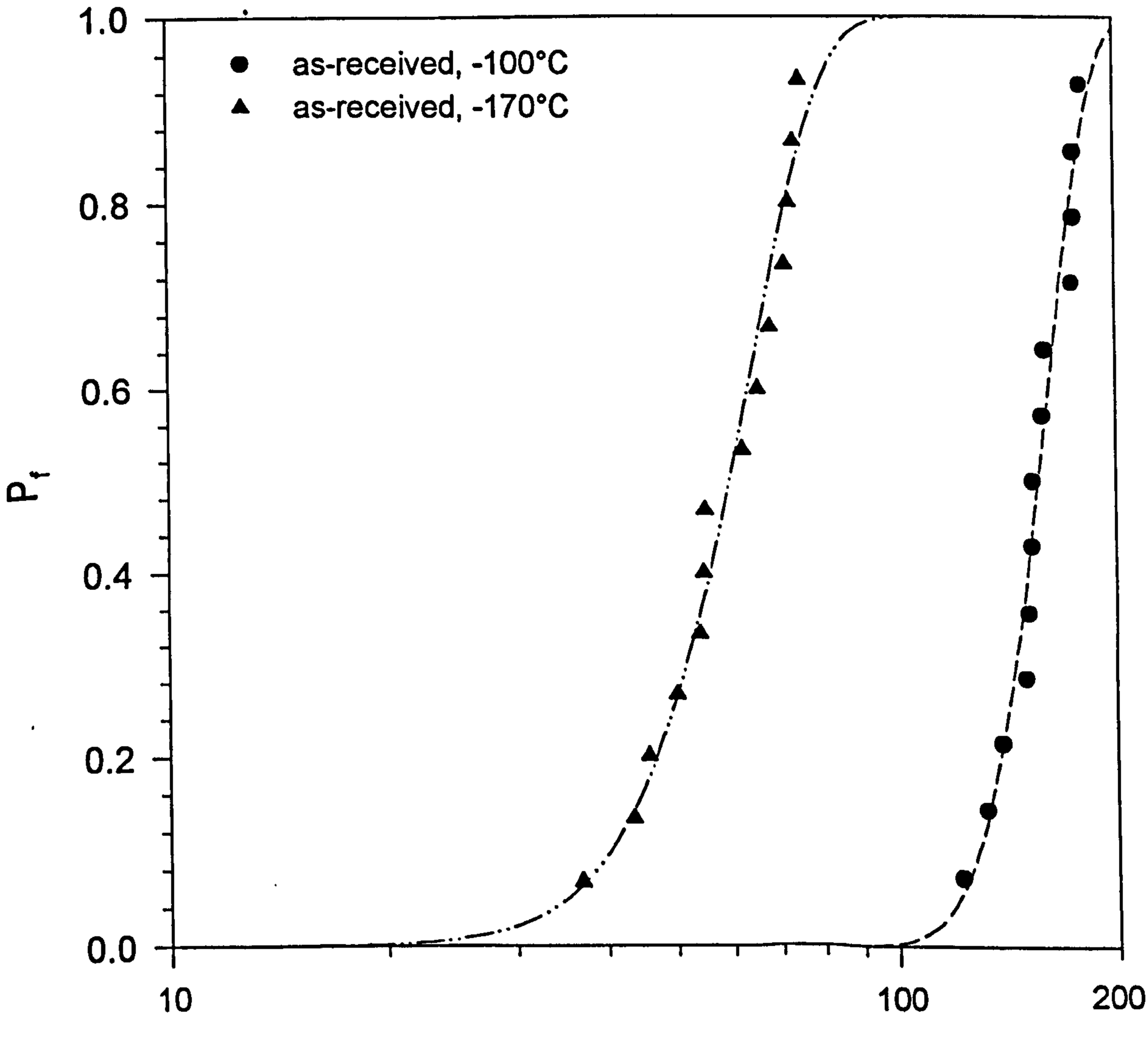

Figure 6.4. Prediction of A533B WPS Cleavage Toughness Distribution using combined Wallin and Chell Models at -170°C

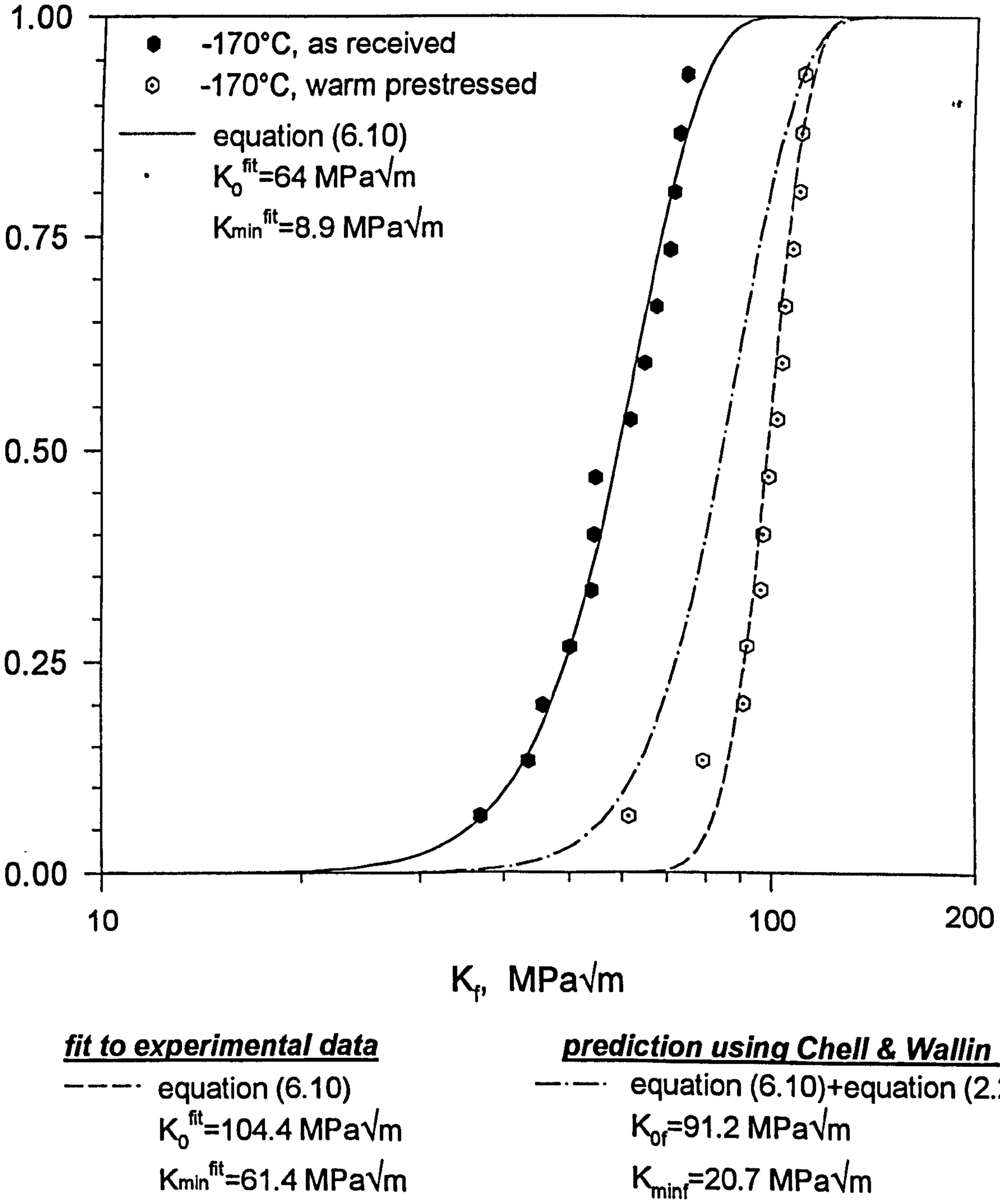

Figure 6.5. Chell Model, normalised by K_{Ic} for use in Statistical Analysis of A533B WPS cleavage toughness data obtained at -170°C

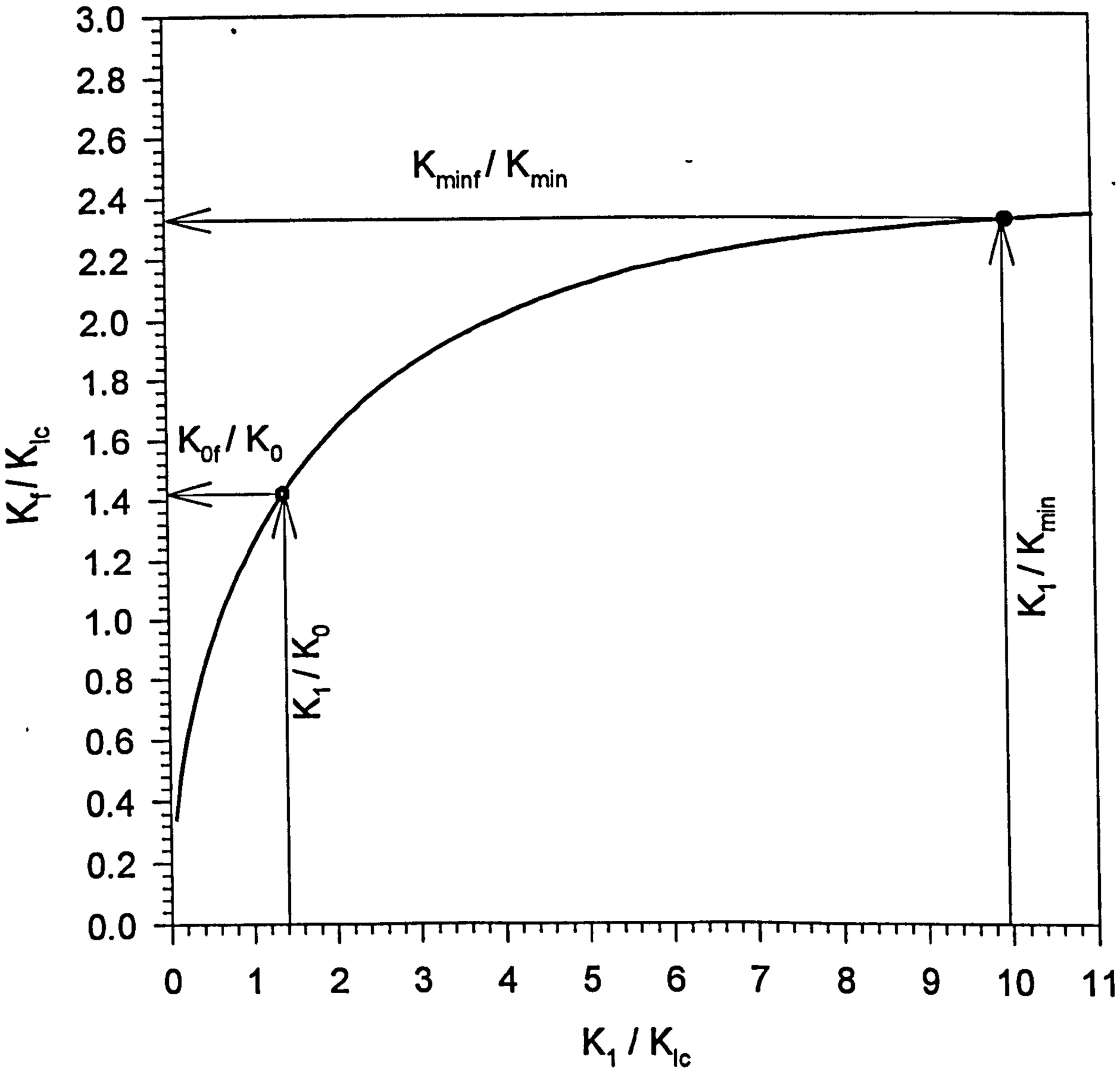

Figure 6.6. Prediction of A533B WPS Cleavage Toughness Distribution using combined Wallin and Chell Models at -100°C

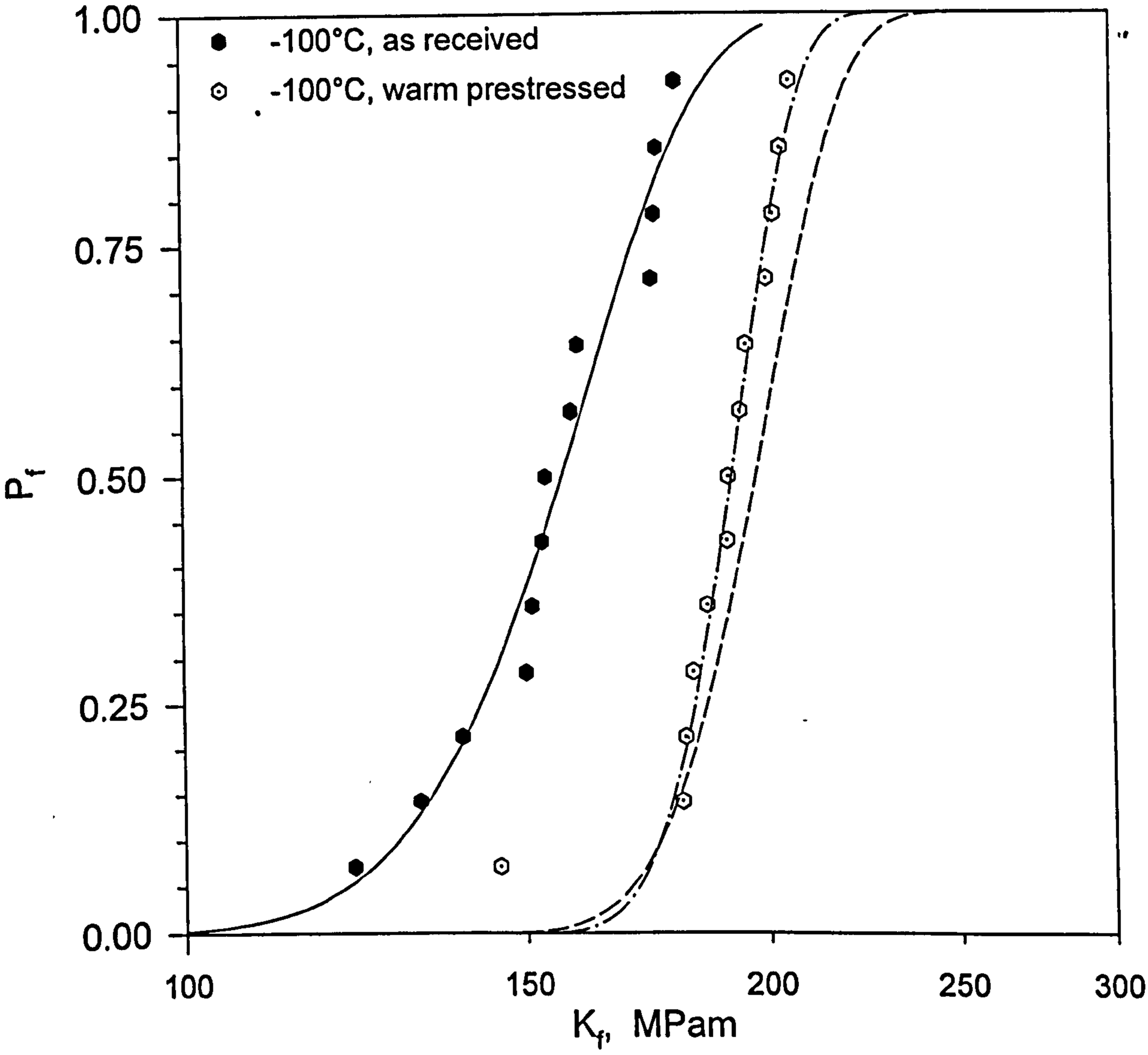

fit to experimental data

——— equation (6.10), as received
K_0=164 MPam
K_{min}=82.5 MPam

—·—·· equation (6.10), warm prestressed
K_0=196 MPam
K_{min}=149 MPam

prediction using Chell & Wallin

– – – equation (6.10) + equation (2.27)
K_{0f}=203 MPam
K_{minf}=140 MPam

Figure 6.7. Effect of warm prestressing on cleavage toughness distribution of BS1501 steel fractured at -120°C

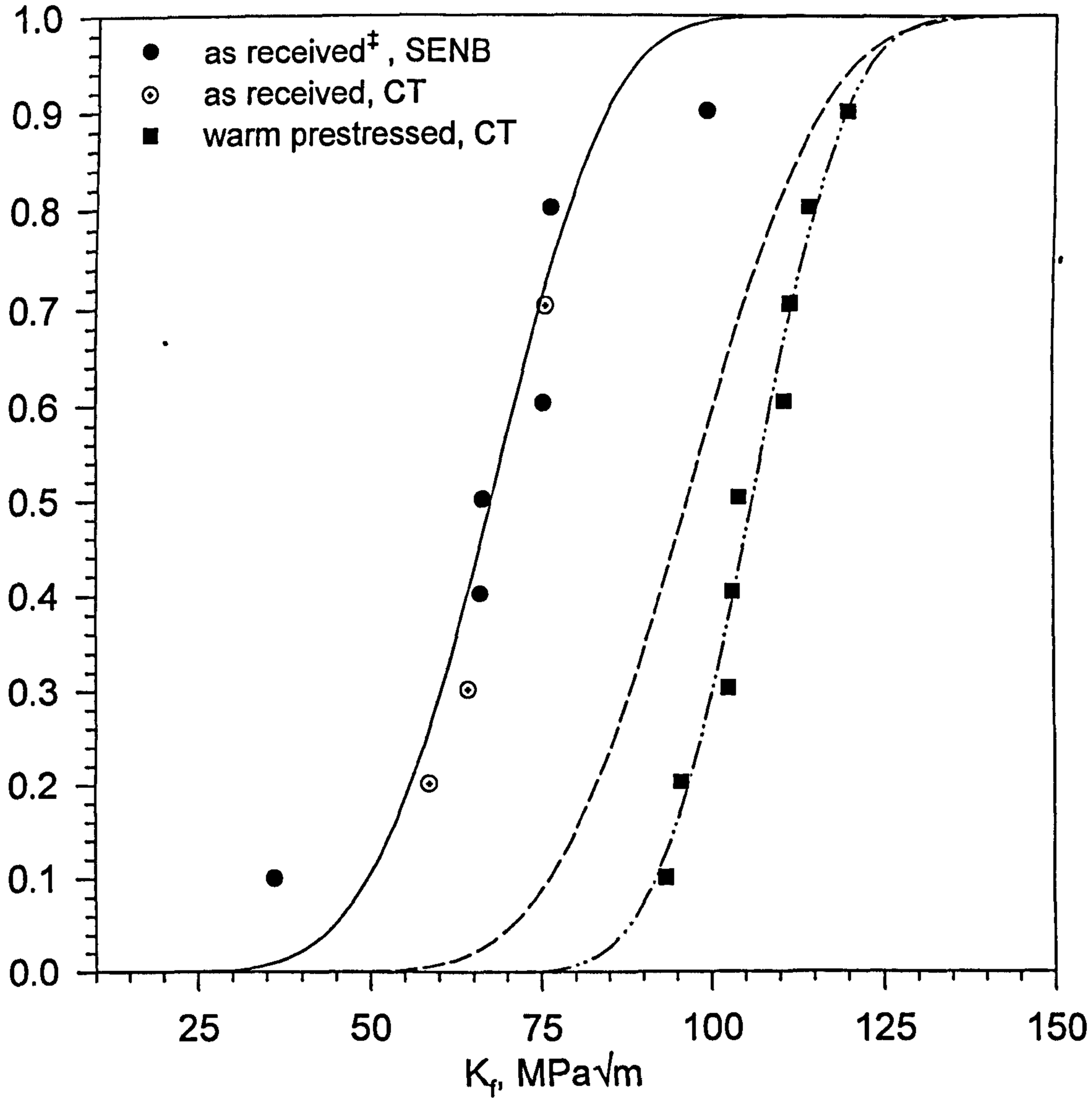

fitted to experimental data

—— equation (6.10)
K_0=72.4 MPa√m
K_{min}=19.7 MPa√m

—·— equation (6.10)
K_0=109.9 MPa√m
K_{min}=68.33 MPa√m

prediction using Wallin & Chell theory

– – – equation (6.10) + equation (2.27)
K_{0f}=100 MPa√m
K_{minf}=42 MPa√m

‡note: six data points obtained from BS1501 SENB specimens fractured at -120°C; specimens were of same geometry as those in A533B SENB study. Data obtained from Bell (1995)

Figure 6.8. A533B Steel data fractured at -170°C in the as-received and warm prestressed conditions.

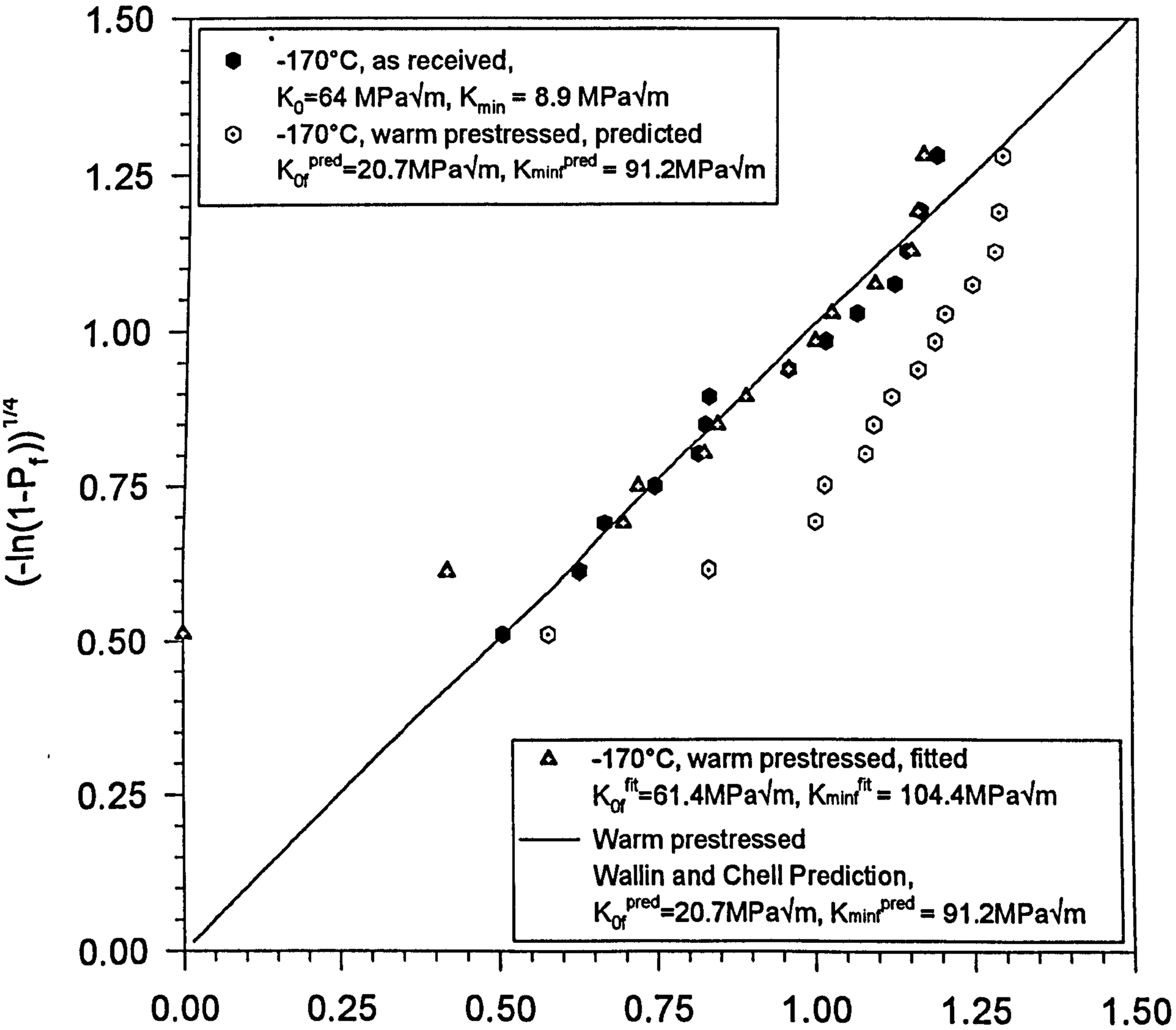

Figure 6.9. A533B Steel data fractured at -100°C in the as received and warm prestressed conditions. Data normalised by K_0 and K_{min}

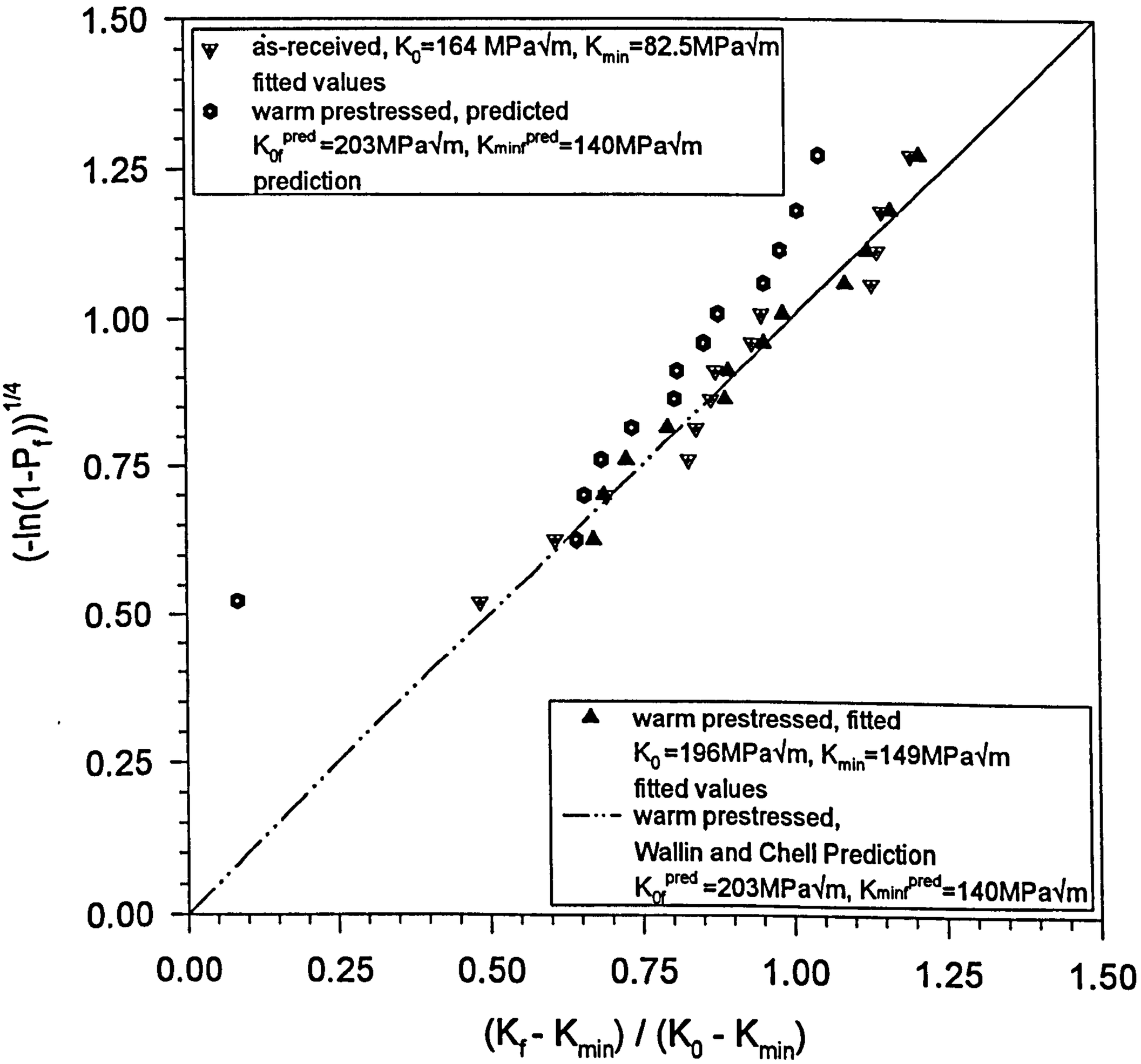

Figure 6.10. BS1501 Steel data fractured at -120°C in the as received and warm prestressed conditions.

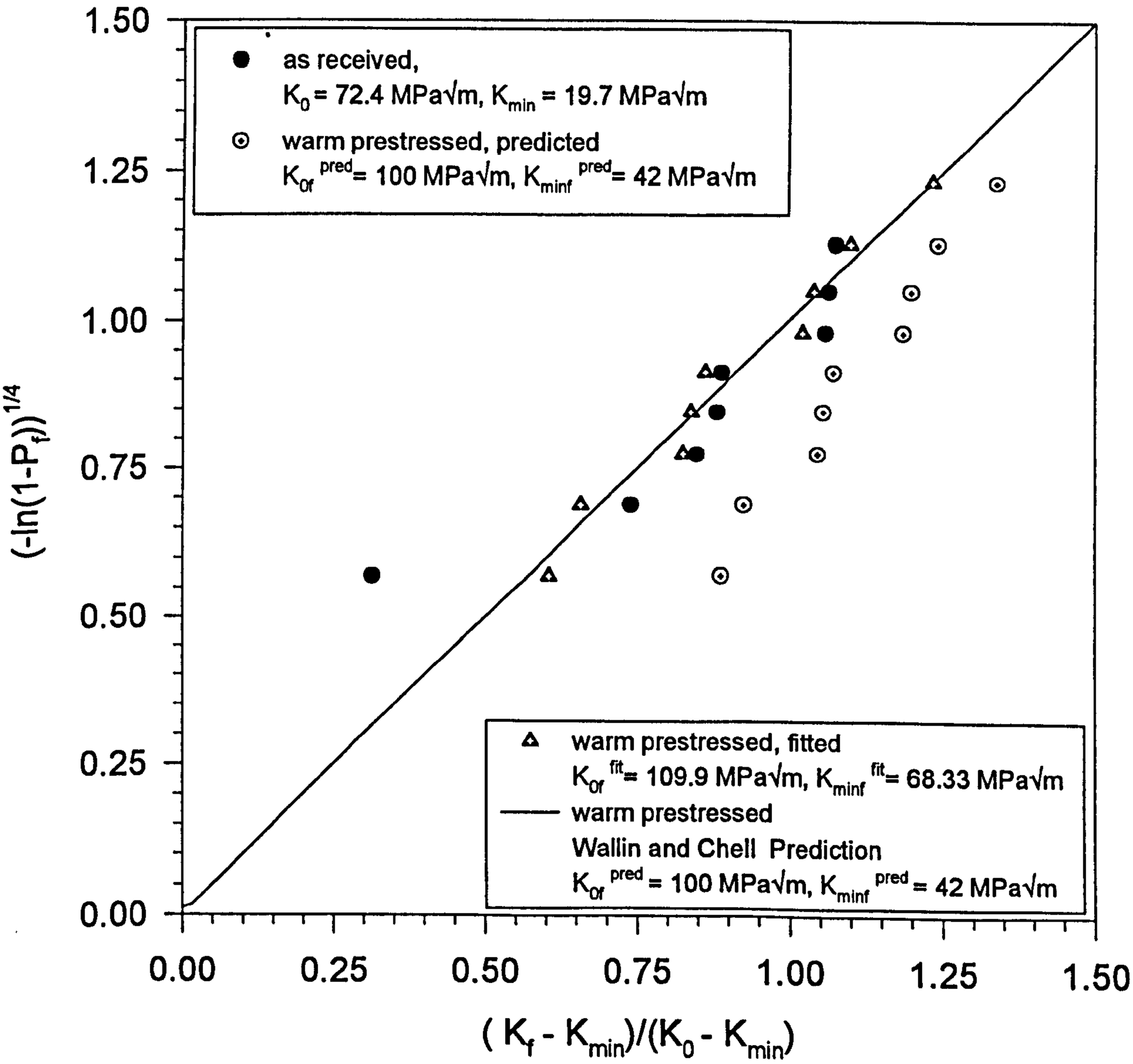

Figure 6.11. Experimental as-received A533B cleavage toughness data at -170°C in original and thickness corrected form

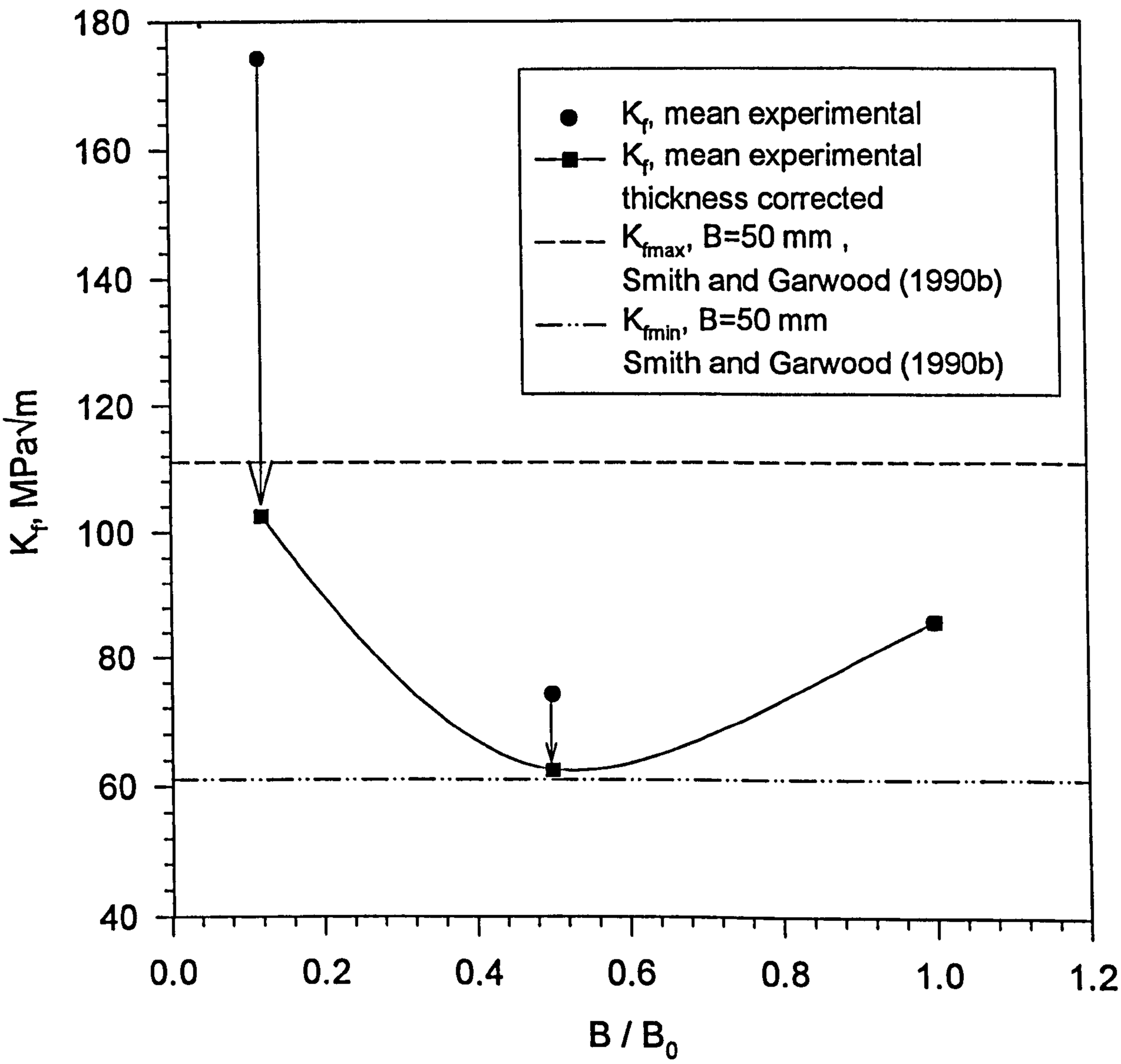

Figure 6.12. Predicted WPS cleavage toughness data using equation (6.21) in original and thickness corrected form

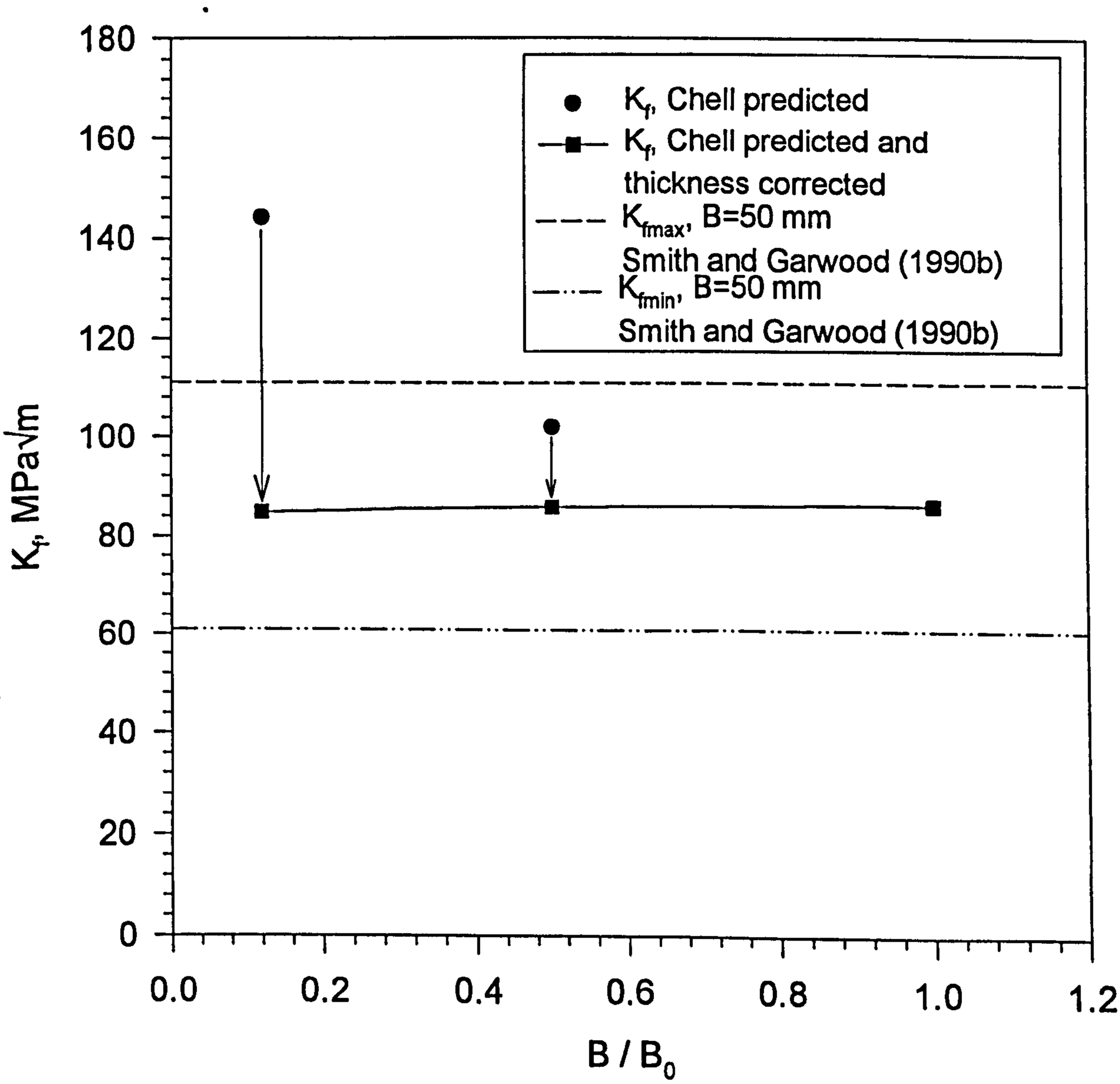

Figure 6.13. Experimental WPS cleavage toughness data, corrected and compared to Chell Model Predictions

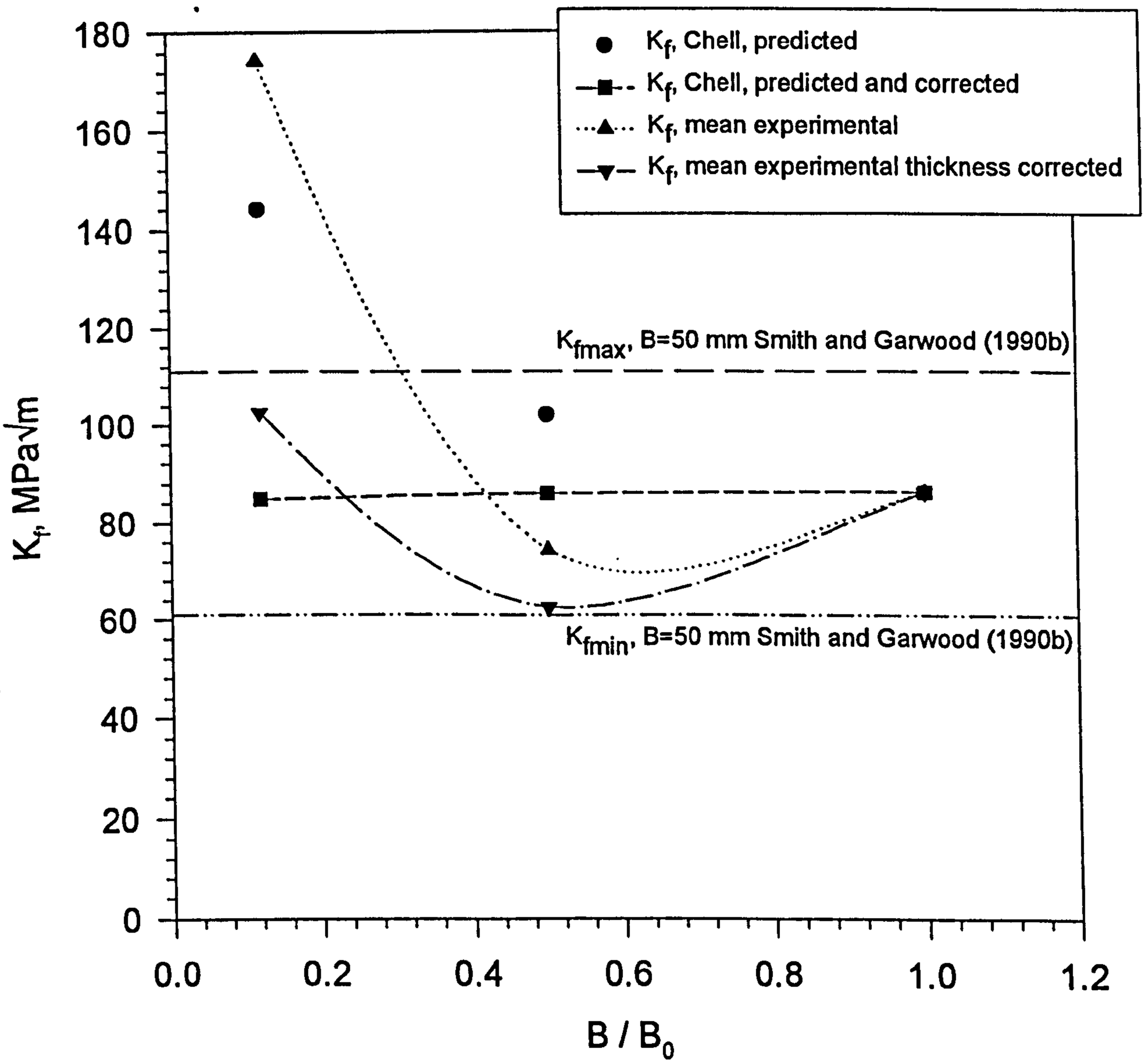

Figure 6.14. Thickness correction of 6mm cleavage toughness data to 50mm reference thickness

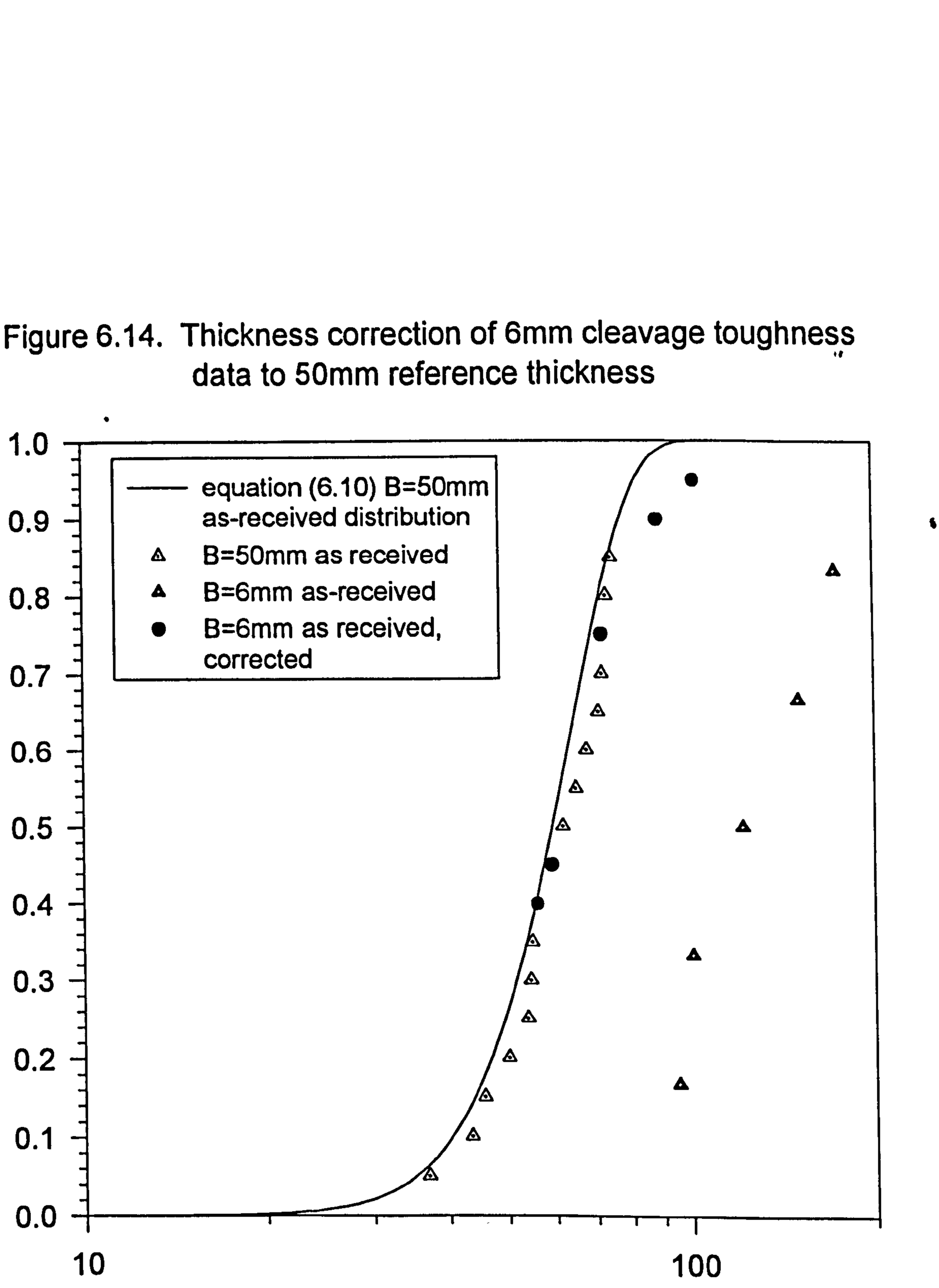

Figure 6.15. Thickness correction of 6mm thick warm prestressed specimens to 50mm reference thickness

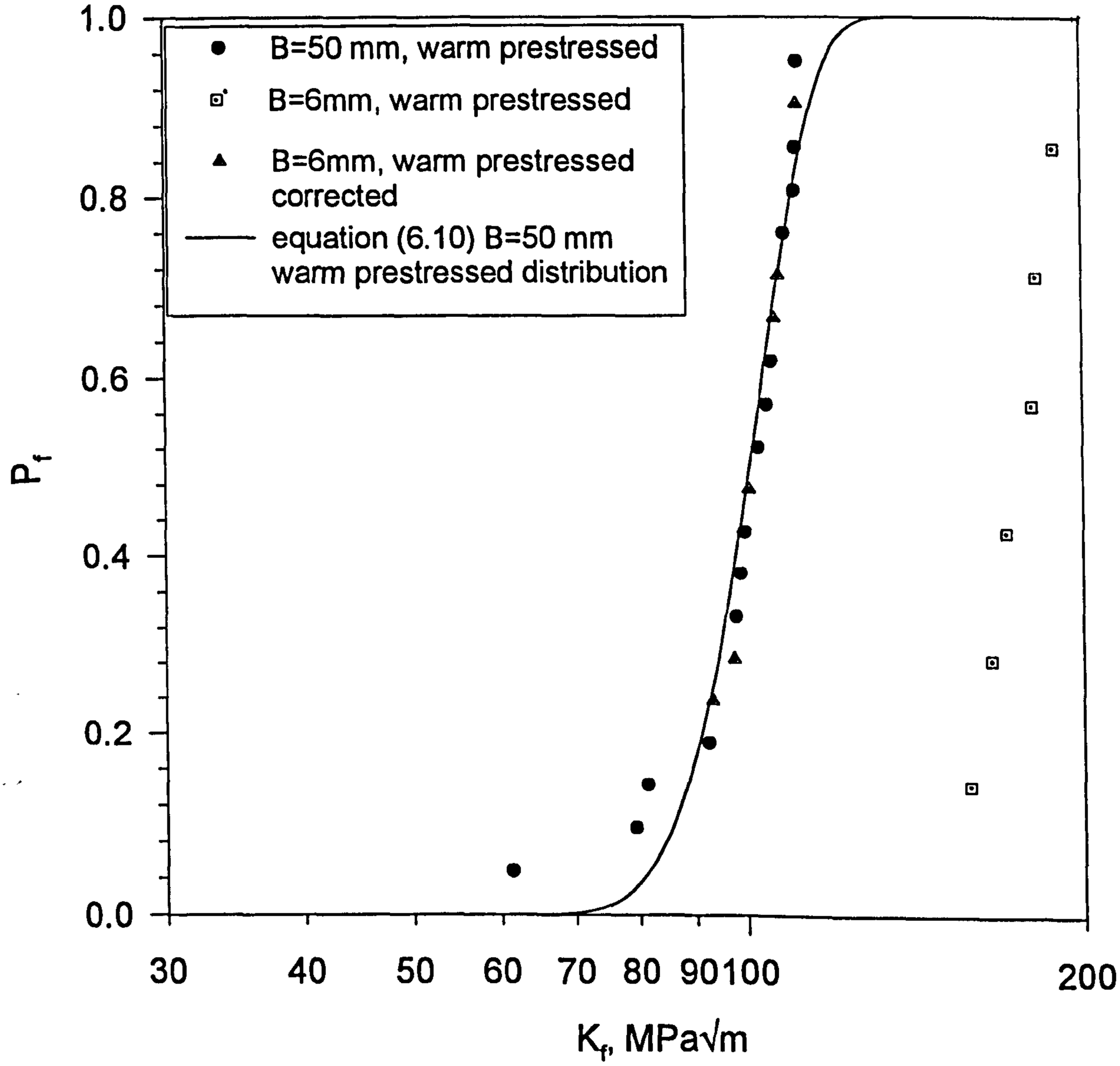

Figure 6.16. Finite element predictions for K_f following warm prestressing compared to experimental results for A533B from various authors.

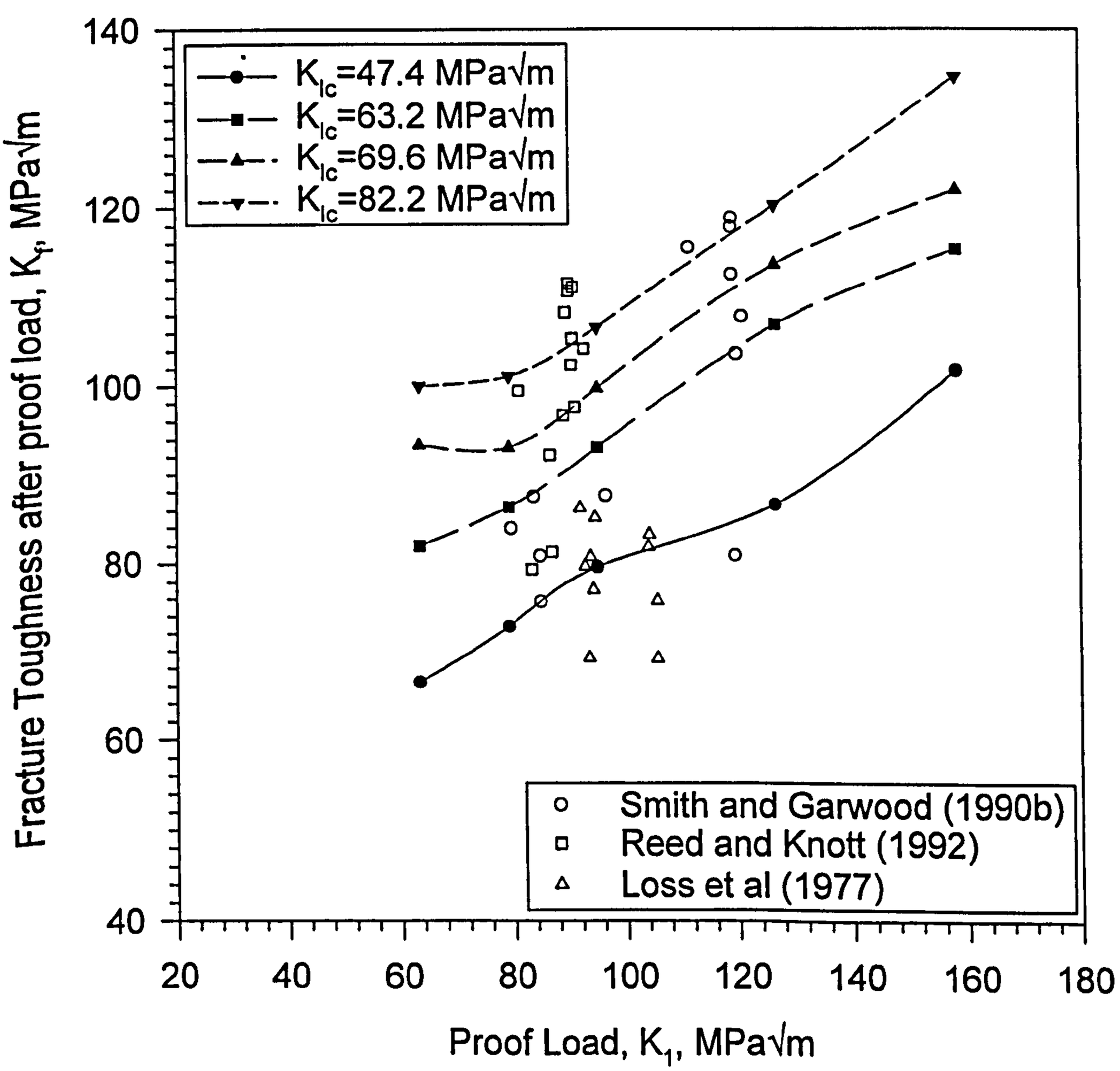

Figure 6.17. Exact Chell Model compared to finite element predictions and predictions obtained via the Curry Model

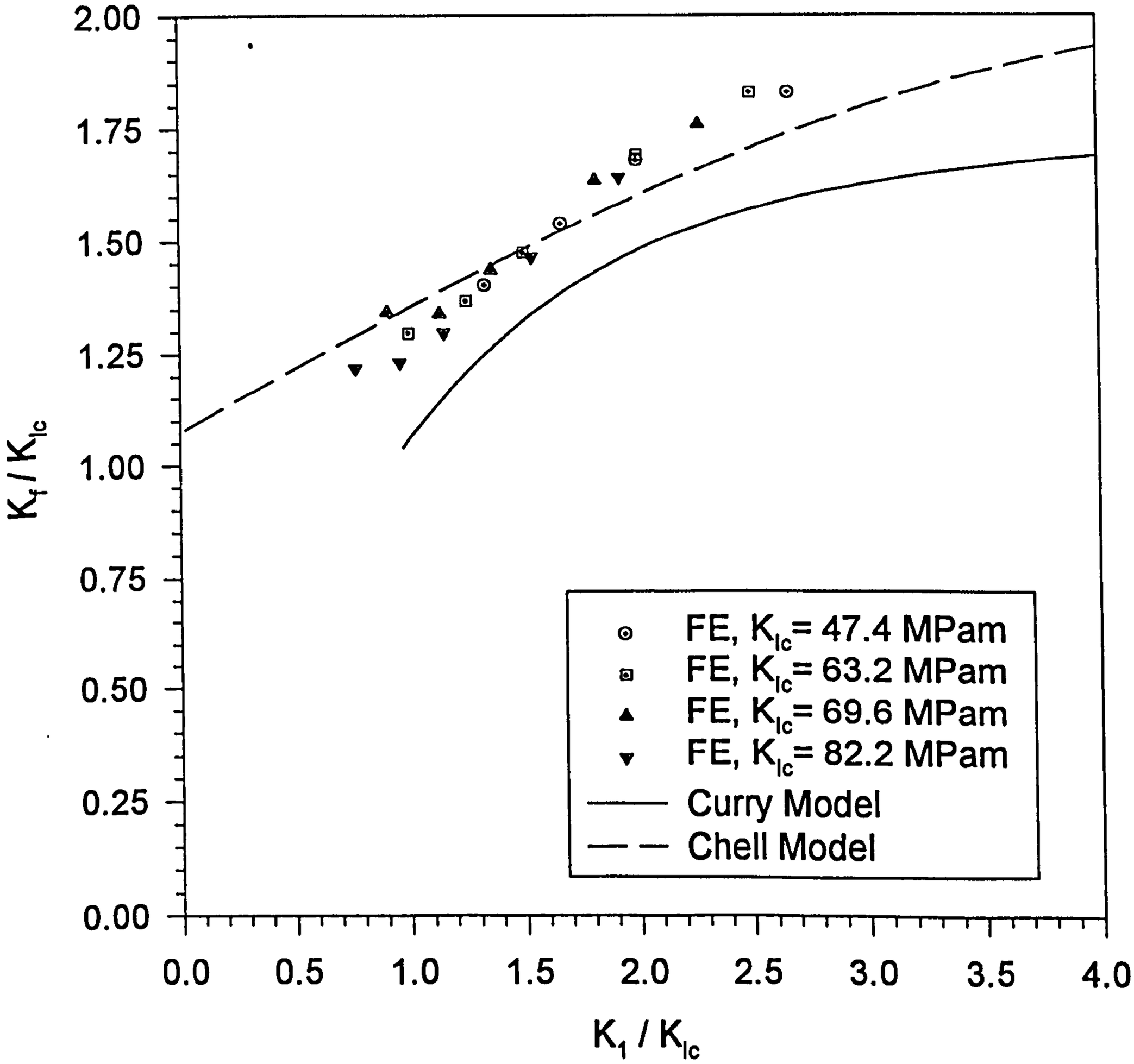

Figure 6.18. Warm Prestressed and as-received fracture stress distribution compared to the elastic HRR field at WPS fracture.

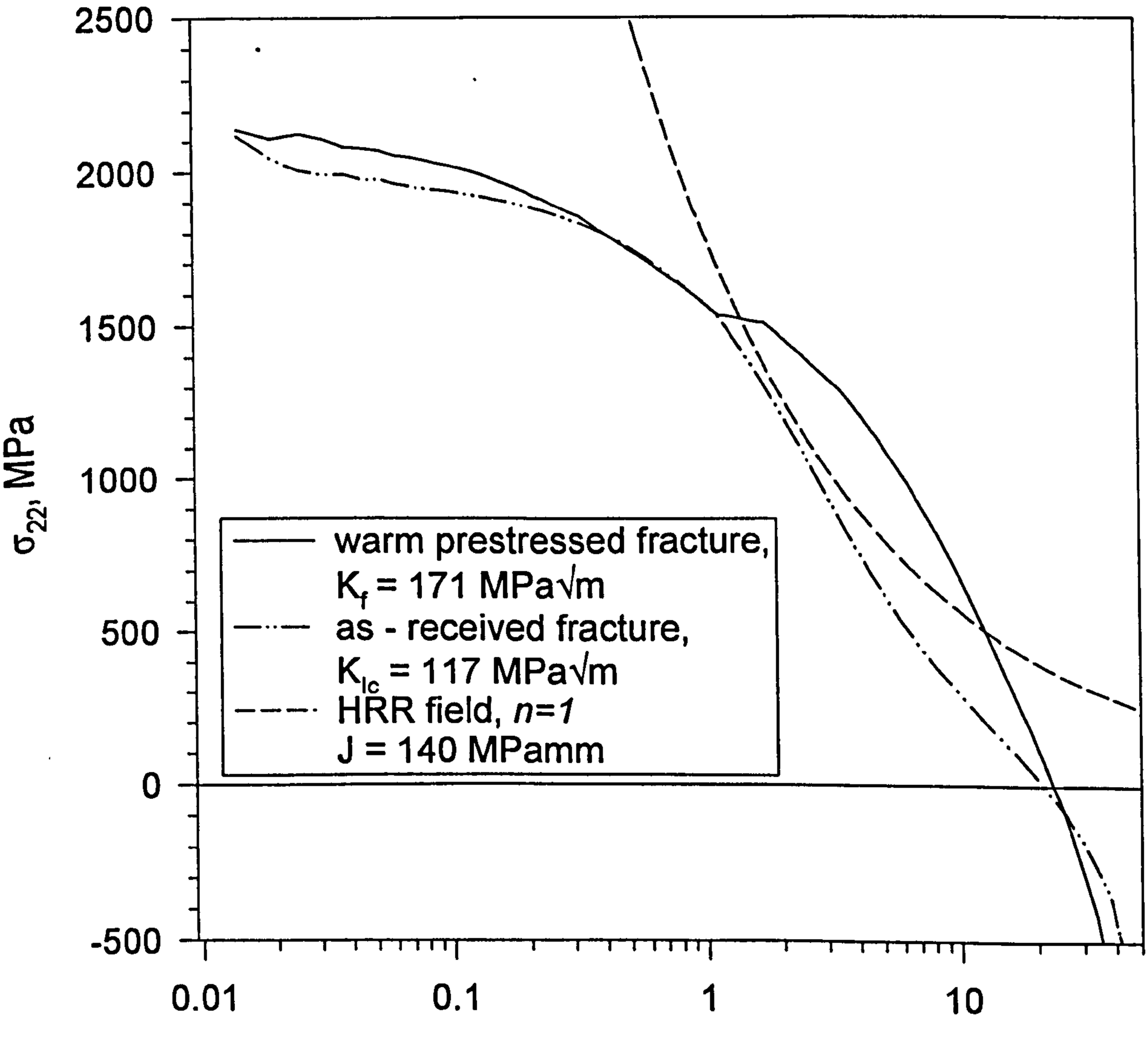

distance ahead of crack tip, r, mm.

Figure 6.19. Curry prediction for final stress field compared to actual stress field at fracture

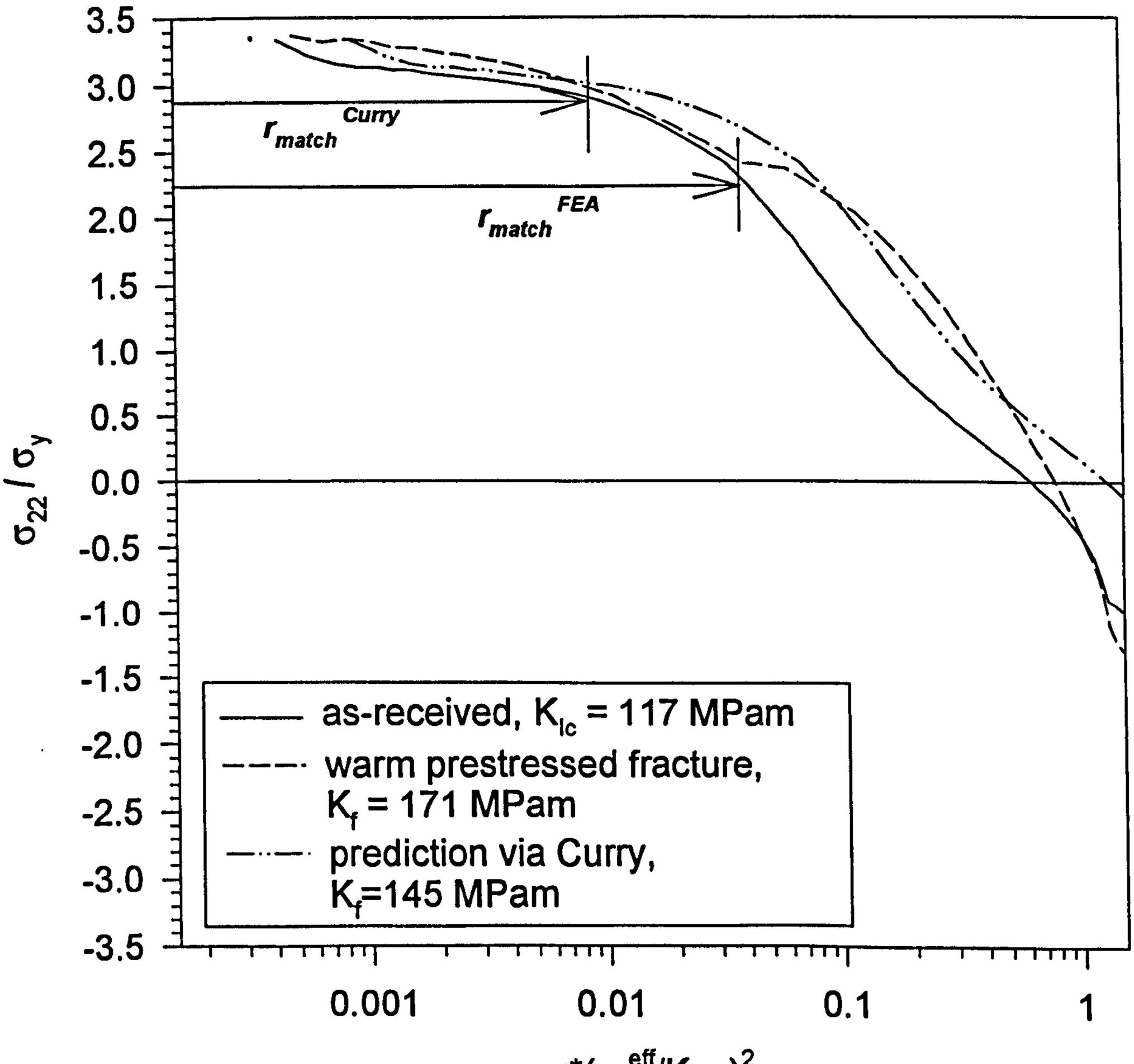

Figure 6.20. Comparison between Chell model of cleavage toughness following warm prestressing and sub critical crack growth and finite element predictions based on matching peak stress

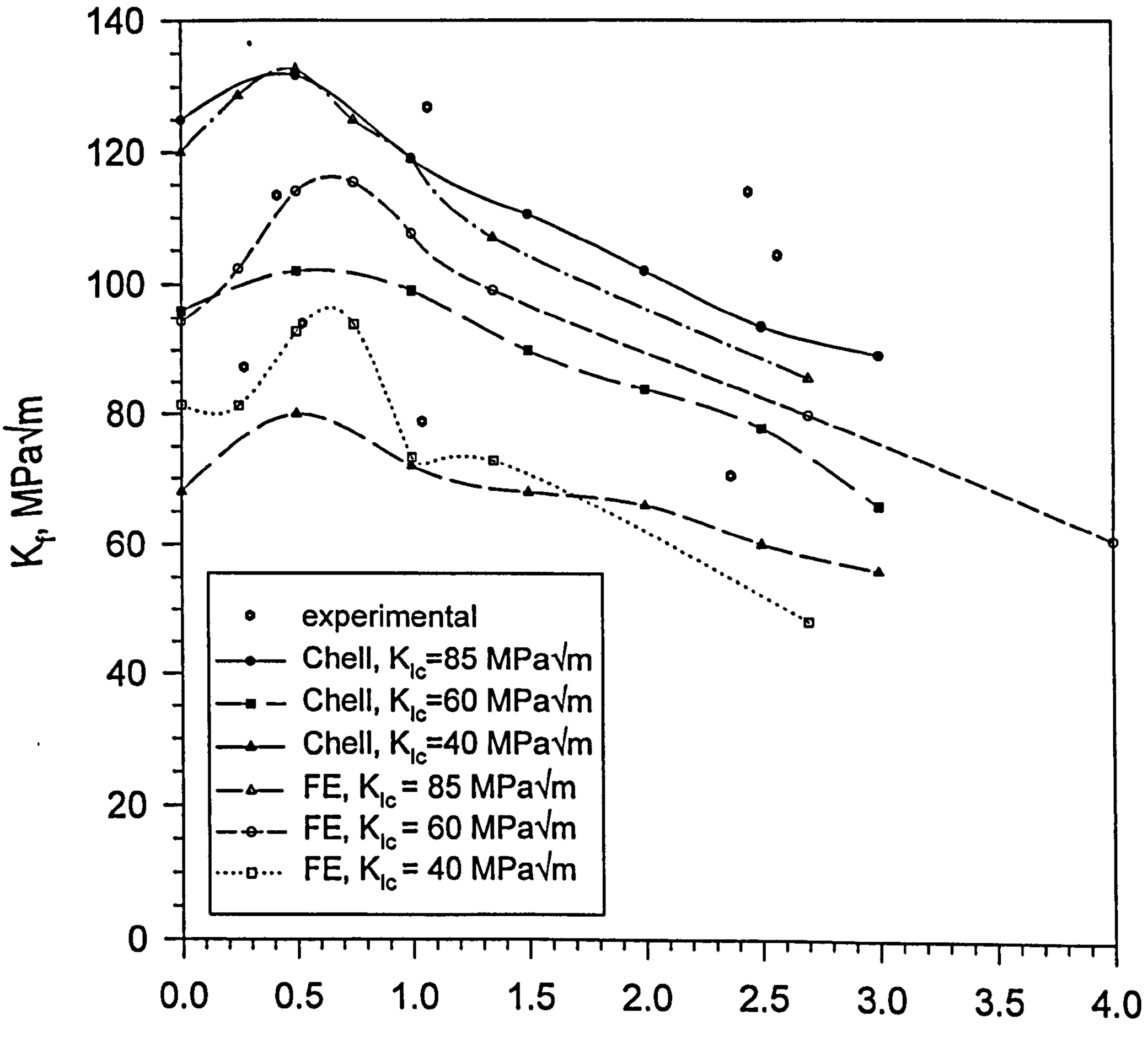

Figure 6.21. Finite element predictions of failure following sub-critical crack growth obtained by matching far field stress compared to experimental results and Chell Model solutions.

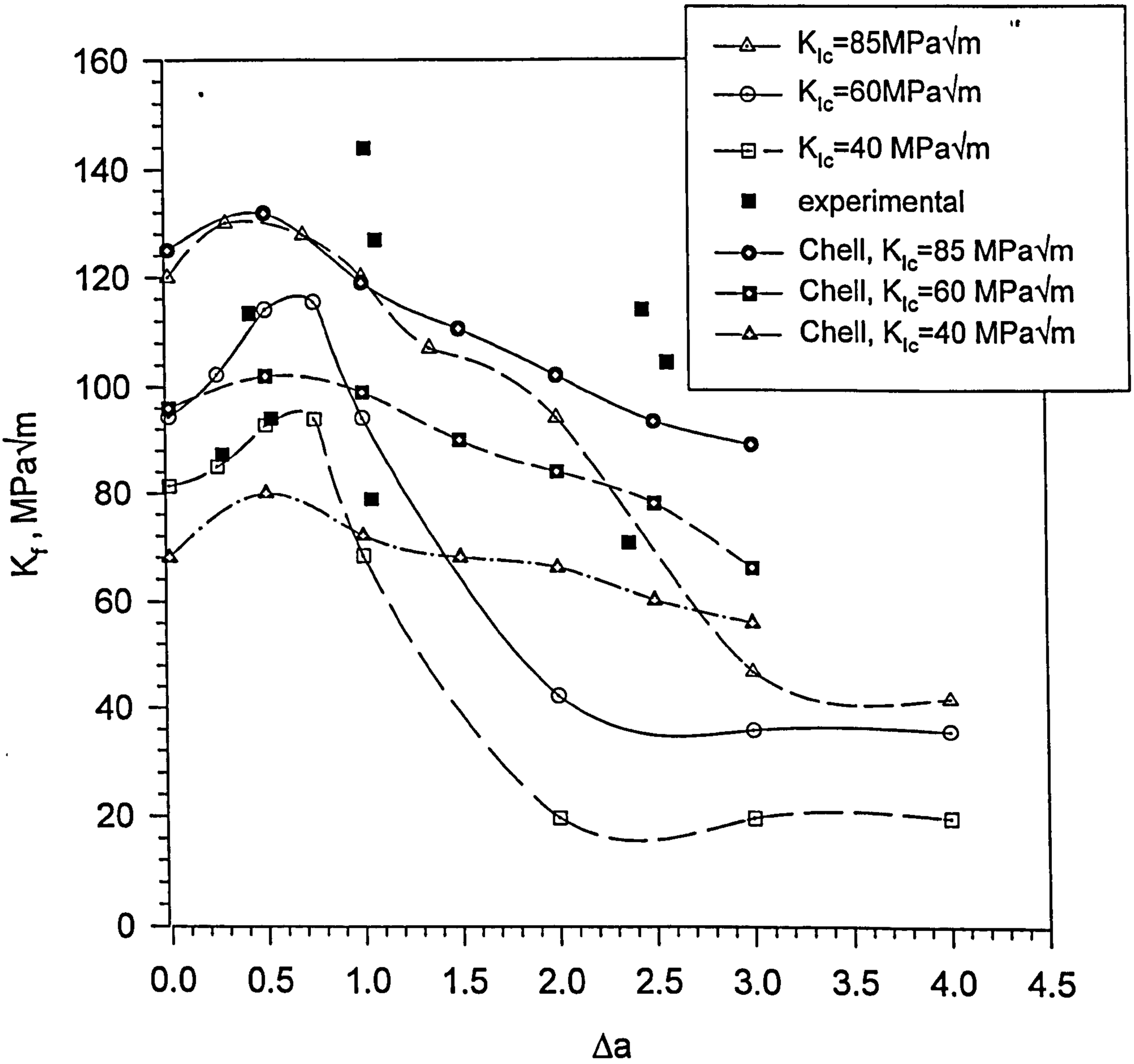

UNIVERSITY OF BRISTOL LIBRARY
ENGINEERING